UNIVERSITY OF CALIFORNIA,
IRVINE

Black Holes and Revelations: Dynamical Mass Measurements of Supermassive Black Holes in Early-Type Galaxies with ALMA and HST

DISSERTATION

submitted in partial satisfaction of the requirements
for the degree of

DOCTOR OF PHILOSOPHY

in Physics

by

Kyle Kristian Muyalde Kabasares

Dissertation Committee:
Professor Aaron J. Barth, Chair
Professor James S. Bullock
Professor David A. Buote

2023

DEDICATION

To my family and friends. In particular, to the loving memory of my late grandfather Cris D. Kabasares, whose elegance with writing I can only hope to emulate.

TABLE OF CONTENTS

LIST OF FIGURES

LIST OF TABLES

ACKNOWLEDGMENTS

Portions of Chapter 2, as well as the entirety of Chapters 3 and 4 of this dissertation, are adapted from the material as it appears in: Kabasares, K. M., Barth, A. J., Buote, D. A., Boizelle, B. D., Walsh, J. L., Baker, A. J., Darling, J., Ho, L. C., & Cohn, J. (2022). Black Hole Mass Measurements of Early-type Galaxies NGC 1380 and NGC 6861 through ALMA and HST Observations and Gas-dynamical Modeling. The Astrophysical Journal, 934(2), 162. https://doi.org/10.3847/1538-4357/ac7a38. The co-authors listed in this publication are Aaron J. Barth, David A. Buote, Benjamin D. Boizelle, Jonelle L. Walsh, Andrew J. Baker, Jeremy Darling, Luis C. Ho, and Jonathan H. Cohn. This material is used with permission from The Astrophysical Journal.

Financial support for the research in this dissertation was provided by the NSF through grant AST-1614212 and through awards SOSPA6-003 and SOSPADA-002 from the National Radio Astronomy Observatory. This dissertation makes use of the following ALMA datasets: ADS/JAO.ALMA#2013.1.00229.S., ADS/JAO.ALMA#2015.1.00878.S, and ADS/JAO.ALMA#2017.1.00301.S. ALMA is a partnership of ESO (representing its member states), NSF (USA) and NINS (Japan), together with NRC (Canada), MOST and ASIAA (Taiwan), and KASI (Republic of Korea), in cooperation with the Republic of Chile. The Joint ALMA Observatory is operated by ESO, AUI/NRAO and NAOJ. The National Radio Astronomy Observatory is a facility of the National Science Foundation operated under cooperative agreement by Associated Universities, Inc. I also acknowledge usage of the NASA/IPAC Extragalactic Database (NED), which is operated by the Jet Propulsion Laboratory, California Institute of Technology, under contract with NASA. Additionally, this dissertation used observations made with the NASA/ESA Hubble Space Telescope under programs GO-15909 and GO-15226, obtained from the data archive at the Space Telescope Science Institute. STScI is operated by the Association of Universities for Research in Astronomy, Inc. under NASA contract NAS 5-26555. Additional archival observations used in this thesis were obtained from the Hubble Legacy Archive (HLA) under GO programs 15181. The HLA is a collaboration between STScI, the Space Telescope European Coordinating Facility (ST-ECF/ESA) and the Canadian Astronomy Data Centre (CADC/NRC/CSA). I would also like to acknowledge and thank the Associated Graduate Students of UC Irvine for providing me a travel grant that was used to attend the 235th Meeting of the American Astronomical Society in Honolulu, Hawaii in January 2020. Finally, I acknowledge and thank the UC Irvine Department of Physics & Astronomy for providing me with a departmental fellowship for the last two quarters of my graduate school career, which allowed me to complete this dissertation in a timely manner.

While it will be nearly impossible to account for every single person who has helped me reach this point in my life, I will do my best.

First, I am eternally grateful for the support I have received from my PhD advisor, Aaron Barth. When I visited Irvine as a prospective graduate student, Aaron was randomly selected to be one of the professors I was scheduled to meet with. Given that I was intent on studying condensed matter physics at the time, I thought it was strange to be paired with

an astronomy professor. Over the course of our 30 minute conversation, however; Aaron's enthusiasm about astronomy and black holes reminded me of how fascinated I was with those topics years ago after reading Stephen Hawking's *A Brief History of Time*, and how disappointed I was that I never had the chance to take an astronomy course. Several months later, after realizing that specializing in condensed matter physics was not the right choice for me, I chose to specialize in astronomy. Aaron was supportive of my decision, and encouraged me to take my first astronomy course with him in the Spring of 2018. Since then, I never looked back. While my PhD has not been easy, Aaron's patience and understanding has allowed me to grow and develop as a scientist. Knowing that I could turn to him for advice whenever I got stuck, especially in the beginning, was a constant reminder that I made the right choice in asking him to be my advisor. I thank him for giving me opportunities to travel to places such as Lick Observatory, the National Radio Astronomy Observatory, Honolulu, Hilo, Pasadena, Sedona, and Seattle. During these trips, I learned multiple skills that were critical to my success as a graduate student and presented my research at international conferences. I am also grateful for his indispensable feedback on all my papers, conference abstracts, and fellowship materials over the years, and I will miss his random and entertaining anecdotes during our meetings.

We all have our giants whose shoulders we stand upon, and mine undoubtedly was my predecessor at Irvine, Prof. Ben Boizelle. Despite our short overlap at Irvine, I benefited greatly from Ben's guidance on gas-dynamical modeling. It was Ben who wrote and provided me the initial snippet of code that eventually became my workhorse program for all of the projects featured in this dissertation. He is also responsible for reducing every ALMA dataset I have ever analyzed, published results from, and will present in this dissertation, and I cannot thank him enough for that. I have sent dozens of distress emails to Ben over the years when confronted with problems I did not know how to solve, and he has always responded in great detail that helped me get back on the right path.

Surviving graduate school would not have been possible without the support of so many valuable friends and colleagues. I could not have endured the rigours of my first-year in the PhD program without the support of friends such as Sophia Nasr, Tae Baxter, Francisco Mercado, Manuel Paul, and Daniel McKeown. I am also appreciative of the support and words of wisdom from the postdocs and research scientists in Aaron's research group such as Dale Mudd, Hengxiao Guo, and Vivian U. I will also be forever thankful for people such as Lisabeth Santana and Olivia Dalager who helped me through a catasrophic knee injury that I dealt with during years two and three of my PhD and always did their best in keeping my spirit up.

Given we are all part of the same academic family tree, I am also incredibly happy to have met, collaborated with, and befriended Dr. Jonathan Cohn and Silvana Delgado Andrade at Texas A&M University. During Labor Day weekend in 2022, fate decided to strand me in Sedona, Arizona with a car breakdown. Thinking I would be left to spend the long weekend by myself, I was kindly invited to join Jonathan, Silvana, and the rest of their travel group on their weekend plans. I am immensely grateful for the friendship and support that they

provided me during my final year of graduate school, which has been one of the greatest gifts of my life.

I would also like to thank the physics faculty at UC Merced, especially Carrie Menke, Linda Hirst, Sayantani Ghosh, Chih-Chun Chien, and Dustin Kleckner for providing me a solid foundation in physics and giving me the confidence that I could succeed in graduate school.

I am also blessed to have developed friendships with various roommates of mine in Irvine such as Jacob Hyatt, Jhih-Yuan Chang, Kai Yoshioka, Ribby Suh, and Teymour Mushfiq. They are responsible for an uncountable amount of enjoyable movie nights and late-night food runs to In-n-Out and McDonalds. In particular, I thank Jacob for watching hundreds of hours of both TV and movies with me in addition to the hundreds of hours of video games we played. Engaging in these activities always lifted my mood on even the toughest days of graduate school.

I thank my family for all of their unconditional love and support over the years. I could not have asked for a better set of parents and grandparents to help foster my love for learning. They have always encouraged me to pursue what I love and always with the utmost confidence that I could succeed at whatever I put my mind to. It is through their support and belief in me that I was able to receive an excellent education at every academic level. Finally, I thank my brother Chad who has taught me more about life and the power of understanding, kindness, and love than anyone else.

VITA

Kyle Kristian Muyalde Kabasares

RESEARCH INTERESTS

Supermassive black holes, gas-dynamical modeling, galaxy formation & evolution, gas kinematics, submillimeter/radio astronomy

EDUCATION

Doctor of Philosophy in Physics **2023**
University of California, Irvine *Irvine, CA*

Master of Science in Physics **2019**
University of California, Irvine *Irvine, CA*

Bachelor of Science in Physics, Minor in Applied Mathematics **2017**
University of California, Merced *Merced, CA*

RESEARCH EXPERIENCE

Graduate Student Researcher **2018–2023**
University of California, Irvine *Irvine, California*

Undergraduate Student Researcher **2015–2017**
University of California, Merced *Merced, California*

Intern **Summer 2016**
NASA Student Airborne Research Program *Irvine, California*

TEACHING EXPERIENCE

Teaching Assistant

Observational Astronomy Laboratory **Fall 2022**
University of California, Irvine
Physics 139

Classical Physics I **Summer 2022**
University of California, Irvine
Physics 7C

Basic Physics III **Summer 2021**
University of California, Irvine
Physics 3C

Introduction to Astronomy **Summer 2021**
University of California, Irvine
Physics 20A

Basic Physics I Laboratory **Spring 2021**
University of California, Irvine
Physics 3LC

Observational Astronomy Laboratory **Fall 2020**
University of California, Irvine
Physics 139

Classical Physics II Laboratory **Spring 2018**
University of California, Irvine
Physics 7LD

Basic Physics II **Winter 2018**
University of California, Irvine
Physics 3B

Classical Physics I **Fall 2017**
University of California, Irvine
Physics 7C

Cal-Bridge Physics Tutor **2019-2021**
Cal-Bridge Program

FIRST-AUTHOR REFEREED JOURNAL PUBLICATIONS

Black Hole Mass Measurements in Early-Type Galaxies NGC 1380 and NGC 6861 through ALMA and HST Observations and Gas-dynamical Modeling **2022**
The Astrophysical Journal

FIRST-AUTHOR PUBLICATIONS SUBMITTED

Molecular Gas-Dynamical Mass Measurements of the Central Black Holes in Early-Type Galaxies NGC 4786 and NGC 5193 Using Observations from ALMA and HST **2023**
The Astrophysical Journal

OTHER REFEREED JOURNAL PUBLICATIONS

An ALMA Gas-dynamical Mass Measurement of the Supermassive Black Hole in the Local Compact Galaxy UGC 2698 **2021**
The Astrophysical Journal

Black Hole Mass Measurements of Radio Galaxies NGC 315 and NGC 4261 Using ALMA CO Observations **2020**
The Astrophysical Journal

Observing Severe Drought Influences on Ozone Air Pollution in California **2019**
Environmental Science & Technology

OTHER JOURNAL PUBLICATIONS IN PREPARATION

ALMA Gas-Dynamical Mass Measurements of the Supermassive Black Holes in Two Local Relic Galaxies

The Seoul National University AGN Monitoring Project IV: the Hα Size-Luminosity Relation

Mapping Dust Attenuation in Luminous Early-Type Galaxies

HONORS AND AWARDS

Honorable Mention, Chambliss Astronomy Achievement Student Award **2022**
240th Meeting of the American Astronomical Society

Travel Grant **2020**
Associated Graduate Students of UC Irvine

Honorable Mention **2019**
NSF Graduate Research Fellowship Program

Senior Thesis Award **2017**
Department of Physics - University of California, Merced

Outstanding Undergraduate Award **2017**
Department of Physics - University of California, Merced

Honorable Mention **2016**
California Alliance for Minority Participation Poster Symposium

1st Place **2016**
Undergraduate Research Poster Competition - University of California, Merced

ABSTRACT OF THE DISSERTATION

Black Holes and Revelations: Dynamical Mass Measurements of Supermassive Black Holes in Early-Type Galaxies with ALMA and HST

By

Kyle Kristian Muyalde Kabasares

Doctor of Philosophy in Physics

University of California, Irvine, 2023

Professor Aaron J. Barth, Chair

This dissertation presents the results of a set of research projects focused on using optical and near-infrared Hubble Space Telescope and CO(2−1) Atacama Large Millimeter/submillimeter observations to measure the masses of central black holes in nearby (< 100 Mpc) early-type galaxies. By modeling the rotation of circumnuclear disks, I dynamically measured the masses of eight supermassive black holes in the following galaxies: NGC 1380, NGC 6861, NGC 4786, NGC 5193, NGC 3245, NGC 4435, NGC 5838, and ESO 208-G21.

I developed a thin disk gas-dynamical modeling framework in Python in order to analyze, model, and interpret the observed ALMA CO(2−1) gas kinematics. Using near-infrared (J and H-band) Hubble Space Telescope data from Wide Field Camera 3, I constructed Multi-Gaussian Expansion models in `GALFIT` to model the gravitational potential of the host galaxy and developed a novel method to account for the effects of circumnuclear dust on molecular gas-dynamical black hole mass measurements using two-band color information. I performed rigorous systematic and statistical tests of my dynamical models to fully explore the error budget of each measurement. Key limiting factors on the precision of mass measurements such as dust extinction, recent star-formation, low level active galactic nuclei activity, insuf-

ficient angular resolution, and lack of dynamical information within the black hole's sphere of influence were identified.

In summary, I provide the following $M_{\rm BH}$ measurements and estimates for the eight early-type galaxies: NGC 1380 ($M_{\rm BH} = [1.02 - 2.04] \times 10^8\,M_\odot$), NGC 6861 ($M_{\rm BH} = [1.13 - 2.89] \times 10^9\,M_\odot$), NGC 4786 ($M_{\rm BH} = [3.7 - 6.4] \times 10^8\,M_\odot$), NGC 5193 ($M_{\rm BH} = [1.3 - 2.9] \times 10^8\,M_\odot$), NGC 3245 ($M_{\rm BH} = [0.9 - 1.4] \times 10^8\,M_\odot$), NGC 4435 ($M_{\rm BH} = [0.5 - 0.8] \times 10^8\,M_\odot$), NGC 5838 ($M_{\rm BH} = [0.01 - 19.4] \times 10^8\,M_\odot$), ESO 208-G21 ($M_{\rm BH} = 2.3 \times 10^8\,M_\odot$). The mass measurements of the central black holes in NGC 1380, NGC 4786, NGC 5193, NGC 5838, and ESO 208-G21 are the first black hole mass measurements of any kind in those galaxies, while the NGC 3245, NGC 4435, and NGC 6861 mass measurements provide independent crosschecks of previous results.

Chapter 1

A Brief History of Supermassive Black Hole Research

> "'The essential result of this investigation is a clear understanding as to why the 'Schwarzschild singularities' do not exist in physical reality."
>
> - Albert Einstein (1939)

1.1 A Preface

This dissertation presents several gas-dynamical mass measurements of supermassive black holes conducted with the Atacama Large Millimeter/submillimeter Array (ALMA) and the Hubble Space Telescope (HST). The introductory chapter will provide a brief overview into the history of supermassive black hole research as a whole, as well as a road map through the rest of the dissertation. This field originated six decades ago and has forever changed our understanding of the universe. Given the narrow scope of this dissertation, this introduction unfortunately cannot encapsulate all the remarkable developments that took place through-

out the field's history. Nevertheless, it is my hope that this summary highlights some of the most important moments and gives the reader the necessary context to appreciate how far research has progressed, ALMA's contributions to our understanding of SMBHs, and the potential future developments. For further reading on the history of supermassive black holes, the reader is encouraged to consult the thorough review by Kormendy and Ho (2013).

1.2 The First 30 Years (1963 - 1993)

The origin of SMBH research can be traced to the discovery that the starlike object associated with the dominant radio source 3C 273 had the remarkably high (for the time) redshift of $z = 0.158$ (Schmidt, 1963). With the assumption that this redshift was attributed to the expansion of the universe, 3C 273 was, at the time, the second-furthest known object in the universe. Even more surprising was the finding that 3C 273 was about 100 times brighter at optical wavelengths than the most luminous galaxies with comparable radio sources, but had to be confined to a region of $\sim$1 kpc. This groundbreaking discovery marked the identification of the first quasar.

Soon after the 3C 273 discovery, other quasars and less luminous active galactic nuclei (AGNs) were discovered, and a new area of astronomical research emerged. With brightness fluctuations occurring on timescales as short as days, theoretical research pioneered by individuals such as Edwin Salpeter, Yakov Zel'dovich, Donald Lynden-Bell, Martin Rees, and others suggested that quasars and other AGN are powered by the accretion of matter onto SMBHs (Salpeter, 1964; Zel'dovich, 1964; Lynden-Bell, 1969; Lynden-Bell and Rees, 1971). These SMBHs were theorized to possess masses of $M_{\rm BH} = 10^6\,M_\odot - 10^9\,M_\odot$, but observations at the time did not have the ability to dynamically detect them. As research progressed, it became evident that quasars were more prevalent earlier in the universe than in the present-day (Schmidt, 1968, 1970; Petrosian, 1973). In addition, once the accretion

process ended, theory suggested that the dark remnants of luminous quasars should remain after the end of accretion episodes. Thus, a new hypothesis was born: dead quasars are hiding at the centers of nearby galaxies. The next challenge was to find them.

1.2.1 Challenges to Dynamical Detection of SMBHs

Dynamically detecting an SMBH is tantamount to measuring its mass. To obtain the mass of an SMBH, one studies the observed motions of dynamical tracers such as stars or gas in the SMBH's vicinity to infer the amount of gravitational force applied, and then uses Newton's laws of gravitation to calculate the mass that produces the force. Every galaxy contains stars near its center, and the velocities of these stars can be measured through either the Doppler broadening of their absorption lines in the integrated spectra, or in the case of the Milky Way and the closest galaxies, observing individual stellar Doppler shifts or their proper motions across the sky. On the other hand, gas is not always present, but when it is, it is often found orbiting somewhat regularly in a nuclear thin disk around the SMBH and can be between a few hundred to a few thousand parsecs in radial length. When these disks are found, estimates of the SMBH mass can be derived from studying the gas's Doppler-shifted emission lines. Therefore, detecting SMBHs requires probing the centers of galaxies on spatially small scales.

A major impediment to dynamical detections of SMBHs in the early years was insufficient telescope resolution. The masses of SMBHs are typically much less than 1% of the mass of a galaxy, so the dynamical effect an SMBH has on the orbits of stars or gas is limited to regions very close to it. In principle, the orbits of stars and gas near a massive, point-like object should be Keplerian, where the circular velocity follows $v_c^2 = GM_{\rm BH}/r$. One important observational property related to a galaxy's gravitational potential is the stellar velocity dispersion of its spheroidal component, $\sigma_\star$. Given that the stellar velocity dispersion reflects

the strength of the host galaxy's gravitational potential and not the SMBH's, and that it is fairly constant out to radii beyond where an SMBH would dominate orbits, an SMBH's gravitational potential should dominate within radii where $v_c \geq \sigma_\star$. Numerically, dynamically detecting an SMBH requires telescope observations that can probe scales comparable to a physical radius of

$$r_{\rm SOI} = \frac{GM_{\rm BH}}{\sigma_\star^2} \approx 10\,{\rm pc} \left(\frac{M_{\rm BH}}{10^8\,M_\odot}\right) \left(\frac{\sigma_\star}{200\,{\rm km\,s^{-1}}}\right)^{-2}, \tag{1.1}$$

or, equivalently, on angular scales for a galaxy at a distance D

$$\theta_{\rm SOI} = \frac{r_{\rm SOI}}{D} \approx 0.2'' \left(\frac{M_{\rm BH}}{10^8\,M_\odot}\right) \left(\frac{\sigma_\star}{200\,{\rm km\,s^{-1}}}\right)^{-2} \left(\frac{D}{10\,{\rm Mpc}}\right). \tag{1.2}$$

The volume centered on the SMBH with this radius is known as the SMBH's sphere of influence (SOI). Until the launch and repair of the HST and the development of adaptive optics for ground-based telescopes in the 1990s, there was little that could be done to overcome the technical challenges of observing SMBH SOIs even in the nearest galaxies outside the Local Group, as the effects of atmospheric blurring ("seeing") typically limited ground-based observatories to telescope resolutions of $\geq 0.5''$.

1.2.2 Dynamical Evidence for SMBHs Prior to HST

The year 1978 featured the first attempt at dynamically detecting an SMBH at the center of a nearby galaxy. Using spectroscopic observations from the University College London Image Photon Counting System, Sargent et al. (1978) detected an increase in the observed stellar velocity dispersion within the innermost $1.5''$ of the Virgo Cluster's giant elliptical galaxy, M87. Follow up photometric observations presented by Young et al. (1978) revealed that M87 contained a bright luminosity cusp and required a steadily increasing mass-to-light ratio at small radii. Using stellar-dynamical models that assumed spherical symmetry

and that the stellar velocity distribution was isotropic, these studies presented a case for an SMBH of about $3 \times 10^9\, M_\odot$ at the center of M87. The case, however, was far from being watertight. Further research by other groups presented alternative interpretations of the same data. By considering different distributions of stars and relaxing the assumption of isotropy, it was shown that the observations by Young et al. (1978) and Sargent et al. (1978) could be explained without the need for an SMBH (Duncan and Wheeler, 1980; Binney and Mamon, 1982; Richstone and Tremaine, 1985). Despite the inconclusive nature of the results in M87, the pre-HST era was not without its own successes. Dynamical detections were made in a handful of galaxies, such as in the Andromeda Galaxy and its satellite galaxy M32 (Tonry, 1984, 1987; Dressler and Richstone, 1988; Kormendy, 1988). These studies laid the foundational groundwork for the dynamical modeling methods used in future studies with HST.

1.3 The Last 30 Years (1993 - 2023)

The 1990s were a period of dramatic change in the history of understanding SMBHs. Technological achievements in astronomy such as the launch of the HST in 1990 (and its subsequent repair in 1993), the construction of large ground-based telescopes such as the 10 meter Keck I and Keck II telescopes, and the development of adaptive optics for ground-based observatories, gave astronomers the necessary tools to obtain higher angular resolution observations of nearby galaxy nuclei than before, including the center of the Milky Way. Additionally, for the first time, Very Long Baseline Interferometry observations of water masers provided virtually conclusive evidence of a disk orbiting in Keplerian rotation around an SMBH in the galaxy NGC 4258. Furthermore, the 1990s saw the development and application of complex orbit-based stellar dynamical models and conceptually simpler thin disk ionized gas-dynamical models to explain the wealth of incoming high-quality data.

Any discussion of SMBH history is incomplete without the inclusion of AGN research. However, given its distinctiveness from the topics in this dissertation, the following discussion will be brief. The most luminous and distant active galaxies harbor SMBHs that populated the early universe. These galaxies are far too distant to apply traditional stellar-dynamical and gas-dynamical methods, and so techniques such as reverberation mapping and single-epoch spectroscopy are used to bridge the study of SMBH demographics to theories of galaxy formation and evolution. Long-term monitoring campaigns studying all types of AGN have increased in number and have sought to understand the physics of these systems and connect them to our understanding of more local and quiescent galaxies. For more information, a recent review of reverberation mapping can be found in Cackett et al. (2021).

More recently, there have been other key developments in SMBH research. The completed construction of additional large (8-10 meters) optical and infrared telescopes across the globe has enabled more ground-based observatories to contribute to understanding SMBH demographics. Moreover, the construction of the Atacama Large Millimeter/submillimeter Array for millimeter wave observations from 2003 to 2013 (the main instrument featured in this dissertation), and the first successful observations from the Event Horizon Telescope in 2017, have opened new avenues for studying SMBHs.

1.3.1 HST

The HST transformed our understanding of the centers of galaxies and SMBHs. With its placement above Earth's atmosphere, HST was able to bypass the limitations of ground-based telescopes and observe more distant galaxies at sufficient resolution to start detecting SMBHs. By 1995, less than two years after its initial servicing mission, there were eight (provisional) detections of SMBHs. Six of these detections were based on stellar-dynamical modeling and two on gas-dynamical models. The Harms et al. (1994) gas-dynamical detec-

tion identified Keplerian-like rotation of ionized gas within the circumnuclear region of M87 and constrained the central mass to be $(2.4 \pm 0.7) \times 10^9\,M_\odot$, thus improving upon the previous work in M87 by Young et al. (1978) and Sargent et al. (1978), and providing stronger evidence for SMBHs at the centers of galaxies. A summary of these eight detections can be found in Kormendy and Richstone (1995).

By the year 2000, the first demographic studies of SMBHs and their host galaxies were presented. Both Ferrarese and Merritt (2000) and Gebhardt et al. (2000) independently demonstrated a correlation between $M_{\rm BH}$ and the stellar velocity dispersion, $\sigma_\star$ of a galaxy bulge. This tight correlation spans over three orders of SMBH mass and demonstrates a potential evolutionary connection between SMBHs and their host galaxies. In the two decades since these initial papers were published, there have been several dozen, if not over a hundred, papers focused on these relations and their implications of SMBH-host galaxy coevolution.

1.3.2 Breakthroughs in Ground-Based Observations

Although HST enabled the study of SMBH demographics, ground-based observations provided the most compelling evidence of SMBHs. These observations include proper motion analysis of the stars in the Milky Way's center (see the review by Genzel et al. (1994) for a compendium of studies of the Milky Way's BH in that era), the observations of H_2O masers in the nearby spiral galaxy NGC 4258 (Miyoshi et al., 1995), and as of 2019, the observations of SMBH shadows from the Event Horizon Telescope (EHT; Event Horizon Telescope Collaboration et al., 2019, 2022).

Two groups led independently by Reinhard Genzel of the Max Planck Institute and Andrea Ghez of the University of California, Los Angeles, have been the primary investigators of the Milky Way's SMBH, Sagittarius A* (Sgr A*) for the past three decades. By continuously

monitoring the motions of stars near the Galactic center, both groups have contributed to making Sgr A* the most precisely measured SMBH mass to date at $4.3 \times 10^6\, M_\odot$ with statistical and systematic uncertainties of 0.25% and 1%, respectively (GRAVITY Collaboration et al., 2022). The stars nearest to Sgr A* are the closest probes of an SMBH event horizon that astronomers have studied. As a case study, it has been used to rule out other astronomical alternatives besides SMBHs that were put forth to explain observations, such as brown dwarfs and stellar remnants (Maoz, 1998; Ghez et al., 1998, 2005). In addition, Sgr A* has been used to test and verify predictions of Einstein's theory of general relativity (Do et al., 2019). Undoubtedly, Sgr A* will continue to be the subject of intense investigation for years to come, as future improvements in technology will enable studies that probe closer to its event horizon.

The observations of the H_2O masers in NGC 4258 at 22 GHz ($\lambda = 1.35$ mm) are the prime example of dynamical tracers exhibiting a Keplerian rise in their central velocities. Using radio interferometric techniques that provide angular resolutions of a few milliarcseconds, Miyoshi et al. (1995) provided persuasive evidence of a $3.6 \times 10^7\, M_\odot$ SMBH at the center of NGC 4258. Despite this fantastic result, the applicability of masers is limited, as their presence is rare, and they have only been found in lower mass, late-type spiral galaxies, though they have since been used to constrain SMBH masses in a handful of these galaxies (Kuo et al., 2011).

The EHT has given us the first glimpses of SMBH shadows in M87 and the Milky Way (Event Horizon Telescope Collaboration et al., 2019, 2022). With its network of telescopes, it has given us the most detailed look of the small scale astrophysics that occurs near an SMBH, has enabled further testing of general relativity, and has the potential to provide important crosschecks on measured masses of SMBHs for targets that have already been dynamically modeled. EHT is still in its infancy, and as of this writing, has only studied M87 and the Milky Way, so while the current results are promising, EHT and the previously

aforementioned breakthroughs in ground-based observing cannot provide a full understanding of SMBH demographics given their limited applicability. Hence, the focus of the next section will be on dynamical modeling, which has comprised the lion's share of SMBH mass measurements.

1.3.3 Dynamical Modeling

The foundational pillars of current dynamical modeling techniques were built in the 1990s during the initial heyday of HST SMBH demographic research. Dynamical studies often use either stars or gas as the tracers of the SMBH potential, so this period saw the construction of multiple independent modeling codes for both cases. Since this dissertation is focused on molecular gas-dynamical modeling with ALMA, this section concentrates mostly on its forerunner, ionized gas-dynamical modeling.

As stated earlier, some galaxies contain disks of ionized gas that rotate regularly around the central SMBH. A solid predictor of ionized gas in a galaxy is the presence of a smooth, well-ordered, and relatively symmetric central dust lane (Ho et al., 2002). While not found in every galaxy, these nuclear gas disks have multiple advantages over stars when it comes to measuring $M_{\rm BH}$. One benefit of modeling a gas disk is simplicity. Stellar-dynamical modeling requires not only modeling the orbits of stars near the SMBH, but must also account for orbits that explore large radii in the extended stellar and dark matter halo of a galaxy. Computationally, gas-dynamical modeling is much less intensive than stellar-dynamical modeling, which requires the simulation of tens of thousands of stellar orbits to fully explore the large model parameter space. Furthermore, the enigmatic nature of a galaxy's intrinsic 3D shape, described by its triaxiality, is another concern for stellar-dynamical models that ionized gas-dynamical models do not have to take into account. For many years, stellar-dynamical models assumed inherent galaxy axisymmetry which reduced

expensive computational costs, although the price has at times been large discrepancies in the derived $M_{\rm BH}$ (Shapiro et al., 2006; van den Bosch and de Zeeuw, 2010).

Fundamentally, under the assumption of spherical symmetry, the rotational velocity of a test particle measures the mass interior to a given radius r:

$$v_c^2(r) = \frac{G(M_\star + M_{\rm BH})}{r}, \tag{1.3}$$

where $M_\star$ is the enclosed mass of the host galaxy's stars at r and $M_{\rm BH}$ is the mass of the SMBH. While apparently simple, there are serious drawbacks and limitations of using gas to trace the SMBH potential. As a collisional fluid, ionized gas not only responds to gravitational forces, but also can be strongly influenced by the presence of shocks or magnetic fields. Consequently, ionized gas within the nuclear region of a galaxy may have complex motions that significantly deviate from ideal circular rotation, and thus be a less effective tracer of the SMBH than initially thought. Additional complications include the fact that the inferred value of $M_{\rm BH}$ depends strongly on the disk's orientation (e.g., the inclination angle to the line of sight), and that the presence of dust in these systems complicates the process of determining an accurate stellar mass profile, $M_\star(r)$.

When comparing SMBH masses that have been measured through both stellar and gas-dynamical modeling, one finds that they tend to disagree by a factor of $2-4$ (Kormendy and Ho, 2013). A quintessential example of this phenomenon is M87. From the early HST years to about 2013, gas-dynamical modeling provided a range on $M_{\rm BH}$ of about $(2.4-3.5)\times10^9\,M_\odot$ (Harms et al., 1994; Macchetto et al., 1997; Walsh et al., 2013), whereas the stellar-dynamical measurement of Gebhardt and Thomas (2009) estimated $M_{\rm BH}$ to be $6.1\times10^9\,M_\odot$. The game-changing EHT observation of M87 in 2019 seemed to break the stalemate in favor of the stellar-dynamical measurement, when observations of the SMBH shadow suggested $M_{\rm BH} = 6.5\times10^9\,M_\odot$ (Event Horizon Telescope Collaboration et al., 2019). However, there

have been multiple recent investigations of the SMBH in M87 that are in conflict with these past measurements. A stellar-dynamical analysis by Liepold et al. (2023) suggests an $M_{\rm BH}$ of $5.4 \times 10^9\,M_\odot$, another independent stellar-dynamical measurement by Simon et al. (2023) suggests an $M_{\rm BH}$ as high as $8.7 \times 10^9\,M_\odot$, and an ionized gas-dynamical measurement with VLT/MUSE claims $M_{\rm BH} = 6.6 \times 10^9\,M_\odot$ if the disk is assumed to be inclined at 25° or $M_{\rm BH} = 3.5 \times 10^9\,M_\odot$ if the inclination is 42° (Osorno et al., 2023). All of these results indicate that the issue has not been settled. With a future James Webb Space Telescope-based measurement on the horizon (Walsh et al., 2021), perhaps a universally accepted and precise range on $M_{\rm BH}$ in M87 will finally be available.

1.3.4 Molecular Gas and SMBH Mass Measurements with ALMA

Molecular gas has emerged as a dynamical tracer capable of circumventing the aforementioned issues with stellar-dynamical and ionized gas-dynamical modeling. Tracers such as H_2, HCN, HCO^+, and CO emission lines have been used to constrain BH masses in late-type galaxies (Neumayer et al., 2007; Scharwächter et al., 2013; den Brok et al., 2015; Onishi et al., 2015). In addition, a number of CO surveys have shown that a fraction of ETGs have dynamically cold and regularly rotating molecular gas disks at their centers (Combes et al., 2007; Young et al., 2011; Alatalo et al., 2013; Bolatto et al., 2017). These molecular gas disks are ideal targets for precision SMBH mass measurements. As with ionized gas, modeling the dynamics of molecular gas on scales comparable to the SMBH's sphere of influence is insensitive to factors such as the distribution of dark matter and triaxial structure, which affect stellar-dynamical models. Molecular gas also has the added benefit that it is much less turbulent than ionized gas (Davis et al., 2013a; Utomo et al., 2015; Boizelle et al., 2017).

Davis et al. (2013b) demonstrated the potential of molecular gas as an effective kinematic tracer by measuring the mass of the SMBH in NGC 4526 with the Combined Array for

Millimeter-wave Astronomy. Since then, the Atacama Large Millimeter/submillimeter Array (ALMA) has emerged as the premier radio interferometer for these types of measurements due to its extremely high angular resolution and sensitivity. Indeed, ALMA has provided some of the most tightly constrained SMBH masses in extragalactic sources in cases where well-resolved molecular gas emission is found within the projected SMBH SOI. Using two sets of ALMA observations, Barth et al. (2016a,b) first detected rapid rotation of CO gas in orbit around the SMBH in NGC 1332. At 0.″3 resolution, the initial ALMA Cycle 2 observations identified a noticeable increase in the projected LOS velocities near the center of NGC 1332, though profound beam-smearing of the central CO line profiles along the disk's minor axis limited the measurement precision of $M_{\rm BH}$ to a range of $(4-8)\times10^8\,M_\odot$. Following up with 0.″04 ALMA Cycle 3 observations provided a more precise measurement of $M_{\rm BH} = 6.64\times10^8\,M_\odot$ with a systematic measurement uncertainty of $\sim$10%. Boizelle et al. (2019) further demonstrated ALMA's superb capabilities by measuring the SMBH in NGC 3258 to be $M_{\rm BH} = 2.249\times10^9\,M_\odot$ with statistical uncertainties of only $\sim$1%. There are now several ALMA-based SMBH mass measurements derived from observations of rotating circumnuclear disks on scales comparable to and even within the SMBHs' SOIs in nearby ETGs (Onishi et al., 2017; Davis et al., 2017; North et al., 2019; Smith et al., 2019; Cohn et al., 2021; Boizelle et al., 2021; Kabasares et al., 2022; Ruffa et al., 2023)

As shown by Ho et al. (2002), galaxies that possess a circumnuclear dust disk that is visible at optical wavelengths are ideal targets to search for high-velocity gas emission. Starting with ALMA Cycle 2 and going through ALMA Cycle 5, Boizelle (2018) studied a sample of 23 such disks found at the centers of ETGs. The selection criteria for these targets included the presence of circularly symmetric dust lanes seen in HST optical images, as well as an estimated SMBH SOI of $r_{\rm SOI} \geq 0.''3$ in angular extent. Among these disks include the ones found at the centers of NGC 1332 and NGC 3258, which, as described earlier, are some of the most precisely measured SMBH masses to date (Barth et al., 2016a; Boizelle et al.,

2019). This sample is the foundational starting point of this dissertation, as the SMBH mass measurements are based off of the ALMA observations collected by Boizelle (2018).

1.4 Dissertation Outline

My dissertation presents the results of a few research projects focused on measuring SMBH masses in eight ETGs. High angular resolution HST near-infrared data and radio observations from ALMA are used and modeled to probe circumnuclear disk dynamics and constrain the SMBH masses. The following sections provide a short content summary of the remaining chapters in this dissertation.

Chapter 2: Methods

This chapter covers the gas-dynamical modeling formalism used for each measurement presented in the dissertation. I describe the construction of thin disk models and the key model parameters. The various features controlling model dynamics including options for the gas's turbulent velocity dispersion, the inclusion of radial motion, and a nonparametric host galaxy modeling formalism are also discussed. I also go into detail on the velocity to frequency conversions used to build dynamical models on the same spectral grid as the ALMA data. Furthermore, I describe how the spatial and spectral regions of each model fit are chosen, the beam convolution process, and the 3D noise model I developed that is used in χ^2 minimization. I conclude with a discussion on how statistical model-fitting uncertainties are derived and various aspects of model systematics that contribute to an $M_{\rm BH}$ measurement's error budget.

Chapter 3: NGC 1380

The first SMBH mass measurement in the galaxy NGC 1380 is presented. I create dynamical models for the highly inclined ($i \sim 75°$) circumnuclear disk. The 0.″2 resolution ALMA observations reveal that the projected velocities of the molecular gas near the galaxy center are $\sim$300 km s^{-1}, and a slight rise in central velocity within the innermost 0.″2 is apparent. I build thin disk dynamical models and fit them to the ALMA data. To include the host galaxy's contribution to the total gravitational potential, I model the observed surface brightness from an HST Wide Field Camera 3 F160W image with Multi-Gaussian Expansions (MGEs). To account for the effects of dust on the observed surface brightness profiles, I also use two-band color maps to identify regions that feature large amounts of interstellar reddening and construct multiple dust-corrected MGE models to ascertain the effects of dust extinction on the inferred SMBH mass. I determine $M_{\rm BH} = 1.47 \times 10^8\,M_\odot$ with an uncertainty of about 40%, with a large portion of the error budget stemming from the uncertainties in the host galaxy modeling process.

Chapter 4: NGC 6861

I present a second and independent mass measurement of the SMBH in NGC 6861. The 0.″28 ALMA data reveal a central hole of about 1″ in radius in the CO distribution within the highly inclined ($i \sim 75°$) circumnuclear disk. Upon extracting the major axis surface brightness profile from an HST F160W image, it is clear that the circumnuclear dust disk in this galaxy causes a reduction in the observed surface brightness. The combination of the hole and extinction precludes tight constraints on the central SMBH mass. I build two host galaxy MGE models to parameterize the observed surface brightness distribution and find a plausible $M_{\rm BH}$ range of $(1-3) \times 10^9\,M_\odot$. Assuming an unlikely amount of extinction due to dust at the center, the models suggest a lower limit of $M_{\rm BH} \sim 10^8\,M_\odot$ in this system.

Chapter 5: NGC 4786

Chapter 5 covers the first SMBH mass measurement in the giant elliptical galaxy NGC 4786. This galaxy contains a circumnuclear disk that is inclined at about 70°, is small in projected size ($r \sim 0\farcs5$), and has projected line-of-sight (LOS) velocities that reach $\sim$270 km s^{-1} towards the disk edge, which remain relatively flat moving inward towards the center. The observed HST F160W image is modeled with three host galaxy MGE models that account for a range in interstellar extinction. By dynamically modeling the ALMA data, I constrain the central SMBH mass to be within the range of $(3.7 - 6.4) \times 10^8\,M_\odot$, and find that the largest contributor to the measurement uncertainty comes from uncertainties in the host galaxy modeling process.

Chapter 6: NGC 5193

This chapter presents the first mass measurement of the SMBH in the galaxy NGC 5193. This galaxy contains a moderately inclined ($i \sim 60°$) and regularly rotating circumnuclear disk with a radius of about $r \sim 1''$. The projected line-of-sight velocities are about $\sim$280 km s^{-1} at the disk edge and stay moderately flat to the center. To construct a mass profile for the extended stellar mass distribution, I deprojected and converted the observed HST F160W surface brightness distribution. I built three MGE models to account for a range in assumed dust extinction in the galaxy. Based on the results of my dynamical models and a set of systematic tests, I determine a range for $M_{\rm BH}$ in NGC 5193 of $(1.3 - 2.9) \times 10^8\,M_\odot$.

Chapter 7: NGC 3245, NGC 4435, NGC 5838, and ESO 208-G21

I showcase four preliminary SMBH mass measurements in the early-type galaxies NGC 3245, NGC 4435, NGC 5838, and ESO 208-G21. Both NGC 3245 and NGC 4435 have previous

ionized gas-dynamical measurements from HST, whereas NGC 5838 and ESO 208-G21 do not have a prior mass measurement. For each galaxy, I use one dust-masked MGE model to derive an initial estimate of $M_{\rm BH}$. The circumnuclear disks in NGC 3245 and NGC 4435 have complex kinematics that simple thin disk models struggle to emulate. As an attempt to fit the larger scale kinematics better, I use a nonparametric $v_{\rm ext}$ model for the host galaxy component in these two galaxies. Preliminary dynamical models find $M_{\rm BH} = (0.9-1.4)\times10^8\,M_\odot$ with $\chi^2_\nu \sim 4$ for NGC 3245 and $M_{\rm BH} = (0.5-0.8)\times10^8$ and $\chi^2_\nu \sim 20$ for NGC 4435. These results suggest shortcomings in the dynamical modeling process that have yet to be fully understood. For NGC 5838, a strong degeneracy between $M_{\rm BH}$ and stellar mass is observed, as a large range of $(1\times10^6\,M_\odot) - (1.9\times10^9\,M_\odot)$ is found for $M_{\rm BH}$. For ESO 208-G21, the preliminary results suggest $M_{\rm BH} = 2.3\times10^8\,M_\odot$. In both NGC 5838 and ESO 208-G21, CO emission near the disk center is faint, and could be a main limiting factor for the measurements.

Chapter 8: Conclusions and Future Work

I conclude with a summary of my findings and highlight numerous potential limitations and pitfalls when dynamically modeling ALMA data that do not resolve the SMBH SOI. Additionally, I provide some key areas that future dynamical studies with ALMA can focus and improve upon. Finally, I speculate on the next thirty years of SMBH research. I discuss the construction of new observatories and future avenues for precision SMBH mass measurement.

Chapter 2

Gas-Dynamical Modeling Framework

> "Measuring the mass of an SMBH from data that do not resolve the sphere of influence is a bit like judging the weight of a turkey that may, or may not, be lurking in a distant bush."
>
> - David Merritt (2013)

2.1 Thin Disk Models and Building Synthetic Data Cubes

In this chapter, I describe the gas-dynamical modeling framework that I developed in Python 3. This framework is an adaptation of the ALMA gas-dynamical modeling codes featured in Barth et al. (2016a) and Boizelle et al. (2019) which were written in the Interactive Data Language (IDL) and were used to dynamically measure the SMBH masses in NGC 1332 and NGC 3258. My version has modifications and additional features that differentiate it from its predecessors, which I expand upon in the ensuing sections.

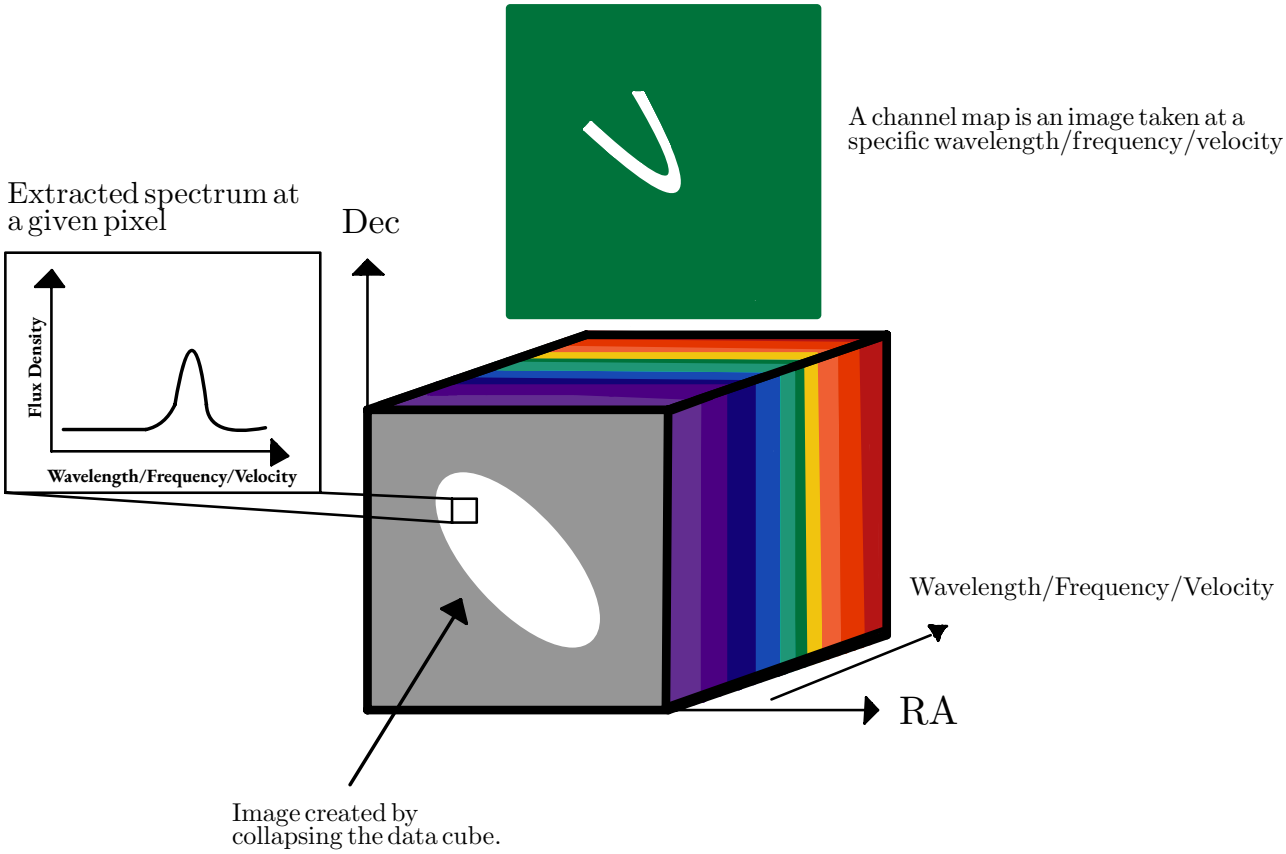

Figure 2.1 An illustration of an ALMA data cube.

In essence, my framework generates thin disk models that are used to construct synthetic data cubes. Each pixel in an ALMA data cube contains a spectrum of the observed line profile and for all data cubes presented in this thesis are of CO(2−1), which has a rest-frame frequency of 230.538 GHz. In the context of rotating molecular disks, this emission line becomes Doppler-shifted along the spectral axis due to the relative motion between the source and the observer. The amount of Doppler-shifting at a given spatial location is proportional to the disk's velocity at that point. My dynamical models emulate the circular rotation of an infinitesimally thin disk that orbits in the combined gravitational potential of the host galaxy's stars, the gas disk, and most importantly, the SMBH. The model's free parameters are optimized through χ^2 minimization in the `LMFIT` framework by Newville et al. (2016). In total, the dynamical models use a minimum of nine free parameters: the SMBH mass $M_{\rm BH}$, the stellar H-band M/L ratio Υ_H, the disk's dynamical center in pixels

(x_c, y_c), the disk's inclination and major axis position angle i and Γ, the turbulent velocity dispersion of the gas σ, the observed redshift $z_{\rm obs}$, and a flux-scaling factor F_0, that scales the model's flux density to the data's.

The key steps of optimizing a dynamical model to an ALMA data cube are as follows:

1. Determine the spatial (x and y) and spectral (z) dimensions of a given ALMA data cube, as well as its pixel scale and synthesized beam angle and size.

2. Construct a model of a thin disk rotating in the gravitational potential of the combined enclosed mass of the system (stars, gas disk, SMBH) on a spatial grid that is oversampled relative to the ALMA data.

3. Assume that the line profiles of the gas are inherently Gaussian, and construct a normalized Gaussian line profile at each subpixel element in the oversampled grid.

4. Weight the line profiles with a 2D map that models the total flux of the emission line at a given pixel. This map is empirically measured from the data.

5. Spatially block-average the synthetic cube back down to the scale of the ALMA data.

6. Convolve each frequency slice of the cube with an elliptical Gaussian point-spread function (PSF) that has the same beam angle, major axis width, and minor axis width as the ALMA synthesized beam.

7. Block-average both the data and synthetic model cubes to a coarser scale to mitigate the effects of neighboring pixel-to-pixel correlations observed in the data.

8. Compute and minimize $\chi^2 = \sum_{i=1}^{N} (d_i - m_i)^2 / \sigma_i^2$ over both spectral and spatial dimensions of the cube, where d is the ALMA data cube, m is the synthetic model cube, and σ is a 3D noise model containing the uncertainty of the flux density at a given pixel, which is explained in further detail below.

2.1.1 Model Geometry and Construction

The construction and geometry of the dynamical models follow conventions described in Macchetto et al. (1997) and Barth et al. (2001). Additional resources with helpful images for understanding the geometry and kinematics of rotating disks include Chapter 9 of Bovy (2023) and Teuben (2002). The models are first built in the rest frame of the disk and then transformed to emulate the data on the plane of the sky. In order to model steep velocity gradients seen in the data, the models are also built on a spatial scale that is oversampled by a factor of 3 relative to the ALMA data. Given that the CO emission in an ALMA data cube is limited to only a minor fraction of the spatial pixels in a given channel map and spans only a portion of all the spectral channels, I start by selecting a subset of the full ALMA data cube to model. Spatially, I select a square region that encompasses the entire length of the CO emission along the major axis. This is determined by first creating a surface brightness map of the data and then examining the spatial extent of the emission. Along the spectral axis, I include every channel that displays visible CO emission, as well as a few extra channels (typically 1-2, depending on the channel velocity spacing) on both the redshifted and blueshifted sides. This is done in order to capture any potential faint spectral features just outside the brightest portions of the emission line.

Next, I define a set of coordinates. On the sky plane, $(x_{\rm sky}, y_{\rm sky})$ are the Cartesian coordinates and (r, ϕ) are the polar coordinates. In the plane of the disk, the corresponding set of coordinates are $(x_{\rm disk}, y_{\rm disk})$ and (R, θ). The coordinate axes are oriented such that $x_{\rm sky} = x_{\rm disk}$ is along the major axis of the disk. Given an inclination angle i, the minor axis of the disk as seen in the two frames are related by $y_{\rm disk} = y_{\rm sky}/\cos i$. In addition, their polar angles are related via: $\tan\theta = \tan\phi/\cos i$. The origin of the model grid, $(0, 0)$ is set as the lower left corner and the disk's kinematic major axis (from the receding/redshifted side) has a position angle Γ when measured from the $+y_{\rm sky}$ axis. If the origin of the coordinate system is set as the disk's rotational center, then when measured in the disk plane, the radial

distance from a point on the disk to the center is given by:

$$R^2 = x_{\rm disk}^2 + y_{\rm disk}^2 = x_{\rm sky}^2 + \left(\frac{y_{\rm sky}}{\cos i}\right)^2 \tag{2.1}$$

The circular velocity $v_{\rm circular}(R)$ of a test particle at each point in the grid is a function of radius from the origin. The total velocity is determined by the combined gravitational potential of the host galaxy, the SMBH, and the extended mass distribution of the molecular gas disk itself:

$$v_{\rm circular}(R) = \left[\frac{GM_{\rm BH}}{R} + \frac{\Upsilon_H}{\Upsilon_{\rm MGE}} v_{\star,\,\rm MGE}^2(R) + v_{\rm gas}^2(R)\right]^{1/2}. \tag{2.2}$$

I use $\Upsilon_{\rm MGE} = 1$ when deriving $v_{\star,\,\rm MGE}$ for each galaxy. A detailed description of how an MGE is created is found in the following chapters for each dynamically-modeled gas disk. At each model iteration, $v_{\star,\,\rm MGE}^2$ is scaled by the ratio $\Upsilon_H/\Upsilon_{\rm MGE}$, which scales the stellar mass profile.

The velocities in the disk's rest frame must be transformed into the frame of the observer viewing the LOS components on the plane of the sky. The observed velocities, $v_{\rm LOS}(x_{\rm sky}, y_{\rm sky})$ are modeled as:

$$v_{\rm LOS}(x_{\rm sky}, y_{\rm sky}) = v_{\rm circular}(R)\cos\theta\sin i \tag{2.3}$$

relative to the systemic velocity of the host galaxy. The relationship between the Cartesian and polar coordinates in the disk's frame is given by:

$$\cos\theta = \frac{(x_{\rm sky} - x_{\rm c})\cos\Gamma - (y_{\rm sky} - y_{\rm c})\sin\Gamma}{R} \tag{2.4}$$

$$\sin\theta = \frac{(x_{\rm sky} - x_{\rm c})\sin\Gamma + (y_{\rm sky} - y_{\rm c})\cos\Gamma}{R\cos i} \tag{2.5}$$

At this stage of the modeling process, for a given set of model free parameters, there is an observed LOS velocity $v_{\rm LOS}$ associated at each $(x_{\rm sky}, y_{\rm sky})$ location. To quantify the broadening or the spread in the velocities of the CO line profiles, I also populate an equivalent model grid with a projected LOS velocity dispersion at each point that can be a function of radius, $\sigma_{\rm LOS}(R)$. For the simplest models, I use a spatially uniform term of $\sigma_{\rm LOS}(R) = \sigma_0$. At maximum complexity, $\sigma_{\rm LOS}(R)$ can be modeled as a Gaussian and/or an exponential function as well:

$$\sigma_{\rm LOS}(R) = \sigma_0 + \sigma_1 \exp\left[-(R - R_0)^2/2\mu^2\right] + \sigma_2 \exp\left(-R/R_1\right) \tag{2.6}$$

In the next section, I describe how these velocities are converted into frequency units and then fitted directly to the ALMA data cubes.

2.1.2 Velocity to Frequency Conversion and Line Profiles

I model the observed CO profiles under the assumption that they can be described mathematically as Gaussian functions. Previous dynamical modeling studies such as Barth et al. (2016b) use the projected LOS velocities $v_{\rm LOS}$ and LOS velocity dispersions $\sigma_{\rm LOS}$ at each point in the model grid as the central velocity and velocity width of the model Gaussian line profiles. My method instead transforms these quantities into frequency units in order to build models that can be fit to the data along the same spectral axis.

Line Profiles

The observed redshift $z_{\rm obs}$ is the parameter that converts velocities to frequencies. The observed redshift of a monochromatic light wave is defined in terms of observed and rest-frame wavelengths: $z_{\rm obs} \equiv (\lambda_{\rm obs} - \lambda_0)/\lambda_0$ or in terms of observed and rest-frame frequencies:

$z_{\rm obs} \equiv (f_0 - f_{\rm obs})/f_{\rm obs}$. However, $z_{\rm obs}$ is influenced by various factors such as cosmological expansion, gravitational redshift, and the peculiar velocities of both sources and observers. This relationship is described through the following equation,

$$1 + z_{\rm obs} = (1 + z_{\rm cos})(1 + z_{\rm pec})(1 + z_{\rm grav}). \tag{2.7}$$

In addition, the peculiar motion component can also be separated into source and observer terms with respect to a given reference frame through

$$1 + z_{\rm pec} = (1 + z_{\rm pec}^{\rm source})(1 + z_{\rm pec}^{\rm observer}). \tag{2.8}$$

I make multiple simplifying assumptions. First, I use the approximation $z_{\rm grav} = 0$. In addition, an astute selection of the assumed reference frame can largely remove the dependence on $z_{\rm pec}^{\rm observer}$. The most reliable point of reference is provided by the cosmic microwave background (CMB) frame, which removes peculiar motions of both the Sun and the Milky Way. Equation 2.7 can now be reduced to:

$$1 + z_{\rm obs} = (1 + z_{\rm cos})(1 + z_{\rm pec}^{\rm source}) \tag{2.9}$$

where the peculiar motion (Equation 2.8) now depends only on the source. Moreover, the relativistic Doppler equation,

$$\frac{1}{1 + z_{\rm pec}^{\rm source}} = \sqrt{\frac{c - v_{\rm pec}^{\rm source}}{c + v_{\rm pec}^{\rm source}}} \tag{2.10}$$

which relates the source's peculiar velocity and its redshift, can be expanded in a Taylor Series around $v_{\rm pec}^{\rm source}/c \approx 0$ to yield:

$$\frac{1}{1 + z_{\rm pec}^{\rm source}} \approx 1 - \frac{v_{\rm pec}^{\rm source}}{c} \tag{2.11}$$

which is the radio astronomy convention for radial velocity.

The $1 + z_{\cos}$ factor represents the expansion of space itself and cannot be computed with the relativistic Doppler equation. Cosmological velocities are typically determined with Hubble's Law: $v_{\cos}(z) = D_C(z)H_0$ where $D_C = D_L/(1 + z_{\rm obs})$ is the co-moving distance to the source. If $z_{\rm obs} \ll 1$, then this equation can be simplified to $v_{\cos} \approx cz_{\cos}$; this is known as the optical astronomy convention of radial velocity. With the aforementioned simplifications, the transformation between observed frequencies $f_{\rm obs}$ and LOS velocities $v_{\rm LOS}$ can be expressed as:

$$f_{\rm obs} \approx \left(\frac{f_0}{1 + z_{\cos}}\right)\left[1 - \left(\frac{v_{\rm pec}^{\rm source} + v_{\rm LOS}}{c}\right)\right] \tag{2.12}$$

which separates the peculiar velocity of the disk $v_{\rm pec}^{\rm source}$ and the gas rotational velocity in the disk's rest-frame $v_{\rm LOS}$. The cosmological redshift and peculiar velocity of the disk are not influenced by the disk rotation. Using this approximation, a change in the disk's LOS rotational velocity $\Delta v_{\rm LOS}$ will result in a proportional change in the observed frequency width $\Delta f_{\rm obs}$. After substituting this change in velocity with the observed LOS velocity dispersion $\sigma_{\rm LOS}$, the observed frequency width is:

$$\Delta f_{\rm obs} = \left(\frac{f_0}{1 + z_{\cos}}\right)\left(\frac{\sigma_{\rm LOS}}{c}\right). \tag{2.13}$$

An important aspect of model construction is choosing a fixed distance to the galaxy. For a galaxy with measured luminosity distance D_L, the angular size distance, which will set the angular to physical scale (arcseconds to parsecs), is $D_A = D_L/(1+z)^2$. Given that the derived $M_{\rm BH}$ is proportional to D_A, percent changes in the assumed z will lead to approximately commensurate changes in $M_{\rm BH}$. The observed redshifts of targets featured in this dissertation are typically of order $z \sim 0.01$ or less. Although it is technically more correct to use both the cosmological redshift $z_{\cos}$ and the source peculiar velocity $v_{\rm pec}^{\rm source}$ to calculate D_A and

determine the conversion between disk rest-frame velocity and observed frequencies, both of these quantities are model dependent on the choice of Hubble constant H_0. Thus, I make use of a final set of approximations. I subsume the combination of peculiar motions from the Sun, Milky Way, and the galaxy under investigation into the cosmological expansion term ($z_{\rm pec} = 0$, $z_{\rm cos} = z_{\rm obs}$), and choose a fixed angular diameter distance D_A to the galaxy. I use $D_A = D_L/(1+z)^2$ and assume a fixed $z \approx v_{\rm rec}^{\rm source}/c$ where z is estimated through an initial dynamical modeling fit to the given ALMA data. The final transformation equations from velocity to frequency that use $z_{\rm obs}$ as a free parameter in the models are:

$$f_{\rm obs} = \left(\frac{f_0}{1+z_{\rm obs}}\right)\left(1 - \frac{v_{\rm LOS}}{c}\right) \tag{2.14}$$

$$\Delta f_{\rm obs} = \left(\frac{f_0}{1+z_{\rm obs}}\right)\left(\frac{\sigma_{\rm LOS}}{c}\right) \tag{2.15}$$

where $v_{\rm LOS}$ is defined in Equation 2.3.

Line Profile Calculation

In essence, my dynamical modeling framework constructs synthetic data cubes from a set of input model parameters. As previously described, these data cubes are constructed on a grid that is oversampled by a factor of 3 relative to the ALMA data and on the same frequency axis. At each spatial pixel in the oversampled model grid, a model Gaussian CO line profile is generated using the given $f_{\rm obs}$ and $\Delta f_{\rm obs}$ at that pixel. My framework has two options for constructing the line profiles: (1) sampling the Gaussian line profile at every frequency along the spectral axis, or (2) integrating the line profile along this axis. The first option, while computationally less expensive, is not ideal when $\sigma_{\rm LOS}$ is close to or less than the channel width of the ALMA data cube, as it results in poor sampling of the CO line profile. Mathematically, the two options for calculating a line profile normalized to 1 at each pixel location is given by the (1) the following integrand, and (2) its definite integral:

$$\int_{f_{\rm initial}}^{f_{\rm final}} \frac{df}{\sqrt{2\pi\Delta f_{\rm obs}^2}} \exp\left[\frac{-(f-f_{\rm obs})}{2\Delta f_{\rm obs}^2}\right] = \frac{1}{2}\left(\mathrm{erf}\left[\frac{(f_i+\Delta f/2)-f_{\rm obs}}{\sqrt{2}\Delta f_{\rm obs}}\right] - \mathrm{erf}\left[\frac{(f_i-\Delta f/2)-f_{\rm obs}}{\sqrt{2}\Delta f_{\rm obs}}\right]\right). \quad (2.16)$$

The terms $f_{\rm initial}$ and $f_{\rm final}$ represent the initial and final frequencies of a given channel in an ALMA data cube. In practice, the provided f_i are the central frequencies of the cube, and so for a given frequency channel f_i, $f_{\rm initial} = f_i - \Delta f/2$ and $f_{\rm final} = f_i + \Delta f/2$ where Δf is the spacing between adjacent frequency channels within the cube.

The line profiles must be weighted by the total flux in the line. A model integrated flux map is constructed by first isolating visible CO emission in each channel of a given ALMA data cube with a mask. The data cube is then multiplied with this mask and summed along the frequency axis to produce a two-dimensional map of line profile flux. Since this map is on the original ALMA scale, and not on the scale of the oversampled model grid, each pixel in the flux map must be subdivided into a grid of subpixels that matches the dimensions of the oversampled model grid. This scaled and deconvolved CO flux map is normalized so that the line profiles at each subpixel element for a given original ALMA pixel have equal fluxes.

2.1.3 Beam Convolution

To simulate the telescope observation, each frequency slice of a synthetic cube is convolved with a model of the ALMA synthesized beam. I model the beam as an elliptical Gaussian that has the same major axis FWHM, minor axis FWHM, and beam position angle listed for the given ALMA data that is being modeled. I use the `Gaussian2DKernel` function from the `astropy` package in Python. For the grid size, I typically build the model beam on a grid that is about 5 times the length of the beam's major axis in order to balance an

accurate representation of the beam with a reasonable computational runtime. Given that beam convolution is the most time-consuming step in the modeling process, the synthetic cube is first block-averaged back down to the original ALMA scale prior to beam convolution. The models are convolved across a rectangular area that extends past the elliptical spatial region of the model fit, described in the subsequent section. The extent of this additional rectangular area is determined by the geometric mean of the FWHM of the synthesized beam's major and minor axes.

2.1.4 Spatial and Spectral Fit Region

A given model is fitted over the same subset of pixels in the cube for each optimization. Spatially, the region is an ellipse, and it is initially created by encompassing all pixels with visible CO emission. Depending on how many resolution elements there are across the disk, this region can be adjusted by changing the length of the ellipse's major axis and fixing the axial ratio. In some cases (such as in NGC 6861) where there is evidence of a hole in the central emission, the ellipse can be modified to an annulus with the pixels in the central hole being excluded from the fit.

While this ellipse is initially created on the scale of the ALMA data, in practice, since the data and model are averaged over $n \times n$ pixel blocks before χ^2 is determined, (to mitigate strong correlation among neighboring pixels) this elliptical spatial region must be averaged over the same blocks as well. Pixels contained in the ellipse are represented by a "1" in a 2D array that matches the size of an ALMA image slice. All other pixels are set to "0". On the block-averaged scale, this leads to pixels that can be between 0 and 1, and some choice must be made whether these should be included in the final fit. In practice, I typically include pixels that have values ≥ 0.5, as this indicates there were more pixels contained in the ellipse on the original scale than pixels that were outside the ellipse.

Spectrally, the models are typically fit to every channel that displays visible emission. Depending on the size of the velocity channel spacing, I also include an additional $1-2$ channels beyond the visible emission on both the redshifted and blueshifted sides of the spectrum. This is to capture fainter emission that may not be readily visible, as well as to avoid potential edge effects in the model fitting process.

2.1.5 Noise Model

In order to calculate χ^2 and assess the goodness-of-fit of the models to the ALMA data, an estimate of the flux uncertainty at each data pixel is needed. The most straightforward approach would be to calculate the standard deviation of pixel values in emission-line free regions of the data cube. However, the background noise in ALMA data cubes is correlated on scales comparable to the synthesized beam in each frequency channel. This correlation prevents the determination of a meaningful χ^2 value without appropriate adjustments. Ideally, one would calculate a covariance matrix accounting for these correlations to compute χ^2, but such an approach would be computationally expensive and challenging to implement. Barth et al. (2016b) and Boizelle et al. (2019) adopted the simpler approach of rebinning the data by block-averaging over $n \times n$ pixel blocks within each frequency channel, where the value of n was the approximate number of pixels across the width of the synthesized beam. Their method creates a data cube with a scale of approximately one rebinned pixel per synthesized beam, and mitigates the noise correlation among neighboring pixels. They then measured the standard deviation of emission-free pixels in the rebinned data cube to produce a unique value of flux uncertainty for each frequency channel, and similarly rebinned their models to compute χ^2 on the block-averaged scale.

I also incorporated the effects of the ALMA primary beam on the background noise level. Prior to primary beam correction, the noise level in an ALMA data cube is spatially uniform,

but it increases with distance from the phase center after correction. Dynamical models are created and fitted to data cubes that have been corrected for the primary beam attenuation, so I incorporated this spatial modification into the noise model. As part of the ALMA data reduction process, a primary beam cube is generated along with the beam-corrected data cube. Multiplying the corresponding slices of these cubes together generates an uncorrected version of the data in which the background noise is spatially uniform. At this step, I block-average the data to a pixel scale corresponding to the synthesized beam. Once the data have been rebinned, I measure the standard deviation of pixel values in blank regions of each frequency channel, and I populate an array having the spatial dimensions of a block-averaged image with the value of the standard deviation at each element. To replicate the spatial modification of the noise in each channel, I block-averaged the primary beam cubes over the same pixel blocks as was done for the data and divided the block-averaged array of standard deviations by the block-averaged primary beam cube at the same frequency. In essence, I create a block-averaged noise cube that captures both the spatial and frequency dependence of the noise, which I use to compute χ^2. This approach differs from previous methods, where the given background noise is assumed to be spatially uniform across a given frequency slice (Barth et al., 2016b; Boizelle et al., 2019).

Although the noise model is designed to represent the RMS noise in emission line-free regions of each frequency channel of the data cube, an additional complication is that the mean background level can be slightly offset from zero (e.g., as a residual of imperfect passband calibration or continuum subtraction). If this is the case, the line-free regions of a cube will indirectly contribute to elevated χ^2 values for model fits. Using the data cubes for NGC 1380 and NGC 6861, I find roughly an equal number of channels having positive and negative mean background levels, with typical magnitudes that are $\sim$10% of the respective channel noise levels. As a simple test using these data cubes, I empirically measured the mean background level in each frequency channel included in the fit and added this value into the corresponding channels in the synthetic model cubes. I found that the values of

reduced χ^2 are smaller by about $\sim$1% with this adjustment, and hence the impact of these background levels can be regarded as minimal.

2.1.6 The Nonparametric $v_{\rm ext}$ Model

Modeling the host galaxy mass profile $M_\star(R)$ in dusty circumnuclear disks through image deprojection will always have systematic uncertainties attributed to the extinction correction. The circular velocity profile arising from this mass component is represented by $v_{\star,\rm MGE}(R)$ in Equation 2.2. An alternative approach for deriving the extended mass distribution of the host galaxy was pioneered by Boizelle et al. (2019). Using well-resolved ALMA Cycle 4 data for the SMBH mass measurement in NGC 3258, they developed a nonparametric model described as the $v_{\rm ext}(R)$ model that represents the extended mass distribution in terms of 10 circular velocity free parameters at 10 distinct radii spanning the length of the disk. This $v_{\rm ext}(R)$ model not only includes the mass of the host galaxy stars, but also additional mass components such as from the gas disk itself and dark matter, although both are typically assumed to be relatively small in comparison to the mass of the stars. I built upon this model as an option for modeling the extended mass distribution within my own framework, and I cover the slight modifications below.

Instead of using free parameters for circular velocity, my version of the $v_{\rm ext}(R)$ model uses free parameters for mass. By doing so, it can impose constraints on the characteristics of the mass distribution. The two constraints the framework employs are enforcing $M_{\rm ext}(R=0) = 0\,M_\odot$, which means that only $M_{\rm BH}$ is present at $R = 0$, as well as the constraint that $M_{\rm ext}$ is a monotonically increasing function of radius: $M(R_i) < M(R_{i+1})$. The mass in between each radius is piecewise interpolated to give a complete $M_{\rm ext}(R)$ model that spans the entire length of the disk. In between $R = 0$ and 1.5 ALMA resolution elements, the mass values at intermediate radii are interpolated linearly and then with a cubic spline out to the disk edge.

The slope of $M_{\rm ext}(R)$, especially near the centers of the disks, can have dramatic effects on the inferred $M_{\rm BH}$ as degeneracies between stellar and SMBH mass arise in datasets that do not have very high angular resolution. Thus, enforcing linear interpolation in the innermost parts of these disks prevents mass profiles that are unreasonably steep and nonphysical from being created. Once $M_{\rm ext}(R)$ is generated, it is then converted into a circular velocity $v_{\rm ext}(R) = \sqrt{GM_{\rm ext}(R)/R}$ under the assumption of spherical symmetry, projected along the LOS, and added in quadrature with the circular velocity component of the SMBH. Because the gas disk's mass is encapsulated within the nonparametric model, $v^2_{\rm gas}(R)$ is set to 0 when using this method.

2.1.7 Incorporating Radial Inflows

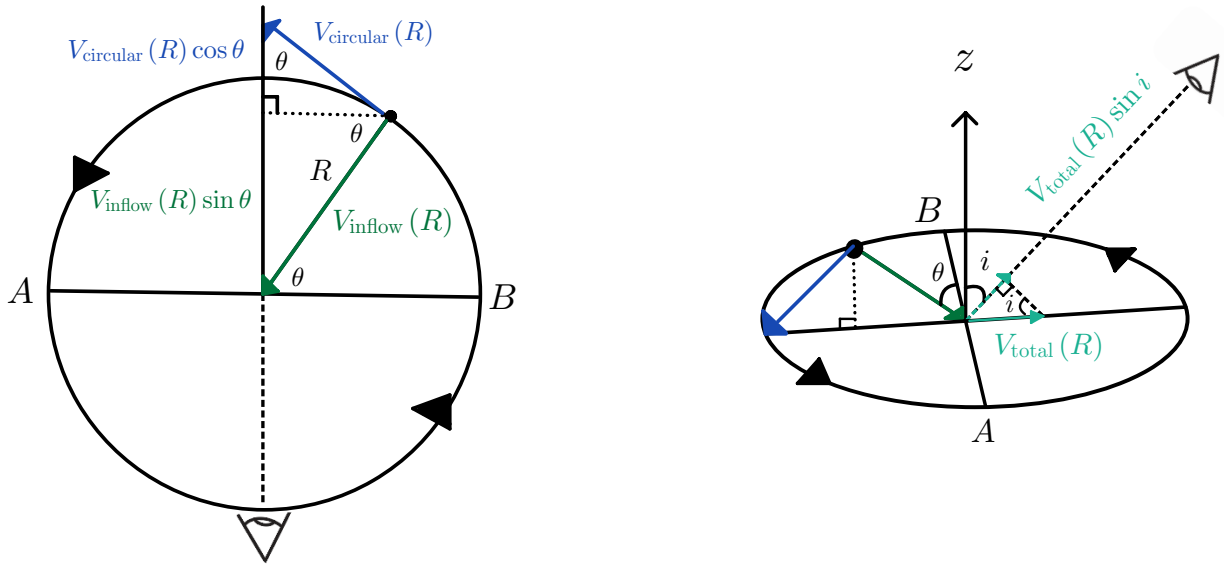

Figure 2.2 Left, a rotating disk as seen from above. The disk's azimuthal angle is θ, and the components of the circular and inflow velocity are shown. Right, the component of the total velocity along the LOS is displayed. This figure is an adaptation of Figure 5.18 from Sparke and Gallagher (2007).

Although the molecular gas disks are dominated by rotational motion, I constructed a simple model that allows for radial motion in the dynamical models. I followed an approach similar

to Boizelle et al. (2019) and Cohn et al. (2021) and incorporated a radially inward velocity term. The additional free parameter α, which lies in the range $[0, 1]$, controls the balance between pure rotational ($\alpha = 1$) and radially inflowing ($\alpha = 0$) motion. Mathematically, I defined α to be the ratio between the rotational velocity, $v_{\rm rot}$, and the ideal circular velocity in the model grid (i.e., $\alpha = v_{\rm rot}/v_{\rm circular}$). I defined the relationship between α, radial inflow velocity, and the ideal circular velocity as $v_{\rm inflow} = \sqrt{2(1-\alpha^2)}v_{\rm circular}$. Thus, when $\alpha = 1$, the model velocities are circular, and when $\alpha = 0$, the velocities are radially inflowing at the ideal free-fall speed of a test particle falling in from infinity. I projected the radial inflow velocity component along the LOS, and added it linearly to the projected LOS rotation velocity at each pixel in the model grid. Figure 2.2 shows the geometric relationship among the velocity components. The total LOS velocity at a given $(x_{\rm sky}, y_{\rm sky})$ has the form:

$$v_{\rm LOS}(x_{\rm sky}, y_{\rm sky}) = \alpha v_{\rm circular}(R)\cos\theta\sin i - \sqrt{2(1-\alpha^2)}v_{\rm circular}(R)\sin\theta\sin i. \tag{2.17}$$

2.2 Error Analysis of Dynamical Models

In this section, I discuss both statistical and systematic uncertainties associated with the dynamical models. The statistical uncertainties arise due to random fluctuations in the signal or noise of the data, whereas systematic uncertainties originate from the choices in model construction. The final error budget of an $M_{\rm BH}$ measurement is typically dominated by model systematics, and thus it is imperative to understand how adjustments to a dynamical model can lead to shifts in $M_{\rm BH}$.

2.2.1 Statistical Uncertainties

The statistical uncertainty of a given dynamical model is derived through a Monte Carlo simulation. To carry out this simulation, I take the best-fitting dynamical model of an ALMA dataset (the fiducial model) and generate anywhere between 100 and 200 realizations of it. Each data element in an ALMA data cube is colloquially referred to as a "voxel" (a portmanteau of "volume" and "pixel") in the radio astronomy community. To create a new realization in the simulation, I add a random number drawn from a Gaussian distribution to each voxel in the best-fitting dynamical model. The Gaussian's mean value is equal to 0 and the standard deviation is set to the value of the same voxel in the 3D noise model described in Section 2.1.5. I then optimize a model fit to each realization in this Monte Carlo simulation and create a distribution for each of the model free parameters. I take the standard deviation of the distribution of $M_{\rm BH}$ as the 1σ statistical uncertainty for the measurement.

2.2.2 Systematic Uncertainties

I perform several tests to investigate how modifications in a dynamical model's construction can bias the inferred $M_{\rm BH}$ value. I describe in general the effects that I account for in my dynamical models and how adjustments to the model could be performed. For ALMA targets where the fiducial dynamical model was extensively tested, I discuss the specific results of each test in that target's respective chapter in this dissertation.

Dust extinction: The host galaxy model is typically parameterized with a Multi-Gaussian Expansion (MGE) model (Cappellari, 2002) that is fit to a near-infrared HST image of the system under study. Deprojecting an observed 2D surface brightness to obtain a 3D luminosity and mass profile is a nontrivial exercise that is made even more complicated when there is significant dust extinction of the stellar light. When ALMA observations do

not resolve $r_{\rm SOI}$, the extended stellar mass distribution dominates the total gravitational potential over the SMBH. In this case, it is prudent to account for a range in slopes of the central stellar mass profile, as the inferred $M_{\rm BH}$ can become highly dependent on the choice of host galaxy model. A common approach in the literature is to create MGE models while masking out the most prominent features of dust in the image. This potentially can remove valuable information from the model fit and can lead to an inaccurate representation of the galaxy. The most rigorous and technically correct approach would be to incorporate radiative transfer models that account for dust disk geometry, thickness, and scattering (De Geyter et al., 2013; Camps and Baes, 2015), though this approach has yet to be tried in gas-dynamical $M_{\rm BH}$ measurements, and is beyond the purview of this dissertation. I developed a simpler approach that uses two-band HST color map information to derive estimates of the intrinsic near-infrared extinction.

While I discuss the process of creating dust-corrected host galaxy models in the later chapters, I will briefly give an overview of how these models are created. In essence, I build dust-corrected HST images that I parameterize with MGEs in `GALFIT`. To create a dust-corrected HST image, I typically mask out the entire dust disk from the image, except for the central nine pixels. These nine pixels are manually adjusted to values that correspond to an assumed intrinsic amount of dust extinction. I have also tried using only the central four pixels of the image, but have found that tuning parameters to achieve an optimal dust-corrected MGE model is more consistent when using the central nine pixels. Once these pixels have been adjusted, I fit a Nuker model (Faber et al., 1997) in `GALFIT` to the central $10'' \times 10''$ region of the image. Nuker models have been shown to fit the inner observed surface brightness profiles of early-type nuclei well, and they are used here to effectively build surface brightness models that interpolate over the dusty regions of the disk. With this new Nuker model, I typically replace the pixels within the dust disk region in the original HST image with the corresponding pixels in the 2D Nuker model and optimize a final MGE model to this dust-corrected image without using a mask.

Unresolved AGN emission: Low luminosity AGN can be present in ETGs. This can lead to MGEs incorporating light that should not be attributed to the stars, especially if the FWHM of the MGE components become very narrow ($\sim$0.″01). To account for this possibility, one can remove the Gaussian component with the narrowest FWHM from the MGE model, deproject the remaining components, and optimize a dynamical model from this altered MGE's circular velocity curve. Alternatively, one can also attempt to fit an unresolved component in the data with the PSF model in `GALFIT` and be sure to exclude the PSF model when deprojecting the Gaussian components. As a useful test, it is illustrative to observe the change in $M_{\rm BH}$ when the MGE with the narrowest FWHM is removed from the model, and compare that change with the differences in enclosed stellar mass within $r_{\rm SOI}$. This test can be particularly helpful in determining if there is a degeneracy between SMBH and stellar mass.

Radial motion: Gas-dynamical $M_{\rm BH}$ measurements typically assume that the gas is on perfectly circular orbits. However, gas is susceptible to non-gravitational forces as well, and thus the gas kinematics within these disks may exhibit deviations from ideal circular motion. As a simple test for radial inflow, my models can incorporate simple inflow motion through the simple toy model I described in Section 2.1.7.

Turbulent velocity dispersion: The circumnuclear disks featured in this dissertation are typically thought to be dynamically cold, where the ratio of the turbulent velocity dispersion to circular velocity ($\sigma/v_{\rm circular}$) is thought to be much less than 1. Even so, the simplest model for the turbulent velocity dispersion is a spatially uniform term, and may not be sufficient in characterizing the possible variations in turbulence across the disk. Thus, my models allow turbulent velocity dispersion profiles that take the form of a Gaussian or exponential function as described in Section 2.1.1 which can add more free parameters to optimize.

Fit region: Model optimizations are carried out over elliptical spatial regions that give equal weight to both the redshifted and blueshifted sides of the disk. Ideally, it is best to fit models

close to spatial pixels that are near or within $r_{\rm SOI}$ so that the SMBH accounts for a larger fraction of the total mass. However, the central region of a disk is heavily beam-smeared, and line profiles can display complex structures that models may be unable to reproduce. At the other extreme, fitting models over the entire disk means that the model is fitted to pixels that are further from the SMBH and the gas kinematics are dominated by the gravitational potential of the host galaxy. One must consider how well-resolved a disk is and find an optimal balance between incorporating enough pixels near or within $r_{\rm SOI}$ so that the models are sensitive to the SMBH and are not fitted to heavily beam-smeared regions, but not too large of a fitting region that any noticeable enhancement of the gas's rotational velocity due to the SMBH is diluted.

Block-averaging factor: As explained in Sections 2.1.4 and 2.1.5, dynamical models are block-averaged along with the data to mitigate spatial noise correlation. While this act mitigates one problem, it comes at the cost of having models with coarser angular resolution. If a given data cube has a pixel scale of p'' and one block-averages over $n \times n$ pixel blocks, the resulting block-averaged product will have a pixel scale of np''. As n increases, the models will gradually lose their ability to constrain $M_{\rm BH}$ as increasingly more spatial information is averaged together and lost. Viewed from another perspective, large values of n means that points on the disk that may exhibit different kinematics will be averaged together on the final scale. Thus, while it is important to mitigate noise correlation, it is also important to assess how the inferred $M_{\rm BH}$ changes with larger block-averaging factors. In principle, models are most sensitive to the SMBH when no block-averaging is done, so it may be beneficial to initially fit dynamical models on the original ALMA scale and compare how the derived $M_{\rm BH}$ changes at coarser scales.

Oversampling factor: The default setting in my models is to create the LOS velocity field on a grid that is oversampled by a factor of 3 relative to the ALMA data. This is done to capture potentially steep velocity gradients in the data that could be missed if no oversampling is

done. Higher values of subsampling factor lead to longer model construction runtimes, so there needs to be an ideal balance of sufficient oversampling with model runtime if a different factor is chosen.

Gas mass: A description of how the gas mass of the circumnuclear disk is incorporated in the dynamical models is presented in Section 5.2.3. The contribution of the gas disk to the gravitational potential is typically the smallest when compared to the extended stellar mass distribution and the SMBH, though it can become important in highly precise measurements of $M_{\rm BH}$. A simple test of its influence on the inferred $M_{\rm BH}$ is to simply set $v_{\rm gas} = 0\,{\rm km\,s^{-1}}$ in the dynamical models.

Input flux map: As described earlier, the model line profiles are normalized to unity and must be weighted by a map of the CO flux. This map can be constructed through a variety of methods. I typically generate a flux map by creating a 3D mask of the data cube first in the `3DBarolo` program (Di Teodoro and Fraternali, 2015) that isolates the CO emission. Then, I multiply the data cube with this mask and sum their product along the spectral axis to create the flux map that is used to weight the line profiles. Alternatively, one can fit the ALMA data using `3DBarolo` and generate a synthetic cube that is based on a tilted ring model (Rogstad et al., 1974) and create a flux map through the same process. Other works such as Barth et al. (2016b) have fit Gauss-Hermite line profiles to the ALMA data with higher order moments such as h_3 and h_4 that characterize deviations from a Gaussian function and have used the resulting products as flux maps as well.

Chapter 3

NGC 1380

3.1 Galaxy Properties

NGC 1380 is classified as an SA0 galaxy in both the Third Reference Catalog of Bright Galaxies (RC3; de Vaucouleurs et al., 1991) and in the Hyperleda database (Paturel et al., 2003). It is located at a luminosity distance of 17.1 Mpc in the Fornax cluster based on surface-brightness fluctuations from Tonry et al. (2001) after applying the Cepheid zero-point correction from Mei et al. (2007). With this assumed luminosity distance, and using an observed redshift of $z = 0.00618$ obtained from initial dynamical modeling results, the corresponding angular scale is 81.9 $\mathrm{pc\,arcsec^{-1}}$. For calculations described later in the chapter, I adopt the Hyperleda average stellar velocity dispersion of $\sigma_\star = 215\,\mathrm{km\,s^{-1}}$ (Makarov et al., 2014), a total apparent K-band magnitude of $m_K = 6.87$ mag from the Two Micron All Sky Survey (2MASS; Jarrett et al., 2003) and a bulge-to-total ratio of $B/T = 0.34$ from the Carnegie-Irvine Galaxy Survey (CGS; Gao et al., 2019).

3.2 Observations

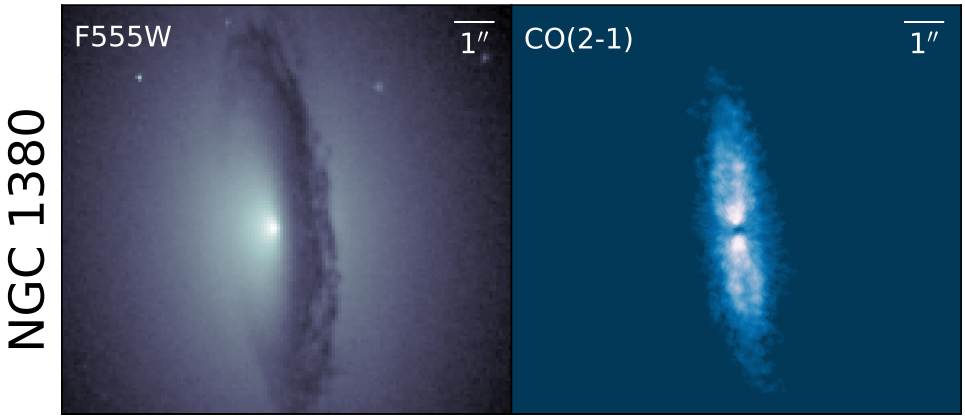

Figure 3.1 Image of NGC 1380 from HST and ALMA observations, showing the co-spatial distributions of the dust and gas. The left panel shows an F555W observation of the dust disk in NGC 1380. For each image, North is up and East is to the left. ALMA intensity maps in the right-side panels were created by summing across channels after using the 3DBarolo program (Di Teodoro and Fraternali, 2015) to generate a mask that identified pixels with CO emission.

3.2.1 HST Data

I retrieved and used archival HST F160W (H-band) images from HST program 11712. The observation was subdivided into 4 separate exposures of 299 seconds each that were taken with the Wide Field Camera 3 (WFC3). The images were processed with the `calwf3` pipeline and subsequently combined in `AstroDrizzle` to produce a cleaned and distortion-corrected image with a pixel scale of $0\farcs08$ pixel^{-1}. Archival F110W observations of NGC 1380 were obtained from HST program 11712 and consisted of 4 separate exposures of 299 seconds each. The F110W images were drizzled and aligned to the final F160W product.

3.2.2 ALMA Data

I obtained ALMA imaging of NGC 1380 as part of Program 2013.1.00229.S. The data were studied by Boizelle et al. (2017) as part of a larger sample of galaxies to map CO(2−1) emission in nearby ETGs, and I review the data reduction process and findings below.

NGC 1380 was observed in ALMA Band 6 for 23 minutes on both 2015 June 11 and 2015 September 18 with maximum baselines of 783 m and 2125 m, respectively. For the redshifted ^{12}CO$(2-1)$ line, the observation covered a 1.875 GHz bandwidth from 228.199 GHz to 230.074 GHz, centered at an estimated redshifted line frequency of 229.136 GHz. The frequency channel widths were 488.281 kHz, corresponding to a velocity channel resolution of 0.64 km s^{-1} at the redshifted frequency. For continuum emission, two separate 2 GHz spectral windows were centered at 227.210 GHz and 244.902 GHz with 15.625 MHz channel widths, equating to velocity resolutions of 20.6 km s^{-1} and 19.1 km s^{-1}, respectively. The data were initially processed through the ALMA pipeline with version 4.3.1 of the Common Astronomy Software Applications package (CASA, McMullin et al., 2007) and then imaged into data cubes using Briggs weighting with a robust parameter of 0.5 following continuum phase self-calibration and continuum subtraction in the *uv* plane. The cube was reimaged to have 10 km s^{-1} velocity channel widths (with respect to the rest frequency of the ^{12}CO$(2-1)$ line) to isolate narrower line features in spatial regions close to the disk center, and a pixel size of $0\farcs03$ was chosen to sufficiently sample the synthesized beam's minor axis. The beam's full width at half maximum (FWHM) is $0\farcs24$ and $0\farcs18$ along the major and minor axis, respectively, and the beam has a position angle of 86.9° measured east of north.

3.2.3 Circumnuclear Disk Properties

Boizelle et al. (2017) determined several properties of the circumnuclear disk in NGC 1380 which I summarize here. The gas is co-spatial with the dust, as seen in the HST optical

images and ALMA integrated intensity maps in Figure 3.1. The disk is very inclined ($i \approx 75°$) and exhibits orderly rotation around its center, with projected line-of-sight (LOS) velocities of $\sim$300 km s^{-1}. LOS velocity and dispersion maps indicate nearly circular and dynamically cold rotation about the disk centers. Independent stellar kinematic observations with the Multi Unit Spectroscopic Explorer (MUSE) have also revealed the presence of a large-scale cold disk component in NGC 1380 (Sarzi et al., 2018). The radial extent of the CO emission was measured to be 5.″2 (426 pc). A major axis position-velocity diagram (PVD) extracted from the NGC 1380 data cube shows a slight rise in velocity within the innermost $\sim$0.″1, although this does not extend past the velocities observed in the outer parts of the PVD. This central upturn in gas velocity indicates the presence of a massive and compact object at the disk center. The gas mass of the disk was determined by summing the CO flux and assuming an $\alpha_{\rm CO}$ factor of 3.1 $M_\odot$ pc^{-2} (K km s^{-1})$^{-1}$ (Sandstrom et al., 2013) as the extragalactic mass-to-luminosity ratio, a CO(2−1)/CO(1−0) $\approx$ 0.7 line ratio in brightness temperature units (Lavezzi et al., 1999), and a correction factor of 1.36 for helium. Given these assumptions, the gas mass was estimated to be $(8.4 \pm 1.6) \times 10^7\, M_\odot$. The assumption about CO excitation can be tested: Zabel et al. (2019) measure a CO(1–0) line flux for NGC 1380 that in combination with the CO(2–1) line flux from Boizelle et al. (2017) implies a CO(2−1)/CO(1−0) ratio of $1.08^{+0.24}_{-0.20}$ in brightness temperature units. This is higher than the assumed value of 0.7, and implies a lower gas mass. Because a ratio > 1 is unphysically high if both CO lines are tracing the same material, I consider a value ≈ 0.9 (still lying within the measurement uncertainties) to be more appropriate, and I later explore the implications of the correspondingly lower gas mass for the dynamical models.

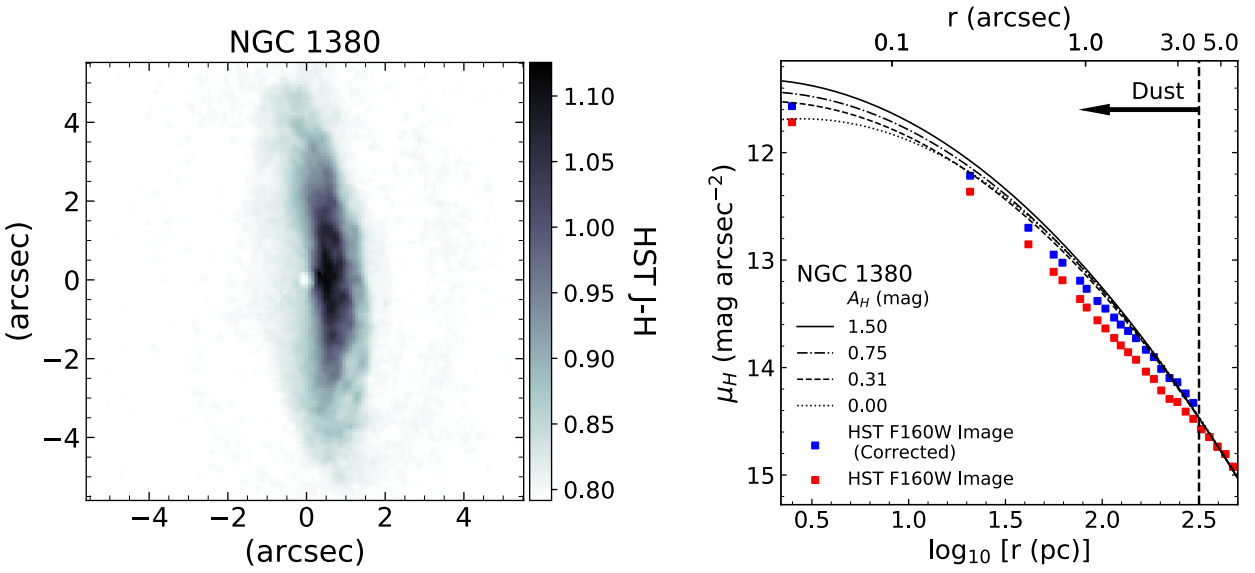

Figure 3.2 NGC 1380 $J-H$ color map (left) constructed using WFC3 F110W and F160W observations, and major axis surface brightness profiles (right) of the different host galaxy MGE models. The $J-H$ map highlights the color asymmetries of the near and far sides of the disks, with the near sides being $\sim 0.2-0.3$ mag redder than the far sides. For the surface brightness models, the red points are the observed values from the H-band image, while the blue points are the dust-corrected values described in Section 3.3.1. The different lines in the panel correspond to extracted major axis surface brightness profiles for the 2D MGE models, which are described in Section 3.3.2. The outer edge of the dust disk is marked with a vertical dashed line, and the arrow indicates that the dust extends down to the nucleus.

3.3 Host Galaxy Surface Brightness Modeling

A key input to the dynamical modeling program is the stellar mass profile, $M_\star(r)$, which is determined by measuring and deprojecting the host galaxy's observed surface brightness profile. One approach to obtaining $M_\star(r)$ is the Multi-Gaussian Expansion (MGE) method, which fits the observed brightness in galaxy images with a series expansion of two-dimensional Gaussian functions (Emsellem et al., 1994; Cappellari, 2002). For galaxies that possess an optically thick dust disk, the impact of dust attenuation on the host galaxy light is mitigated by using observations in the near-infrared (NIR) regime, but the impact is not completely negligible. To assess the variation of H-band extinction across the dust disk, I performed a simple correction to the observed H-band major axis surface brightness profile. This was

done as an attempt to quantify the possible impact of dust on the host galaxy's surface brightness. I then proceeded to fit dust-masked and dust-corrected MGE models to the drizzled H-band image of NGC 1380.

3.3.1 Major Axis Dust Extinction Corrections

The central dust disk in NGC 1380 is clearly visible in Figure 3.2, due to its dimming and reddening of the observed stellar light. I attempted to estimate the amount of dust extinction with a color-based correction method, which was complicated by the fact that the dust disk is embedded within the galaxy and cannot be treated as a simple foreground screen. To estimate the amount of dust extinction, I extracted and corrected the observed H-band major axis surface brightness profile. Using the `sectors_photometry` routine from the `MgeFit` package in Python (Cappellari, 2002), I plotted the surface brightness profile in Figure 3.2. A slight dip in the profile can be seen at around $r = 4''$, which marks the outer edge of the dust disk.

To determine the pixels that are most affected by dust, I created a $J - H$ color map as seen in Figure 3.2. I note that all H and J-band magnitudes in this work are in the Vega magnitude system. The color map revealed that the dust extends from the nuclei, and the pixels most affected by dust are about 0.25 mag redder than the median $J - H$ color of $\sim$0.80 mag outside the disk. Furthermore, the nucleus has a bluer color that is about 0.1 mag more blue than the median color outside the disk. A blue nucleus suggests the presence of star formation or a weak active galactic nucleus (AGN) and I discuss these possibilities below.

I attempted to correct the major axis H-band surface brightness profiles by examining $\Delta(J-H)$, the observed color excess relative to the median $J - H$ color outside the disk, along the major axis. Using equation 1 from Boizelle et al. (2019), which predicts the ratio of observed

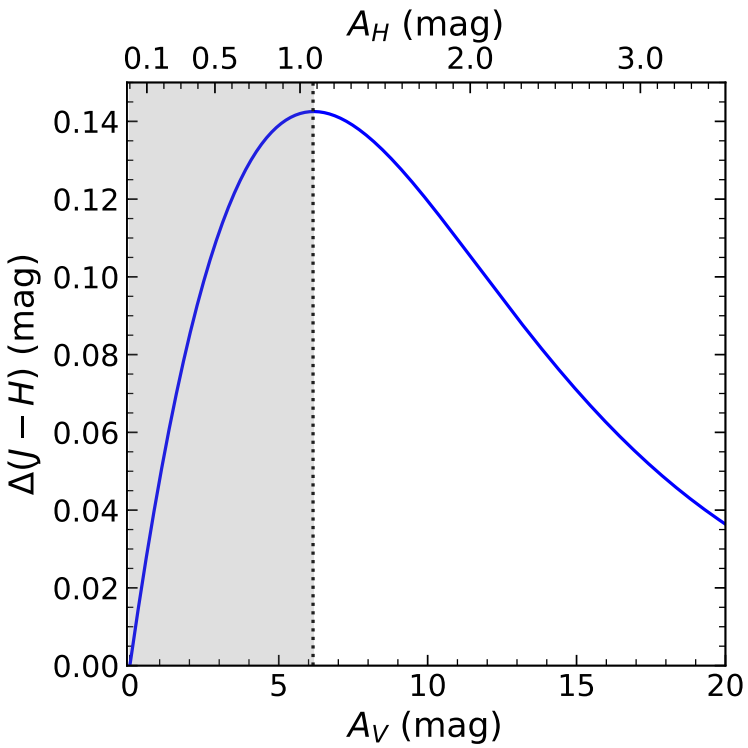

Figure 3.3 Modeled $\Delta(J-H)$ curve as a function of A_V (bottom axis) and A_H (top axis). The curve was generated using equation 1 from Boizelle et al. (2019) and a standard Galactic ($R_V = 3.1$) extinction curve (Rieke and Lebofsky, 1985), under the assumptions that along the major axis, the fractions of light in front of and behind the disk are equal ($f = b = 0.50$), and that only the starlight originating from behind the disk is subject to dust extinction. The gray region left of the dotted line indicates the part of the curve I used to define a one-to-one correspondence between $\Delta(J-H)$ and A_V and A_H for the low-extinction branch of the curve.

to intrinsic integrated stellar light based on the embedded-screen model described by Viaene et al. (2017), I generated a model (seen in Figure 3.3) $\Delta(J-H)$ curve as a function of intrinsic V-band extinction, A_V, to compare with the observations.

The embedded-screen model assumes that the obscuring dust lies in a thin, inclined disk that bisects the galaxy, and that the fraction of stellar light originating behind the disk, b, is obscured by simple screen extinction, while the fraction of stellar light in front of the disk, f, is unaffected. In addition, the model assumes that there is no scattering of stellar light back into the LOS, and that the $J-H$ color outside the disk is the intrinsic color of

the host galaxy. One important aspect of this color excess model is that $\Delta(J-H)$ is not a strictly monotonically increasing function of intrinsic extinction. As seen in Figure 3.3, the color excess increases approximately linearly with increasing A_V up to a turnover point, after which it will begin to decrease to zero as the light originating behind the disk becomes completely obscured. As a result, there are two possible A_V values for a given $\Delta(J-H)$. To maintain a one-to-one correspondence between $\Delta(J-H)$ and A_V, I considered only the low extinction branch of the curve, and therefore adopted the lesser of the two possible A_V values. I inverted the relationship to derive A_V as a function of observed $\Delta(J-H)$ by fitting a third-order polynomial up to the turnover point and determining its inverse. Using a standard Galactic ($R_V = 3.1$) extinction curve (Rieke and Lebofsky, 1985) where $A_H/A_V = 0.175$, and assuming that the fractions of stellar light originating in front of and behind the disk are equal ($f = b = 0.5$) along the major axis, I associated the observed major axis $\Delta(J-H)$ values with corresponding values of A_H.

I generated point by point corrections to the major axis surface brightness profile using the fact that the modeled A_H values only applied to the fraction of light originating behind the disk. The corrected values are shown in blue in Figure 3.2 for points within the dust disk. The corrected surface brightness profile still exhibits a slight dip near the edge of the dust disk.

Since the method described above appears to underestimate the extinction, I also tried applying the method using the high-extinction branch of the $\Delta(J-H)$ vs. A_V curve; however, this approach led to overcorrection all along the major axis, as each point's H-band surface brightness was raised by nearly the theoretical maximum of 0.75 mag arcsec^{-2}. While this method provides some insight on how extinction varies across the disk, based on the results from both branches of the color excess curve, it is clear that a simple extinction correction for a thin embedded disk does not fully correct for dust extinction or give us accurate host galaxy profiles. Thus, I opted to create dust-masked and dust-corrected MGEs to model the

host galaxy's light, following methods used for similar galaxies by Boizelle et al. (2019, 2021) and Cohn et al. (2021).

3.3.2 MGE Models

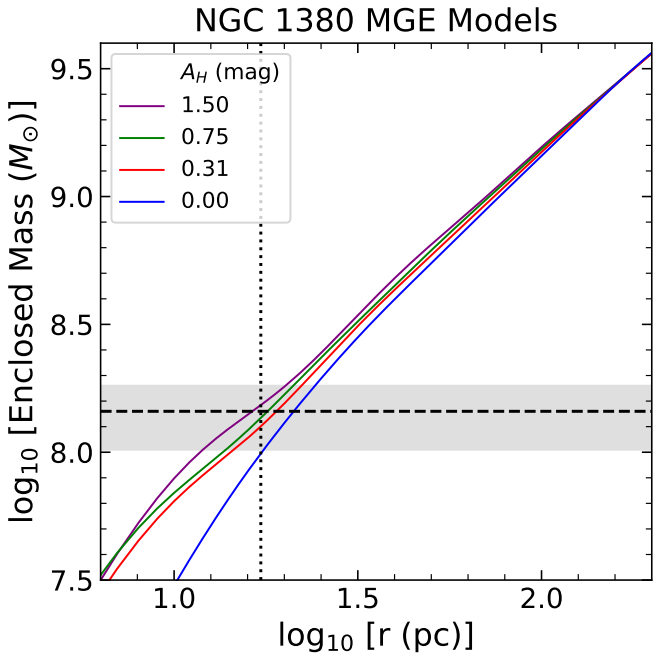

Figure 3.4 Plot of $\log_{10} M_\star(r)$ vs. $\log_{10} r$ in NGC 1380 for the four different MGE models, determined by calculating $M_\star(r) = r v^2_{\star,\mathrm{MGE}}/G$, where the $v_{\star,\mathrm{MGE}}$ values have been scaled by their respective $\sqrt{\Upsilon_H}$ values in Table 3.2. The resolution of the ALMA observation is denoted by the vertical dotted line and is comparable to the BH's expected radius of influence. The BH mass determined from the fiducial model is represented by the horizontal dashed line, and the range of BH masses determined from Models A-D is indicated by the gray shaded region.

Before I constructed an MGE model for NGC 1380, I created a mask that isolated the host galaxy light from the light of foreground stars and background galaxies and identified pixels affected by dust. For the NGC 1380 drizzled H-band image, I masked out foreground stars and background galaxies in the image and corrected for a foreground Galactic reddening in the H-band of $A_H = 0.009$ mag based on reddening measurements from Sloan Digital Sky Survey data by Schlafly and Finkbeiner (2011). Using the $J - H$ color map I constructed

k	$\log_{10} I_{H,k}(L_\odot\,\mathrm{pc}^{-2})$	σ'_k (arcsec)	q'_k	$\log_{10} I_{H,k}(L_\odot\,\mathrm{pc}^{-2})$	σ'_k (arcsec)	q'_k
	$A_H = 0.00$ mag			$A_H = 0.31$ mag		
1	4.931	0.094	0.988	5.560	0.059	0.739
2	4.968	0.193	0.761	4.996	0.197	0.710
3	4.700	0.409	0.840	4.662	0.391	0.726
4	4.389	0.879	0.752	4.513	0.743	0.722
5	4.359	1.375	0.809	4.356	1.461	0.807
6	4.000	3.280	0.608	3.973	3.414	0.613
7	3.462	3.493	0.999	3.386	3.880	0.997
8	3.734	6.119	0.720	3.757	6.018	0.723
9	3.381	12.981	0.715	3.382	12.932	0.732
10	3.068	15.372	0.400	3.043	18.800	0.400
11	2.711	41.875	0.400	2.689	42.731	0.400
12	2.179	53.560	0.785	2.101	55.077	0.851
13	1.757	68.038	0.449	0.926	92.556	0.948
	$A_H = 0.75$ mag			$A_H = 1.50$ mag		
1	4.998	0.145	0.807	3.639	0.542	0.400
2	5.648	0.052	0.677	5.669	0.068	0.745
3	4.859	0.303	0.648	5.073	0.251	0.706
4	4.628	0.610	0.802	4.669	0.595	0.789
5	4.433	1.346	0.797	4.459	1.324	0.788
6	4.019	3.214	0.634	4.032	3.151	0.642
7	3.401	3.622	0.999	3.408	3.528	0.999
8	3.734	6.151	0.702	3.727	6.223	0.691
9	3.353	13.136	0.740	3.352	13.185	0.737
10	3.037	18.912	0.400	3.050	18.752	0.400
11	2.730	41.804	0.400	2.749	41.369	0.400
12	2.401	49.166	0.642	2.462	48.099	0.639
13	2.137	57.557	0.400	2.215	54.962	0.401

Table 3.1 MGE solutions created from the combination of HST H-band images and best-fitting `GALFIT` Nuker models. The MGE used in the statistically best-fitting dynamical model is the $A_H = 0.31$ mag MGE. For each MGE, the first column is the component number, the second is the central surface brightness corrected for Galactic extinction and assuming an absolute solar magnitude of $M_{\odot,H} = 3.37$ mag (Willmer, 2018), the third is the Gaussian standard deviation along the major axis, and the fourth is the axial ratio, which was constrained to have a minimum value of 0.400 to allow for a broader range in the inclination angle during the deprojection process. Primes indicate projected quantities.

earlier, I also masked pixels that had $J - H > 1.05$ mag, which were on the disk's near side. This step prevented pixels with the most apparent dust obscuration from being used in the MGE fit, but there is still clear evidence of extinction in other regions of the disk.

I modeled the observed H-band surface brightness within the inner $10'' \times 10''$ with an MGE created in `GALFIT` (Peng et al., 2002) and required each Gaussian component to have the same center and position angle. To account for the HST PSF, I generated a model H-band PSF using `TinyTim` (Krist and Hook, 2004). This PSF was drizzled and dithered in the same manner as the H-band image and, along with the mask, was used during the `GALFIT` optimization to create the MGE. This initial, dust-masked MGE is referred to as the $A_H = 0.00$ mag model, since it does not attempt to correct for the impact of extinction at locations that were not masked out.

A robust pixel-by-pixel dust correction model would require radiative transfer modeling to account for factors such as disk geometry, thickness, scattering from dust, and extinction within the disk itself (De Geyter et al., 2013; Camps and Baes, 2015). Additionally, light originating from recent star formation or a weakly active nucleus would add further complications to a dust correction model. In the $J-H$ color map, the nucleus of NGC 1380 is bluer than the most reddened pixels in the mask by about $\sim$0.2 mag, suggesting the presence of star formation and/or a weak AGN. Zabel et al. (2020) used combined MUSE and ALMA data to study the relationship between molecular gas surface density and star formation rate in NGC 1380. They concluded that there was no Hα emission from star formation, and that the presence of Hα in NGC 1380 was primarily due to what they defined as composite regions such as shocks or an AGN. Indeed, through integral field spectroscopy, Ricci et al. (2014) determined that NGC 1380 contains a low ionization nuclear emission-line region (LINER).

Viaene et al. (2019) also study the dust mix and gas properties in NGC 1380 with MUSE observations and detect low-level star formation within the inner portion of the disk. They construct 2D A_V maps of the dust lane area by comparing MGE model fits (after having masked out the dust lane) to MUSE V-band images and estimated a maximum A_V value of 1.00 mag, corresponding to $A_H \approx 0.18$ mag for a standard Galactic ($R_V = 3.1$) extinction curve. In addition, they use 3D radiative transfer models to reproduce the observed V-

band attenuation (defined as the combination of extinction and scattering of light back into the LOS) curve. However, their methods assume that only the near side of the dust disk experiences any V-band extinction, whereas the $J-H$ map shows that pixels on the far side are redder relative to the median color outside the disk, indicating that light from the far side is still affected by extinction.

I used the simpler method described by Boizelle et al. (2019), which assumed an analytic surface brightness profile model to correct for dust extinction. Their method examined the impact of extinction on the inferred host galaxy circular velocity profile by adjusting the central H-band surface brightness profile to correct for three fiducial values of dust extinction. I chose the same values of H-band extinction as Boizelle et al. (2019), which were $A_H = 0.31, 0.75$, and 1.50 mag. These values correspond to fractions of 1/4, 1/2, and 3/4 of the stellar light originating behind the dust disk. I emphasize that these values were chosen to explore the impact of dust on the inferred host galaxy models (and subsequently, the values of $M_{\rm BH}$ derived from the dynamical models) over a range in extinction and note that among the major axis surface brightness profiles shown in Figure 3.2, the $A_H = 0.31$ mag MGE model most closely resembles the observed profile after correction using the low-extinction branch of the reddening curve.

I created three dust-corrected MGE models based on the three fiducial H-band extinction values mentioned above. I followed the steps outlined by Boizelle et al. (2021) and describe the process below. To start, I fit a 2D Nuker model (Faber et al., 1997) in `GALFIT` to the central $10'' \times 10''$ region of the H-band image, using the same dust mask and PSF model as before. Nuker profiles are known to effectively model the central surface brightness profiles of ETGs, and their parameters can be easily adjusted to produce dust-corrected models matching the H-band image. The Nuker model's surface brightness profile is characterized by inner and outer power-law profiles, with γ and β representing the inner and outer profile logarithmic slopes. The transition between these two regimes occurs at a break radius, $r_{\rm b}$,

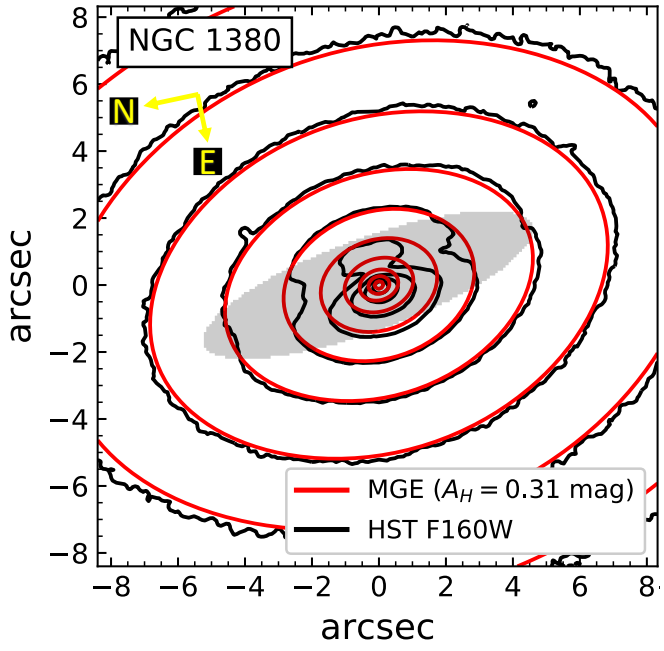

Figure 3.5 Isophotal contour map of the HST F160W image of NGC 1380 displayed on an $8'' \times 8''$ scale. I superpose the surface brightness contours of the intrinsic $A_H = 0.31$ mag MGE model. The shapes and sizes of the central dust disks are indicated by the shaded gray ellipses.

and the transition sharpness is controlled by the parameter α. I allowed all free parameters of the Nuker model to vary in this initial fit. The Nuker model parameters converged to $\alpha = 0.42$, $\beta = 1.49$, $\gamma = 0.31$, and $r_b = 2\farcs5$ ($\approx$200 pc). These parameters characterized the Nuker model fit to the H-band image prior to any dust correction. I then manually corrected the central surface brightness values of the H-band image for extinction levels of $A_H = 0.31$, 0.75, and 1.50 mag, and fit three separate Nuker models to these three dust-corrected images, keeping all parameters other than γ fixed. This approach allowed the Nuker model to adjust its inner slope to the dust-corrected values of the central pixels, but retain its outer slope shape from the initial fit. For extinctions of $A_H = 0.31$, 0.75, and 1.50 mag, the value of γ converged to values of 0.39, 0.44, and 0.47, respectively. Finally, to create dust-corrected MGE models, I replaced the H-band data within the disk region with the corresponding pixels in the Nuker models, and fit MGE models in `GALFIT` to these dust-corrected H-band images without using a mask. The major axis surface brightness

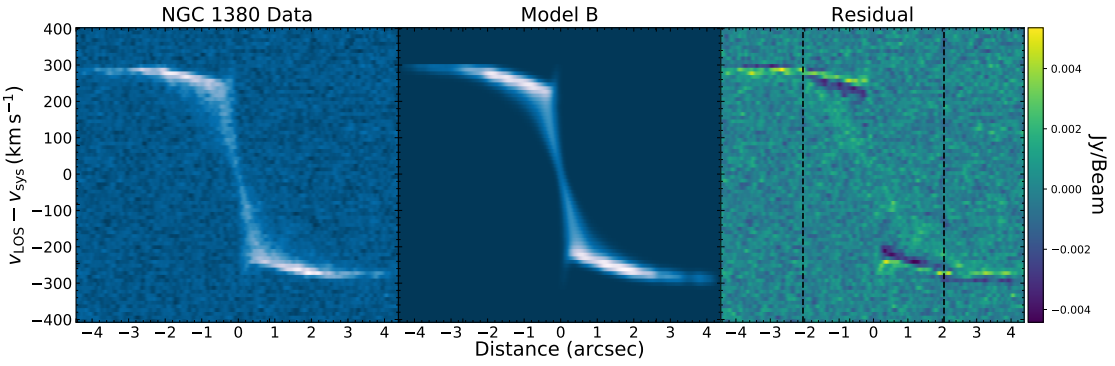

Figure 3.6 PVD along the major axis of NGC 1380 and the respective best-fit dynamical model. Columns show ALMA Cycle 2 CO(2−1) data (left), model (center), and (data-model) residual (right). The PVDs were generated with a spatial extraction width equivalent to a resolution element. The black dashed lines indicate the boundaries of the elliptical fit regions along the major axis.

profiles of these three MGE models are shown in Figure 3.2, and a plot of their enclosed mass profiles is shown in Figure 3.4. As I discuss in Section 3.4.3, the best-fit dynamical model uses the $A_H = 0.31$ mag MGE model. I display and compare this model's isophotes to those of the data in Figure 3.5. While there is good agreement between data and model outside the central dust lane, there is some deviation between the two within the dusty region. The observed isophotes become non-elliptical towards the center, which is attributed to the presence of the dust disk. The components of all the MGE models are presented in Table 3.1.

3.4 Dynamical Model Optimization

To dynamically model the ALMA data cube, I used the formalism I described in Chapter 2. Here, I will briefly cover the specific characteristics of the model fit to the NGC 1380 data cube.

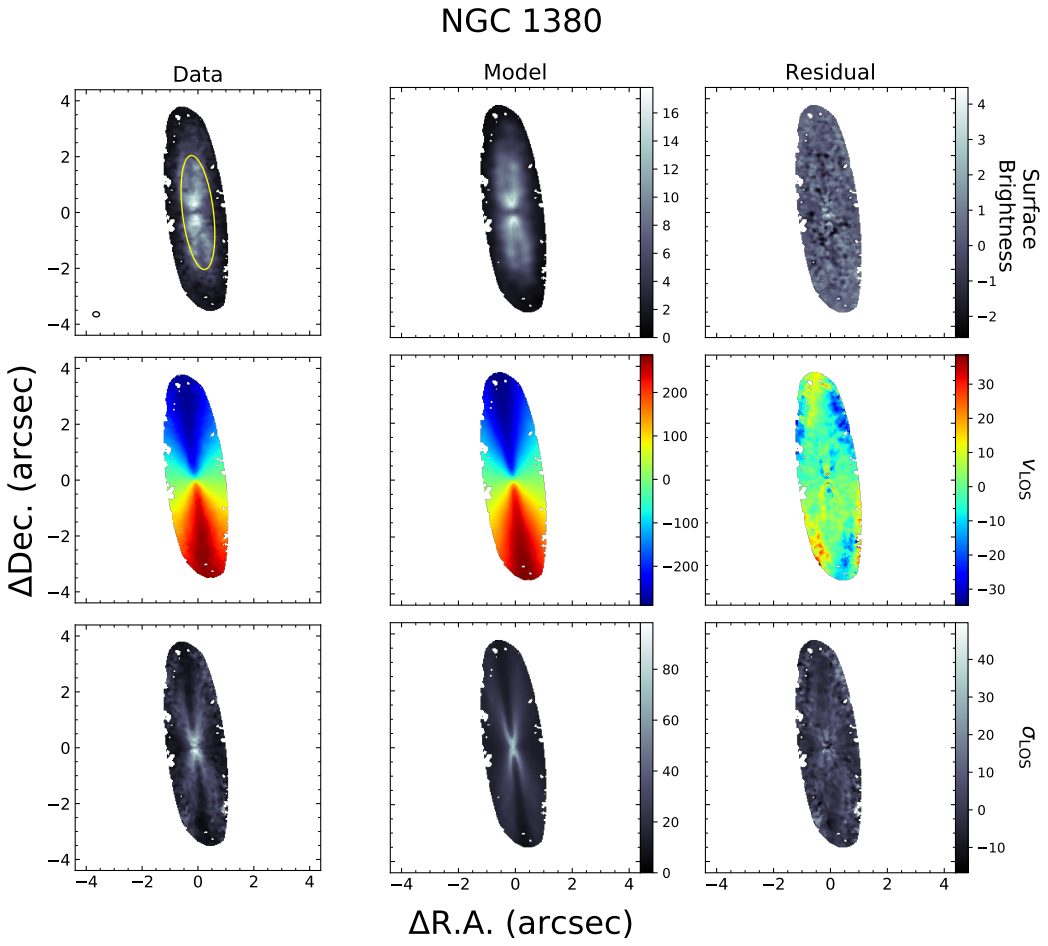

Figure 3.7 Moment maps for NGC 1380 constructed from the ALMA CO(2−1) data cube (left) and its fiducial model (center, model B; see Section 3.4.2). Shown are maps of moments 0, 1, and 2, corresponding to surface brightness, line-of-sight velocity $v_{\rm LOS}$, and turbulent velocity dispersion $\sigma_{\rm LOS}$. The units for the surface brightness map are mJy km s^{-1} pixel^{-1}, and the units for the $v_{\rm LOS}$ and $\sigma_{\rm LOS}$ maps are km s^{-1}. The systemic velocity of 1854 km s^{-1} estimated from the dynamical models has been removed from $v_{\rm LOS}$. Maps of (data-model) residuals are shown in the rightmost column. While the line profile fits have been determined at each pixel of the full disk, the elliptical fitting region used in calculating χ^2 is denoted in the top left panel with a yellow ellipse. The synthesized beam is represented by an open ellipse in the bottom left corner of the same image.

For a given model parameter set, I create a simulated data cube with the same spatial and spectral dimensions as the ALMA data. Therefore, the model can be fitted directly to the ALMA data cube and can be optimized by χ^2 minimization. I optimized the dynamical models with the Levenberg-Marquardt algorithm (Levenberg, 1944; Marquardt, 1963) within

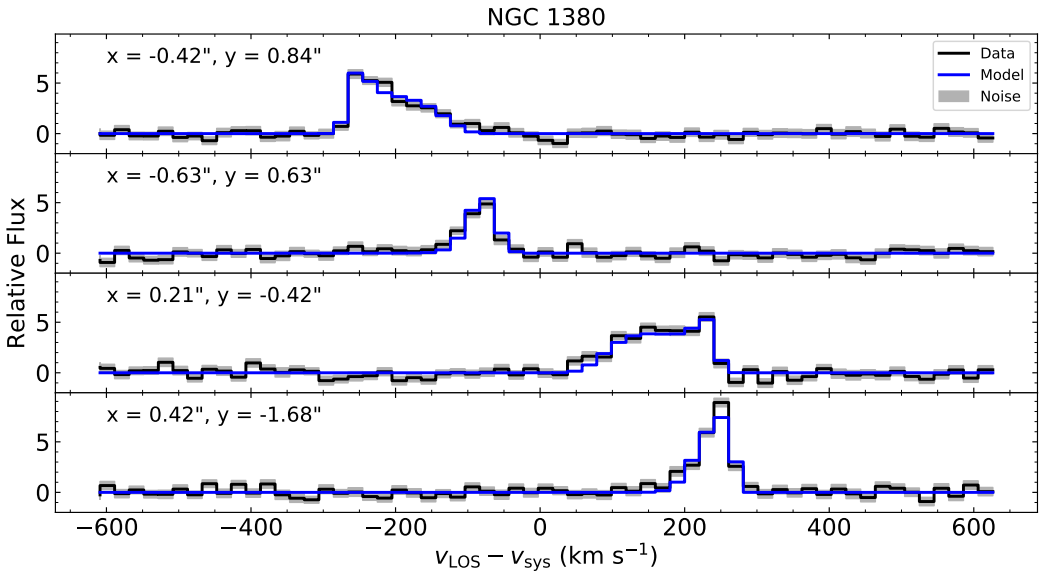

Figure 3.8 Representative line profiles of NGC 1380 measured by extracting single pixel cuts through the data, model, and noise cubes at four locations. The model line profiles are assumed to be intrinsically Gaussian at the sub-pixel level, with the asymmetric structure coming from beam-smearing. The noise band represents values in the range of data $\pm 1\sigma$. These line profiles were extracted from the cubes on the final scale of 1 block-averaged pixel per synthesized beam. The x and y labels indicate the pixel locations in terms of offsets in arcseconds from the disk dynamical centers.

the `LMFIT` framework (Newville et al., 2016) in Python and fit to pixels that lay within the elliptical region illustrated in the data moment 0 map in Figure 3.7.

3.4.1 Fit Region

I initially created an ellipse centered on the disk center with an axial ratio of $q = 0.27$, and a position angle of $\Gamma = 187°$ based on results from Boizelle et al. (2017). For the fiducial dynamical model, I chose to fit within an ellipse that encompassed the inner half of the CO disk in order to limit the sensitivity of the dynamical models to the shape of the stellar mass profile and the disk's slightly warped structure. I also modified the size of this ellipse to see how the choice of fit region affected the inferred value of $M_{\rm BH}$ in Section 3.4.3. The final

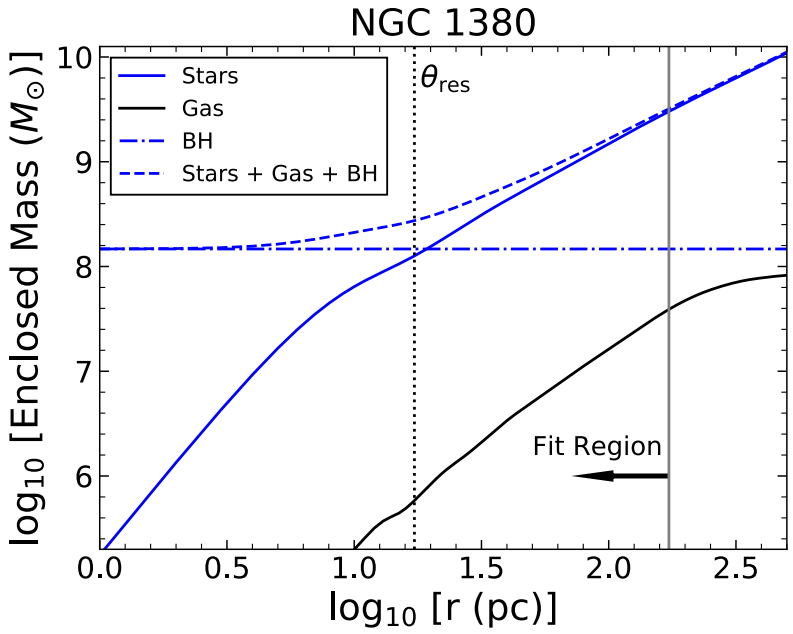

Figure 3.9 Enclosed mass profiles as a function of radius used in the dynamical modeling of NGC 1380. I show the mass contributions from the stars, gas, and BH, as well as the sums of their masses. The stellar mass profile is derived from the $A_H = 0.31$ mag MGE used in the fiducial model. The dotted lines correspond to the $0\farcs21$ resolution of the NGC 1380 observations.

fitting ellipse has a semimajor axis of $a = 2\farcs05$ and a semiminor axis of $b = 0\farcs55$. This ellipse was used across 62 consecutive frequency channels that spanned the full width of the visible CO emission in the data and can be seen in Figure 3.7. On the final rebinned scale, this choice of spatial and spectral regions resulted in 61 block-averaged pixels over 62 frequency channels for a total of 3782 data points used to calculate χ^2.

3.4.2 Modeling Results

I present results for four models for NGC 1380, which I refer to as models A, B, C, and D in Table 3.2. The key difference among them is the input host galaxy circular velocity profile, based on one of the four MGE models described in Section 3.3.2, which accounted for four fiducial values of central dust extinction (A_H = 0.00, 0.31, 0.75, and 1.50 mag for models

A, B, C, and D, respectively). These dynamical models use a uniform turbulent velocity dispersion across the entire disk and are optimized over the elliptical region described in Section 3.4.1.

Models A-D yield best-fit values of $M_{\rm BH}$ in the range of $(1.02 - 1.85) \times 10^8\,M_\odot$, Υ_H between 1.30 and 1.42, and a range in reduced χ^2 (χ^2_ν) between 1.525 and 1.563 over 3773 degrees of freedom. The measured range of Υ_H is slightly above the predictions made from single stellar population (SSP) models (Vazdekis et al., 2010) that assume either a Kroupa (2001) or Chabrier (2003) initial-mass function (IMF) and is lower than predictions made with a Salpeter (1955) IMF. These SSP models assume an old stellar population (10-14 Gyr) and solar metallicity, which are consistent with 2D IMF analyses of NGC 1380 by Martín-Navarro et al. (2019). As seen in Table 3.2, all other free parameters remained virtually unchanged among the different dynamical models. I discuss the interplay between $M_{\rm BH}$ and Υ_H in Section 3.5.1.

The major axis PVD, moment maps, and example line profiles for the best-fit model (model B) for NGC 1380 are presented and compared with the ALMA data in Figures 3.6, 3.7, and 3.8. The moment maps and PVD reveal that the data and model are in good agreement over a majority of the disk, although a mismatch in the observed surface brightness is seen in both the moment 0 (surface brightness) map and in the structure of the PVD, especially within the innermost $\sim$0.″5. Moment 1 ($v_{\rm LOS}$) maps show that data and model velocity fields are also in good agreement, although differences of $\sim$30 km s^{-1} are noticeable towards the disk edge, outside the fit region, and at the disk center, where the impact of beam-smearing is most severe. Most likely, these differences are a result of the differences between the model and intrinsic stellar velocity profiles. The extracted line profiles of the block-averaged data and best-fit model highlight the models' ability to reproduce the observed shapes of the line profiles, even when they display asymmetric structure.

To determine the statistical uncertainties of the free parameters, I performed a Monte Carlo simulation for model B. I created 150 realizations of the best-fit model by adding noise to each pixel of the model cube. The value of the noise at each pixel was determined by choosing a random value drawn from a Gaussian distribution with a standard deviation equal to the value of the corresponding pixel in the noise cube described in Section 2.1.5. I re-fit to each noise-added model realization using the values found in Table 3.2 as initial guesses; the standard deviation of each recovered parameter was identified as the 1σ uncertainty. For $M_{\rm BH}$, I found a tight distribution centered at the initial guess of $M_{\rm BH} = 1.47 \times 10^8\,M_\odot$ with a standard deviation of $2 \times 10^6\,M_\odot$, or 1.4% of the mean. The statistical uncertainties for the free parameters are listed under model B's best-fit values in Table 3.2. Based on other Monte Carlo simulations I ran, these statistical uncertainties are representative of those for models A, C, and D.

Model	MGE (A_H mag)	$M_{\rm BH}$ ($10^8\,M_\odot$)	Υ_H ($M_\odot/L_\odot$)	i (°)	Γ (°)	σ_0 (km s^{-1})	$v_{\rm sys}$ (km s^{-1})	F_0	χ^2_ν
A	0.00	1.85	1.33	76.9	187.1	10.8	1853.83	0.99	1.544
B	0.31	1.47	1.42	76.9	187.2	10.5	1853.86	0.99	1.525
		(0.02)	(0.003)	(0.04)	(0.04)	(0.13)	(0.15)	(0.003)	
C	0.75	1.27	1.36	76.9	187.2	10.5	1853.86	0.99	1.545
D	1.50	1.02	1.30	76.8	187.2	10.5	1853.88	0.99	1.563

Table 3.2 Best-fit parameter values obtained by fitting thin disk dynamical models to the NGC 1380 data cube. I derive 1σ statistical uncertainties for the parameters of fiducial model B based on a Monte Carlo resampling procedure described in Section 3.4.2 and list them under the results for model B. This model has 3773 degrees of freedom. The major axis PA Γ, is measured east of north for the receding side of the disk. The disk dynamical center is found to be about $\sim$0.″01 from the nuclear continuum centroid for NGC 1380 determined in Boizelle et al. (2017). The observed redshift, $z_{\rm obs}$, is used in the dynamical models as a proxy for the systemic velocity of the disk, $v_{\rm sys}$, in the barycentric frame via the relation: $v_{\rm sys} = cz_{\rm obs}$ and is used to translate the model velocities to observed frequency units.

3.4.3 Error Budget for NGC 1380

While the statistical uncertainties from the Monte Carlo simulation are small, there are several other sources of uncertainty that stem from the choices made when building the

dynamical models. Thus, I conducted numerous tests to determine the impact these choices had on the value of $M_{\rm BH}$.

Dust Extinction: The value of $M_{\rm BH}$ in the model optimizations is highly sensitive to the choice of MGE model. Using the initial, dust-masked MGE, the models converge on $M_{\rm BH} = 1.85 \times 10^8\,M_\odot$. As I increase the central extinction from $A_H = 0.00$ mag to $A_H = 0.31$ mag, corresponding to a loss of 25% of the total stellar light behind the dusty disk, $M_{\rm BH}$ decreases to $1.47 \times 10^8\,M_\odot$, representing a $\sim$20% decrease from the initial fit. This particular model also shows a decrease in the resultant χ^2_ν, as model A with the initial MGE returns $\chi^2_\nu = 1.544$, while model B with $A_H = 0.31$ mag yields $\chi^2_\nu = 1.525$. Increasing the extinction further to $A_H = 0.75$ mag and $A_H = 1.50$ mag further decreases $M_{\rm BH}$, as models C and D converge to values of $1.27 \times 10^8\,M_\odot$ and $1.02 \times 10^8\,M_\odot$, i.e., $\sim$31% and $\sim$45% decreases from the model A value, respectively. However, both models C and D result in higher χ^2_ν values.

I chose the $A_H = 0.31$ mag MGE model (model B) to use as the fiducial model for a number of reasons. First, this MGE model accounts for the impact of dust extinction, whereas the initial MGE simply masks dust out. Next, the dynamical model that uses the $A_H = 0.31$ mag MGE has the lowest value of χ^2 out of all the models, signifying the best overall match to the ALMA data. Lastly, extracting the major axis surface brightness profile from this MGE model reveals that it most closely resembles the surface brightness profile after correction for the low-extinction branch of the reddening curve shown in Figure 3.2. Therefore, for all the remaining systematic tests, I use the $A_H = 0.31$ mag MGE as the host galaxy model.

Radial motion: Although there is no evidence of strong deviations from circular motion in the NGC 1380 gas disk, I constructed a simple model that allows for radial motion in the dynamical models. I followed an approach similar to Boizelle et al. (2019) and Cohn et al. (2021) and added a radially inward velocity term to the dynamical models. I included an additional free parameter, α, which lies in the range $[0, 1]$ and controls the balance between pure rotational ($\alpha = 1$) and radially inflowing ($\alpha = 0$) motion. Mathematically, I defined

α to be the ratio between the rotational velocity, $v_{\rm rot}$, and the ideal circular velocity in the model grid (i.e., $\alpha = v_{\rm rot}/v_c$). I defined the relationship between α, radial inflow velocity, and the ideal circular velocity as $v_{\rm infl} = \sqrt{2(1-\alpha^2)}v_c$. Thus, when $\alpha = 1$, the model velocities are circular, and when $\alpha = 0$, the velocities are radially inflowing at the ideal free-fall speed of a test particle falling in from infinity. I projected the radial velocity component along the LOS, and added it linearly to the projected LOS rotation velocity at each pixel in the model grid. Upon optimizing, I found that the models strongly favored pure rotation, with a best-fitting value of $\alpha = 1$. This model converged on $M_{\rm BH} = 1.47 \times 10^8\,M_\odot$, leaving the results found for the fiducial model unchanged.

Turbulent velocity dispersion: The ratio of the turbulent velocity dispersion to the rotational velocity ($\sigma/v_{\rm rot}$) determines if the disk can be treated as dynamically cold (where $(\sigma/v_{\rm rot})^2 \ll 1$), or if dynamical pressure effects from turbulence must be accounted for. By using the $A_H = 0.31$ mag MGE model, the radial gas mass profile, the fiducial BH mass, and the best-fit value of $\sigma_0 = 10.5\,{\rm km\,s^{-1}}$, I find a maximum value of $\sigma_0/v_{\rm c} = 0.05$ (where I have set $v_{\rm rot} = v_{\rm c}$, the ideal circular velocity) at about $r = 50$ pc, indicating that treating the disk as dynamically cold and neglecting dynamical pressure effects are justified. Nevertheless, a spatially uniform turbulent velocity dispersion term might be insufficient to characterize possible variations in turbulence across the entire disk. Therefore, in addition to using a spatially uniform gas turbulent velocity dispersion term, $\sigma(r) = \sigma_0$, I also tried incorporating a Gaussian turbulent velocity dispersion profile $\sigma(r) = \sigma_0 + \sigma_1 \exp[-(r-r_0)^2/2\mu^2]$ into the fiducial model. This profile adds three free parameters and allows for more flexibility in characterizing the overall velocity dispersion. However, the model is not physically motivated, and is used here as a simple tool for exploring possible variations in $\sigma(r)$. The preferred turbulent velocity dispersion parameters of $\sigma_0 = 10.6$ km s^{-1}, $\sigma_1 = 0.21$ km s^{-1}, $r_0 = 0.06$ pc, and $\mu = 0.02$ pc yield a turbulent velocity dispersion profile that is dominated by the spatially uniform term of $10.6\,{\rm km\,s^{-1}}$, and is nearly identical to the fiducial model's spatially uniform $\sigma_0 = 10.5\,{\rm km\,s^{-1}}$.

The modified model yields $M_{\rm BH} = 1.47 \times 10^8\,M_\odot$ and $\chi^2_\nu = 1.526$, demonstrating almost no effect on the results of the fiducial model.

Fit region: I tested the sensitivity of $M_{\rm BH}$ to the fit regions of the dynamical models by making two separate adjustments to the spatial fitting ellipse described in Section 3.4.1 and used to calculate χ^2. The first adjustment was expanding the fitting ellipse to cover the entirety of the gas disk, with semimajor axis length $4\farcs1$ and semiminor axis length $1''$. For this fitting ellipse, the models converged on $M_{\rm BH} = 1.63 \times 10^8\,M_\odot$, an increase of 10.9% from the fiducial model, and $\chi^2_\nu = 1.451$. This larger fitting ellipse includes nearly four times as many data points, but a majority of points are at radii where the extended stellar mass distribution dominates the total enclosed mass.

The second adjustment was reducing the fitting ellipse to fit only the inner third of the disk, with semimajor and semiminor axis lengths of $1\farcs37$ and $0\farcs33$. The resultant value of $M_{\rm BH}$ was $1.52 \times 10^8\,M_\odot$, an increase of 3.4% relative to the fiducial model, with $\chi^2_\nu = 1.337$. On this scale, the fit contains a higher fraction of data points that display unresolved gas kinematics, particularly along the disk's minor axis, where beam-smearing effects are more severe.

Pixel oversampling: Other molecular gas-dynamical studies such as Barth et al. (2016a) have found that $M_{\rm BH}$ is relatively insensitive to the choice of pixel oversampling factor, s. I tested the fiducial dynamical model with oversampling factors of $s = 1$ and $s = 4$. For $s = 1$, the result was $M_{\rm BH} = 1.45 \times 10^8\,M_\odot$, a decrease of 1.4% relative to model B, with a higher χ^2_ν of 1.543, as expected for no pixel oversampling. At $s = 4$, the resulting $M_{\rm BH}$ was $1.47 \times 10^8\,M_\odot$, identical to the fiducial model result, with a slightly improved χ^2_ν of 1.524. These results show that $M_{\rm BH}$ has little sensitivity to the choice of s, even in the no-oversampling case of $s = 1$.

Gas mass: I performed two tests to observe the dependence of $M_{\rm BH}$ on the inclusion or exclusion of the gas disk's contribution to the mass model. First, I optimized a dynamical model that did not include the circular velocity contribution from the gas disk which was derived from the mass surface densities in Boizelle et al. (2017), but otherwise used the same inputs as model B. Without this contribution, the model converged upon $M_{\rm BH} = 1.43 \times 10^8\,M_\odot$, a decrease of 2.7%, and the same $\chi^2_\nu = 1.525$ as the fiducial model. In addition, I rescaled the gas mass surface densities to the lower value implied by a CO(2–1)/CO(1–0) intensity ratio ≈ 0.9 (see Section 2.2.2) and reoptimized the dynamical model with this adjusted circular velocity contribution. With this adjustment, the model converged upon $M_{\rm BH} = 1.45 \times 10^8\,M_\odot$, and an identical $\chi^2_\nu = 1.525$. These results suggest the inclusion or exclusion of the gas component in models can be important in percent-level precision BH mass measurements. However, in this case, it is a relatively minor contribution to the error budget in comparison to that of the dust extinction.

Unresolved Active Galactic Nucleus Emission: Given that there is evidence of a weak AGN in NGC 1380, I explored the possibility that the MGEs could be incorporating the light from this AGN in addition to the stars. As a test, I removed the innermost component (FWHM $= 0\farcs14 = 11.5$ pc) of the $A_H = 0.31$ mag MGE model, and deprojected the remaining components. Using this altered MGE model, the BH mass rose to $M_{\rm BH} = 2.04 \times 10^8\,M_\odot$, an increase of 38.7% from the fiducial BH mass ($1.47 \times 10^8\,M_\odot$) found when I included the innermost component, but the reduced χ^2 value also rose to 1.528, indicating a poorer fit to the data. If I deproject this innermost component individually, and assume it is composed entirely of starlight, the corresponding stellar mass is $0.59 \times 10^8\,M_\odot$ (assuming $\Upsilon_H = 1.42$), which is slightly higher (by $2 \times 10^6\,M_\odot$) than the difference in BH mass. While it is difficult to determine the amount of AGN light in the innermost MGE component, given that the increase in BH mass between the two dynamical models is commensurate with the decrease in assumed stellar masses, this test shows that the BH and stellar mass of the innermost component are degenerate.

The large range of $M_{\rm BH}$ found in Table 3.2 and the sensitivity tests performed above show that the systematic error is dominated by the uncertainties associated with the host galaxy models. Specifically, these uncertainties are associated with the amount of stellar mass, which changes depending on the assumed dust extinction and/or the presence or absence of an AGN contributing to the central host galaxy light, as shown when I removed the innermost component of the MGE. I chose model B as the fiducial model for the reasons described in Section 3.4.3 and treat the $\Delta M_{\rm BH}$ between its $M_{\rm BH}$ value of $1.47 \times 10^8\,M_\odot$ and the maximum ($1.85 \times 10^8\,M_\odot$) and minimum $M_{\rm BH}$ ($1.02 \times 10^8\,M_\odot$) values found in Table 3.2 as a rough estimate of the uncertainty due to the dust correction. These maximum and minimum values are about 26% larger and 31% smaller than the fiducial $M_{\rm BH}$ value, respectively.

It is clear that the systematic uncertainties exceed the statistical uncertainty ($\approx 1\%$) and the uncertainty associated with the distance to the galaxy ($\approx 8\%$) (Tonry et al., 2001). Considering that the uncertainties from the dust correction and the host galaxy mass modeling dominate the total systematic uncertainty, I adopt the BH mass of $1.47 \times 10^8\,M_\odot$ from the fiducial model and the aforementioned uncertainties as the estimate for $M_{\rm BH}$. Therefore, the expected range of $M_{\rm BH}$ in NGC 1380 is $(1.02 - 2.04) \times 10^8\,M_\odot$.

3.5 Discussion

The molecular gas-dynamical measurement is the first attempt to determine the mass of the central BH in NGC 1380. The presence of dust limits the measurement precision on $M_{\rm BH}$. I find $M_{\rm BH} = 1.47 \times 10^8\,M_\odot$ with an uncertainty of $\sim$40% which is dominated largely by the dust corrections. Below, I discuss the importance of resolving the BH sphere of influence and accounting for the presence of dust. I also discuss how parameter degeneracies emerge

within the dynamical model from these factors, and I compare the measured $M_{\rm BH}$ values to predictions from the BH-host galaxy scaling relations given by Kormendy and Ho (2013).

3.5.1 The BH Sphere of Influence

The precision of a BH mass measurement is highly dependent on how well the observations resolve the radius of the BH's dynamical sphere of influence, $r_{\rm SOI}$. Within $r_{\rm SOI}$, the central BH is the dominant contributor to the total gravitational potential. If $r_{\rm SOI}$ is unresolved, then the measured value of $M_{\rm BH}$ depends heavily on the accuracy of the assumed host galaxy model, and dynamical models are susceptible to parameter degeneracies. I estimated $r_{\rm SOI}$ in two distinct ways. The first was to determine the radius where $M_{\rm BH}$ is equal to the enclosed stellar mass, and the second was to calculate $r_{\rm SOI} \approx GM_{\rm BH}/\sigma_\star^2$ using the measured values of $M_{\rm BH}$ and a known literature value of $\sigma_\star$ for NGC 1380.

For NGC 1380, I used the best-fit value of $M_{\rm BH} = 1.47 \times 10^8 M_\odot$ from the fiducial model to determine $r_{\rm SOI}$. The radius where the enclosed stellar mass (derived from the MGE used in the fiducial model) equaled $M_{\rm BH}$ was $r_{\rm SOI} = 18$ pc ($0\farcs22$), which is nearly identical to the average beam size of $0\farcs21$. If I instead calculate $r_{\rm SOI}$ as $r_{\rm SOI} = GM_{\rm BH}/\sigma_\star^2$, using the average value of $\sigma_\star = 215\,{\rm km\,s^{-1}}$ from Hyperleda (Makarov et al., 2014), I find $r_{\rm SOI} = 14$ pc ($0\farcs17$). I display both the total enclosed mass profile and the separate contributions from each component to the dynamical model in Figure 3.9. These estimates demonstrate it is likely that the observations only marginally resolve $r_{\rm SOI}$.

While there is evidence of a slight central upturn in gas velocity within the innermost $\sim 0\farcs2$ of NGC 1380, given that the observations do not fully resolve $r_{\rm SOI}$, it is unsurprising that the measurement of $M_{\rm BH}$ carries a large uncertainty of about 40% (dominated mostly by the uncertainties from the dust correction and host galaxy modeling), and that the dynamical models have a degeneracy between BH and stellar mass. In essence, the dynamical models'

ability to distinguish their separate contributions is severely limited when $r_{\rm SOI}$ is not fully resolved. This limitation was demonstrated by the test removal of the innermost component of the host galaxy MGE model, as the increase in $M_{\rm BH}$ was commensurate with the decrease in stellar mass. While the total enclosed mass is well-constrained at large radii, the mass contributions from the BH and the stars within the central regions are not. This degeneracy is highlighted in Figure 3.4, which shows stellar mass versus radius for the dust-masked and dust-corrected host galaxy models. With each progressive increase in assumed dust extinction, the stellar mass becomes a larger fraction of the total enclosed mass. While the differences in the stellar mass profiles are minimal at radii greater than ∼100 pc, it is their differences within the innermost ∼30 pc that lead to decreases in $M_{\rm BH}$ and variations in Υ_H. Given that the total enclosed mass is tightly constrained by the well-resolved kinematics at large radii, the cuspier surface brightness models require smaller $M_{\rm BH}$ values.

3.5.2 BH Mass Comparisons

Although there is no prior dynamical BH mass measurement for NGC 1380, Pota et al. (2013) did predict $M_{\rm BH} = 2.2^{+1.8}_{-0.9} \times 10^8\,M_\odot$ based on velocity dispersion measurements of the globular clusters in the galaxy, which is consistent with my findings.

Using equations 6, 7, and 8 from Kormendy and Ho (2013), I derived predictions of $M_{\rm BH}$ from the estimated total K-band luminosity, the estimated bulge mass, and the stellar velocity dispersion for NGC 1380. For the $M_{\rm BH} - L_{{\rm bul},K}$ relation, I converted the total K-band apparent magnitudes from 2MASS into corresponding total K-band luminosities using the assumed luminosity distances. For NGC 1380, I adopted the measured R-band $B/T = 0.359$ from Gao et al. (2019) to determine $L_{{\rm bul},K}$. Schulz et al. (2003) studied the wavelength dependence of B/T in ETGs through evolutionary synthesis modeling, and found that while B/T does change substantially from the U through I bands, the changes diminish at redder

wavelengths. In addition, Li et al. (2011) determined that the observed $B-I$, $V-I$, and $R-I$ profiles in NGC 1380 remained flat over a large radial range. Based on this information, I expect that the difference between R and K-band B/T values are relatively small, and given that there are no presently available B/T measurements in the K-band, I use the R-band value as an estimate in the calculations of $L_{\mathrm{bul},K}$. To compare with the $M_{\mathrm{BH}}-M_{\mathrm{bul}}$ relation, I calculated $L_{\mathrm{bul},H}$ by assuming $H-K=0.2$ mag based on SSP models and an absolute H-band (K-band) magnitude of 3.37 (3.27) for the Sun (Willmer, 2018), and multiplied $L_{\mathrm{bul},H}$ by the best-fit Υ_H values to derive an estimate for M_{bul}. Finally, to compare the BH mass measurements to the $M_{\mathrm{BH}}-\sigma_\star$ relation, I used the $\sigma_\star$ values of 215 km s^{-1}. I note that the $M_{\mathrm{BH}}-L_{\mathrm{bul},K}$, $M_{\mathrm{BH}}-M_{\mathrm{bul}}$, and $M_{\mathrm{BH}}-\sigma_\star$ relations of Kormendy and Ho (2013) have intrinsic scatters of 0.28, 0.30, and 0.28 dex.

With a best-fit value of $M_{\mathrm{BH}}=1.47\times10^8\,M_\odot$ and an associated uncertainty of about 40%, the estimate of M_{BH} in NGC 1380 generally agrees with predictions made by the BH-host galaxy scaling relations. For NGC 1380, I derived a total K-band bulge luminosity of $3.8\times10^{10}\,L_\odot$ and a bulge mass of $M_{\mathrm{bul}}=5.0\times10^{10}\,M_\odot$ to use in the $M_{\mathrm{BH}}-L_{\mathrm{bul},K}$ and $M_{\mathrm{BH}}-M_{\mathrm{bul}}$ relations. These relations predict ranges of $M_{\mathrm{BH}}=(1.4-2.0)\times10^8\,M_\odot$ and $M_{\mathrm{BH}}=(1.8-2.5)\times10^8\,M_\odot$, respectively. The range predicted from the stellar velocity dispersion of 215 km s^{-1} is $(3.7-4.8)\times10^8\,M_\odot$. Thus, the measurement of M_{BH} in NGC 1380 directly overlaps with the predictions made from the $M_{\mathrm{BH}}-L_{\mathrm{bul},K}$ and $M_{\mathrm{BH}}-M_{\mathrm{bul}}$ relations, and lies slightly below and outside the scatter from the $M_{\mathrm{BH}}-\sigma_\star$ relation.

3.6 Conclusion

I present the first gas-dynamical measurement of the BH mass in NGC 1380 using ALMA CO(2−1) observations at 0.″21 resolution. A slight central increase is observed in its maxi-

mum LOS velocity in the PVD, reaching approximately ± 300 km s^{-1} relative to the systemic velocity, as expected of rotation around a central BH.

For NGC 1380, I determine $M_{\rm BH} = 1.47 \times 10^8\,M_\odot$ with an uncertainty of about 40% by optimizing thin disk models to the ALMA observations with four different host galaxy models. I find that the measured values of $M_{\rm BH}$ are degenerate with the enclosed stellar mass, and that the uncertainties associated with the dust corrections and host galaxy models dominate the error budget. Given the slight central rise in observed LOS velocity, it is possible that higher resolution ALMA observations could provide a more confident determination of the BH mass by lifting the stellar and BH mass degeneracy.

When comparing the measurement of $M_{\rm BH}$ to the BH-host galaxy scaling relations determined by Kormendy and Ho (2013), the measured values of $M_{\rm BH}$ for NGC 1380 are generally consistent with the $M_{\rm BH} - L_{\rm bul}$ and $M_{\rm BH} - M_{\rm bul}$ relations, but are below the expected values predicted by the $M_{\rm BH} - \sigma_\star$ relation. More precise BH mass measurements on the high-mass end of these scaling relations are needed to understand the differences among them and to determine whether there is more intrinsic scatter than previously thought.

My work highlights a number of factors that limit gas-dynamical BH mass measurements with ALMA. Factors such as dust obscuring the stellar light, a lack of high-velocity emission within $r_{\rm SOI}$, and the presence of a hole in the CO distribution lead to degeneracies among model parameters and large systematic uncertainties that are important to account for. A key area of improvement would be to incorporate realistic 3D radiative transfer modeling codes (De Geyter et al., 2013; Camps and Baes, 2015) to recover the intrinsic stellar surface brightness of the host galaxy from NIR images. This goal is especially important for ALMA observations of dusty ETGs that do not resolve gas deep within the sphere of influence. Nevertheless, ALMA observations in this regime provide high-resolution information on circumnuclear disks in ETGs and meaningful constraints on $M_{\rm BH}$.

Chapter 4

NGC 6861

4.1 Galaxy Properties

NGC 6861 is located at a luminosity distance of 27.3 Mpc in the Telescopium galaxy group, which corresponds to an angular scale of 129.9 $\mathrm{pc\,arcsec^{-1}}$ when using a redshift of $z = 0.00944$ from the initial dynamical models. This galaxy is classified as an E/S0 in Hyperleda and as an S0A-(s) in RC3. Kormendy and Ho (2013) note that the main body of NGC 6861 does not deviate significantly from an $n \simeq 2$ Sérsic-function profile, although the galaxy has extra central light; I adopt that paper's classification as an extra-light elliptical. In addition, I also adopt the stellar velocity dispersion of $\sigma_\star = 389\,\mathrm{km\,s^{-1}}$ measured within the effective radius by Rusli et al. (2013), and the 2MASS total apparent K-band magnitude of $m_K = 7.75$ mag (Vaddi et al., 2016) for calculations described in later sections of this chapter.

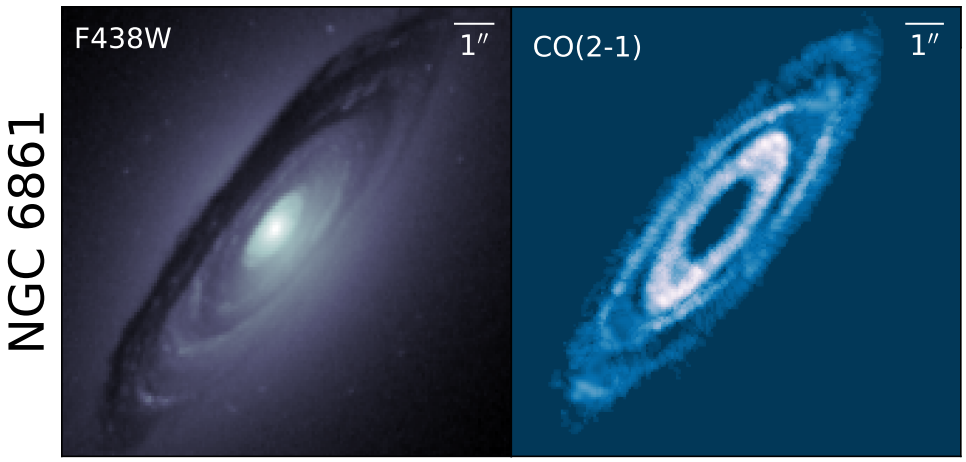

Figure 4.1 Image of NGC 6861 from HST and ALMA observations, showing the co-spatial distributions of the dust and gas. The left panel shows an F438W observation of the dust disk in NGC 6861. For each image, North is up and East is to the left. ALMA intensity maps in the right-side panels were created by summing across channels after using the 3DBarolo program (Di Teodoro and Fraternali, 2015) to generate a mask that identified pixels with CO emission.

4.2 Observations

4.2.1 HST Data

I used archival HST data for NGC 6861 from Program 15226, which was designed to obtain host galaxy imaging to complement ALMA program 2013.100229.S. The observation consisted of 4 separate exposures of 249 seconds, each taken with the F160W filter on WFC3. I processed and combined the images with `calwf3` and `AstroDrizzle` to produce a composite image with a $0\farcs08$ pixel^{-1} scale. Archival F110W observations of NGC 6861 were obtained from HST program 15226 and consisted of 2 separate exposures of 249 seconds each. The F110W images were drizzled and aligned to the drizzled F160W image.

4.2.2 ALMA Data

NGC 6861 was observed on 2014 September 01 in ALMA Band 6 for 24 minutes with a maximum baseline of 1091 m. The line observation was centered at an estimated redshifted ^{12}CO$(2-1)$ line frequency of 228.390 GHz, while the continuum windows were centered at 226.466 GHz and 244.098 GHz, with the same bandwidth and channel spacing properties as the NGC 1380 observation. The data were processed using CASA version 4.2.2 and imaged into a data cube with 20 km s^{-1} velocity channel widths following standard continuum phase self-calibration and continuum subtraction processes. The NGC 6861 data cube has the following properties: a synthesized beam size of $0\farcs32 \times 0\farcs23$ with a position angle of 58.2° and a pixel size of $0\farcs065$.

4.2.3 Circumnuclear Disk Properties

The circumnuclear disk of NGC 6861 was studied in detail by Boizelle et al. (2017), and I summarize the findings here. As with other galaxies in that sample, the CO gas in NGC 6861 is co-spatial with the dust, as seen in Figure 4.1. The disk exhibits regular rotation around its center, with LOS velocities reaching $\sim$500 km s^{-1}. The radial extent of the CO emission was measured to be $6''$ (784 pc). Examining the PVD and moment maps of NGC 6861 reveals a central $\sim 1''$ radius hole in CO emission. The gas mass of the disk was determined by summing the CO flux and assuming an $\alpha_{\rm CO}$ factor of 3.1 $M_\odot$ pc^{-2} (K km s^{-1})$^{-1}$ (Sandstrom et al., 2013) as the extragalactic mass-to-luminosity ratio, a CO(2−1)/CO(1−0) $\approx$ 0.7 line ratio in brightness temperature units (Lavezzi et al., 1999), and a correction factor of 1.36 for helium. Given these assumptions, the gas mass was estimated to be $(25.6 \pm 8.9) \times 10^7\, M_\odot$.

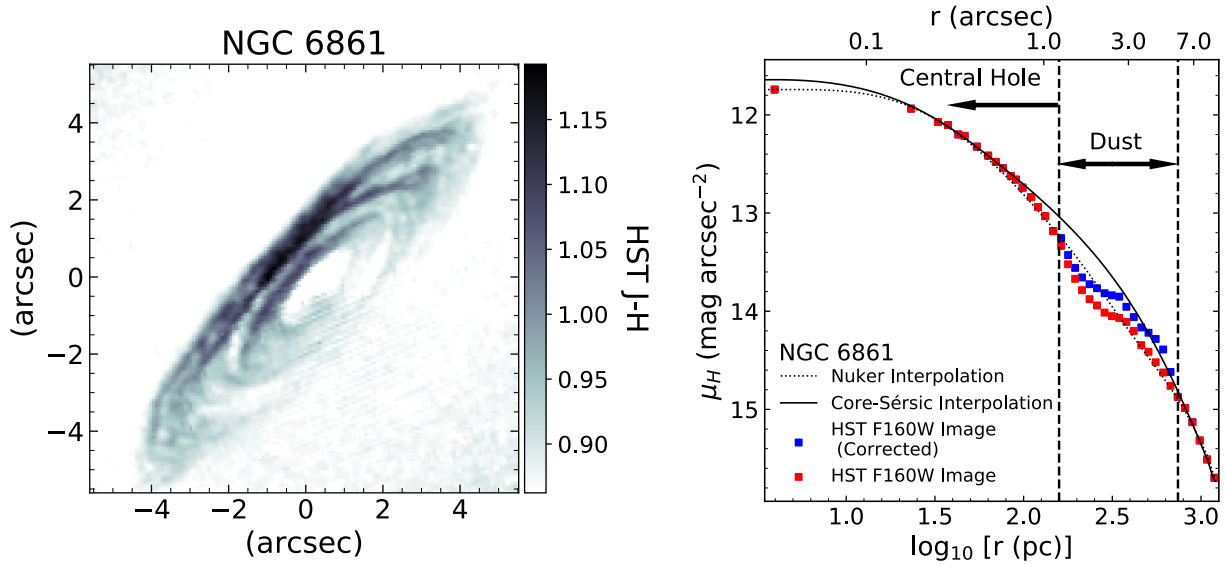

Figure 4.2 NGC 6861 $J - H$ color map (left) constructed using WFC3 F110W and F160W observations, and major axis surface brightness profiles (right) of the different host galaxy MGE models. For the surface brightness models, the red points are the observed values from the H-band image, while the blue points are dust-corrected values. The different lines in the panel correspond to extracted major axis surface brightness profiles for the 2D MGE models. The inner and outer edges of the dust disk are marked with the dashed lines.

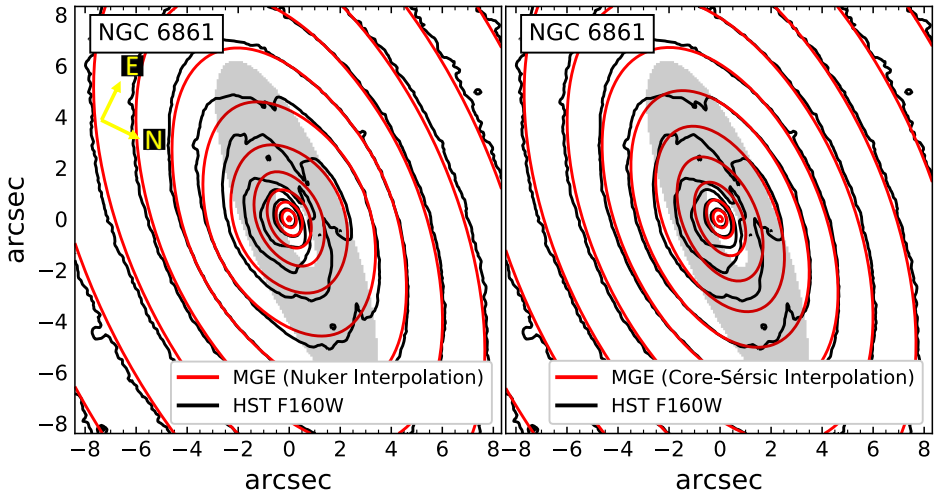

Figure 4.3 Isophotal contour map of the HST F160W image of NGC 6861 displayed on an $8'' \times 8''$ scale. I superpose the surface brightness contours of both the Nuker and Core-Sérsic MGE models. The shapes and sizes of the central dust disks are indicated by the shaded gray ellipses.

k	$\log_{10} I_{H,k}(L_\odot\,\mathrm{pc}^{-2})$	σ'_k (arcsec)	q'_k	$\log_{10} I_{H,k}(L_\odot\,\mathrm{pc}^{-2})$	σ'_k (arcsec)	q'_k
	$A_H = 0.00$ mag (Nuker Model)			$A_H = 0.00$ mag (Core-Sérsic)		
1	4.960	0.091	0.934	4.991	0.170	0.562
2	4.874	0.179	0.563	4.183	0.502	0.567
3	4.455	0.369	0.624	5.580	0.060	0.481
4	4.175	0.370	0.624	4.600	0.343	0.554
5	4.334	0.372	0.625	4.005	0.547	0.542
6	4.228	0.630	0.788	4.097	1.046	0.623
7	4.061	0.787	0.686	4.255	0.843	0.535
8	4.391	1.120	0.512	4.153	2.254	0.593
9	4.165	1.824	0.879	4.148	3.581	0.556
10	4.085	4.227	0.542	4.174	1.677	0.501
11	3.658	7.591	0.506	3.800	6.991	0.508
12	3.299	13.064	0.562	3.305	11.455	0.635
13	2.508	27.828	1.000	1.368	21.274	0.988
14	1.662	33.017	0.641	2.619	24.889	0.999
15	1.684	52.142	0.883	···	···	···
16	1.700	62.263	0.743	···	···	···

Table 4.1 MGE solutions created from the combination of HST H-band images with the best-fitting `GALFIT` Nuker model and `imfit` Core-Sérsic model. The MGE used in the statistically best-fitting dynamical is the Nuker model MGE. For each MGE, the first column is the component number, the second is the central surface brightness corrected for Galactic extinction and assuming an absolute solar magnitude of $M_{\odot,H} = 3.37$ mag (Willmer, 2018), the third is the Gaussian standard deviation along the major axis, and the fourth is the axial ratio. Primes indicate projected quantities.

4.3 MGE Models

I created two MGE models for NGC 6861. I started by creating a $J - H$ color map using the drizzled J and H-band HST images of NGC 6861 to identify the pixels most affected by dust and corrected for Galactic reddening based on a foreground $A_H = 0.028$ mag (Schlafly and Finkbeiner, 2011). The color map revealed the presence of a ring-like structure within the disk with a $1''$ radius hole at its center, and a measurement of the surface brightness along the major axis of the disk revealed a clear decrease of stellar light due to dust, as seen in Figure 4.2. This decrease is most noticeable between $1''$ (the outer radius of the central hole) and $5\farcs5$ (the outer edge of the dust disk).

Given the lack of dynamical tracers in the central region, I tested how the choice of host galaxy model impacted the inferred value of $M_{\rm BH}$. I explored systematic effects due to the choice of surface brightness model used to interpolate over the dusty region, by constructing MGEs using two different models for the correction of the H-band image for extinction: (1) a 2D Nuker model, and (2) a 2D Core-Sérsic model (Graham et al., 2003). Similar to the Nuker model, the Core-Sérsic model was designed to characterize the surface brightness profiles of ETGs. Unlike the Nuker model, however, it characterizes the outer structure of ETGs with a Sérsic profile (Sérsic, 1963) and the inner structure as a power-law.

To fit a Nuker model to the H-band image, I followed a process similar to that for NGC 1380, but I did not make any adjustments to the central pixels in the drizzled H-band image. I first created H-band PSF models in `TinyTim` that were dithered and drizzled in an identical fashion to the H-band image, and built a mask for foreground stars, background galaxies, and the dust disk itself. Because the $J-H$ color map indicated a lack of color excess in the central hole, I masked the entire dust disk as seen in the $J-H$ image, but kept the pixels within the hole to anchor the model. I fit the inner $10'' \times 10''$ of the H-band image with a Nuker model in `GALFIT` and allowed all free parameters to vary. The Nuker model parameters converged to $\alpha = 0.65$, $\beta = 1.29$, $\gamma = 0.0002$, and $r_{\rm b} = 0\farcs31 (\approx 40\,{\rm pc})$. Finally, I replaced pixels in the original H-band image located in the dust disk with the corresponding pixels in the Nuker model, and proceeded to fit this image with an MGE model in `GALFIT` without using a mask. I measured and compared this MGE model's major axis surface brightness profile and isophotal contours to those of the H-band image in Figure 4.2 and Figure 4.3; I refer to this model as the Nuker interpolation model.

I constructed a 2D Core-Sérsic model for NGC 6861's H-band image using the `imfit` program (Erwin, 2015) and used the same mask, model PSF, and fitting region as for the Nuker model. The parameters that characterize the Core-Sérsic model include the Sérsic index n, break-radius $r_{\rm b}$, effective half-light radius $r_{\rm e}$, inner slope parameter γ, and transition sharpness α.

The optimization in `imfit` converged on $n = 7.1$, $r_{\rm b} = 3\farcs5$ ($\approx$455 pc), $r_{\rm e} = 7\farcs9$ ($\approx$1 kpc), $\gamma = 0.61$, and $\alpha = 2.13$. I replaced the pixels in the dust disk region in the original H-band image with the corresponding pixels in the Core-Sérsic model, and proceeded to fit this new image with an MGE in `GALFIT`. I deprojected this MGE in an identical fashion to the MGE created with the 2D Nuker model, and refer to it as the Core-Sérsic interpolation model. I extracted its major axis surface brightness profile and compared it with both the H-band image and the Nuker interpolation in Figure 4.2. Over the extent of the dust disk, the Core-Sérsic interpolation produces higher corrected surface brightness values than the Nuker interpolation. At the nucleus, the Nuker interpolation matches the observed central surface brightness better than the Core-Sérsic interpolation, whose innermost point slightly exceeds the observed value. A comparison with the observed H-band isophotes is shown in Figure 3.5. As in the case of NGC 1380, the observed isophotes became noticeably non-elliptical towards the center, although there appears to be reasonable agreement between the data and models within the central hole region. The MGE components for both models are presented in Table 4.1.

4.4 Dynamical Modeling Optimizations

To dynamically model the NGC 6861 ALMA data cube, I used the formalism I described in Chapter 2. I briefly cover the specific characteristics of the model fit to the NGC 6861 data cube.

4.4.1 Fit Region

For NGC 6861, I initially followed the same procedure described for NGC 1380, starting with the values of $q = 0.32$ and $\Gamma = 141°$ found by Boizelle et al. (2017). However, the disk

structure in NGC 6861 is more complicated than in NGC 1380. The NGC 6861 gas disk contains a central hole that is $\sim 1''$ in radius along the major axis. Thus, the innermost CO emission is at a radius that is 3 times larger than the BH's estimated radius of influence. Additionally, the presence of rings and spiral-like substructure can be seen towards the edge of the disk. Fitting models to the entire disk led to reduced χ^2 values between 2.5 and 3, as the thin disk models struggled to reproduce kinematic features in the outer disk. The inner half of the gas disk shows the most regularity in its structure, and I found that fitting dynamical models in this region led to lower reduced χ^2 values and better overall fits to the data. Therefore, I created an elliptical fitting region with dimensions $a = 3''$ and $b = 0\farcs96$. In order to prevent pixels within the hole from contributing to the fit, I masked out a $1''$ ellipse with the same axial ratio ($q = 0.32$) at the center of the fitting region, which yielded a final annular fitting region. Along the spectral axis, I fit across 52 frequency channels that extended slightly beyond the channels with visible emission. On the final rebinned scale, with 75 rebinned pixels per channel, there are a total of 3900 data points in the fit.

Model	MGE (Nuclear Profile)	$M_{\rm BH}$ ($10^9\,M_\odot$)	Υ_H ($M_\odot/L_\odot$)	i (°)	Γ (°)	σ_0 ($\rm km\,s^{-1}$)	$v_{\rm sys}$ ($\rm km\,s^{-1}$)	F_0	χ^2_ν
A	Nuker	1.13	2.52	72.7	142.5	7.2	2795.63	1.03	1.987
		(0.04)	(0.01)	(0.07)	(0.05)	(0.29)	(0.29)	(0.006)	
B	Core-Sérsic	2.89	2.14	73.6	142.6	7.4	2795.65	1.04	2.004

Table 4.2 Best-fit parameter values obtained by fitting thin disk dynamical models to the NGC 6861 data cube. I derive 1σ statistical uncertainties for the parameters of fiducial model E based on a Monte Carlo resampling procedure and list them under the results for model E. This model has 3891 degrees of freedom. The major axis PA, Γ, is measured east of north for the receding side of the disk. The disk dynamical center is found to be within $\sim 0\farcs05$ of the nuclear continuum centroid for NGC 6861 determined in Boizelle et al. (2017). The observed redshift, $z_{\rm obs}$ is used in the dynamical models as a proxy for the systemic velocity of the disk, $v_{\rm sys}$ in the barycentric frame via the relation: $v_{\rm sys} = cz_{\rm obs}$ and is used to translate the model velocities to observed frequency units.

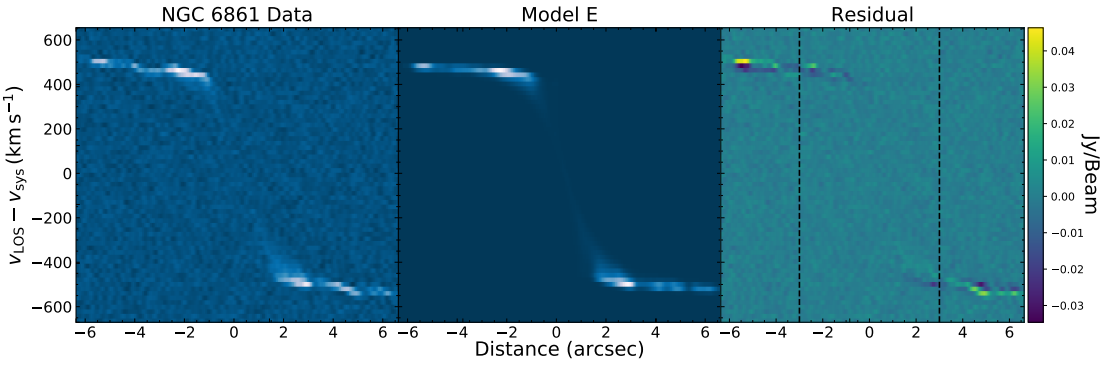

Figure 4.4 PVD along the major axis of NGC 6861 and the respective best-fit dynamical models. Columns show ALMA Cycle 2 CO(2−1) data (left), model (center), and (data-model) residual (right). The PVDs were generated with a spatial extraction width equivalent to a resolution element. The black dashed lines indicate the boundaries of the elliptical fit regions along the major axes.

4.4.2 NGC 6861 Modeling Results

I optimized two different dynamical models for NGC 6861, which I refer to as models E and F in Table 4.2. The difference between them is the input stellar circular velocity profile, based on one of the two NGC 6861 MGE models described in Section 4.3 which model the nuclear region in the H-band image with either a Nuker (E) or Core-Sérsic (F) model. These two dynamical models used a uniform turbulent velocity dispersion across the entire disk and are optimized over the annular region described in Section 4.4.1.

Model E converges on $M_{\rm BH} = 1.13 \times 10^9\, M_\odot$ and $\Upsilon_H = 2.52$ with $\chi^2_\nu = 1.987$, while model F returns values of $M_{\rm BH} = 2.89 \times 10^9\, M_\odot$ and $\Upsilon_H = 2.14$ with $\chi^2_\nu = 2.004$. The Υ_H values are higher than the ranges predicted by the SSP models of Vazdekis et al. (2010). Similarly, the range of $\Upsilon_I = (5.7 - 6.3)$ determined observationally by Rusli et al. (2013) is higher than SSP model predictions. All other free parameters remain consistent between the two models, although the inclination angle i slightly increases from 72.7° to 73.6° from model E to F.

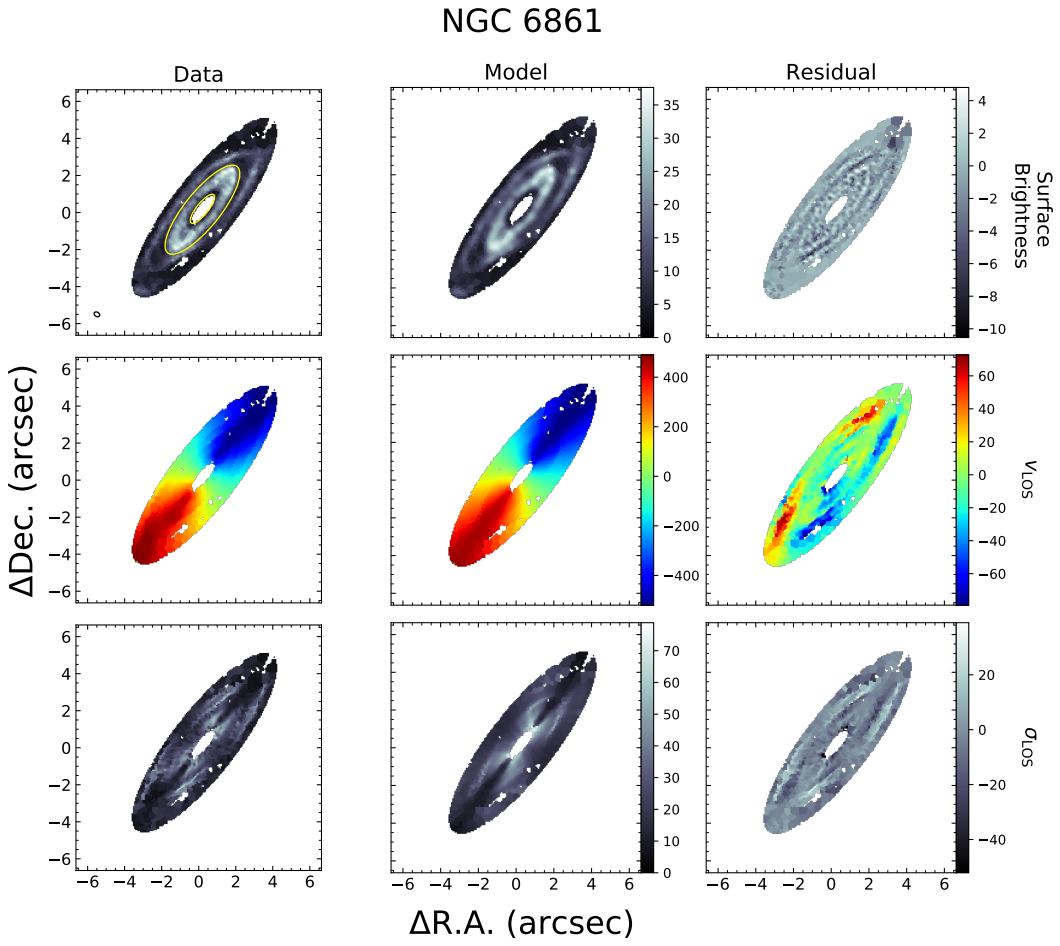

Figure 4.5 Moment maps for NGC 6861 constructed from the ALMA CO(2−1) data cube (left) and its fiducial model (center, model E). Shown are maps of moments 0, 1, and 2, corresponding to surface brightness, line-of-sight velocity $v_{\rm LOS}$, and turbulent velocity dispersion $\sigma_{\rm LOS}$. The units for the surface brightness map are mJy km s^{-1} pixel^{-1}, and the units for the $v_{\rm LOS}$ and $\sigma_{\rm LOS}$ maps are km s^{-1}. The systemic velocity of 2796 km s^{-1} estimated from the dynamical models has been removed from $v_{\rm LOS}$. Maps of (data-model) residuals are shown in the rightmost column. While the line profile fits have been determined at each pixel of the full disk, the annular fitting region used in calculating χ^2 is denoted in the top left panel with a yellow ellipse. The synthesized beam is represented by an open ellipse in the bottom left corner of the same image.

I created moment maps and a major axis PVD, and extracted line profiles for model E to compare with the ALMA data. The residuals between the data and model $v_{\rm LOS}$ maps show that the thin disk model emulates the data's observed $v_{\rm LOS}$ well within the designated fitting region, but discrepancies in excess of $\sim$60 km s^{-1} are seen at larger radii. These discrepancies highlight kinematic substructure within the disk at these larger radii that the models are

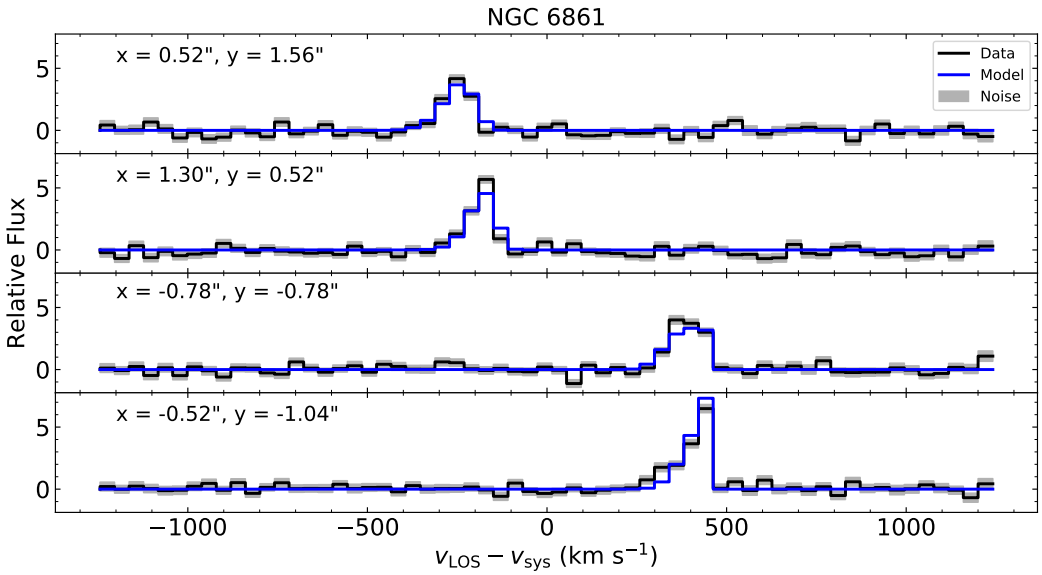

Figure 4.6 Representative line profiles of NGC 6861 measured by extracting single pixel cuts through the data, model, and noise cubes at four locations. The model line profiles are assumed to be intrinsically Gaussian at the sub-pixel level, with the asymmetric structure coming from beam-smearing. The noise band represents values in the range of data $\pm\, 1\sigma$. These line profiles were extracted from the cubes on the final scale of 1 block-averaged pixel per synthesized beam. The x and y labels indicate the pixel locations in terms of offsets in arcseconds from the disk dynamical centers.

unable to reproduce, although given that the maximum value of $\sigma_0/v_{\rm c}$ across the NGC 6861 disk is $\sim$0.02, the treatment of the disk as dynamically cold is justified. The PVD also shows discrepancies along the major axis, as structural differences between the data and model PVDs are prevalent at radii larger than $\sim 3''$, which corresponds to the semimajor axis of the elliptical fitting region. The extracted line profiles in Figure 4.6 show that the models are able to reproduce the observed line profile shapes well, although slight inconsistencies in the peak amplitude, in terms of both overall height and velocity channel, are evident in some spectra.

I conducted a Monte Carlo simulation to determine the statistical uncertainties on $M_{\rm BH}$. For model E, I found a distribution centered at its best-fit $M_{\rm BH}$ value of $1.13 \times 10^9\, M_\odot$ with a standard deviation of $4 \times 10^7\, M_\odot$, or 1.4% of $M_{\rm BH}$. Model F's Monte Carlo simulation was

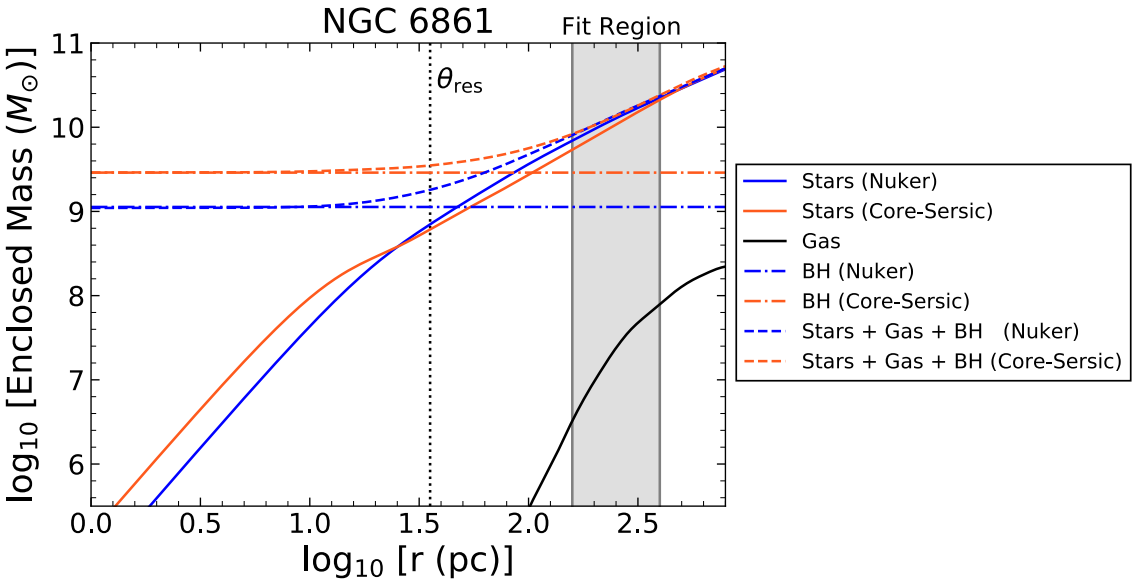

Figure 4.7 Enclosed mass profiles as a function of radius used in the dynamical modeling of NGC 6861. I show the mass contributions from the stars, gas, and BH, as well as the sums of their masses. The stellar mass profiles are derived from both the Nuker and Core-Sérsic MGE models. The dotted line corresponds to the 0.″28 resolution of the NGC 6861 observations.

centered at $M_{\rm BH} = 2.89 \times 10^9\,M_\odot$ and also had a standard deviation of $4 \times 10^7\,M_\odot$, or 3.5% of $M_{\rm BH}$. I chose to use the standard deviations of each of the free parameters from model E as representative of statistical uncertainties associated with these values and list them in Table 4.2.

The Monte Carlo simulations show that the statistical model-fitting uncertainties are significantly smaller than the systematic uncertainty associated with the choice of host galaxy model, as the resulting $M_{\rm BH}$ values are different by a factor of $\sim$3. Because of this large difference in $M_{\rm BH}$ between models E and F, I did not perform extensive systematic tests on these models as I did for the fiducial model B of NGC 1380 in Section 3.4.3, as the uncertainty associated with the choice of host galaxy model dominates the total error budget.

To determine a lower limit on $M_{\rm BH}$, I adjusted the central flux in NGC 6861's H-band image in the same manner as was done for the H-band image of NGC 1380 in Section 3.3.2. I

corrected the Nuker interpolation MGE model under the assumption that the disk resides in the midplane of the galaxy and that only the starlight originating from behind the dust disk experiences any extinction. The modified Nuker interpolation model explored the extreme limit where $A_H = \infty$, signifying that all the light behind the disk is lost, and raising the innermost value of the major axis surface brightness profile by 0.75 mag arcsec^{-2}. Even with this maximally peaked surface brightness model, the value of $M_{\rm BH}$ was non-zero and converged on $9.7 \times 10^7\,M_\odot$, which serves as the measurement's lower limit. I emphasize that even with the assumption that the central region of NGC 6861 is optically thick (which is highly unlikely given the $J-H$ color map) and the absence of dynamical information within the inner $1''$, the dynamical models still require a central compact mass to reproduce the observations.

4.5 Discussion

This is the second BH mass measurement of any kind in NGC 6861, and the first with gas dynamics. The measurement precision for NGC 6861's BH is limited due to the lack of dynamical tracers within the BH's sphere of influence, as the resulting values of $M_{\rm BH}$ differ by a factor of $\sim$3 depending on the model used for the host galaxy. I go into detail on the measurement limitations and compare my measurement to predictions from local BH-host galaxy scaling relations.

4.6 The BH Sphere of Influence

I estimated $r_{\rm SOI}$ using the best-fit values of $M_{\rm BH}$ from both model E and model F. The BH mass and the enclosed stellar mass were equal at 47 pc ($0\farcs36$) when adopting the stellar mass profile from model E, and at 94 pc ($0\farcs72$) for model F. If I instead use the velocity

dispersion of $\sigma_\star = 389\,\mathrm{km\,s^{-1}}$ from Rusli et al. (2013), I obtain $r_{\mathrm{SOI}} = 32$ pc ($0\farcs25$) when adopting the best-fit M_{BH} from model E and 82 pc ($0\farcs63$) from model F. Considering that the average ALMA beam size for the NGC 6861 data is $0\farcs28$, these estimates suggest that r_{SOI} would be resolved in NGC 6861.

Despite having observations that could in principle resolve r_{SOI} if the gas disk extended to the center of NGC 6861, the lack of CO emission within the innermost $\sim1''$ precludes a high-precision BH mass measurement, as the two dynamical models found BH mass values that differed by a factor of $\sim$3 and were degenerate with Υ_H. I attribute this large disparity to the central hole, and to the differences between the Nuker and Core-Sérsic interpolation MGE models in the dust-affected regions. These differences, especially in the slope of the surface brightness profile, led to distinct Υ_H values in the dynamical models. Additionally, the dearth of CO emission within the innermost $1''$ meant that model fits were optimized over pixels that were more sensitive to differences in the stellar mass distribution. Figure 4.7 shows the separate and combined enclosed mass profiles of the stars, gas, and BH for each host galaxy model used. Using these mass profiles, I determined the total enclosed mass within the central hole (which is divided between contributions from the BH and the stars, due to the absence of gas) to be $7.46 \times 10^9\,M_\odot$ ($M_{\mathrm{BH}} = 1.13 \times 10^9\,M_\odot$) when using the Nuker interpolation and $8.74 \times 10^9\,M_\odot$ ($M_{\mathrm{BH}} = 2.87 \times 10^9\,M_\odot$) for the Core-Sérsic interpolation, which are both consistent with results from Boizelle et al. (2017). Considering that the available dynamical information is restricted to radii extending beyond the hole radius, and that the best-fit values of M_{BH} represent a minor fraction of the total dynamical mass within the hole, it is unsurprising that the two dynamical models find very different but ostensibly precise values of M_{BH}. This precision is seen in the results of Monte Carlo simulations, and it highlights the importance of accounting for these types of systematic uncertainties when making gas-dynamical BH mass measurements in this regime.

4.6.1 BH Mass Comparisons

Using equations 6, 7, and 8 from Kormendy and Ho (2013), I derived predictions of $M_{\rm BH}$ from the estimated total K-band luminosity, the estimated bulge mass, and the stellar velocity dispersion for NGC 6861.

The range of $M_{\rm BH} = (1 - 3) \times 10^9\,M_\odot$ is consistent with the previous measurement of $M_{\rm BH} = (2.0 \pm 0.2) \times 10^9\,M_\odot$ by Rusli et al. (2013), and generally agrees with predictions from the BH-host galaxy scaling relations. I derived a total K-band bulge luminosity of $1.2 \times 10^{11}\,L_\odot$, which estimates $M_{\rm BH} = (0.6 - 0.8) \times 10^9\,M_\odot$. The estimated bulge mass of $M_{\rm bul} = 2.8 \times 10^{11}\,M_\odot$ is higher than the value provided in Kormendy and Ho (2013) of $M_{\rm bul} = 1.8 \times 10^{11}\,M_\odot$. Using this value, the predicted range of $M_{\rm BH}$ is $(1.4 - 2.0) \times 10^9\,M_\odot$, while using the lower Kormendy and Ho (2013) estimate of $M_{\rm bul}$ gives $(0.8 - 1.1) \times 10^9\,M_\odot$. The stellar velocity dispersion of 389 km s^{-1} in NGC 6861 is one of the highest measured in an ETG. It predicts $(5.4 - 11.4) \times 10^9\,M_\odot$ from the $M_{\rm BH} - \sigma_\star$ relation, which is higher than the measured value, although the measurement is still contained within the relation's intrinsic scatter. Machacek et al. (2010) suggests that NGC 6861 may have had strong gravitational encounters in its past with neighboring galaxies that has elevated its central velocity dispersion, and that it could be the dominant galaxy in a galaxy subgroup that is merging based on Chandra X-ray observations. While this possibility has yet to be confirmed, my measured range of $M_{\rm BH}$ and the measurement by Rusli et al. (2013) suggest that the $M_{\rm BH} - \sigma_\star$ relation slightly overpredicts $M_{\rm BH}$ in NGC 6861. Whether this excess should be attributed to larger intrinsic scatter at the high-$\sigma_\star$ end of the relation or physical mechanisms that have affected the growth and evolution of NGC 6861 and its BH remains unclear.

4.7 Conclusion

I present the second and independent $M_{\rm BH}$ measurement in NGC 6861 using molecular gas-dynamical modeling. I optimize dynamical modeling fits to the ALMA CO data using two different host galaxy models, and find that the results for $M_{\rm BH}$ differ by a factor of $\sim$3 due to the lack of dynamical tracers within the innermost $1''$, and to the structural differences in the shape of the dust-corrected surface brightness and stellar mass profiles of the host galaxy. Given the large difference between the two results, the value of $M_{\rm BH}$ in NGC 6861 cannot be precisely constrained, although the models suggest a plausible range of $M_{\rm BH} = (1 - 3) \times 10^9\,M_\odot$ and a lower limit of $\sim 1 \times 10^8\,M_\odot$ derived by assuming an unlikely amount of central dust extinction. This range encompasses the stellar-dynamical mass measurement of $(2.0 \pm 0.2) \times 10^9\,M_\odot$ determined by Rusli et al. (2013).

When comparing my measurement of $M_{\rm BH}$ to the BH-host galaxy scaling relations determined by Kormendy and Ho (2013), I find that the measurement is broadly consistent with the predictions from the $M_{\rm BH} - L_{\rm bul}$, $M_{\rm BH} - M_{\rm bul}$, and $M_{\rm BH} - \sigma_\star$ relations.

Chapter 5

NGC 4786

5.1 Galaxy Properties

NGC 4786 is classified as a cD pec galaxy in the Third Reference Catalog of Bright Galaxies (RC3; de Vaucouleurs et al., 1991). Redshift-independent distances for this galaxy in the NASA/IPAC Extragalactic Database (NED) are between 65 - 75 Mpc when using a ΛCDM cosmology with $H_0 = 67.8\,\mathrm{km\,s^{-1}\,Mpc^{-1}}$. I adopt a value of $H_0 = 73\,\mathrm{km\,s^{-1}\,Mpc^{-1}}$ based on more recent estimates of H_0 from nearby (< 100 Mpc) galaxies (Blakeslee et al., 2021; Riess et al., 2022; Kenworthy et al., 2022), a recessional velocity of $cz = 4623\,\mathrm{km\,s^{-1}}$ from preliminary dynamical models, $\Omega_M = 0.31$, and $\Omega_\Lambda = 0.69$. These assumptions set a luminosity distance of 64.1 Mpc, an angular diameter distance of 62.1 Mpc, and an angular scale where $1''$ corresponds to 301 pc. The measured SMBH mass scales linearly with the assumed distance, so any differences in assumed distance to the galaxy will correspond to an equivalent rescaling of the measured M_{BH}. There are no previous studies that have measured the mass of the SMBH in this galaxy.

5.2 Observations

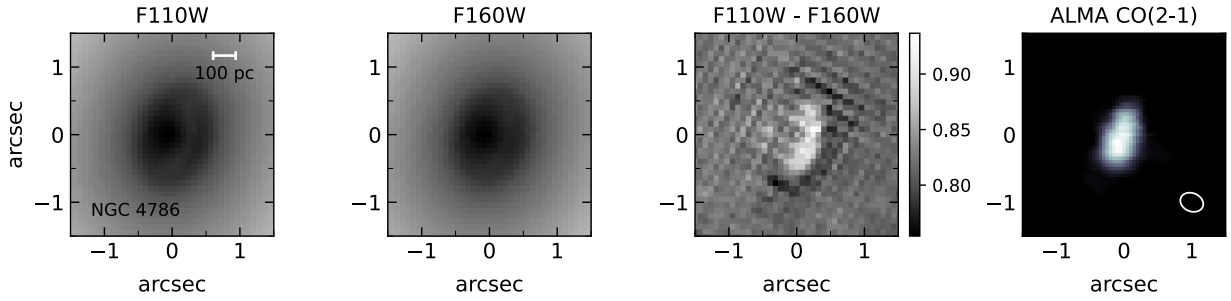

Figure 5.1 HST F110W (J-band), F160W (H-band), F110W $-$ F160W ($J-H$), and ALMA CO(2$-$1) images of NGC 4786 showing the co-spatial alignment of the gas and dust. The ALMA intensity maps were created by summing channels in the data cubes that displayed visible CO emission. Pixels with emission were identified with an automatically generated mask by the `3DBarolo` program (Di Teodoro and Fraternali, 2015). In the $J-H$ maps, light regions correspond to redder colors and dark regions are bluer than the surrounding starlight. North is up and East is to the left in each image.

5.2.1 HST Data

For NGC 4786 I used data from HST program 15226. F110W (J-band), and F160W (H-band) images taken with the Wide Field Camera 3 (WFC3) were retrieved. For NGC 4786, the H-band image was taken with a four-point dither pattern with four separate exposures that lasted 249 seconds each. For the J-band images, a two-point dither pattern was used and two separate 249-second exposures were taken.

The HST data was processed through the `calwf3` pipeline, and `AstroDrizzle` was used to combine and align the separate exposures. The flat-fielded H-band images were first aligned and then drizzled to a pixel scale of $0\farcs08$. The drizzled H-band image was used as the reference image to drizzle and align the flat-fielded J-band images. Offsets between the H and J-band images from the luminosity-weighted galaxy center coordinates of each image were determined and used to interpolate and align them to within $\sim$0.2 subpixels of accuracy based on inspection of the $J-H$ maps. Additionally, a `TinyTim` model PSF was generated,

dithered, and drizzled in the same fashion as the H-band image. The H, J, and $J-H$ images are shown in Figure 5.1 along with the ALMA CO(2−1) intensity map.

5.2.2 ALMA Data

I obtained ALMA imaging of NGC 4786 from ALMA Program 2015.1.00878.S. NGC 4786 was observed on 23 July 2016 for approximately 21 minutes with a maximum baseline of 1110 m. The observation consisted of three spectral windows targeting continuum emission and one spectral window targeting the redshifted CO(2−1) emission line. The continuum windows had a channel resolution of 15.625 MHz and covered the following frequency ranges: 227.14 − 231.14 GHz, 239.47 − 243.47 GHz, and 241.78 − 245.78 GHz. The emission line spectral window had a channel resolution of 3.906 MHz and spanned the frequencies between 225.14 − 228.89 GHz. The uv visibility data were reduced and calibrated in version 4.5.3 of the Common Astronomy Software Applications package (CASA; McMullin et al., 2007), and then imaged into a data cube with 20 $\mathrm{km\,s^{-1}}$ velocity channel spacing (with respect to the rest frequency of the CO(2−1) emission line at 230.538 GHz) using a robust parameter of 0.5. A pixel size of $0\farcs05$ was chosen to adequately sample the synthesized beam's minor axis. The beam's position angle is 67.3° measured East of North. The major axis full width at half maximum (FWHM) of the beam is $0\farcs35$, whereas the minor axis has a FWHM of $0\farcs27$, which gives it a geometric mean FWHM of $0\farcs31$.

5.2.3 Circumnuclear Disk Properties

A detailed description of the CO(2−1) properties of the NGC 4786 disk was presented by Boizelle (2018). I describe some of these properties below. As seen in Figure 5.1, the CO emission is cospatial with the optical dust disk. The CO surface brightness extends about $0\farcs65$ in radius along the disk's major axis. The disk displays orderly rotation about its center,

with projected LOS velocities reaching $\sim$270 $\mathrm{km\,s^{-1}}$. Examination of the PVD extracted along the major axis reveals that the velocities remain relatively flat over a majority of the disk and decrease slightly towards their respective disk center. The PVD also highlights a lack of CO-bright gas well within the expected SMBH r_{SOI}.

To incorporate the mass of the gas disk in the total gravitational potential of a dynamical model, I convert the integrated CO(2−1) flux measurements into M_{gas} profiles. The M_{gas} profile is dominated by molecular hydrogen and helium and is calculated as $M_{\mathrm{gas}} = M_{\mathrm{H_2}}(1 + f_{\mathrm{He}})$, where I set $f_{\mathrm{He}} = 0.36$.

The process of generating a M_{gas} profile starts with the construction of an integrated CO(2−1) flux map. To build this map, I multiply the data cube with a 3D mask generated by the `3DBarolo` program (Di Teodoro and Fraternali, 2015) and sum the channel maps along the spectral axis to generate a 2D map of integrated flux density. Upon converting the map into units of integrated flux, I average the flux on elliptical annuli centered on the disk centers. Upon summing the integrated flux across the entire region of each disk, I find $I_{\mathrm{CO(2-1)}} = (6.90 \pm 0.14)\,\mathrm{Jy\,km\,s^{-1}}$. These statistical uncertainties are calculated through Monte Carlo simulations, but there is an additional 10% systematic uncertainty that stems from the flux scale. For each elliptical annulus, the integrated CO(2−1) flux is converted into a CO(1−0) luminosity using:

$$L'_{\mathrm{CO}} = 3.25 \times 10^7 S_{\mathrm{CO}} \Delta v \frac{D_L^2}{(1+z)^3 \nu_{\mathrm{obs}}^2}\,\mathrm{K\,km\,s^{-1}\,pc^2} \tag{5.1}$$

(Carilli and Walter, 2013) assuming a CO(2−1)/CO(1−0) line ratio of 0.7 (Lavezzi et al., 1999). Then, a mass of H_2 is obtained by multiplying the CO(1−0) luminosity by $\alpha_{\mathrm{CO}} = 3.1\,M_\odot\ \mathrm{pc^{-2}}\ (\mathrm{K\,km\,s^{-1}})^{-1}$ (Sandstrom et al., 2013) and then multiplying this result by 1.36 as described above to generate an estimate of M_{gas}, though it should be noted that the most appropriate α_{CO} value for ETGs is unknown, and thus the estimated M_{gas} value should be

taken as a rough approximation. I find $M_{\rm gas} = 6.9 \times 10^7\, M_\odot$ for the disk in NGC 4786. Along with the unknown ideal value of $\alpha_{\rm CO}$, the uncertainty in D_L contributes ≈15% based on the range of redshift-independent distances in NED for NGC 4786. This distance uncertainty is in addition to the 10% systematic and $(1-2)$% statistical uncertainty associated with the integrated flux measurements. As will be discussed in a later section, the inclusion or exclusion of the gas mass in the total gravitational potential of the system only contributes a small amount to the total error budget on $M_{\rm BH}$.

5.3 Host Galaxy Surface Brightness Modeling

I built three unique MGE models for NGC 4786 following an approach similar to that used by Cohn et al. (2021). The three models correspond to an unmasked, dust-masked, and dust-corrected MGE model that account for the effects of dust differently, and are used to assess the systematic impact of the chosen MGE model on the SMBH mass measurement. As seen in Figure 5.2, the H-band dust attenuation does not appear severe in NGC 4786, hence I first explored both unmasked and dust-masked MGE models to explore the impact on the measurement of $M_{\rm BH}$.

5.3.1 Dust-Masked and Unmasked MGE Models

Prior to fitting MGEs to the drizzled H-band image, the host galaxy light in each image was isolated from extraneous sources such as neighboring galaxies, foreground stars, cosmic rays, and detector artifacts by masking these objects. In addition, $J-H$ maps were constructed in order to better identify and mask out regions where dust obscuration was highest, typically corresponding to areas where $J-H > 0.88$ mag. For all reported H and J-band magnitudes in this work, I use the Vega magnitude system.

k	$\log_{10} I_{H,k}(L_\odot\,\mathrm{pc}^{-2})$	σ'_k (arcsec)	q'_k	$\log_{10} I_{H,k}(L_\odot\,\mathrm{pc}^{-2})$	σ'_k (arcsec)	q'_k
	NGC 4786 (Unmasked MGE)			NGC 4786 (Dust-Masked MGE)		
1	4.753	0.056	0.789	4.314	0.321	0.995
2	4.540	0.521	0.800	4.435	0.569	0.730
3	4.153	1.278	0.816	4.177	1.263	0.819
4	3.584	2.606	0.759	3.566	2.731	0.736
5	3.463	4.725	0.795	3.439	4.735	0.811
6	2.670	5.783	0.902	2.592	5.713	0.886
7	2.560	8.842	0.690	2.592	7.899	0.690
8	2.682	13.650	0.690	2.687	12.792	0.690
9	2.204	15.762	0.934	2.320	14.940	0.876
10	2.118	23.990	0.690	2.134	23.646	0.690
11	1.690	29.132	0.952	1.769	27.513	0.967
12	1.389	60.476	0.690	1.364	59.220	0.690
13	0.269	47.056	0.690	0.527	45.221	0.690
14	1.045	122.830	0.982	1.099	113.697	0.963
	NGC 4786 (Dust-Corrected MGE)					
1	4.472	0.226	0.830			
2	4.474	0.545	0.784			
3	4.152	1.282	0.820			
4	3.580	2.654	0.756			
5	3.451	4.758	0.794			
6	2.638	5.479	0.949			
7	2.570	8.493	0.690			
8	2.716	12.896	0.690			
9	2.115	16.166	0.999			
10	2.217	21.964	0.690			
11	1.558	29.934	0.975			
12	1.454	56.294	0.690			
13	1.085	32.662	0.690			
14	1.062	125.555	0.958			

Table 5.1 NGC 4786 unmasked, dust-masked, and dust-corrected MGE solutions. The first column is the component number, the second is the central surface brightness corrected for Galactic extinction and assuming an absolute solar magnitude of $M_{\odot,H} = 3.37$ mag (Willmer, 2018), the third is the Gaussian standard deviation along the major axis, and the fourth is the axial ratio. Primes indicate projected quantities.

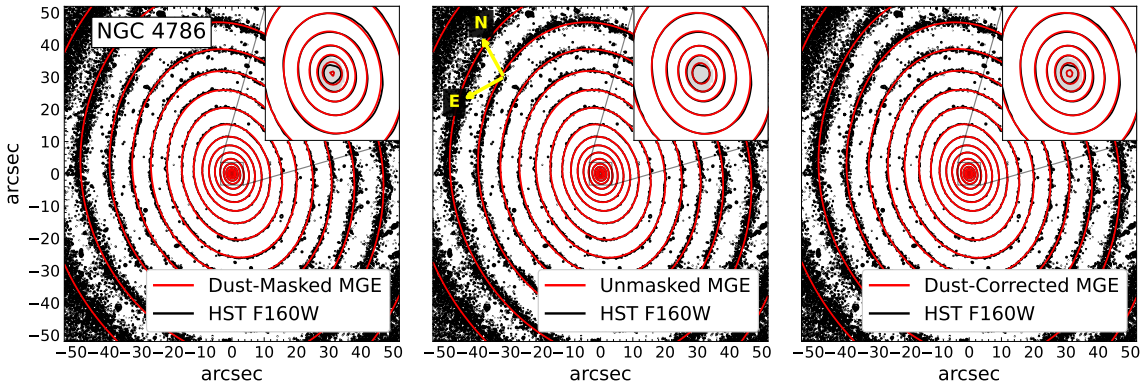

Figure 5.2 2D isophote maps comparing the observed HST WFC3 F160W isophotes to those of the three MGEs for NGC 4786. Black contours represent isophotes from the F160W images, while red contours are for the MGE models. For each image, the central $\approx 100'' \times 100''$ region is displayed with an inset of the innermost $3\farcs5 \times 3\farcs5$ region in the top right corner. The gray ellipse shown within each inset indicates the size and orientation of the circumnuclear dust disk. Arrows in the middle panels indicate the orientation of North and East.

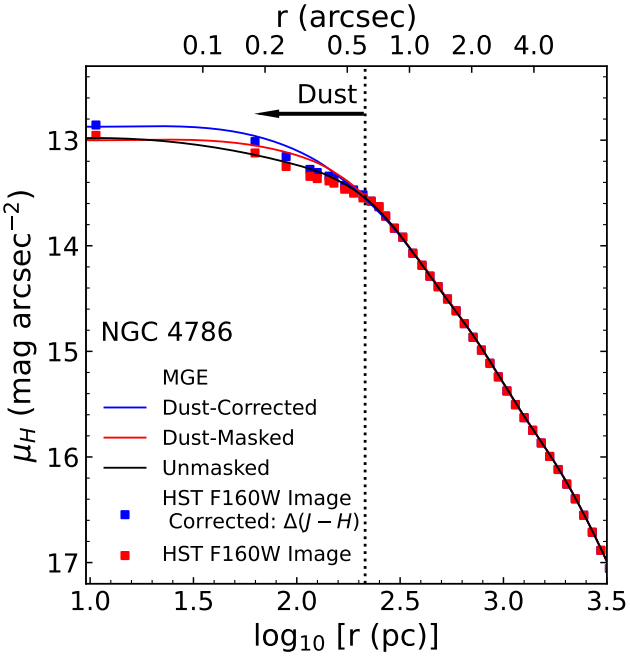

Figure 5.3 NGC 4786 major axis surface brightness profiles of the different host galaxy MGE models. The red points are the observed values from the H-band image, while the blue points are the dust-corrected values. The different lines in the panel correspond to extracted major axis surface brightness profiles for the 2D MGE models. The outer edge of the dust disk is marked with a vertical dashed line, and the arrow indicates that the dust extends down to the nucleus.

The observed H-band surface brightness was modeled with routines from the `MgeFit` package in Python (Cappellari, 2002). The components of this initial MGE were then used as initial guesses for a second MGE fit using the `GALFIT` program (Peng et al., 2002). `GALFIT` was chosen for the final MGEs because it allows for an asymmetric 2D PSF to be incorporated in the modeling process. This is in contrast to `MgeFit` which requires decomposing the PSF into a sum of circular Gaussian functions when used in the MGE construction. For both programs, the blurring due to the H-band PSF was accounted for by incorporating the `TinyTim` H-band PSF models. In addition, the MGEs account for a foreground H-band Galactic reddening of $A_H = 0.019$ mag in NGC 4786 (Schlafly and Finkbeiner, 2011). Each MGE for NGC 4786 is presented in Table 5.1.

The MGE assumes that the galaxy has an oblate and axisymmetric shape, and that each Gaussian component shares the same center and position angle. While individual Gaussian components may not correspond to physically distinct galaxy components, their projected axial ratios, q'_k, may converge to values below $\cos(i)$ in the MGE optimization process, where i is the inclination of the circumnuclear disk. A useful proxy for the inclination is $i = \arccos(b/a)$ where b/a is the observed axial ratio of the disk as measured from the HST images. This proxy typically agrees with kinematic inclinations derived from dynamical models to within $\sim$5° based on previous studies (Boizelle et al., 2019, 2021; Cohn et al., 2021; Kabasares et al., 2022), and so a lower bound on the possible MGE component axial ratios of 0.69 was set. This enables deprojection of the MGE down to an inclination angle as low as 46°.

The initial MGE was constructed with the dust mask that identified pixels with observed values of $J - H > 0.88$ mag on the near side of the disk. Examination of the 2D isophotes in Figure 5.2 shows that the model isophotes are an excellent match to those seen in the H-band data out to $\sim$100″. Within the central dusty regions, the observed H-band isophotes remain relatively symmetrical and are modeled well by their dust-masked MGEs. Extracting

surface brightness profiles from both the MGE model and the H-band data in Figure 5.3 also shows good agreement at large radii, though discrepancies within the dusty region are noticeable, with NGC 4786 exhibiting a cored surface brightness profile at its center. Cores are hypothesized to originate through scouring by massive SMBH binaries (Ravindranath et al., 2002; Thomas et al., 2014). Despite slight mismatches in the model and data surface brightness profiles, the dust in NGC 4786 appears to have a less noticeable impact on the observed H-band surface brightness distribution in comparison to what has been seen in previous work, such as in the ETGs NGC 1380 and NGC 6861, where the H-band isophotes become non-elliptical and asymmetric within the dust disk (Kabasares et al., 2022).

5.3.2 Dust-Corrected MGE Models

The final MGE I created involved fitting an MGE model to a dust-corrected H-band image. The process of developing this MGE model follows methods described by Boizelle et al. (2019, 2021), Cohn et al. (2021), and Kabasares et al. (2022). I summarize the key steps below.

I fit a 2D Nuker model (Faber et al., 1997) to the innermost $10'' \times 10''$ of the drizzled H-band image using `GALFIT`. This fit included the mask used for the dust-masked MGE, and acts as the starting point of the dust correction. The Nuker model in `GALFIT` includes the H-band PSF, so the resulting solutions correspond to intrinsic parameters. Nuker models have been shown to accurately model the surface brightness distribution within the innermost few arcseconds of early-type galactic nuclei, and they characterize this distribution with an inner and outer power-law profile (Lauer et al., 2007). Mathematically, the Nuker law has the following form: $I(r) = I_b 2^{\frac{\beta-\gamma}{\alpha}} (r/r_\mathrm{b})^{-\gamma} [1 + (r/r_\mathrm{b})^\alpha]^{\frac{\gamma-\beta}{\alpha}}$, with γ and β representing the slopes of inner and outer power laws, respectively. The transition between these two regimes occurs at a given break radius, r_b, and the sharpness of this transition is described by the

parameter α. For NGC 4786, the `GALFIT` optimization converged on the following values: $\alpha = 1.94$, $\beta = 1.56, \gamma = 0.00$, and $r_{\rm b} = 0\farcs46$, which are typical values for cored-elliptical galaxies (Lauer et al., 2007).

The next step involves estimating how much extinction to the observed H-band stellar light there is at the center of the galaxy. I follow the approach described by Kabasares et al. (2022), which uses the observed $J-H$ color map of each galaxy to determine an estimate of A_H, the extinction of the H-band stellar light originating behind the disk. First, I determined a median $J-H$ color of 0.81 mag outside the dust disk of NGC 4786, and I determined the color excess, $\Delta(J-H) = (J-H) - (J-H)_{\rm median}$ as a function of position along the disk's major axis, averaging over a width of 4 pixels.

To establish a relationship between extinction and color excess, I used Equations (1) and (2) from Boizelle et al. (2019) to generate a curve of $\Delta(J-H)$ as a function of V-band extinction, A_V (see Figure 4 of Kabasares et al., 2022). This assumes the Viaene et al. (2017) embedded-screen model, which effectively models the circumnuclear dust disk as a thin, inclined disk that bisects the galaxy. Along a given LOS, the fraction of light that originates in front of the disk (f) is unaffected by dust, while the fraction behind it (b) is obscured by screen extinction. The ratio of observed to intrinsic integrated H-band stellar light is represented mathematically as $F_{\rm observed}/F_{\rm intrinsic} = f + b[10^{-A_H/2.5}]$. This is from Equation (1) in Boizelle et al. (2019), and assumes an intrinsically thin disk, where $w = 0$. Along the major axis of each disk, the fractions of light originating in front of and behind of the dust disk are assumed to be equal ($f = b = 0.50$).

The next key step in this process is converting the observed $\Delta(J-H)$ as a function of position along the disk's major axis into values of A_H. Using the curve of $\Delta(J-H)$ versus A_V, I can associate a unique value of A_V (as well as A_H) to an observed $\Delta(J-H)$ value. As seen in Figure 4 of Kabasares et al. (2022), this is only valid up to a given turnover point. This is due to the fact that at large ($A_V > 5$ mag) optical depths, variations in color begin

to rapidly diminish, and so the same value of $\Delta(J-H)$ can correspond to both low and high A_V values. Following the procedure outlined by Kabasares et al. (2022), I assumed the lower A_V value, as the higher value implies that effectively all the light originating behind the disk is lost due to extinction. I fit the color excess curve with a third-order polynomial up to the turnover point. To generate predictions of A_V as a function of $\Delta(J-H)$, I use this polynomial's inverse. Then, I found the lower A_V values corresponding to the observed $\Delta(J-H)$ along the disk's major axis. Finally, I set $A_H = 0.175 A_V$ based on the standard interstellar extinction law described in Rieke and Lebofsky (1985), which gives a unique A_H value for each observed color excess along the major axis. As stated earlier, this A_H value applies only to light originating behind the disk.

This simple dust correction implies $A_H = 0.22$ mag at the center of the circumnuclear disk in NGC 4786, which corresponds to a reduction of approximately 20% of the stellar light originating behind the disk. I note that a proper treatment of determining the intrinsic stellar light distribution in the presence of a dusty circumnuclear disk requires the usage of radiative transfer models (De Geyter et al., 2013; Camps and Baes, 2015) that account for the combined effects of extinction, light scattering, and the geometry of the dust disk itself. Even still, this simple method gives a relatively straightforward way of producing an estimate of the assumed extinction, and consequently, the impact it has on the measured value of $M_{\rm BH}$.

With this estimated value of A_H, I proceeded to mask the entirety of the dust disk in the H-band images, except for the central nine pixels. This was done to anchor the model fit to the observed values at the center. The fluxes of these nine pixels are subsequently boosted by a factor of $(0.50 + 0.50 \times 10^{-A_H/2.5})^{-1}$. I also tested this procedure with the central four pixels as well and found no significant difference between the two cases. With the entire dust disk masked out except for the pixels that have had their flux values increased, I re-fit the central $10'' \times 10''$ region again with a new Nuker model, but fixed the values of α, β,

and $r_{\rm b}$ to their values from the previous Nuker model to retain the larger scale properties outside the dusty region. I then adjusted the inner slope parameter γ to find an optimal value where the central pixels of the Nuker model are nearly equal to the scaled flux values of the H-band image. This value is $\gamma = 0.11$.

With this new Nuker model, the final steps in the dust correction process are to replace the pixels within the dust disk region in the H-band image with the corresponding pixels in the Nuker model, and to fit this dust-corrected H-band image with a new MGE. As will be discussed in Section 5.4, the dust-corrected MGE is used in the fiducial dynamical model for NGC 4786. The dust-corrected MGE components are displayed in Table 5.1.

5.4 Dynamical Modeling Results

Model	MGE	$M_{\rm BH}$ ($10^8\,M_\odot$)	Υ_H ($M_\odot/L_\odot$)	i (°)	Γ (°)	σ_0 ($\mathrm{km\,s^{-1}}$)	$v_{\rm sys}$ ($\mathrm{km\,s^{-1}}$)	F_0	χ^2_ν
A	Unmasked	3.9	2.76	70.8	162.5	10.8	4620.47	1.56	1.488
B	Dust-Masked	5.8	1.98	70.8	164.4	9.3	4621.63	1.56	1.449
C	Dust-Corrected	5.0	1.80	69.3	166.6	9.9	4621.26	1.54	1.421
		(0.2)	(0.04)	(0.7)	(1.2)	(3.0)	(1.10)	(0.03)	

Table 5.2 Best-fit parameter values obtained by fitting thin disk dynamical models to the NGC 4786 data cube. I derive 1σ statistical uncertainties for the parameters of fiducial model C, based on a Monte Carlo resampling procedure, and list them under the results for model C. This model has 363 degrees of freedom. The major axis PA, Γ, is measured east of north for the receding side of the disk. I found the dynamical center of the fiducial model to be at RA=$12^{\rm h}54^{\rm m}32.4115^{\rm s}$, Dec=$-06°51'33\farcs920$ for NGC 4786. This is within $0\farcs001$ of the dynamical centers of the other models. The observed redshift, $z_{\rm obs}$, is used in the dynamical models as a proxy for the systemic velocity of the disk, $v_{\rm sys}$, in the barycentric frame via the relation: $v_{\rm sys} = cz_{\rm obs}$ and is used to translate the model velocities to observed frequency units.

Given the small number of resolution elements across the disk, I opted to fit dynamical models to nearly the full extent of it, though I explore the systematic impact of this choice in Section 5.4.1. The elliptical fitting region has an axial ratio of $q = 0.50$ and a semimajor axis length of $a = 0\farcs55$. Additionally, to mitigate the impact of neighboring pixel-to-pixel

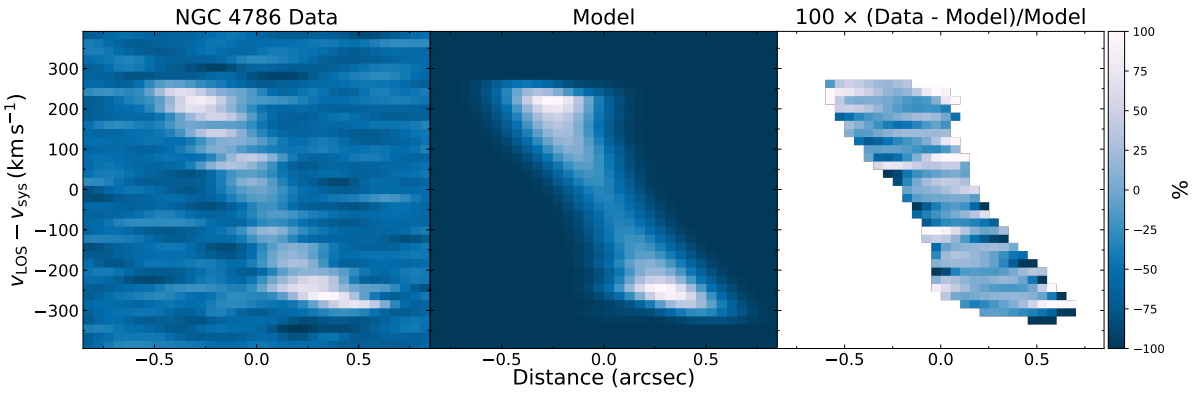

Figure 5.4 PVDs along the major axes of the NGC 4786 ALMA data and the best-fit model. Columns show ALMA CO(2−1) data (left), model (center), and fractional residual (right). The PVDs were extracted with a spatial width equivalent to a resolution element.

correlation, I block-averaged the data and model cubes by a factor of 4. I fit three dynamical models across 31 frequency channels in the NGC 4786 data cube that correspond to velocities of $|v_{\rm LOS} - v_{\rm sys}| \leq \sim 300\,{\rm km\,s^{-1}}$. This velocity range extends slightly past the channels with visible CO emission. After block-averaging the model and data cubes, the elliptical spatial region contains 12 pixels per channel, or a total of 372 data points in the entire model fit.

I present the results for the three dynamical models (A,B,C) for NGC 4786 in Table 5.2. The difference among them is the input host galaxy MGE model, which I described in Sections 5.3.1 and 5.3.2. In summary, dynamical models A-C yield a range in $M_{\rm BH}$ that spans $(3.9-5.8)\times10^8\,M_\odot$ with reduced χ^2 (χ^2_ν) values between 1.421 and 1.488 over 363 degrees of freedom. Using the dust-corrected MGE as an input, dynamical model C is the statistically best-fitting model, and I adopt it as the fiducial model to use in the systematic tests of the error budget. With $\chi^2_\nu = 1.421$, model C is not a formally acceptable fit when considering the degrees of freedom, which should achieve $\chi^2_\nu \leq 1.125$ when using a significance level of 0.05. An in-depth analysis of the systematic uncertainties of the measurement is described in Section 5.4.1. I present the major axis PVDs, moment maps, and CO line profiles extracted from the data and fiducial model cubes in Figures 5.4, 5.5, and 5.6. The comparisons highlight good overall agreement between the data and model. The model PVD is able to

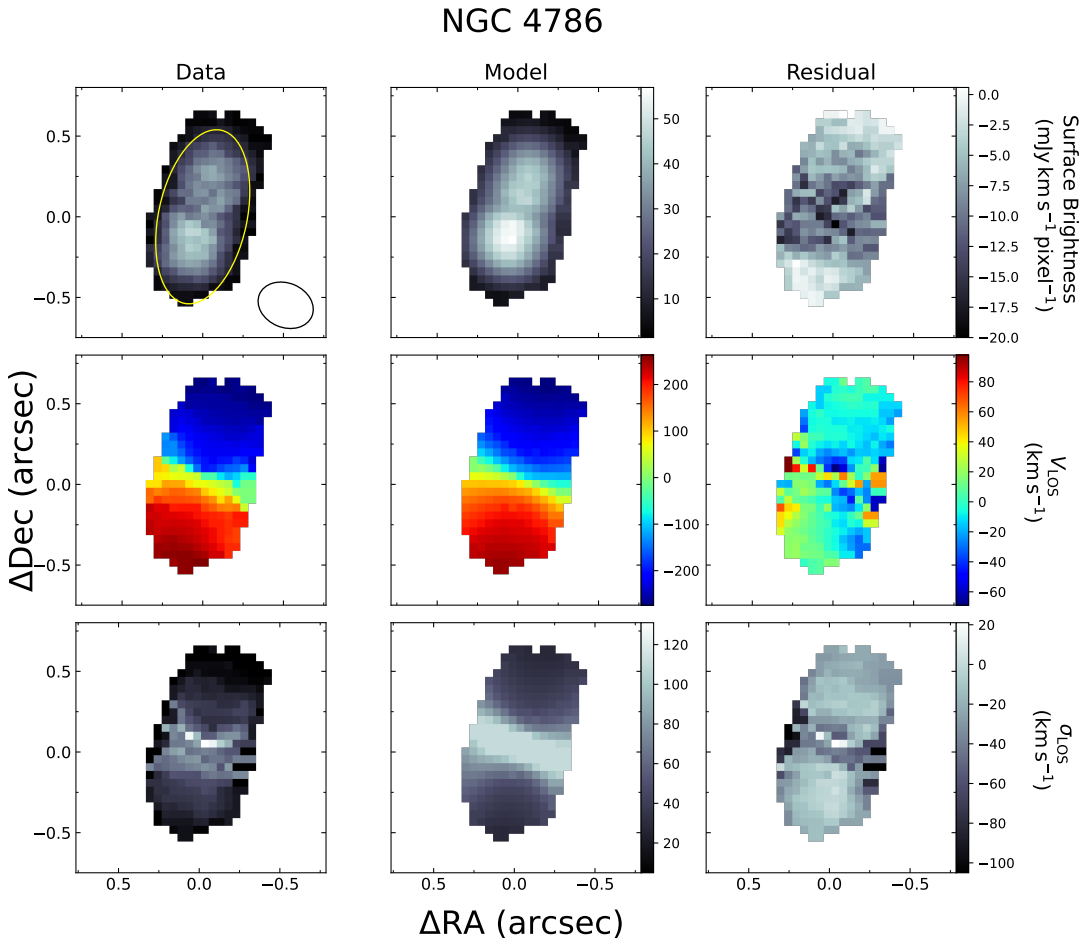

Figure 5.5 Moment maps for NGC 4786 constructed from the ALMA CO(2−1) data cube (left) and its fiducial model. Shown are maps of moments 0, 1, and 2, corresponding to surface brightness, LOS velocity $v_{\rm LOS}$, and LOS velocity dispersion $\sigma_{\rm LOS}$. The units for the surface brightness map are mJy km s^{-1} pixel^{-1}, and the units for the $v_{\rm LOS}$ and $\sigma_{\rm LOS}$ maps are km s^{-1}. The systemic velocity of 4621 km s^{-1} estimated from the dynamical models has been removed from $v_{\rm LOS}$. Maps of (data-model) residuals are shown in the rightmost column. The coordinate system is oriented such that $+x$ corresponds to East and $+y$ corresponds to North. While the line profile fits have been determined at each pixel of the full disk, the elliptical fitting region used in calculating χ^2 is denoted in the top left panel with a yellow ellipse. The synthesized beam is represented by an open ellipse in the bottom left corner of the same image.

emulate features such as the broad distribution in rotational velocity that is observed within $r \leq 0\farcs5$ on both the approaching and receding sides of the disk, as well as the decrease in velocity towards the center. An analysis of the moment maps shows that the model velocity field captures most of the behavior seen in the outer portions of the disk, where discrepancies

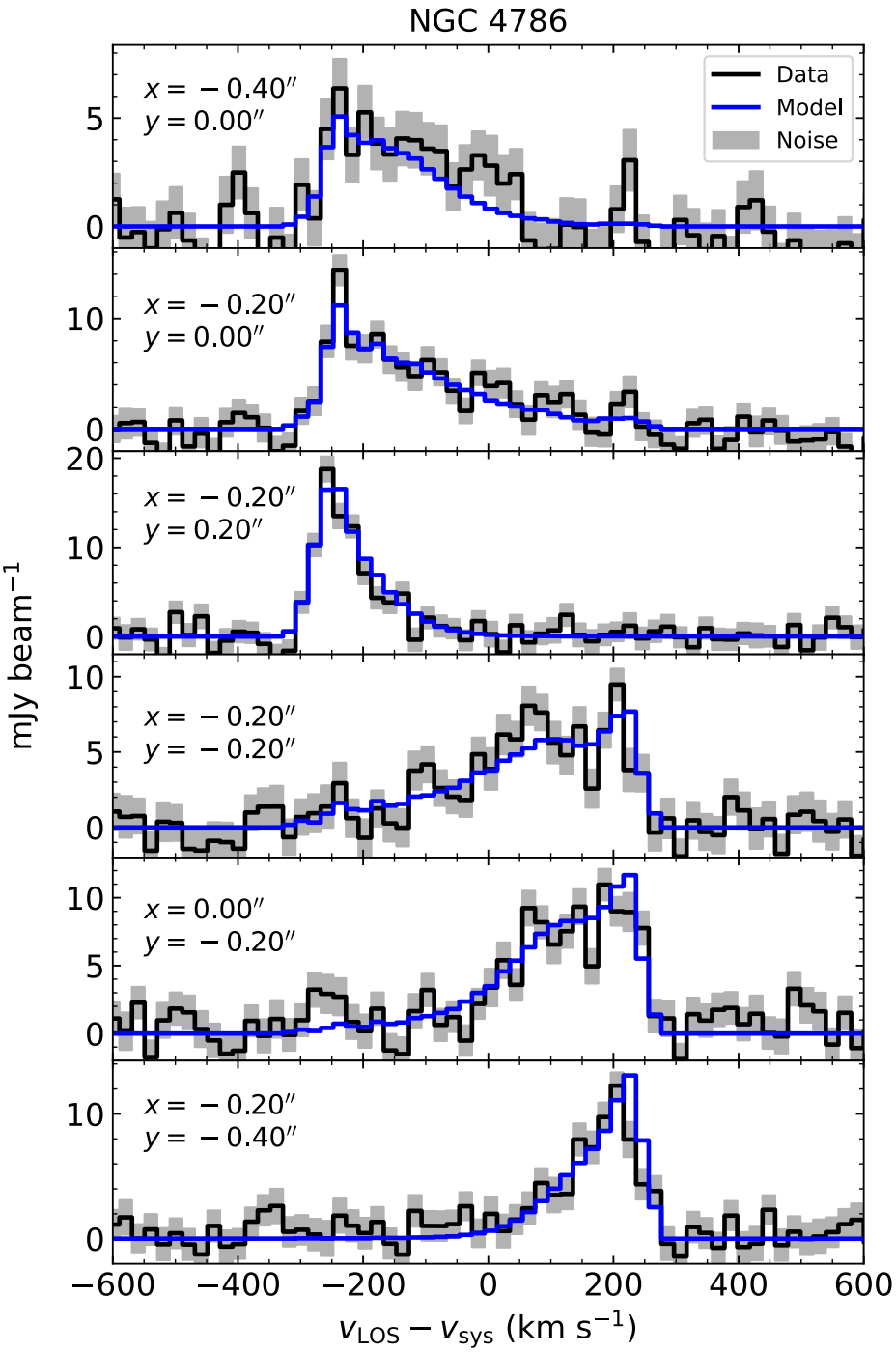

Figure 5.6 CO line profiles extracted from six spatial locations within the block-averaged NGC 4786 data cube, along with the fiducial model (model C). The x and y positions are given relative to the disk dynamical center, with $+y$ indicating North and $+x$ indicating East. The gray shaded area represents values in the range of data $\pm 1\sigma$, where the 1σ value is from the 3D noise model used in the χ^2 optimization.

in LOS velocity are $< \sim$20 $\mathrm{km\,s^{-1}}$, although noticeable disagreement is seen at the center, particularly along the minor axis. As described by Barth et al. (2016b), along an inclined disk's minor axis, the projected distance between the nucleus of a galaxy and a point along the minor axis is compressed by a factor of $\cos(i)$, and poor spatial resolution across the minor axis can lead to pronounced beam smearing. Given the large ALMA beam (FWHM $= 0\farcs31 = 93$ pc) relative to this small disk, it is unsurprising that beam-smearing effects are most evident in this region. The moment 0 map also highlights discrepancies between data and model in the central region, with the moment 0 map indicating a higher model CO surface brightness than what is observed. The CO line profiles can display complex characteristics, but even though the fine details within the broad and asymmetric data line profiles may be missed, the model CO line profiles generally capture their overall shape.

As for other free parameters in the model, the dynamically determined Υ_H values, especially for model A, are higher than typical Υ_H values ($\Upsilon_H \leq 1.30$) seen in single stellar population models that assume either a Kroupa (2001) or a Chabrier (2003) initial-mass function for an old (10-14 Gyr) stellar population with solar metallicity. The σ_0 parameter remains fairly low between $9.3 - 10.8\,\mathrm{km\,s^{-1}}$, which is less than the data cube's channel spacing and is consistent with other gas-dynamical modeling of ALMA data (Barth et al., 2016a; Boizelle et al., 2019, 2021; Cohn et al., 2021; Kabasares et al., 2022). The flux normalization factor F_0 is found to be between $1.54 - 1.56$ in the models and is higher than values seen in previous works, where it is typically closer to unity. Upon inspecting Figure 5.5, a comparison of the data and best-fit model's moment 0 map reveals a noticeable difference in surface brightness, particularly close to the disk's center, where the data appears to have faint CO emission. I explore the systematic effect of the input flux map on the mass measurement's error budget in Section 5.4.1.

Based on previous dynamical modeling work, the statistical uncertainty on a given dynamical model fit is expected to be much smaller than the uncertainty associated with the extinction

corrections in the host galaxy models. To determine the statistical uncertainty for the NGC 4786 SMBH mass measurement, I used a Monte Carlo resampling procedure. I generated 100 noise-added realizations of the fiducial model by adding noise to each pixel of the model cube. At each pixel, I drew a randomly sampled value from a Gaussian distribution with a mean of zero and a standard deviation equal to the value of the 3D noise cube at the same pixel. I re-optimized a dynamical model to each of the 100 altered realizations, using the values in Table 5.2 as initial guesses. I list the standard deviation of each free parameter as the 1σ uncertainty under the results for model C. For $M_{\rm BH}$, the distribution has a mean of $M_{\rm BH} = 5.0 \times 10^8\,M_\odot$ and a standard deviation of $0.2 \times 10^8\,M_\odot$ or approximately 4% of the mean.

5.4.1 Error Budget of the Mass Measurement

While the statistical uncertainties on $M_{\rm BH}$ derived from the Monte Carlo procedure are small, there are other sources of uncertainty that stem from different aspects of the model construction. It has been shown by previous dynamical-modeling studies (Boizelle et al., 2019, 2021; Cohn et al., 2021; Kabasares et al., 2022) that the statistical model-fitting uncertainties for a given dynamical model vastly underestimate the total error budget of a given measurement when considering the uncertainties from model systematics. To assess the impact of the systematic uncertainties on the error budget, I took the statistically best-fit dynamical model (model C) and performed a number of systematic tests that involved changing aspects of the model construction. I briefly describe and list these changes below:

- *Dust extinction*: I explored the impact of dust extinction by creating the three MGE host galaxy models (unmasked, dust-masked, and dust-corrected) described in Sections 5.3.1 and 5.3.2. Dust is clearly present at the center of the galaxy, and previous gas-dynamical studies (Boizelle et al., 2019, 2021; Cohn et al., 2021; Kabasares et al.,

2022) have also shown that even in the best cases where the BH SOI is well-resolved, differences in the assumed host galaxy profile can lead to large discrepancies in $M_{\rm BH}$. Therefore, while the intrinsic host galaxy mass profile and the uncertainty in its inner slope may be difficult to ascertain, by building a set of MGE models that account for the presence of dust in different ways, I can effectively produce a set of models that bracket the likely range of profiles.

I adopt model C for NGC 4786 as the fiducial model and perform the remaining systematic tests on this model for a number of reasons. First, this model is the statistically best-fitting dynamical model for NGC 4786. In addition, previous ALMA BH mass measurements (Boizelle et al., 2019, 2021; Cohn et al., 2021; Kabasares et al., 2022) have shown that the statistical model fitting uncertainties for a given dynamical model vastly underestimate the total error budget of a given measurement when considering uncertainties associated with the host galaxy extinction corrections, and the dust-corrected MGE model used in model C is the best estimate of the underlying host galaxy profile.

- *Radial motion*: Following the approach described by Kabasares et al. (2022), I allow for radial motion in the dynamical models, by incorporating a simple toy model which is controlled by a parameter α. This parameter controls the balance between purely rotational ($\alpha = 1$) and purely radial inflow ($\alpha = 0$) motion.

- *Turbulent velocity dispersion*: The velocity dispersion of the gas is changed from a spatially uniform term of $\sigma(r) = \sigma_0$ to a Gaussian that is a function of radius: $\sigma(r) = \sigma_0 + \sigma_1 \exp[-(r-r_0)^2/2\mu^2]$. This model adds three additional free parameters, with σ_1, r_0, and μ representing the Gaussian's velocity amplitude, radial offset from $r = 0$, and standard deviation, respectively. While this model is not motivated by any physical mechanism, it allows for more variation in the form of the velocity dispersion.

- *Fit region*: I adjust the elliptical spatial region used to optimize the dynamical model. The new fitting region for NGC 4786 is an ellipse with a semimajor axis of approximately 1.25 ALMA resolution elements centered on the disk's dynamical center. With this setup, the models are fit to parts of the disk that are more sensitive to the BH's gravitational potential as opposed to the host galaxy's, but there is now a larger fraction of pixels that are in the central beam-smeared region of the disk.

- *Gas mass*: The gas disk's mass contribution to the gravitational potential is removed, and model fits incorporate only the gravitational potential of the BH and the host galaxy. This is done by setting the gas disk's contribution to the total circular velocity to $0\,\mathrm{km\,s^{-1}}$.

- *Block-averaging factor*: The process of block-averaging dynamical models leads to coarser angular resolution, and could potentially limit the models' ability to constrain M_{BH}. To test for this possibility, I optimized a dynamical model where no block-averaging was performed.

- *Oversampling factor*: The models are originally built on a grid that is oversampled by a factor of 3 relative to the ALMA data. I set this factor to 1 to test the effect of building models on a grid that is equal in size to the original ALMA spatial scale.

- *Input flux map*: I built a different input flux map to weight the CO line profiles. This flux map was constructed by fitting an azimuthally normalized 3D tilted-ring model (Rogstad et al., 1974; Begeman, 1989) in the `3DBarolo` program to the ALMA data cube (Di Teodoro and Fraternali, 2015). The program returns a 3D model data cube, from which I can produce a flux map in the same manner as a regular ALMA data cube and use as an input in the dynamical models.

The largest shifts in M_{BH} are seen in the systematic tests that involve changing the host galaxy model to account for extinction. I describe the changes observed from these tests

	NGC 4786	
Systematic Test	$M_{\rm BH,new}(10^8\,M_\odot)$	$\Delta M_{\rm BH}$
Radial motion	5.0	0%
Turbulent velocity dispersion	5.0	0%
Fit region	4.7	−6%
Gas mass	5.0	0%
Block-averaging factor	5.0	0%
Oversampling factor	4.3	−15%
Input flux map	6.2	+21%

Table 5.3 Results of the systematic tests performed on the fiducial dynamical model for NGC 4786, not including tests that involved changes to the host galaxy MGEs. I list the new value of $M_{\rm BH}$ that the optimization converged to, as well as the percent change from the $M_{\rm BH}$ determined for the fiducial model.

below, and list the results of the other systematic tests that do not involve changes to the host galaxy MGE model in Table 5.3.

The value of $M_{\rm BH}$ is highly sensitive to how dust extinction is accounted for. This is highlighted by the differences in the unmasked, dust-masked, and dust-corrected MGE models shown in Table 5.2. The value of $M_{\rm BH}$ decreases by about 22% to $M_{\rm BH} = 3.9 \times 10^8\,M_\odot$ when using the unmasked MGE and increases by 16% to $M_{\rm BH} = 5.8 \times 10^8\,M_\odot$ when using the dust-masked MGE.

As a final systematic test, I fixed $M_{\rm BH} = 0\,M_\odot$ in the dynamical model and reoptimized with the dust-corrected MGE as an input to see if the model could still reliably emulate the observed gas kinematics without the need for a BH. Again, this resulted in poorer fits to the data, with $\chi^2_\nu = 1.974$ in addition to a large increase in Υ_H to 2.60 $M_\odot/L_\odot$ to compensate for the lack of a supermassive BH. As mentioned earlier, this is a higher Υ_H value than what is seen in single stellar population models.

As shown in Table 5.3, most of the systematic tests that did not involve adjustments to the MGE model led to relatively insignificant changes to $M_{\rm BH}$, but there were a few exceptions. The most profound ($> 10\%$) changes were a 15% decrease due to the change in oversampling

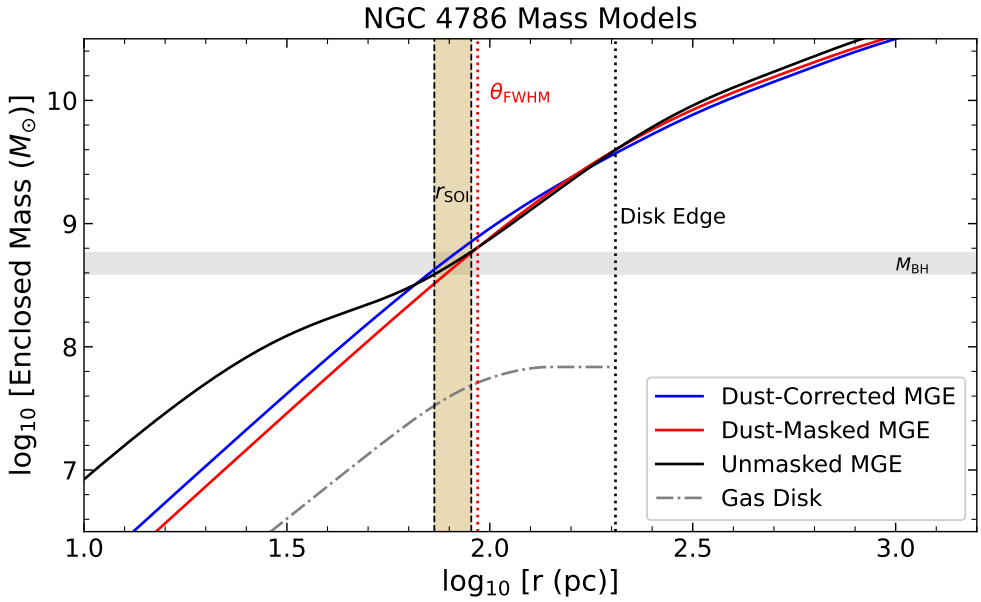

Figure 5.7 Plot of $\log_{10} M_\star(r)$ vs. $\log_{10} r$ in NGC 4786 for the three host galaxy MGE models and gas mass profile used. $M_\star(r)$ is calculated via $M_\star(r) = rv^2_{\star,\rm MGE}/G$, where the $v_{\star,\rm MGE}$ values have been scaled by their respective $\sqrt{\Upsilon_H}$ values listed in Table 5.2. $M_{\rm gas}(r)$ is calculated via: $rv^2_{\rm gas}/G$. The red dotted line indicates the angular resolution of the observation, whereas the black dotted line represents the outer edge of the dust disk as measured along the major axis. The gray shaded region indicates the range of $M_{\rm BH}$ determined by the dynamical models using the different input MGE models, while the yellow shaded region enclosed within the black dotted lines indicate the range of the radius of the black hole sphere of influence, $r_{\rm SOI}$. I have defined $r_{\rm SOI}$ to be the radius where the stellar and BH masses of a given dynamical model are equal.

factor and a 21% increase due to the choice of flux map. The models are constructed on an oversampled grid in order to account for potentially steep velocity gradients in the disk, as pixels near the disk center can contain molecular gas spanning a large velocity range. Without any oversampling, these velocity gradients can be missed, and can subsequently lead to models converging on a less massive BH. As for using the new flux map, the dynamical models not only converged on a higher BH mass, but also substantially different values of $F_0 = 0.93$ and $i = 58.6°$ with an improved $\chi^2_\nu = 1.354$. The change of over 10° in inclination angle, as well as a 40% decrease in the flux normalization factor, indicates significant differences when modeling the disk's structure. As stated earlier, this flux map was created from a 3D model data cube generated from an automated 3D tilted-ring fit in `3DBarolo`.

The tilted-ring model allows Γ and i to be different for each ring, and converged on ring inclinations of approximately 60°, a significant difference from the flat disk models. The differences in the empirically measured and tilted-ring model flux maps can be attributed to the assumptions in the `3DBarolo` model fit as well as variations in the CO surface brightness across the disk, especially near the disk's center, where the disk is CO-faint. These features are not encapsulated in the azimuthally normalized tilted-ring model, which has a relatively constant surface brightness across the disk. This leads to large differences in the overall flux normalization factor and the inferred disk structure.

These tests highlight a clear degeneracy between the BH and stellar mass components in the dynamical models. The systematic uncertainties from the host galaxy modeling dominate over the statistical ($\approx$2%) and the distance uncertainty of $\approx$15%, as well as most of the other systematic uncertainties ($\approx 5-20\%$) not associated with the host galaxy models. While the mass range for $M_{\rm BH}$ found in Table 5.2 is at the $\approx$20% level, the dynamical models prefer the presence of a central supermassive BH to reproduce the observed gas kinematics, as opposed to models where no BH is present.

When considering only the fiducial host galaxy MGE model, and including the uncertainties from the systematic tests in Table 5.3, the distance to the galaxy, and the statistical fluctuations in the data, the range in $M_{\rm BH}$ is $(M_{\rm BH}/10^8\,M_\odot) = 5.0 \pm 0.2\,[1\sigma\,\text{statistical}]\,^{+1.2}_{-0.8}\,[\text{systematic}] \pm 0.75\,[\text{distance}]$ if the negative and positive systematic uncertainties from Table 5.3 are added in quadrature. However, these ranges in $M_{\rm BH}$ neglect contributions from the uncertainties in the extinction correction of the host galaxy models.

I will incorporate these systematic uncertainties for a number of reasons. First, while the dust-corrected MGE model is the best estimate of the underlying host galaxy model, the potentially large variation in the inner slope of the stellar mass profile must be accounted for. While dust attenuation on the host galaxy light may not appear obvious when comparing the

data and model isophotes or surface brightness profiles in Figures 5.2 and 5.3, the resulting deprojected host galaxy models produce a broad range in $M_{\rm BH}$.

In other works that feature $M_{\rm BH}$ measurements in ETGs (Davis et al., 2017, 2018; Smith et al., 2021; Ruffa et al., 2023), the surface brightness of the host galaxy has typically been parameterized with only dust-masked MGEs. While masking out the most dust-obscured features in the image prior to fitting an MGE may yield better models than without any masking, it does not fully address the problem of extinction, and limits the model fit to the remaining pixels that are not completely unaffected by dust. As shown by the results in this dissertation and in other previous ALMA $M_{\rm BH}$ measurements (Boizelle et al., 2019, 2021; Cohn et al., 2021; Kabasares et al., 2022), uncertainties from the extinction correction far exceed the formal statistical uncertainties, so accounting for a range in the inner stellar mass profile slope and its effect on the inferred $M_{\rm BH}$ should be explored. Therefore, future $M_{\rm BH}$ studies with ALMA should incorporate and explore this often overlooked component of an $M_{\rm BH}$ measurement's error budget.

After adding the systematic uncertainties associated with the extinction correction in quadrature with the uncertainties associated with the systematic tests in Table 5.2, the final measured range in $M_{\rm BH}$ for NGC 4786 is,

$$(M_{\rm BH}/10^8\,M_\odot) = 5.0 \pm 0.2\,[1\sigma\,\text{statistical}]\,^{+1.4}_{-1.3}\,[\text{systematic}] \pm 0.75\,[\text{distance}]. \tag{5.2}$$

I compare this range in $M_{\rm BH}$ with predicted values of $M_{\rm BH}$ from BH-host galaxy scaling relations in the following section.

5.5 Discussion

This ALMA gas-dynamical $M_{\rm BH}$ measurement is the first attempt to measure $M_{\rm BH}$ in NGC 4786. In the following subsections, I determine a range for $r_{\rm SOI}$, and describe how using ALMA observations that do not fully resolve this scale leads to large systematic uncertainties in the mass measurement. In addition, I compare my measured range of $M_{\rm BH}$ to predicted ranges from the scaling relations of Kormendy and Ho (2013).

5.5.1 The Impact of Resolving the BH Sphere of Influence in ALMA Gas-dynamical Measurements

The results indicate that $r_{\rm SOI}$ is not completely resolved in NGC 4786, which leads to a degeneracy between stellar and BH mass in the models. I calculated $r_{\rm SOI}$ by determining the radius where $M_\star = M_{\rm BH}$ for each of the three input MGE models and highlight the range of $r_{\rm SOI}$ in Figure 5.7. $r_{\rm SOI}$ is between 73 pc (0.″24) and 90 pc (0.″30), whereas the ALMA beam FWHM is 93 pc (0.″31), indicating that the SOI is nearly resolved along the major axis of the disk. As pointed out by Barth et al. (2016b), however, the threshold for a successful BH mass measurement rises considerably at higher inclination angles, as projected distances along the minor axis of an inclined disk become compressed by a factor of $\cos(i)$. At an inclination angle of 70°, $r_{\rm SOI}$ in NGC 4786 is unresolved along the disk's projected minor axis by a factor of nearly 3.

Following the work of Rusli et al. (2013), I compare the measured $r_{\rm SOI}$ values to the average ALMA beam size through $\xi = 2r_{\rm SOI}/\theta_{\rm FWHM}$. I find $\xi = (1.6 - 1.9)$. Davis (2014) suggests that observations that satisfy $\xi \sim 2$ are adequate for the purpose of conducting molecular gas-dynamical BH mass measurements. This figure of merit was designed to aid in the planning of observational campaigns focused on estimating central BH masses, and is a less stringent

threshold than traditional considerations. However, as the results show, measurements based on observations in this regime can have uncertainties at the 30% level driven by uncertainties in the extinction correction.

While the ALMA observations for NGC 4786 approximately satisfy the aforementioned figure of merit, the sensitivity of $M_{\rm BH}$ to the choice of host galaxy model in NGC 4786 is still readily apparent. Detecting the enhancement of a tracer particle's circular velocity due to the presence of a supermassive BH is more difficult when the slope of the stellar mass profile in the central region of a galaxy is not well constrained. As seen in Figure 5.7, differences in the overall shape of the different host galaxy mass profiles are minimal at the disk edge and beyond, as expected. However, at radii less than the projected ALMA resolution limit, there are noticeable differences in the overall shape of the stellar mass profiles. The process of converting the observed brightness distributions into mass profiles is complicated by the presence of dust, which limits a dynamical model's ability to reliably separate the BH and galaxy contributions to the overall gravitational potential. Figure 5.7 reveals an inner bump in the $M_{\star}(r)$ profile for the unmasked MGE. The bump is unphysical and is a limitation of MGEs that is exacerbated by both the annular extinction of the dust and the constraint that the enclosed mass of each MGE should match at the disk edge. This aspect of MGEs highlights the need for dust-masked and dust-corrected MGEs when modeling the host galaxy's light in cases where dust is readily apparent.

An additional factor in the measurement uncertainty is the apparent deficit of CO emission in the central region. This deficit is apparent in the surface brightness map of NGC 4786 shown in Figure 5.5, as the residual map between the data and best-fit model highlight prominent discrepancies at the center of each disk. In previous work, such as in the case of NGC 6861, these deficits can limit the measurement of $M_{\rm BH}$ to using kinematic information beyond $r_{\rm SOI}$ and prevent tight constraints (Kabasares et al., 2022).

5.5.2 Comparison to Predictions from BH Scaling Relations

The ALMA observation was designed to probe scales comparable to $r_{\rm SOI}$ using SMBH mass estimates from the $M_{\rm BH} - \sigma_\star$ relation of Kormendy and Ho (2013) using the definition: $r_{\rm SOI} = GM_{\rm BH}/\sigma_\star^2$. For NGC 4786, the relation predicts a BH mass of $M_{\rm BH} = 1.5 \times 10^9\,M_\odot$ when using the $\sigma_\star$ value of $286\,{\rm km\,s^{-1}}$ from Hyperleda (Makarov et al., 2014). Thus, the measured $M_{\rm BH}$ of $5.0 \times 10^8\,M_\odot$ falls below the predicted value and the intrinsic scatter of 0.28 dex in the $M_{\rm BH} - \sigma_\star$ relation.

To compare my measured $M_{\rm BH}$ range with the $M_{\rm BH} - L_{{\rm bulge},K}$ relation of Kormendy and Ho (2013), I used the dust-corrected MGE model in Table 5.1 and assumed a color of $H - K = 0.2$ mag based on stellar population models of an old stellar population with solar metallicity (Vazdekis et al., 2010), as well as absolute solar magnitudes of $M_{\odot,H} = 3.37$ mag and $M_{\odot,K} = 3.27$ mag (Willmer, 2018). By adding the total luminosity of each component in the dust-corrected H-band MGE and converting it to the K-band, I found that $L_{{\rm bulge},K} = 3.5 \times 10^{11}\,L_\odot$. This yields a predicted value of $M_{\rm BH} = 2.5 \times 10^9\,M_\odot$. Given the scatter of 0.30 dex, the dynamically measured $M_{\rm BH}$ range falls well below this predicted value.

Finally, I compared the measured $M_{\rm BH}$ range with the $M_{\rm BH} - M_{\rm bulge}$ relation by converting the total H-band luminosity of the dust-corrected MGE and multiplying it by $\Upsilon_H = 1.80$. This was done under the assumption that there are no gradients in Υ_H. I found $M_{\rm bulge} = 5.7 \times 10^{11}\,M_\odot$. As discussed in Zhu et al. (2021), a non-negligible fraction of the mass in elliptical galaxies may not belong to the "bulge" component of the galaxy, and thus, a more nuanced mass decomposition of the host galaxy is needed to reliably calibrate empirical correlations between $M_{\rm BH}$ and bulge properties. Therefore, the calculated mass should be taken as an approximation that likely overestimates $M_{\rm bulge}$. Indeed, the estimated $M_{\rm bulge}$ value corresponds to a predicted value of $M_{\rm BH} = 3.8 \times 10^9\,M_\odot$, which is nearly an order of magnitude higher than the fiducial dynamical model's $M_{\rm BH}$ value.

5.6 Conclusion

I present the first dynamical measurement of the central SMBH mass in NGC 4786 using ALMA observations with 0.″31 resolution. A circumnuclear disk in orderly rotation with LOS velocities of $\sim$270 km s^{-1} relative to the systemic velocity is observed.

The dynamical models constrain $M_{\rm BH}$ within the range of

$$(M_{\rm BH}/10^8\,M_\odot) = 5.0 \pm 0.2\,[1\sigma\,\text{statistical}]\,^{+1.4}_{-1.3}\,[\text{systematic}] \pm 0.75\,[\text{distance}]$$

using three separate host galaxy models. Upon conducting numerous systematic tests, I found that the systematic uncertainties associated with the extinction correction of the host galaxy MGE models were the dominant contributor to the overall error budget.

Dynamical models that contain a central supermassive BH fit the observed ALMA data better than models without one. Additionally, these models underscore the importance of incorporating a range of plausible inner slopes in the host galaxy mass models when calculating the error budget of an $M_{\rm BH}$ measurement. This incorporation is necessary when conducting $M_{\rm BH}$ measurements in dusty systems with ALMA observations that do not fully resolve the projected BH SOI, as stellar mass and BH mass in a dynamical model can become degenerate. In conclusion, my measurement is the first of its kind for the SMBH mass in NGC 4786 and highlights important limiting factors and considerations for future gas-dynamical $M_{\rm BH}$ measurements with ALMA.

Chapter 6

NGC 5193

6.1 Galaxy Properties

NGC 5193 is classified as an E pec galaxy by RC3. In past literature, this galaxy has been associated with and sometimes identified as the brightest cluster galaxy in the Abell 3560 (Abell et al., 1989) cluster, with a recessional velocity of $cz \sim 3800 - 4000\,\mathrm{km\,s^{-1}}$ (Lauer et al., 1998; Okoń and Harris, 2002). However, Vettolani et al. (1990) and Willmer et al. (1999) instead associate NGC 5193 with the Abell 3565 cluster based on findings from Melnick and Moles (1987) that indicate Abell 3560 has a recessional velocity of $cz \sim 14,850$ $\mathrm{km\,s^{-1}}$. This implies that Abell 3560 is a background galaxy cluster and that NGC 5193 is not a member. Tonry et al. (2001) determined a distance modulus of $m - M = 32.66 \pm 0.29$ mag for NGC 5193 with ground-based I-band surface brightness fluctuation (SBF) data while distinguishing it as separate from Abell 3560. This distance modulus translates to a luminosity distance of 34.0 ± 4.5 Mpc, but they list this measurement as uncertain. Jensen et al. (2003) independently measured a distance modulus of $m - M = 33.35 \pm 0.15$ mag, using SBF measurements from HST NICMOS F160W data. The corresponding luminosity

distance is 46.8 ± 3.2 Mpc, and I adopt this distance for my dynamical modeling purposes. Using a recessional velocity of $cz = 3705\,\mathrm{km\,s^{-1}}$ from initial gas-dynamical models, this gives an angular diameter distance of 45.7 Mpc, where $1''$ corresponds to 221 pc. There are no previous works that have constrained the central BH mass in this galaxy.

6.2 Observations

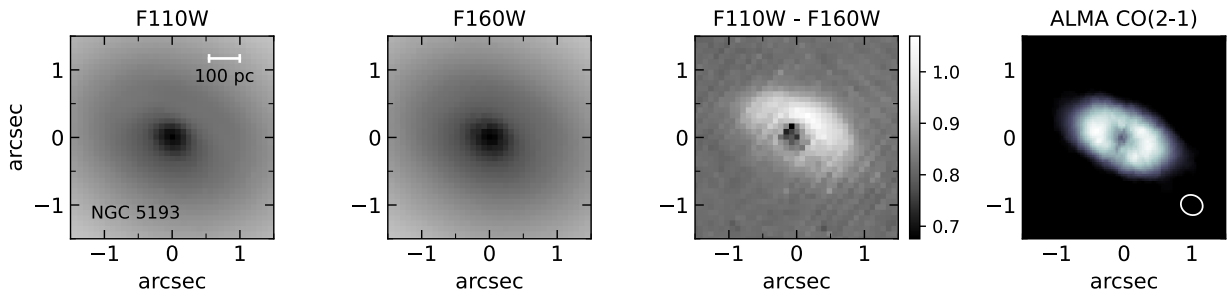

Figure 6.1 HST F110W (J-band), F160W (H-band), F110W $-$ F160W ($J-H$), and ALMA CO(2$-$1) images of NGC 5193 showing the co-spatial alignment of the gas and dust. The ALMA intensity maps were created by summing channels in the data cubes that displayed visible CO emission. Pixels with emission were identified with an automatically generated mask by the `3DBarolo` program (Di Teodoro and Fraternali, 2015). In the $J-H$ maps, light regions correspond to redder colors and dark regions are bluer than the surrounding starlight. North is up and East is to the left in each image.

6.2.1 HST Data

I used HST WFC3 J and H-band data from HST proposal 15909 (PI: Boizelle) to model the host galaxy's contribution to the total gravitational potential. The H-band data were taken with a four-point dither pattern to optimally sample the H-band PSF, whereas a two-point dither pattern was used for the J-band data. The H-band observation consisted of four separate exposures lasting 299 seconds each, whereas the J-band observation consisted of two 128-second exposures. The data were processed through the `calwf3` pipeline and were aligned and drizzled with `AstroDrizzle`. The H-band images were aligned and drizzled to

a scale of 0.″08 first. The drizzled H-band product was used as a reference for the alignment and drizzling process of the J-band images. `TinyTim` H and J-band PSFs were also generated and drizzled in the same fashion as the exposures. A $J - H$ map was created to determine regions with significant reddening of the host galaxy's light. The J, H, and $J - H$ images are shown in Figure 6.1 along with the ALMA CO(2−1) intensity maps.

6.2.2 ALMA Data

The ALMA data for NGC 5193 is from ALMA Program 2017.1.00301.S. NGC 5193 was observed on 15 January 2018 for approximately 29 minutes with a maximum baseline of 2386 m. The observation targeted the redshifted CO(2−1) emission line along with a corresponding spectral window for the continuum. The emission line spectral window had a channel resolution of 3.904 MHz, and covered the frequency range of 226.84 − 228.71 GHz. The continuum windows had a channel resolution of 31.25 MHz, and covered frequencies between 224.78 − 226.76 GHz. The interferometric visibility data was calibrated in CASA version 5.1.1, and then imaged into a data cube with 10 $\mathrm{km\,s^{-1}}$ velocity channel spacing, with a pixel size of 0.″035. The synthesized beam has a position angle of 63.1° measured East of North, has a major axis FWHM of 0.″33, and has a minor axis FWHM of 0.″29, giving it a geometric mean FWHM of 0.″31.

6.3 Host Galaxy Surface Brightness Modeling

I used three separate host galaxy MGE models to incorporate in the dynamical modeling of the NGC 5193 ALMA data cube. The process of creating these MGEs was described in detail in Sections 5.3.1 and 5.3.2 for NGC 4786. Given that this process was very similar for

k	$\log_{10} I_{H,k}(L_\odot\,\mathrm{pc}^{-2})$	σ'_k (arcsec)	q'_k	$\log_{10} I_{H,k}(L_\odot\,\mathrm{pc}^{-2})$	σ'_k (arcsec)	q'_k
	NGC 5193 (Unmasked MGE)			NGC 5193 (Dust-Masked MGE)		
1	5.813	0.033	0.895	5.412	0.078	0.805
2	4.713	0.218	0.750	4.371	0.435	0.750
3	4.405	0.848	0.756	4.351	0.931	0.752
4	4.022	1.910	0.814	3.979	1.980	0.809
5	3.469	4.511	0.750	3.445	4.649	0.750
6	3.039	9.706	0.842	3.034	9.919	0.851
7	2.507	18.437	0.980	2.476	19.507	0.986
8	1.692	44.349	0.963	1.569	50.580	0.930
	NGC 5193 (Dust-Corrected MGE)					
1	5.274	0.094	0.768			
2	4.550	0.334	0.794			
3	4.338	0.933	0.756			
4	3.982	2.015	0.814			
5	3.436	4.716	0.750			
6	3.020	10.017	0.848			
7	2.472	19.064	0.984			
8	1.654	45.548	0.962			

Table 6.1 NGC 5193 unmasked, dust-masked, and dust-corrected MGE solutions. The first column is the component number, the second is the central surface brightness corrected for Galactic extinction and assuming an absolute solar magnitude of $M_{\odot,H} = 3.37$ mag (Willmer, 2018), the third is the Gaussian standard deviation along the major axis, and the fourth is the axial ratio. Primes indicate projected quantities.

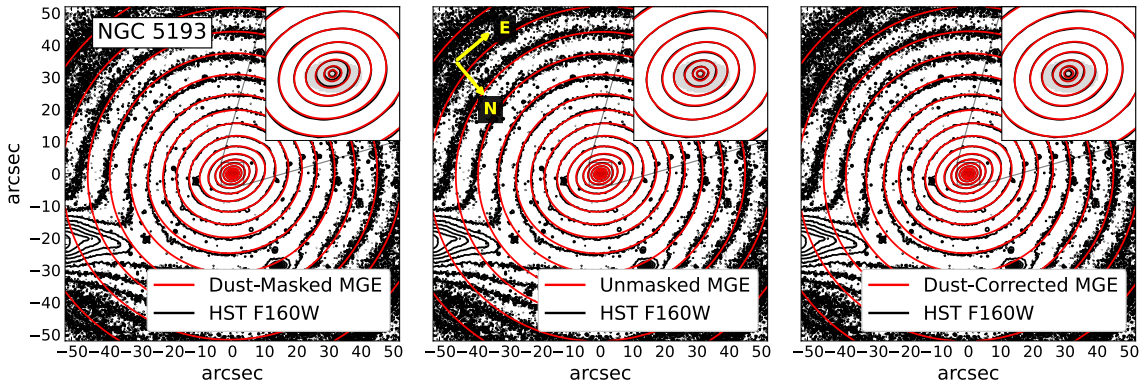

Figure 6.2 2D isophote maps comparing the observed HST WFC3 F160W isophotes to those of the three MGEs for NGC 5193. Black contours represent isophotes from the F160W image, while red contours are for the MGE models. For each image, the central $\approx 100'' \times 100''$ region is displayed with an inset of the innermost $3\farcs5 \times 3\farcs5$ region in the top right corner. The gray ellipse shown within each inset indicates the size and orientation of the circumnuclear dust disk. Arrows in the middle panel indicate the orientation of North and East.

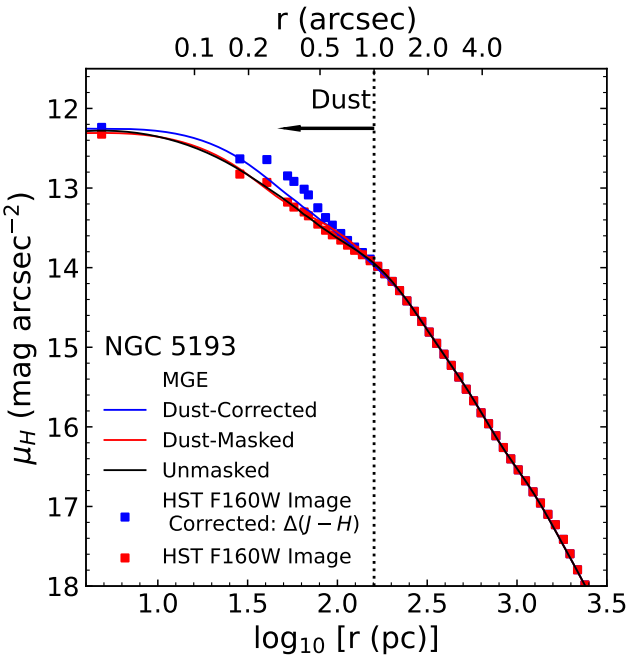

Figure 6.3 NGC 5193 major axis surface brightness profiles of the different host galaxy MGE models. The red points are the observed values from the H-band image, while the blue points are the dust-corrected values. The different lines in the panel correspond to extracted major axis surface brightness profiles for the 2D MGE models. The outer edge of the dust disk is marked with a vertical dashed line, and the arrow indicates that the dust extends down to the nucleus.

NGC 5193, I will only highlight the unique considerations taken into account when building the NGC 5193 MGEs in this section.

As in the case of NGC 4786, I used an unmasked, dust-masked, and dust-corrected MGE for NGC 5193 as well. The dust-masked MGE was fitted to the drizzled H-band image after isolating the host galaxy light from foreground stars, background galaxies, cosmic rays, detector artifacts, and the most reddened regions of the disk. There was careful consideration regarding whether to include a PSF component in `GALFIT` to account for a potential unresolved nuclear source of non-stellar origin. Optical spectra of the nuclear region showed no evidence of prominent emission lines typically associated with an active galactic nucleus (Jones et al., 2009). While the NGC 5193 H-band surface brightness profile exhibits a cuspy nature, an examination of the galaxy center in multiple wavelength filters revealed that the

central light is radially extended and not point-like. Based on these findings, a central PSF component was not included.

To create a dust-corrected H-band image of NGC 5193, I fit a 2D Nuker model to the innermost $10'' \times 10''$ of the image in `GALFIT`. The values of the NGC 5193 Nuker model are: $\alpha = 6.28$, $\beta = 1.40, \gamma = 0.70$, and $r_{\rm b} = 1\farcs39$, which are values characteristic of power law galaxies (Lauer et al., 2007). By using the observed $\Delta(J-H)$ values, I estimated a central H-band extinction of $A_H = 0.18$ mag, which corresponds to an approximate 15% reduction in the host galaxy starlight. It is also important to note that the $J-H$ map of NGC 5193 is indicative of a central hole in the dust distribution and is supported by the CO(2−1) moment 0 map, which displays a deficit of central CO emission as well. I discuss the potential impact this has on the measurement of $M_{\rm BH}$ in a later section. To create the final dust-corrected image that accounts for $A_H = 0.18$ mag of extinction at the center, I fixed the initial Nuker model parameters and tuned γ until I found an optimal value where the central pixels of the Nuker model are nearly equal to the scaled flux values of the H-band image based on the assumed H-band extinction. I determined this optimal value to be $\gamma = 0.75$. The components of all the NGC 5193 MGE models are shown in Table 6.1. The isophotes and surface brightness profiles are presented in Figures 6.2 and 6.3. The model isophotes are in good agreement with the data's out to large radii and even in the nuclear region where dust present. The H-band isophotes remain elliptical and symmetric even within the dusty region, suggesting that dust attenuation in this system may not be particularly severe.

6.4 Dynamical Modeling Results

I opted to fit dynamical models to nearly the full disk region, given the relatively few resolution elements across the disk. The elliptical fitting region has an axial ratio of $q = 0.50$ and a semimajor axis length of $a = 1''$. I also block-averaged the data and model cubes by

Model	MGE	$M_{\rm BH}$ ($10^8\,M_\odot$)	Υ_H ($M_\odot/L_\odot$)	i (°)	Γ (°)	σ_0 (km s^{-1})	$v_{\rm sys}$ (km s^{-1})	F_0	χ^2_ν
D	Unmasked	1.5	1.69	60.6	66.4	6.7	3705.02	1.15	2.274
E	Dust-Masked	2.9	1.55	60.5	66.4	3.1	3704.50	1.16	2.541
F	Dust-Corrected	1.4	1.46	60.7	66.4	5.1	3704.77	1.14	2.096
		(0.02)	(0.005)	(0.1)	(0.1)	(0.1)	(0.10)	(0.003)	

Table 6.2 Best-fit parameter values obtained by fitting thin disk dynamical models to the NGC 5193 data cube. I derive 1σ statistical uncertainties for the parameters of fiducial model F, based on a Monte Carlo resampling procedure, and list them under the results for model F. This model has 3181 degrees of freedom. The major axis PA, Γ, is measured east of north for the receding side of the disk. I found the dynamical center of the fiducial model to be at RA=$13^{\rm h}31^{\rm m}53.5289^{\rm s}$, Dec=$-33°14'03\farcs546$ for NGC 5193. This is within $0\farcs001$ of the dynamical centers of the other models. The observed redshift, $z_{\rm obs}$, is used in the dynamical models as a proxy for the systemic velocity of the disk, $v_{\rm sys}$, in the barycentric frame via the relation: $v_{\rm sys} = cz_{\rm obs}$ and is used to translate the model velocities to observed frequency units.

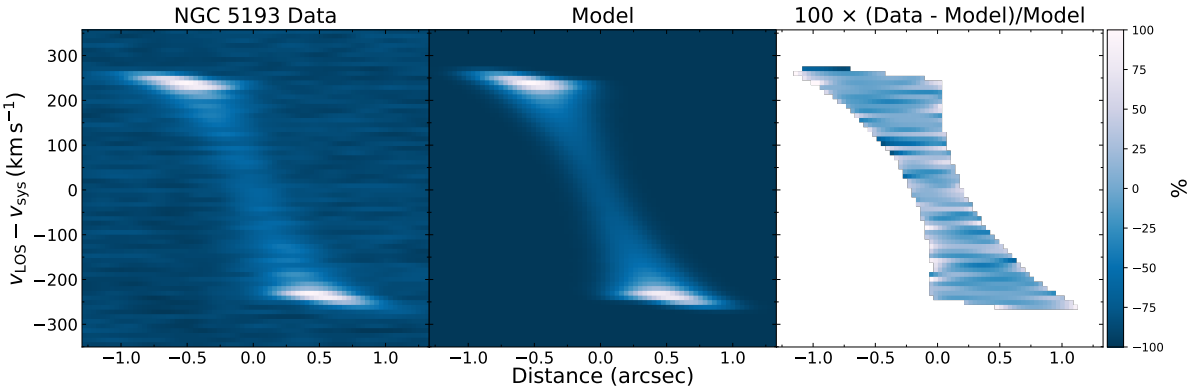

Figure 6.4 PVDs along the major axes of the NGC 5193 ALMA data and the best-fit model. Columns show ALMA CO(2−1) data (left), models (center), and (data-model) residuals (right). The PVDs were extracted with a spatial width equivalent to a resolution element.

a factor of 4 to mitigate the impact of pixel-to-pixel correlation in the minimization of χ^2. I fit three dynamical models across 55 frequency channels in the NGC 5193 data cube that correspond to velocities of $|v_{\rm LOS} - v_{\rm sys}| \leq \sim 280\,{\rm km\,s^{-1}}$. After block-averaging the model and data cubes, the elliptical spatial region contains 58 pixels per channel, or a total of 3190 data points in the entire model fit.

I present three dynamical models (D,E,F) for the NGC 5193 data cube in Table 6.2. As in the case of NGC 4786, these dynamical models used three unique host galaxy MGEs that

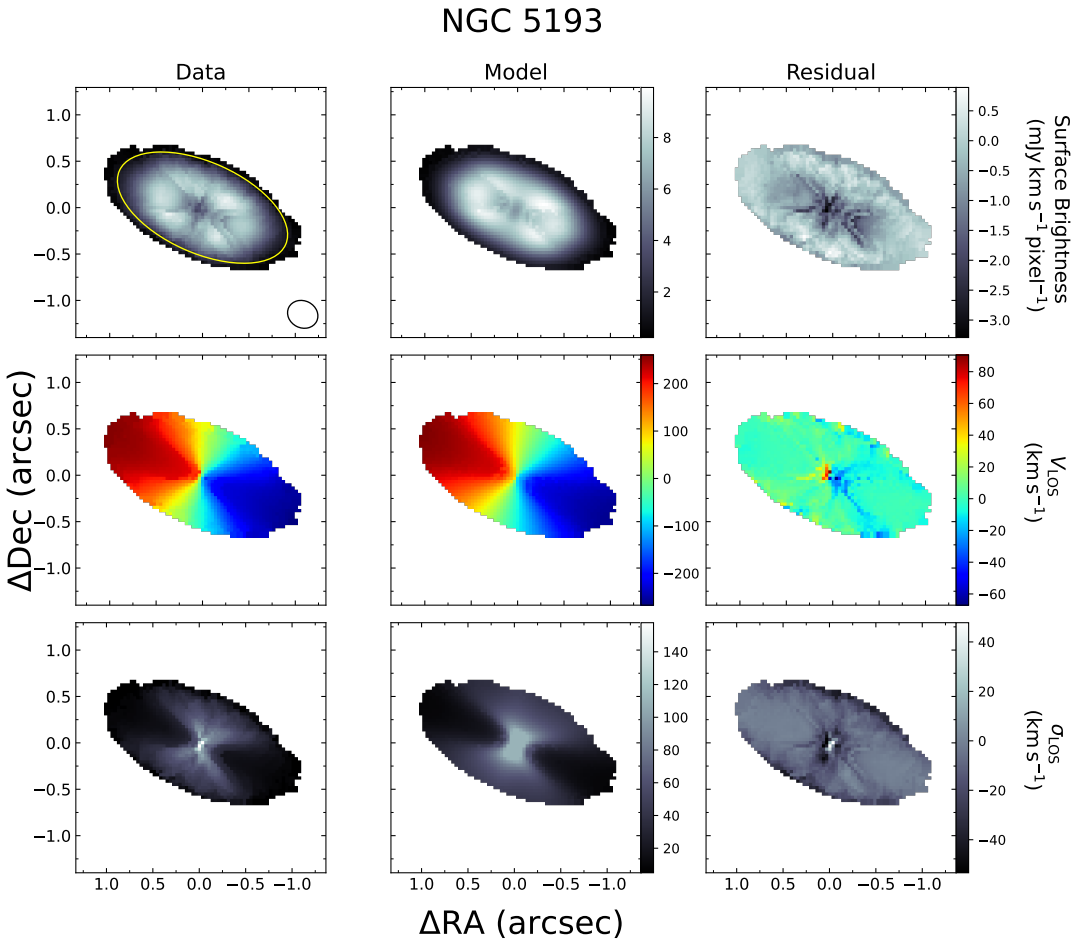

Figure 6.5 Moment maps for NGC 5193 constructed from the ALMA CO(2−1) data cube (left) and its fiducial model (center). Shown are maps of moments 0, 1, and 2, corresponding to surface brightness, LOS velocity $v_{\rm LOS}$, and LOS velocity dispersion $\sigma_{\rm LOS}$. The units for the surface brightness map are mJy km s^{-1} pixel^{-1}, and the units for the $v_{\rm LOS}$ and $\sigma_{\rm LOS}$ maps are km s^{-1}. The systemic velocity of 3705 km s^{-1} estimated from the dynamical models has been removed from $v_{\rm LOS}$. Maps of (data-model) residuals are shown in the rightmost column. The coordinate system is oriented such that $+x$ corresponds to East and $+y$ corresponds to North. While the line profile fits have been determined at each pixel of the full disk, the elliptical fitting region used in calculating χ^2 is denoted in the top left panel with a yellow ellipse. The synthesized beam is represented by an open ellipse in the bottom left corner of the same image.

treat the effects of the dust on the stellar light differently. Dynamical models D-F yield a range of $M_{\rm BH} = (1.4 - 2.9) \times 10^8\,M_\odot$, $\Upsilon_H = 1.46 - 1.69$, $\sigma_0 = 3.1 - 6.7\,{\rm km\,s^{-1}}$, and $F_0 = 1.14 - 1.16$ with $\chi^2_\nu = 2.096 - 2.541$ over 3181 degrees of freedom. While the models are generally successful at reproducing the observed kinematics over a majority of the disk,

a formally acceptable fit would achieve $\chi^2_\nu \leq 1.042$ assuming a level of significance of 0.05. The dynamically determined Υ_H values are higher than the expected Υ_H from single stellar population models, and the σ_0 values are small and are less than the channel spacing in the data cube. The range in F_0 is close to unity, though a lack of central CO emission is noticeable in the data visualizations. The major axis PVD, moment maps, and CO line profiles that compare the data and the best-fit model (model F), are shown in Figures 6.4, 6.5, and 6.6. The PVDs and moment maps show that model F emulates the observed PVD structure and disk kinematics over nearly the full extent of the disk. Similarly to NGC 4786, the most noticeable differences are in the central parts of the disk, as the data appears to be more CO-faint than the model. Additionally, the observed line profiles seen in Figure 6.6 extracted near the center of the disk show complex and asymmetric structure that the model cannot fully describe, as channel-to-channel variations in the amplitudes of the data line profiles are not entirely reproduced, although model F does generally capture their overall shapes well.

I performed a Monte Carlo simulation to determine the statistical uncertainty of the measurement. I created 100 realizations of model F by adding Gaussian noise. Then, I optimized each realization to produce a new estimate of $M_{\rm BH}$ and create a distribution. The distribution of $M_{\rm BH}$ was centered around a mean of $1.4 \times 10^8\,M_\odot$, and had a standard deviation of $0.03 \times 10^8\,M_\odot$, or 2% of the mean. The standard deviation of all other free parameters determined by this simulation are listed under the results of model F in Table 6.2.

6.4.1 Error Budget of the Mass Measurement

I carried out the same systematic tests that were performed for NGC 4786 described in Section 5.4.1 with model F as the NGC 5193 fiducial model. As was the case for NGC 4786, the largest shifts in $M_{\rm BH}$ occur in the systematic tests that involve changing the host

	NGC 5193	
Systematic Test	$M_{\rm BH,new}(10^8\,M_\odot)$	$\Delta M_{\rm BH}$ (%)
Radial motion	1.4	0%
Turbulent velocity dispersion	1.5	+7%
Fit region	1.3	−7%
Gas mass	1.3	−7%
Block-averaging factor	1.4	0%
Oversampling factor	1.5	+7%
Input flux map	1.6	+13%

Table 6.3 Results of the systematic tests performed on the fiducial dynamical model for NGC 5193, not including tests that involved changes to the host galaxy MGEs. I list the new value of $M_{\rm BH}$ that the optimization converged to, as well as the percent change from the BH masses determined for the fiducial model.

galaxy model to account for extinction. For NGC 5193, the dynamical model using the unmasked MGE converged to an SMBH mass of $M_{\rm BH} = 1.5 \times 10^8\,M_\odot$, only 7% higher than when using the fiducial model's dust-corrected MGE, but a large factor of 2 increase to $M_{\rm BH} = 2.9 \times 10^8\,M_\odot$ is observed when using the dust-masked MGE. The dust-corrected MGE model is the best estimate of the intrinsic host galaxy profile. The results of all the other systematic tests that did not involve changes to the host galaxy component are presented in Table 6.3. The final test of setting $M_{\rm BH} = 0\,M_\odot$ in the dynamical model resulted in the model fit yielding a much higher $\chi^2_\nu = 2.978$ and a higher $\Upsilon_H = 1.58\,M_\odot/L_\odot$. This shows that $M_{\rm BH} = 0\,M_\odot$ is highly disfavored.

The tests highlight a clear degeneracy between the BH and stellar mass components in the dynamical models of NGC 5193. After adding the systematic uncertainties associated with the extinction correction in quadrature with the uncertainties associated with the systematic tests in Table 6.3, the final measured range in $M_{\rm BH}$ for NGC 5193 is

$$(M_{\rm BH}/10^8\,M_\odot) = 1.4 \pm 0.03\,[1\sigma\,\text{statistical}]\,^{+1.5}_{-0.1}\,[\text{systematic}] \pm 0.1\,[\text{distance}]. \tag{6.1}$$

6.4.2 The Black Hole Sphere of Influence

I determined a range for $r_{\rm SOI}$ by determining the radii in each of the dynamical models where the stellar and SMBH masses were equal. I found that $r_{\rm SOI}$ is between 11 pc ($0\farcs05$) and 26 pc ($0\farcs12$), which is well below the resolution limit of $\sim$69 pc ($0\farcs31$). When comparing the $r_{\rm SOI}$ values to the average ALMA beam size, as was done for NGC 4786, I find $\xi = (0.3 - 0.8)$.

There is nearly a factor of 2 discrepancy in the measured BH mass from the dynamical models. Quantifying the uncertainty in the inner slope of the NGC 5193 host galaxy mass profile is challenging with the central dust disk, and because the projected BH SOI is unresolved, the range in the measured $M_{\rm BH}$ is broad. With the BH SOI unresolved by a factor of 2 to 3, the BH mass is a smaller fraction of the total enclosed mass on scales comparable to the observation's resolution limit, and thus, the measurements are even more sensitive to the differences among the stellar mass models. Similarly to NGC 4786, the stellar mass models for NGC 5193 shown in Figure 6.7 are well-matched at the edge of the disk, but are noticeably different within the central ALMA resolution element. Moreover, as in the case of NGC 4786, the unmasked MGE displays an unphysical bump at small radii in the $M_\star(r)$ profile, which is attributed to the aforementioned reasons provided for NGC 4786.

Additionally, there is evidence of a central hole in the CO distribution of NGC 5193. This is highlighted in the surface brightness map shown in Figure 6.5, as residuals between the data and best-fit model highlight prominent discrepancies at the center of each disk. Furthermore, the $J - H$ map of NGC 5193 shows additional evidence of a central hole in the circumnuclear disk. As was shown for NGC 6861 (Kabasares et al., 2022), an absence of kinematic tracers within the projected SMBH $r_{\rm SOI}$ can fundamentally limit the precision of an $M_{\rm BH}$ measurement.

6.4.3 Comparison to Predictions from BH Scaling Relations

I compare my measured range of $M_{\rm BH}$ in NGC 5193 to predictions from the local SMBH-host galaxy scaling relations presented by Kormendy and Ho (2013). The $M_{\rm BH} - \sigma_\star$ relation predicts $3.4 \times 10^8\,M_\odot$ when using $\sigma_\star = 205\,{\rm km\,s^{-1}}$ from Hyperleda (Makarov et al., 2014). Thus, the higher end of my dynamically measured range of $M_{\rm BH}$ is contained within the scatter of this relation. For the $M_{\rm BH} - L_{{\rm bulge},K}$ relation, I determined the total luminosity of each component in the dust-corrected MGE and converted it into an estimated K-band luminosity. I found $L_{{\rm bulge},K} = 1.3 \times 10^{11}\,L_\odot$, which predicts $M_{\rm BH} = 7.4 \times 10^8\,M_\odot$, so the measured $M_{\rm BH}$ range falls well below this prediction. Finally, I converted the total H-band luminosity into an estimate of the spheroidal component's mass by multiplying this luminosity by the fiducial model's $\Upsilon_H = 1.46$. As noted in Section 5.5.2, this should be viewed as a rough approximation to the true mass of the spheroidal component and is likely an overestimate. Indeed, the estimated $M_{\rm bulge} = 1.7 \times 10^{11}\,M_\odot$ predicts $M_{\rm BH} = 9.0 \times 10^8\,M_\odot$ and far exceeds the range in $M_{\rm BH}$ I derived.

6.4.4 Conclusion

I present the first dynamical mass measurement of the SMBH in NGC 5193. With a set of host galaxy models accounting for a range in dust attenuation and numerous systematic tests, I constrained $M_{\rm BH}$ to be within a range of

$$(M_{\rm BH}/10^8\,M_\odot) = 1.4 \pm 0.03\,[1\sigma\,{\rm statistical}]\,^{+1.5}_{-0.1}\,[{\rm systematic}] \pm 0.1\,[{\rm distance}].$$

A strong degeneracy in the stellar and SMBH mass components in the dynamical models was observed and is attributed to a deficit of CO in the central parts of the disk as well as the observations not resolving the projected $r_{\rm SOI}$. Regardless, dynamical models that include a

central SMBH fit the observed gas kinematics better than models that do not. The measured range in $M_{\rm BH}$ is broadly consistent with the $M_{\rm BH} - \sigma_\star$ relation presented by Kormendy and Ho (2013) but falls below the predictions from the $M_{\rm BH} - L_{{\rm bulge},K}$ and $M_{\rm BH} - M_{\rm bulge}$ relations. To summarize, this measurement highlights the importance of creating multiple host galaxy models to assess the sensitivity of $M_{\rm BH}$ on the choice of host galaxy model, while also demonstrating ALMA's unique capability to map out the kinematics of circumnuclear disks in great detail and provide meaningful constraints on $M_{\rm BH}$.

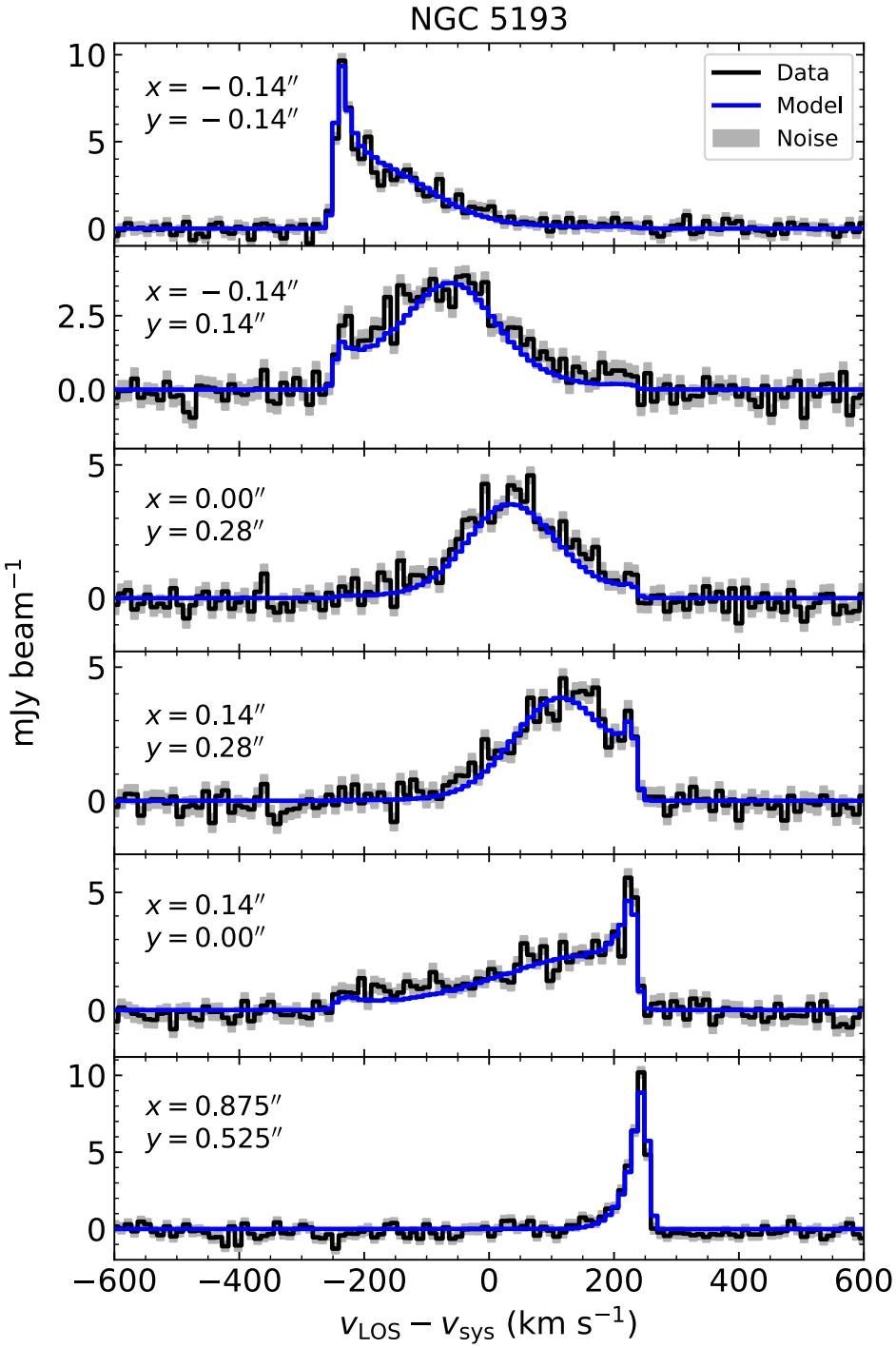

Figure 6.6 CO line profiles extracted from six spatial locations within the block-averaged NGC 5193 data cube, along with the fiducial model (model C). The x and y positions are given relative to the disk dynamical center, with $+y$ indicating North and $+x$ indicating East. The gray shaded area represents values in the range of data $\pm 1\sigma$, where the 1σ value is from the 3D noise model used in the χ^2 optimization.

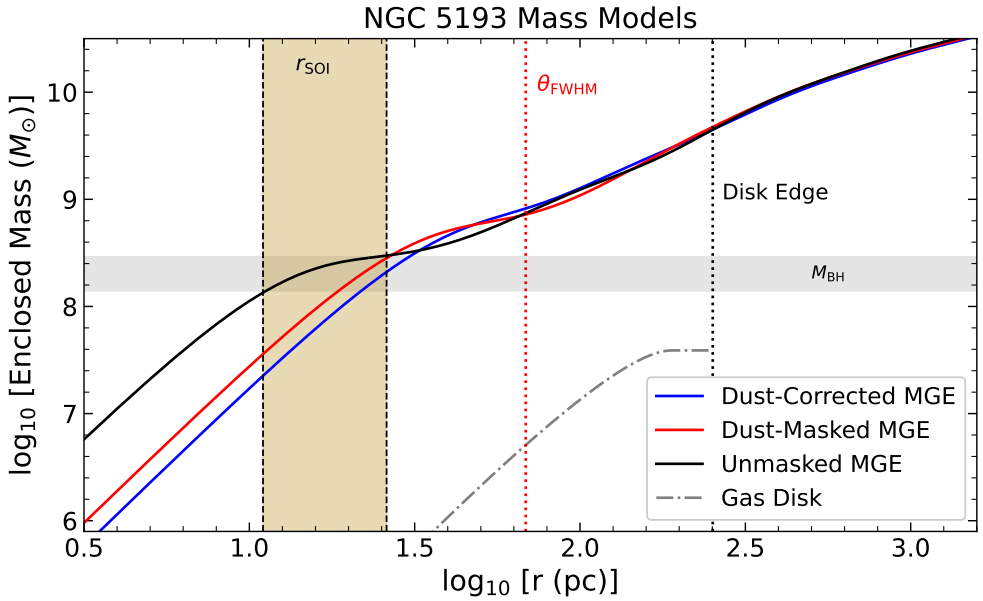

Figure 6.7 Plot of $\log_{10} M_\star(r)$ vs. $\log_{10} r$ in NGC 5193 for the three host galaxy MGE models and gas mass profile used. $M_\star(r)$ is calculated via $M_\star(r) = rv^2_{\star,\mathrm{MGE}}/G$, where the $v_{\star,\mathrm{MGE}}$ values have been scaled by their respective $\sqrt{\Upsilon_H}$ values listed in Table 6.2. $M_{\mathrm{gas}}(r)$ is calculated via: rv^2_{gas}/G. The red dotted line indicates the angular resolution of the observation, whereas the black dotted line represents the outer edge of the dust disk as measured along the major axis. The gray shaded region indicates the range of M_{BH} determined by the dynamical models using the different input MGE models, while the yellow shaded region enclosed within the black dotted lines indicate the range of the radius of the black hole sphere of influence, r_{SOI}. I have defined r_{SOI} to be the radius where the stellar and BH masses of a given dynamical model are equal.

Chapter 7

Preliminary Results for NGC 3245, NGC 4435, NGC 5838, and ESO 208-G21

7.1 Overview

The following chapter presents first stage dynamical modeling results of the ETGs NGC 3245, NGC 4435, NGC 5838, and ESO 208-G21. Each target will be presented as its own section. The contents of each section include the observational properties of the HST and ALMA data used in the dynamical modeling process. In addition, I provide information on the host galaxy MGEs created for each galaxy. Finally, I conclude each section with a discussion on the implications of the initial findings.

7.2 NGC 3245

NGC 3245 is an S0 galaxy with a low luminosity active nucleus located at a luminosity distance of approximately 20.9 Mpc (Tonry et al., 2001). The SMBH mass in this galaxy

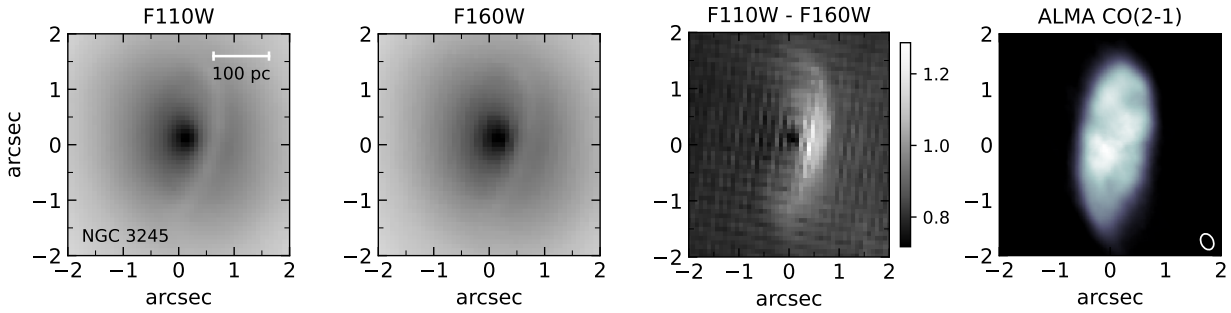

Figure 7.1 HST F110W (J-band), F160W (H-band), F110W $-$ F160W ($J-H$), and ALMA CO(2$-$1) images of NGC 3245 showing the co-spatial alignment of the gas and dust. The ALMA intensity maps were created by summing channels in the data cubes that displayed visible CO emission. Pixels with emission were identified with an automatically generated mask by the `3DBarolo` program (Di Teodoro and Fraternali, 2015). In the $J-H$ maps, light regions correspond to redder colors and dark regions are bluer than the surrounding starlight. North is up and East is to the left in each image.

was measured by Barth et al. (2001) to be $(2.1 \pm 0.5) \times 10^8\,M_\odot$ using ionized gas-dynamical models with data from HST's Space Telescope Imaging Spectrograph (STIS), making it a prime target to compare ionized and molecular gas-dynamical modeling techniques.

7.2.1 ALMA Data

I used ALMA Cycle 5 CO(2$-$1) observations of NGC 3245. The data were taken as part of program 2017.1.00301.S on 28 December 2017, and NGC 3245 was observed for approximately 42 minutes. The array configuration had a maximum baseline of 2516 m. For the CO(2$-$1) line, the observation consisted of 480 spectral channels spanning $228.582 - 230.453$ GHz with a frequency resolution of 3.904 GHz. In order to separate the continuum and emission line features, the continuum contributions were first subtracted in the uv-plane. The data were reduced and calibrated in CASA version 5.1.1 with a Briggs weighting of $r = 0.5$ and were subsequently imaged into a data cube with velocity channel widths of $5\,\mathrm{km\,s^{-1}}$. A pixel size of $0\farcs025$ was chosen to properly sample the synthesized beam's minor

axis. The synthesized beam has a major axis FWHM of 0.″30, a minor axis FWHM of 0.″22, and a position angle of 26.8° East of North.

7.2.2 HST Data and Host Galaxy Model

k	$\log_{10} I_{H,k}(L_\odot\,\mathrm{pc}^{-2})$	σ'_k (arcsec)	q'_k
	NGC 3245 (Dust-Masked MGE)		
1	5.552	0.128	0.599
2	4.647	0.340	0.981
3	4.743	0.555	0.870
4	4.508	1.026	0.982
5	4.096	1.981	0.736
6	4.005	3.387	0.705
7	3.473	9.673	0.520
8	2.895	29.874	0.523
9	1.574	265.707	0.946
10	1.648	282.888	0.520
11	1.577	261.298	1.000

Table 7.1 Dust-masked MGE solution for NGC 3245. The first column is the component number, the second is the central surface brightness corrected for Galactic extinction and assuming an absolute solar magnitude of $M_{\odot,H} = 3.37$ mag (Willmer, 2018), the third is the Gaussian standard deviation along the major axis, and the fourth is the axial ratio. Primes indicate projected quantities.

To build a host galaxy model for NGC 3245, J and H-band images from HST WFC3 were used. The observations were taken as part of HST program 15909 (PI: Boizelle). For the H-band, a four-point dither pattern was employed to optimally sample the PSF, with each observation lasting 299 seconds in duration. The J-band observations employed a two-point dither pattern lasting 128 seconds each and were drizzled and aligned to the H-band images with a pixel scale of 0.″08 in order to construct $J-H$ color maps. These color maps were used to identify regions of noticeable dust attenuation on the host galaxy's starlight. The H, J and $J-H$ maps are presented in Figure 7.1 along with the ALMA CO(2−1) intensity map.

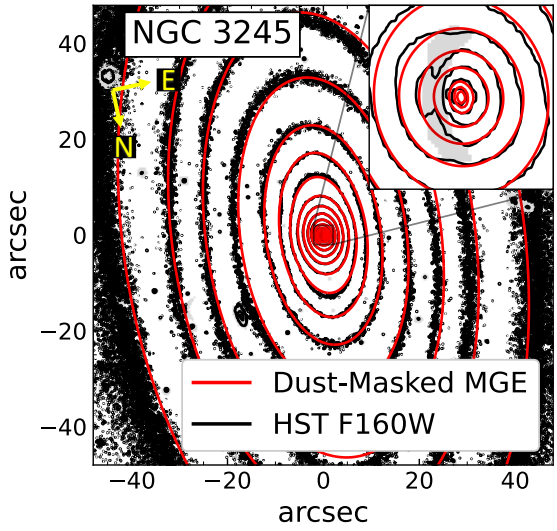

Figure 7.2 2D isophote map comparing the observed HST WFC3 F160W isophotes to those of the dust-masked MGE of NGC 3245. Black contours represent isophotes from the F160W images, while red contours are for the MGE models. For each image, the central $\approx 100'' \times 100''$ region is displayed with an inset of the innermost $3\farcs5 \times 3\farcs5$ region in the top right corner. The dust-masked region is shown in gray in the inset.

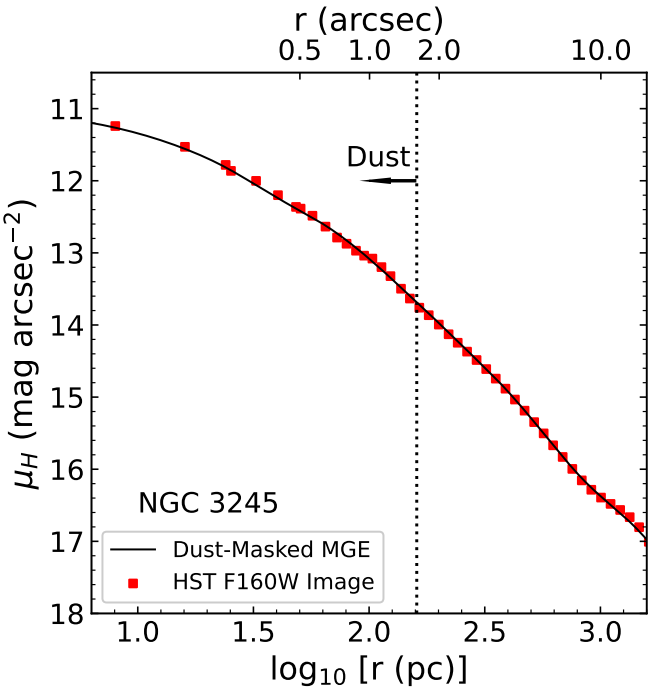

Figure 7.3 NGC 3245 major axis surface brightness profile of the dust-corrected MGE model. The red points are the observed values from the H-band image. The outer edge of the dust disk is marked with a vertical dashed line.

Using the $J-H$ color map, a mask identifying regions where $J-H > 0.88$ mag was constructed. This map was used as an input in the `GALFIT` galaxy-fitting program (Peng et al., 2002) along with `TinyTim` (Krist and Hook, 2004) HST H-band PSF models in order to parameterize the NGC 3245 2D surface brightness with a sum of concentric Gaussian functions. Given that NGC 3245 is known to contain a low-luminosity AGN at its center (Barth et al., 2001), I incorporated a PSF model in `GALFIT` to include with the concentric Gaussian components, and removed it from the model before deprojecting the Gaussian components. The MGE components are shown in Table 7.1. A comparison of the data and MGE model isophotes and surface brightness profiles is shown in Figures 7.2 and 7.3.

7.2.3 Preliminary Dynamical Modeling Results

Host Galaxy Model	$r_{\rm fit}$	$M_{\rm BH}$ ($10^8\,M_\odot$)	Υ_H ($M_\odot/L_\odot$)	i (°)	Γ (°)	σ_0 ($\rm km\,s^{-1}$)	$v_{\rm sys}$ ($\rm km\,s^{-1}$)	F_0	χ^2_ν
Dust-Masked MGE	0.″5	1.4	1.5	64.4	175.6	12.9	1326.8	0.96	3.322
$v_{\rm ext}$	1.″6	0.9	···	63.3	174.9	15.2	1325.5	0.95	4.010

Table 7.2 Best-fit parameter values obtained by fitting thin disk dynamical models to the NGC 3245 data cube. This model has 75,456 degrees of freedom when fitting over an ellipse with $r_{\rm fit} = 0.''5$ and an axial ratio of $q = 0.467$. There are 798,888 degrees of freedom when $r_{\rm fit} = 1.''6$. The major axis PA, Γ, is measured east of north for the receding side of the disk. I found the dynamical center of the fiducial model to be at RA=$10^{\rm h}27^{\rm m}18.3846^{\rm s}$, Dec=+28°30′26.″598 for NGC 3245. The observed redshift, $z_{\rm obs}$, is used in the dynamical models as a proxy for the systemic velocity of the disk, $v_{\rm sys}$, in the barycentric frame via the relation: $v_{\rm sys} = cz_{\rm obs}$ and is used to translate the model velocities to observed frequency units.

I optimized two dynamical models to the NGC 3245 data cube. One dynamical model incorporated the dust-masked MGE model for the host galaxy component, whereas the other used the nonparametric $v_{\rm ext}$ model. Using the dust-masked MGE, I initially tried fitting models over the entire disk, but found that these models were a statistically poor fit to the data with $\chi^2_\nu > 6$. Therefore, I opted to fit models over an elliptical spatial region with a major axis of $r_{\rm fit} = 0.''5$ and an axial ratio of $q = 0.467$, based on measurements of the optical dust disk in the HST images. Also, I chose to not block-average the dynamical

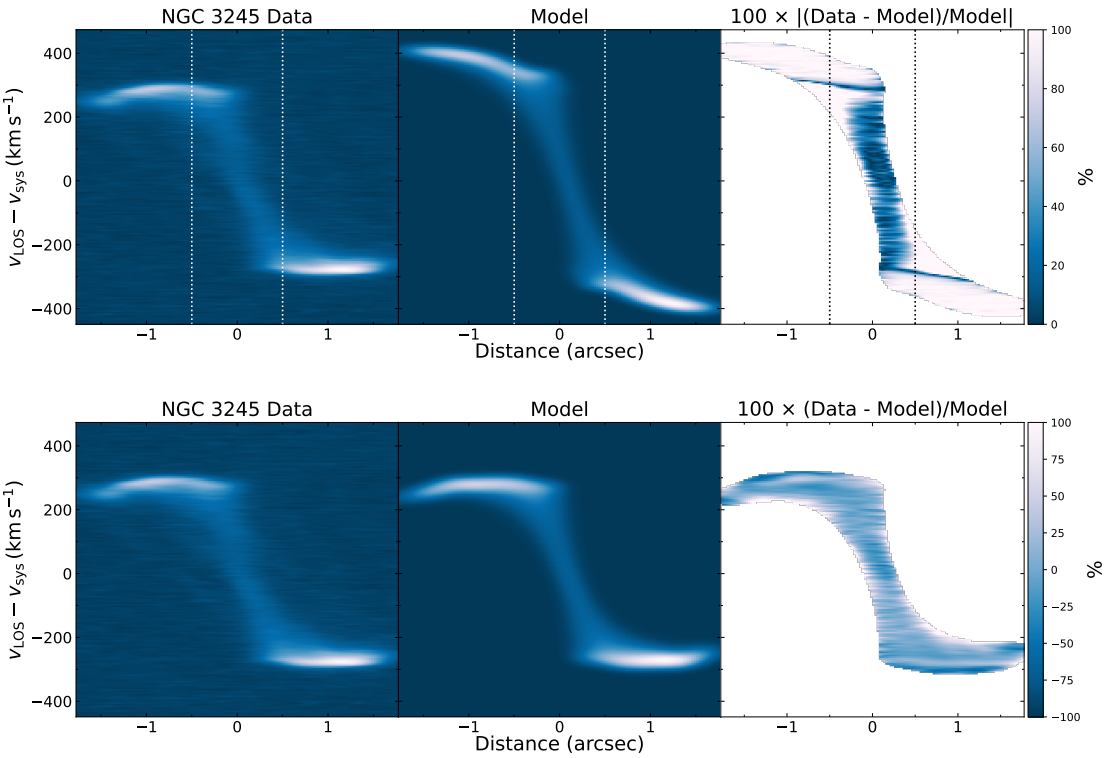

Figure 7.4 PVDs along the major axes of the NGC 3245 ALMA data and the best-fit dynamical model that uses a dust-masked MGE for the host galaxy component. Columns show ALMA CO(2−1) data (left), models (center), and fractional residuals (right). The top panel features the dynamical model that uses a dust-masked MGE as the host galaxy component, whereas the dynamical model in the bottom panel uses the $v_{\rm ext}$ nonparametric model. The dotted lines represent the region where dynamical models were fit to the ALMA data along the major axis. The PVDs were extracted with a spatial width equivalent to a resolution element.

model or the data when calculating χ^2_ν with the intention of preserving the angular resolution of the pixels. The higher the block-averaging factor, the more the dynamical models lose their ability to constrain $M_{\rm BH}$. Furthermore, Barth et al. (2001) also chose to fit models over a similar region, given that data points further out appeared to deviate from circular rotation. Over this smaller elliptical region, the molecular gas-dynamical model returned $M_{\rm BH} = 1.4 \times 10^8\,M_\odot$, but the fit still remains statistically inadequate with $\chi^2_\nu = 3.322$. This measured $M_{\rm BH}$ value is slightly outside the 1σ confidence interval of $(1.6 - 2.6) \times 10^8\,M_\odot$ reported by Barth et al. (2001). I extracted data and model PVDs and show them in Figure 7.4. There is a significant discrepancy in the structure of the PVDs, with the model

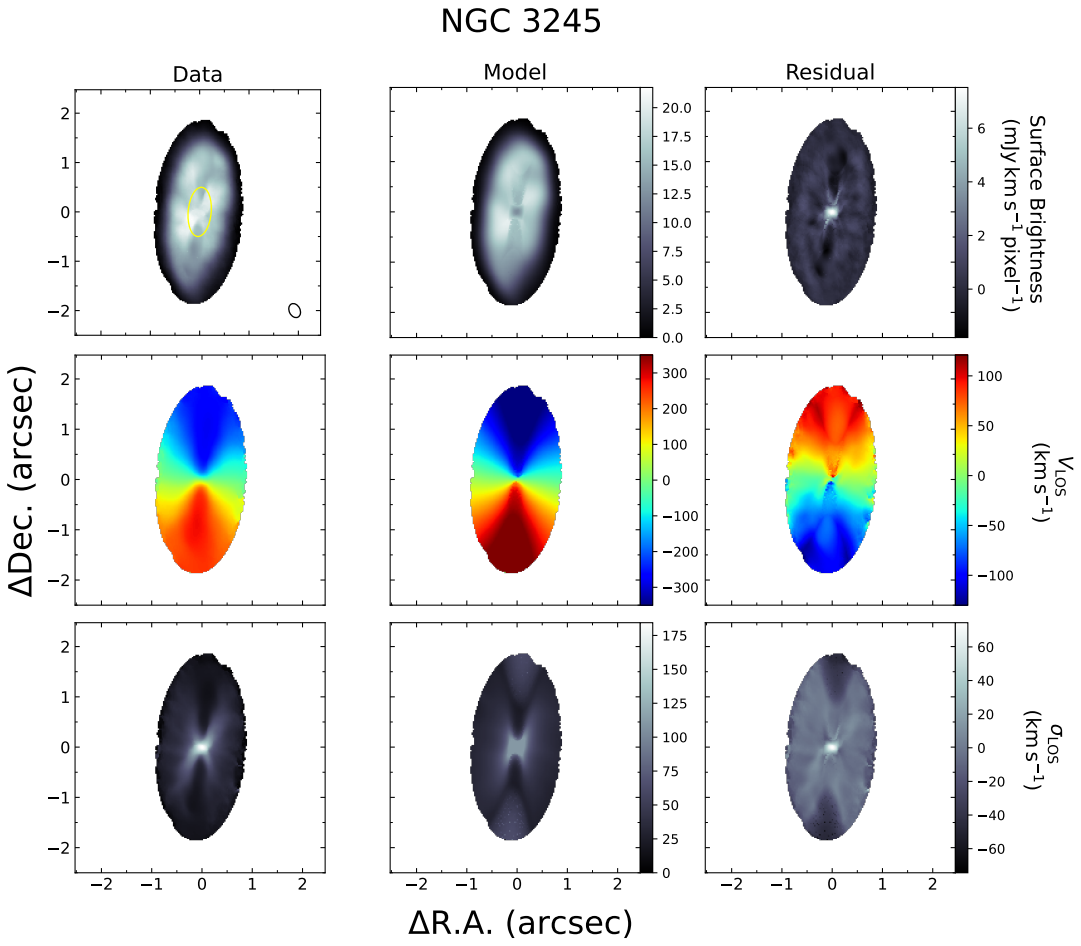

Figure 7.5 Moment maps for NGC 3245 constructed from the ALMA CO(2−1) data cube (left) and its fiducial model. The dynamical model uses the dust-masked MGE for the host galaxy component. Overall, the model is a poor fit to the data outside the elliptical spatial region where the fit was optimized.

velocities increasing at larger radii as opposed to remaining relatively flat and starting to decrease towards the disk edge as observed in the data. The data and model moment maps in Figure 7.5 also show observable disparities. Large ($> 50\,\mathrm{km\,s^{-1}}$) velocity residuals are seen in the v_{LOS} maps, particularly outside the region where models were optimized. In terms of the disk inclination angle, this particular dynamical model converges on $i = 64.3°$ and is similar to the result ($i = 63°$) found by Barth et al. (2001). Given the formally unacceptable fit to the ALMA data, the results from this initial dynamical model warrant a cautious interpretation.

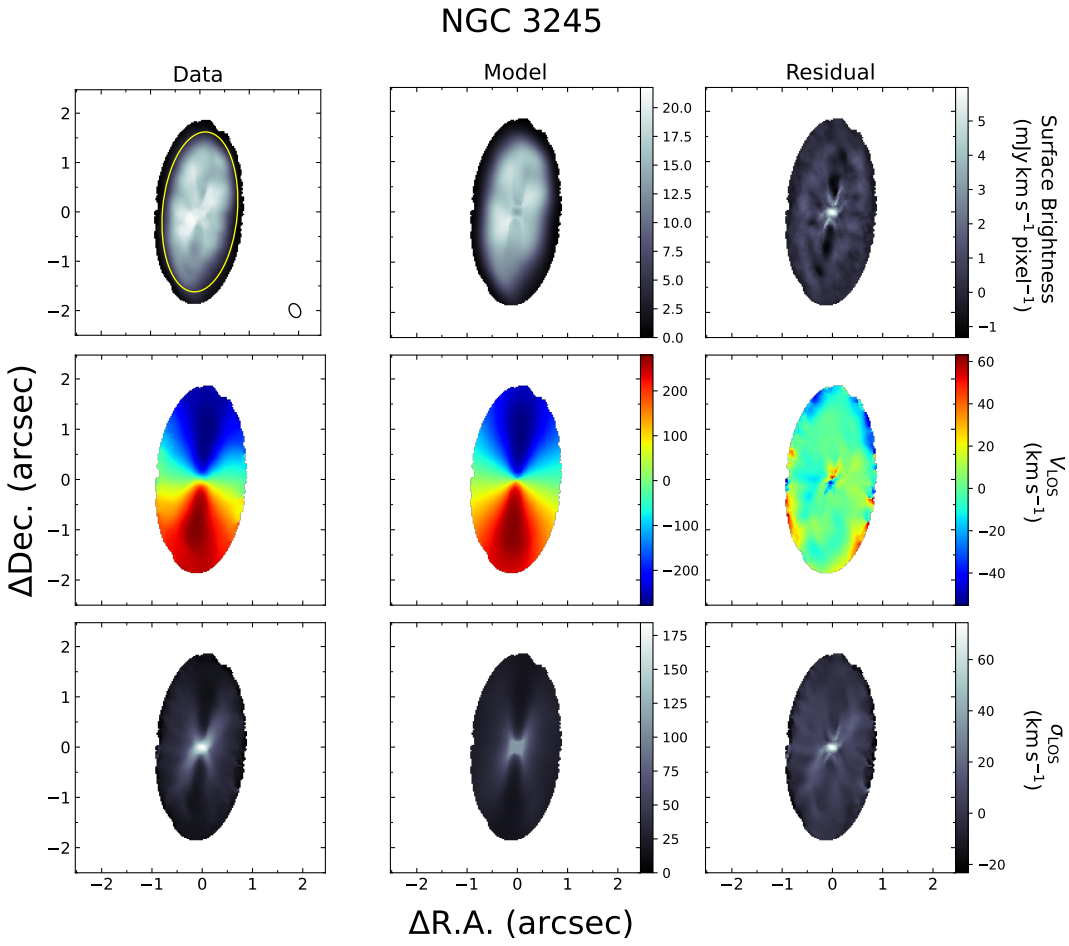

Figure 7.6 Same as Figure 7.5, but with the dynamical model that uses the nonparametric $v_{\rm ext}$ model as the host galaxy component.

To expand upon this initial fit, I also optimized a dynamical model using the nonparametric $v_{\rm ext}$ model for the host galaxy component. I carried out the model fit over the entire disk region in order to test whether a statistically superior model fit for the full disk was attainable. Although a majority of pixels are outside the projected $r_{\rm SOI}$, $M_{\rm BH}$ is not driven down to $0\,M_{\odot}$, but to $0.9 \times 10^{8}\,M_{\odot}$, a 35% decrease from the previous dynamical model. While the fit over the full disk converged on a statistically poor $\chi^2_{\nu} = 4.010$, the flexibility of the $v_{\rm ext}$ model led to some improvements in regard to reproducing observed features in the data. The bottom panel of Figure 7.4 shows the PVD of this dynamical model. Unlike the dynamical model that used the dust-masked MGE for the host galaxy component, the $v_{\rm ext}$ model is flexible enough to reproduce the overall shape of the observed PVD. While

noticeable discrepancies still remain, particularly in the model's velocity dispersion, one notable aspect of interest is that the decrease of LOS velocity towards the edge of the disk is emulated in the dynamical model. The moment maps are shown in Figure 7.6. The model $v_{\rm LOS}$ map emulates the observed velocity field over a majority of the disk, though the surface brightness and LOS velocity dispersion maps highlight some inconsistencies. Prominent negative residuals are apparent in the surface brightness maps, indicating that the model is brighter. In addition, large positive residuals are observed in the LOS velocity dispersion. These residuals could be attributed to a number of different factors such as inadequately incorporating beam smearing effects, a nonuniform distribution of the molecular gas, and genuine radial gradients in the gas's intrinsic turbulent velocity dispersion.

The gas disk in NGC 3245 exhibits complex kinematics that challenge the simplistic assumptions of the thin disk models, which primarily assume circular rotation. While using the $v_{\rm ext}$ model improves the overall model fit over the entire disk, it still cannot fully describe the observed data. Future dynamical models may need to incorporate more complex features, such as using a tilted ring model to account for the possibly warped nature of the disk, as well as incorporating non-circular motions in the construction of the initial LOS velocity field. Moreover, as noted by Barth et al. (2001), there is evidence of recent star formation in the disk and a mildly active nucleus is present. These elements introduce additional layers of complexity to the host galaxy modeling process. Nevertheless, NGC 3245 remains a compelling target given its previous ionized gas-dynamical modeling $M_{\rm BH}$ result, and thus future efforts should seek to derive meaningful constraints from the ALMA data if possible.

7.3 NGC 4435

NGC 4435 is a barred lenticular galaxy located at a distance of about 16.5 Mpc based on surface brightness fluctuation measurements (Tully et al., 2013). Coccato et al. (2006)

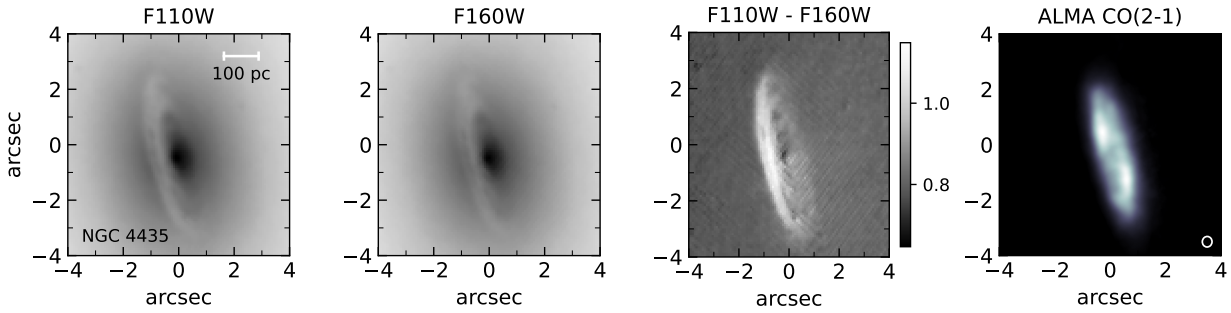

Figure 7.7 Same as Figure 7.1, but for NGC 4435.

obtained spectral data from HST STIS and used ionized-gas dynamical models to derive an upper limit of $M_{\rm BH} = 7.5 \times 10^6\,M_\odot$.

7.3.1 ALMA Data

NGC 4435 was observed on 19 January 2018 for 51 minutes and 18 September 2018 for 53 minutes as part of ALMA program 2017.1.00301.S with a maximum baseline of 1398 m. To detect the CO(2−1) line, the observation consisted of a spectral window that spanned between 228.962 − 230.834 GHz, with a frequency resolution of 3.904 MHz. The continuum of the measurement set was imaged using a Briggs weighting factor of $r = 0.5$. To isolate the CO(2−1) emission, the continuum contributions were first subtracted in the *uv*-plane. The continuum-subtracted visibility data were then imaged into a data cube with a channel spacing of $10\,{\rm km\,s^{-1}}$. The synthesized beam has a major axis FWHM of 0.″38, a minor axis FWHM of 0.″35, and a beam position angle of −3.9° measured East of North. The data cube has a spatial pixel scale of 0.″035.

7.3.2 HST Data and Host Galaxy Model

I used *J* and *H*-band images of NGC 4435 taken with HST WFC3 as part of HST program 15909 (PI: Boizelle). For the *H*-band, the observation used a 4-point dither pattern with

k	$\log_{10} I_{H,k}(L_\odot\,\mathrm{pc}^{-2})$	σ'_k (arcsec)	q'_k
	NGC 4435 (Dust-Masked MGE)		
1	5.386	0.109	0.410
2	4.702	0.482	0.999
3	4.384	1.404	0.728
4	4.153	2.639	0.705
5	3.919	4.696	0.757
6	3.397	14.260	0.410
7	2.413	30.445	0.466
8	2.591	17.360	0.880
9	2.081	40.686	0.866
10	1.221	137.585	0.410
11	1.818	201.080	0.999

Table 7.3 Same as Table 7.1, but for NGC 4435.

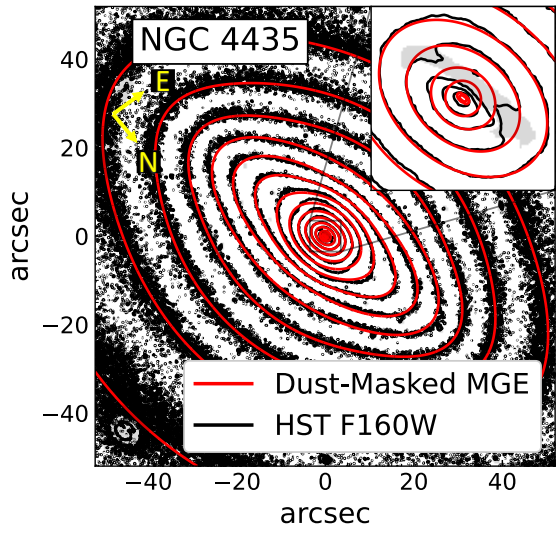

Figure 7.8 Same as Figure 7.2, but for NGC 4435. The innermost $3\farcs5 \times 3\farcs5$ region is shown in the inset.

4 separate exposures of 299 seconds each. Using `AstroDrizzle`, the images were drizzled and aligned to a pixel scale of $0\farcs08$. A 2-point dither pattern was used for the J-band with individual exposures lasting 174 seconds. The J-band images were drizzled and aligned to the H-band images. A $J-H$ color map was constructed and used to identify substantial dust attenuation on the central host galaxy light. The J, H, and $J-H$ images are shown in Figure 7.7 along with the ALMA intensity map. A dust mask which identified pixels with values of $J-H > 0.88$ mag was made and inputted in `GALFIT` to construct a dust-masked

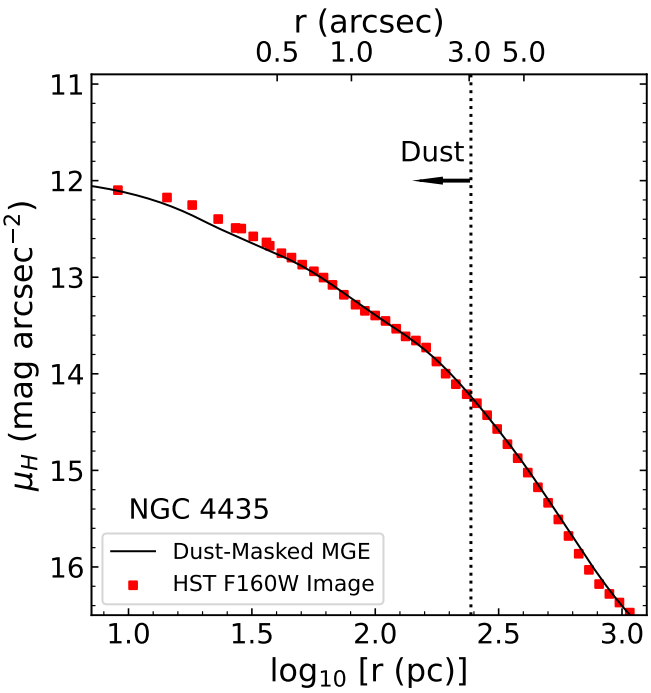

Figure 7.9 Same as Figure 7.3, but for NGC 4435.

MGE model for NGC 4435. The components of this MGE are presented in Table 7.3. A 2D isophote map for the H-band image and the dust-masked MGE model is displayed in Figure 7.8. The MGE isophotes are well-matched to the data's within the inner $100'' \times 100''$ of NGC 4435. Near the nucleus, the H-band isophotes become asymmetric and non-elliptical within the most reddened parts of the dust disk, which were masked out in the fit. The H-band major axis surface brightness distribution of the H-band image and the MGE are shown in Figure 7.9. Slight deviations between the model and data are seen in the innermost parts of the disk within the dust lane.

7.3.3 Preliminary Dynamical Modeling Results

I optimized two dynamical models to the NGC 4435 data cube. Results for both dynamical models are presented in Table 7.4. The differences between the models include the prescription for the host galaxy component of NGC 4435 and the elliptical spatial region where the

Host Galaxy Model	$r_{\rm fit}$	$M_{\rm BH}$ ($10^8\,M_\odot$)	Υ_H ($M_\odot/L_\odot$)	i (°)	Γ (°)	σ_0 (km s^{-1})	$v_{\rm sys}$ (km s^{-1})	F_0	χ^2_ν
Dust-Masked MGE	1″	0.5	0.99	76.6	191.3	16.9	783.6	0.98	14.231
$v_{\rm ext}$	3″	0.8	···	74.1	190.6	14.3	786.8	0.95	20.709

Table 7.4 Best-fit parameter values obtained by fitting thin disk dynamical models to the NGC 4435 data cube. This model has 45,252 degrees of freedom when fitting to an elliptical spatial region with $r_{\rm fit} = 1''$ and an axial ratio of $q = 0.34$. There are 362,963 degrees of freedom when $r_{\rm fit} = 3''$. I found the dynamical center of the fiducial model to be at RA=12$^{\rm h}$27$^{\rm m}$40.5025$^{\rm s}$, Dec=+13°04′44.″334 for NGC 4435.

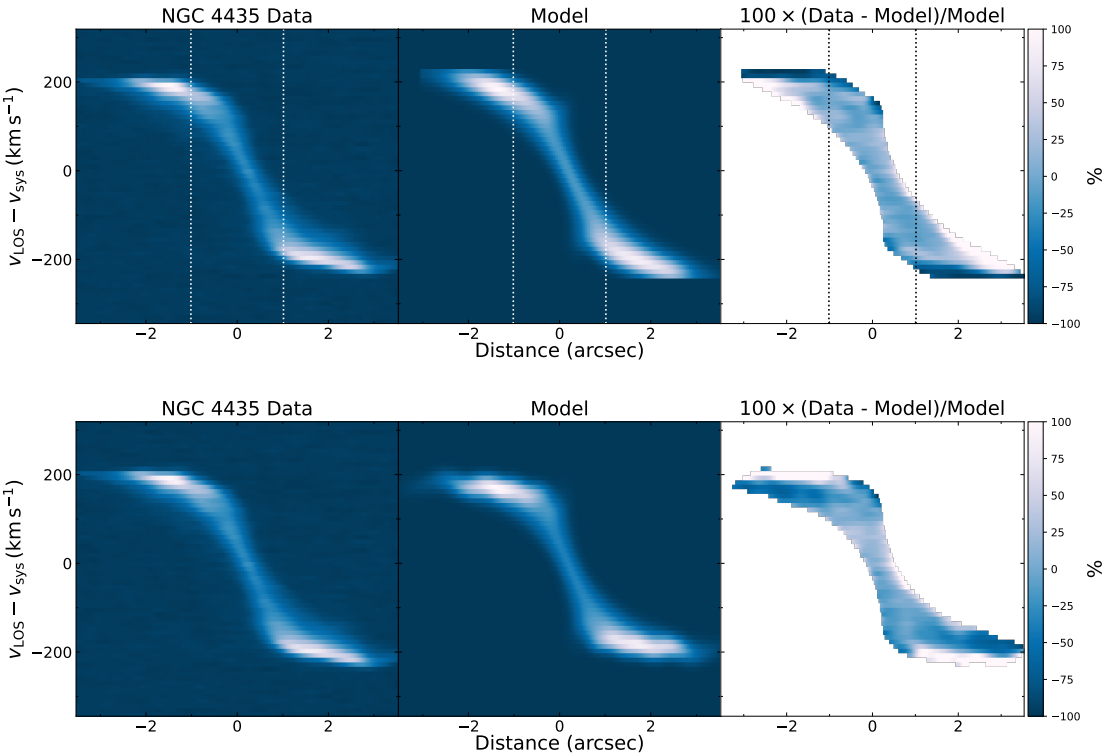

Figure 7.10 Same as Figure 7.4, but for NGC 4435.

models were optimized. When using the dust-masked MGE as the host galaxy component, I chose to fit models to the inner 1″ of the disk. The gas kinematics beyond this radius are dominated by the gravitational potential of the host galaxy, as opposed to the SMBH. Additionally, I chose to not block-average models when minimizing χ^2_ν to preserve the maximum angular resolution of the pixels. Block-averaging pixels limits the model's ability to constrain $M_{\rm BH}$, and given a large ALMA synthesized beam that has a geometric FWHM of 0.″365, retaining sensitivity to $M_{\rm BH}$ is critical, especially given the supposed undermassive

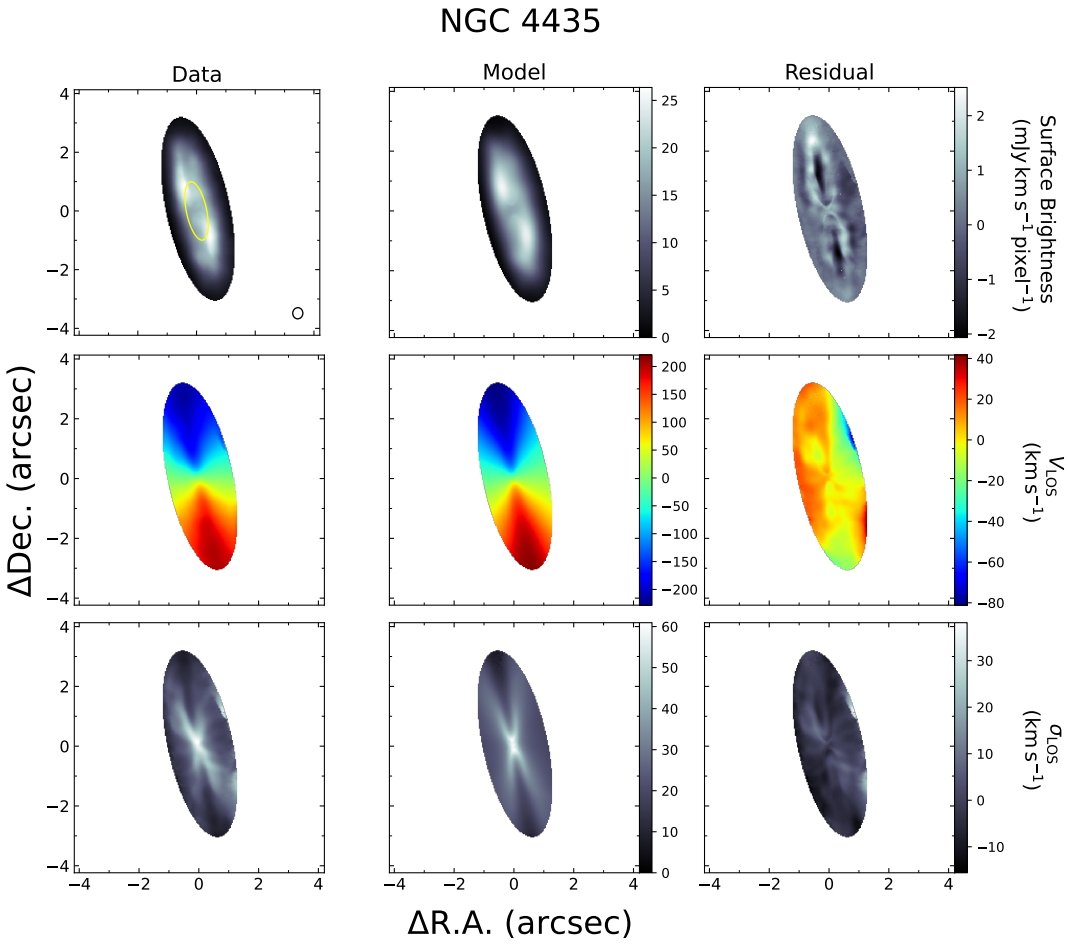

Figure 7.11 Same as Figure 7.5, but for NGC 4435.

SMBH (Coccato et al., 2006). The optimization returned a statistically poor $\chi^2_\nu = 14.231$, so the results should be viewed cautiously. In terms of the disk's inclination angle, my model finds $i = 76.6°$, which is close to the inclination angle of $i = 70° \pm 2°$ from the ionized gas-dynamical models reported by Coccato et al. (2006). Given the limited spatial coverage provided by long-slit spectrographs, Coccato et al. (2006) constrained the inclination by assuming the dust lanes are a good tracer of the orientation of the gas disk and that the dust lanes are circularly symmetric. Their ellipse fitting procedure provided the initial estimate of $i = 70° \pm 2°$. It should also be noted that they also explored the uncertainty in $M_{\rm BH}$ due to the orientation of the gas disk by building a grid of models that explored the space of the

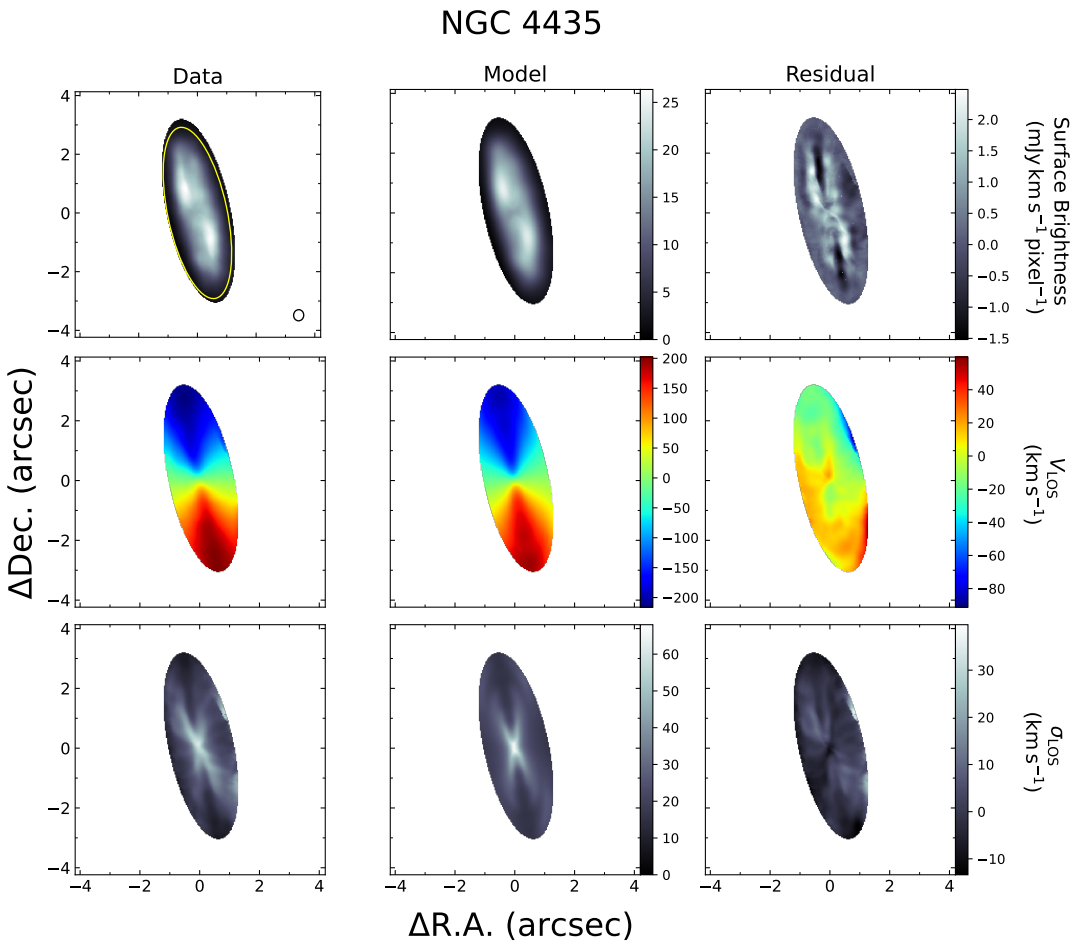

Figure 7.12 Same as Figure 7.11, but with the dynamical model that uses the nonparametric $v_{\rm ext}$ model as the host galaxy component.

inclination angle, and determined a range of $i = 75° \pm 3°$, which is more consistent with my model's value.

For $M_{\rm BH}$, Coccato et al. (2006) determined an upper limit of $7.5 \times 10^6\,M_\odot$ at the 3σ level when using a host galaxy model derived from HST F814W (I-band) images from the Wide Field Planetary Camera 2 (WFPC2). Besides this, it is also important to acknowledge that they attempted to correct for the effects of dust absorption on the host galaxy starlight by incorporating WFPC2 F450W (B-band) data and creating $B-I$ maps. By assuming that the intrinsic galaxy color varies linearly with radius, they generated a map of I-band extinction, A_I, to correct the I-band image and generate an I-band MGE model. Nevertheless, dust

is still clearly visible in both the longer wavelength F110W and F160W images shown in Figure 7.7, and the correction method applied by Coccato et al. (2006) assumed a foreground screen model for the dust, which can underestimate the intrinsic extinction (Boizelle et al., 2019). Using the dust-masked H-band MGE model I created for the host galaxy component, the molecular gas-dynamical model converged on a value of $0.5 \times 10^8\,M_\odot$, nearly a full order of magnitude larger than the upper limit provided by Coccato et al. (2006). The result is surprising for multiple reasons. First, given that the Coccato et al. (2006) I-band MGE model most likely underestimates the intrinsic stellar light distribution (and correspondingly, the stellar mass distribution), their estimate of $M_{\rm BH}$ should be taken as an overestimate, and they acknowledge it as such. Additionally, using their adopted central velocity dispersion of $\sigma_\star = 157\,{\rm km\,s^{-1}}$ in the Kormendy and Ho (2013) $M_{\rm BH} - \sigma_\star$ relation yields $M_{\rm BH} = 1.0 \times 10^8\,M_\odot$. This is broadly consistent with my dynamically measured $M_{\rm BH}$ value when considering the intrinsic scatter in the relation. However, it should be emphasized that the results from this model optimization should be viewed cautiously. Statistically, it is an overall poor fit to the ALMA data. Qualitatively, inspecting the data and model PVDs in Figure 7.10 reveals that the velocity dispersion of the model is much larger than what is observed in the data. The moment maps in Figure 7.11 also show that the model does not accurately reproduce the observed gas kinematics beyond the elliptical spatial region which was used in the optimization. Prominent discrepancies in surface brightness are apparent along the major axis of the disk. Given this dynamical model's inability to emulate the observed features in the data, I fit another dynamical model over the full disk using the nonparametric $v_{\rm ext}$ model.

I used the $v_{\rm ext}$ model in an attempt to fit the observed gas kinematics over the entire disk. This was done to see if statistically superior fits to the data could be obtained with 10 additional free parameters and gauge other potential shortcomings in the dynamical model. Furthermore, it is pertinent to note that most pixels in the fit are at radii much larger than the projected SMBH $r_{\rm SOI}$. The PVDs and moment maps of this dynamical model

are presented in Figures 7.10 and 7.12. Over the full extent of the disk, the PVD of this model matches the observed PVD structure better than the dynamical model, which used the dust-masked MGE for the host galaxy component. However, the model PVD again features a larger velocity dispersion than what is seen in the data and contains excess flux. The optimization converged on a higher $M_{\rm BH} = 0.8 \times 10^8\,M_\odot$, with relatively similar disk orientation parameters, but $\chi^2_\nu = 20.709$, indicating a poor overall fit.

Given my findings, I tentatively conclude that simple thin disk dynamical models are insufficient to adequately model the observed molecular gas kinematics in NGC 4435. While the MGE model appears to be a fairly accurate representation of the intrinsic host galaxy profile, the dynamical model cannot emulate the gas kinematics beyond the inner $1''$. Similarly, using the nonparametric $v_{\rm ext}$ host galaxy model with 10 additional free parameters does not improve the statistical quality of the fit, although it does qualitatively fit the kinematics better when considering the disk as a whole. There are potentially several factors at play that affect the dynamical modeling process. One factor could be warping of the disk structure that the thin disk models fail to capture. Another factor could be radial motions of the gas, either through inflows or outflows, that would undermine the assumption of gas traveling on nearly circular orbits. The large ALMA synthesized beam also entangles both surface brightness and velocity information over large scales, which could lead to complex line profile shapes that my models are unable to replicate. Taking all of these factors into consideration, it is difficult to conceive of potential solutions to these problems using the currently available ALMA data. However, one avenue worth considering would be to incorporate a tilted-ring model approach to the data as implemented by Boizelle et al. (2019) to address kinematic warping of the disk. This, coupled with the inclusion of non-circular motions in the dynamical modeling process, may lead to better fits of the gas kinematics over the full extent of the disk. Building new MGEs that account for a plausible range in dust extinction and optimizing dynamical models with them will be important in assessing

the sensitivity of $M_{\rm BH}$ on the assumed host galaxy profile, and will help determine if the SMBH in NGC 4435 is as undermassive as reported by Coccato et al. (2006).

7.4 NGC 5838

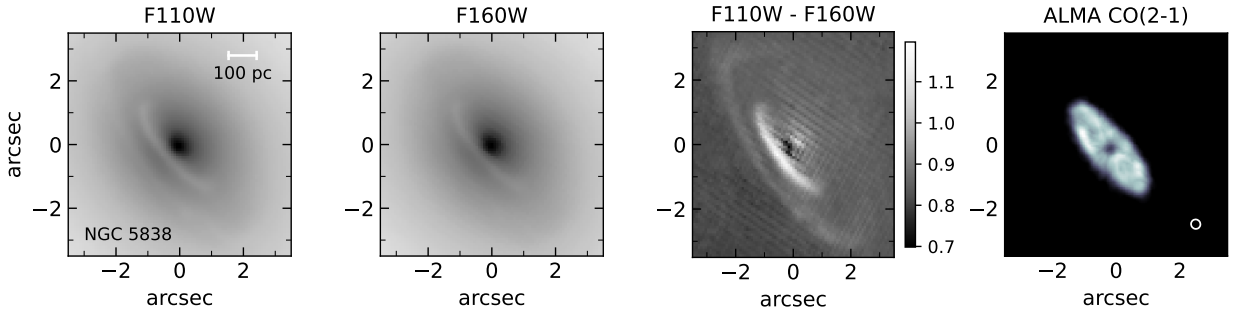

Figure 7.13 Same as Figure 7.1, but for NGC 5838.

NGC 5838 is classified as an SA0 galaxy by de Vaucouleurs et al. (1991) and is located at a luminosity distance of about 22.2 Mpc measured using the Fundamental Plane (Willick et al., 1997; Lauer et al., 2007). There is no previous $M_{\rm BH}$ mass measurement in this galaxy, so the contents of this section represent the first attempt to constrain its SMBH mass through dynamical modeling.

7.4.1 ALMA Data

ALMA observed NGC 5838 on two separate occasions: 22 June 2016 and 18 August 2016 as part of project 2015.1.00878.S. Each observation was approximately 21 minutes in duration and the maximum array baseline in each observation was 704 m and 1462 m respectively. To target the redshifted CO(2−1) line, the observation featured a spectral window covering the frequencies between $228.547 - 230.418$ GHz, with a frequency resolution of 3.904 MHz. The raw *uv* visibility data were calibrated in CASA version 4.7.1, and the continuum features

were subtracted in the uv-plane in order to isolate CO(2−1) emission. The continuum-subtracted visibility data was subsequently imaged into a data cube with a velocity channel spacing of $20\,\mathrm{km\,s^{-1}}$. The synthesized beam has a major axis FWHM of $0\farcs30$, a minor axis FWHM of $0\farcs29$, and a major axis position angle of $-58.4°$ measured East of North. The pixel scale of the data is $0\farcs05$.

7.4.2 HST Data and Host Galaxy Model

k	$\log_{10} I_{H,k}(L_\odot\,\mathrm{pc}^{-2})$	σ'_k (arcsec)	q'_k
	NGC 5838 (Dust-Masked MGE)		
1	5.482	0.095	0.999
2	5.375	0.191	0.560
3	4.874	0.479	0.942
4	4.367	1.216	0.761
5	4.277	2.195	0.749
6	3.909	4.674	0.856
7	3.393	11.061	0.578
8	2.584	31.099	0.560
9	2.462	36.518	0.560
10	1.815	424.393	0.569

Table 7.5 Same as Table 7.1, but for NGC 5838.

J and H band images from HST program 15226 (PI: Boizelle) were used to construct a host galaxy model for NGC 5838. The H-band images were taken with a 4-point dither pattern to sufficiently sample the PSF, and the duration of each exposure was 249 seconds. `AstroDrizzle` was used to properly combine and align the separate exposures into a final drizzled image with a pixel scale of $0\farcs08$. The J-band observation consisted of two separate exposures of 199 seconds each. The J-band images were subsequently drizzled and aligned to the aforementioned H-band image. A $J-H$ color map was used to identify pixels where $J-H > 0.88$ mag. To create a dust-masked MGE, this mask was inputted into `GALFIT` along with `TinyTim` H-band PSF models in order to model the observed 2D H-band surface brightness distribution. The components of the dust-masked MGE are presented in Table

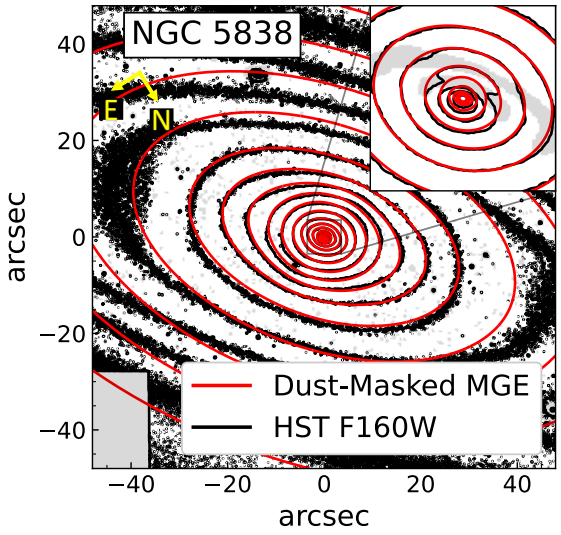

Figure 7.14 Same as Figure 7.2, but for NGC 5838. The innermost $2\farcs0 \times 2\farcs0$ region is shown in the inset.

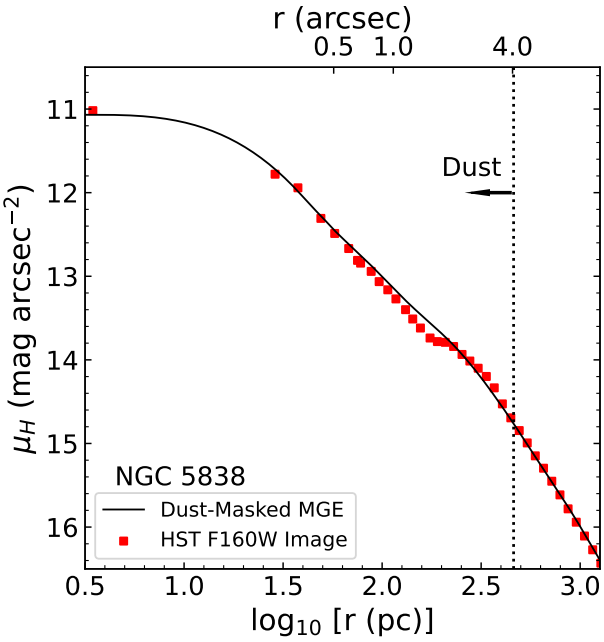

Figure 7.15 Same as Figure 7.3, but for NGC 5838.

7.5. A comparison of the data and MGE model isophotes is shown in 7.14 and their respective H-band major axis surface brightness profiles are shown in Figure 7.15.

7.4.3 Preliminary Dynamical Modeling Results

Host Galaxy Model	$r_{\rm fit}$	$M_{\rm BH}$ ($10^8\,M_\odot$)	Υ_H ($M_\odot/L_\odot$)	i (°)	Γ (°)	σ_0 (km s^{-1})	$v_{\rm sys}$ (km s^{-1})	F_0	χ^2_ν
Dust-Masked MGE	1″	0.01	2.05	72.6	38.1	4.4	1346.3	1.02	1.661
Dust-Masked MGE	1″	0.7	2.00 (Fixed)	72.5	37.7	1.0	1345.0	1.02	1.634
Dust-Masked MGE	1″	9.2	1.50 (Fixed)	71.8	37.9	16.1	1347.3	1.06	2.667
Dust-Masked MGE	1″	19.4	1.00 (Fixed)	71.0	37.9	19.7	1347.0	1.01	3.116

Table 7.6 Best-fit parameter values obtained by fitting thin disk dynamical models to the NGC 5838 data cube. This model has 24,606 degrees of freedom when allowing Υ_H to be free and 24,607 when fixing Υ_H to a specific value. I found the dynamical center of the initial dynamical model to be at RA=15$^{\rm h}$05$^{\rm m}$26.2508$^{\rm s}$, Dec=+02°05′57.″324 for NGC 5838.

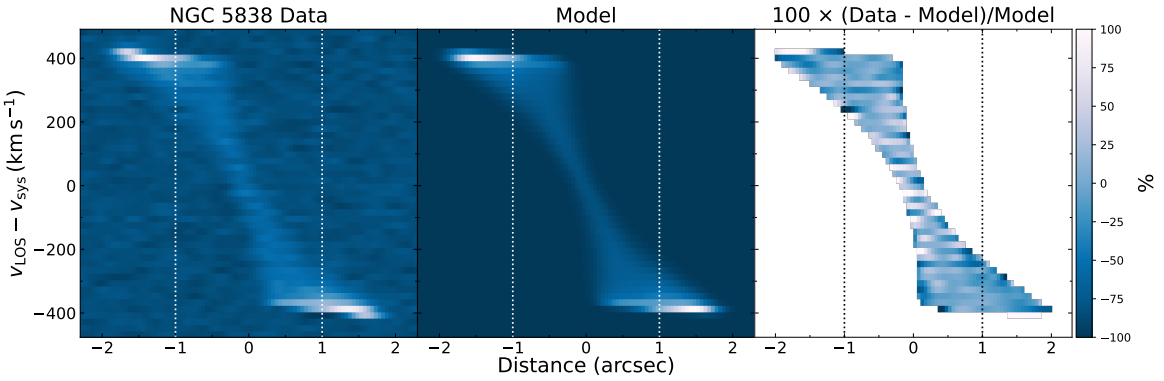

Figure 7.16 Same as Figure 7.5, but for NGC 5838.

I optimized dynamical models to the NGC 5838 data cube using an elliptical spatial region with a major axis of $r_{\rm fit} = 1''$ and an axial ratio of 0.43. Given the extended nature of the disk and that CO emission appears faint at the center, I chose this region to fit models closer to the projected SMBH $r_{\rm SOI}$. The axial ratio was determined based on measurements of the optical dust disk in the HST images. Upon optimizing the initial dynamical model, I found that $M_{\rm BH}$ was driven down to its lower boundary of $1 \times 10^6\,M_\odot$ that I enforced. This indicated the possibility of a strong degeneracy between stellar mass and $M_{\rm BH}$. To investigate this possibility, I optimized dynamical models where Υ_H were set to values of 1.00, 1.50, and 2.00, but all other model parameters were allowed to freely vary. The results of these tests and the parameter values from the initial dynamical model are given in Table 7.6. With decreasing Υ_H, there is a dramatic increase in $M_{\rm BH}$ as it is $0.01 \times 10^8\,M_\odot$ when

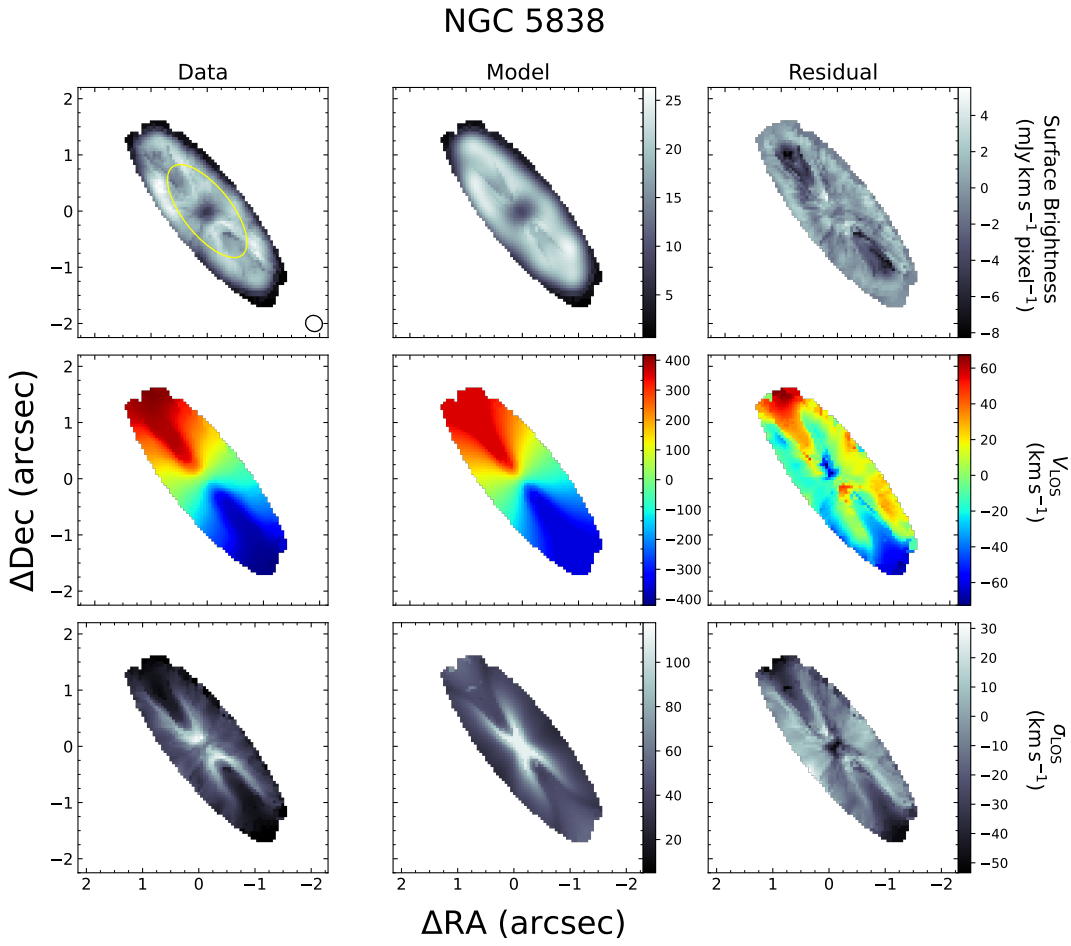

Figure 7.17 Same as Figure 7.5, but for NGC 5838.

$\Upsilon_H = 2.05$ and rises to $1.94 \times 10^9\, M_\odot$ when Υ_H is fixed at 1.00. The difference of three orders of magnitude provides compelling evidence that $M_{\rm BH}$ is highly degenerate with stellar mass in the models. Besides this, it should be noted that while the inclination angle and position angle free parameters remain relatively unchanged between the tests, there is a large change in gas velocity dispersion σ_0. This parameter converges on the imposed boundary of $1.0\,{\rm km\,s^{-1}}$ when Υ_H is fixed to 2.00 and rises to nearly $20\,{\rm km\,s^{-1}}$ when $\Upsilon_H = 1.00$. While there is a noticeable increase in χ^2_ν as Υ_H decreases, given that some model parameters are converging on unlikely values due to physical considerations, the models with statistically superior χ^2_ν should be viewed skeptically. An examination of the major axis PVDs of both the data and model in Figure 7.16 highlights the dearth of CO emission inward of about

0.″5 of the nucleus, and no rise in central velocity is observed. The data and model surface brightness maps in Figure 7.17 also highlight the presence of a hole in the CO distribution. Furthermore, there are large residuals in surface brightness, especially along the major axis, suggesting that imperfections in the surface brightness model may also be a contributing limiting factor in the dynamical models. The $v_{\rm LOS}$ maps show that over the spatial region where the model was fitted to the data, velocity residuals agree to within about $\sim$20 km s^{-1}, though beam smearing is evident in the central regions. This is also apparent in the $\sigma_{\rm LOS}$ maps. Given the modeling results and the visualizations, it is evident that the simple thin disk models struggle to constrain $M_{\rm BH}$ within a narrow range.

7.5 ESO 208-G21

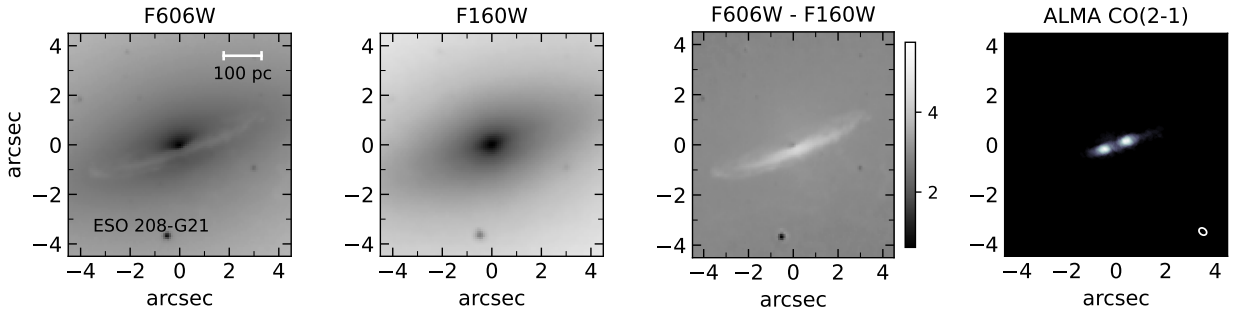

Figure 7.18 Same as 7.1, but with F606W observations (V-band) as opposed to F110W observations.

The galaxy ESO 208-G21 is classified as an SAB0 galaxy by de Vaucouleurs et al. (1991) and has a measured luminosity distance of 13.6 Mpc by Tonry et al. (2001). Furthermore, as of this writing, there is no prior $M_{\rm BH}$ measurement in this galaxy, thus the preliminary results in this section are the first attempt at quantifying the mass of its SMBH.

7.5.1 ALMA Data

ESO 208-G21 was observed by ALMA on 15 January 2018 for 31 minutes with a maximum baseline of 2386 m. To target the redshifted CO(2−1) line, the observation featured a spectral window between $228.814 - 230.685$ GHz with a frequency resolution of 3.904 MHz. The continuum was subtracted in the uv-plane to isolate it from the CO(2−1) emission. The complex visibility data were subsequently imaged into a data cube with velocity channel widths of $20\,\mathrm{km\,s^{-1}}$ and pixel sizes of $0\farcs035$. Properties of the synthesized beam include a major axis FWHM of $0\farcs34$, a minor axis FWHM of $0\farcs26$ and a beam position angle of 51.5° measured East of North.

7.5.2 HST Data and Host Galaxy Model

k	$\log_{10} I_{H,k}(L_\odot\,\mathrm{pc}^{-2})$	σ'_k (arcsec)	q'_k
	ESO 208-G21 (Dust-Masked MGE)		
1	5.615	0.071	0.967
2	5.235	0.211	0.693
3	4.996	0.469	0.655
4	3.849	2.015	0.736
5	4.207	0.894	0.857
6	3.352	3.833	0.764
7	4.400	1.190	0.427
8	4.151	2.945	0.303
9	2.525	6.795	0.976
10	3.804	5.260	0.396
11	2.550	25.852	0.665
12	3.474	9.259	0.467
13	1.607	87.545	0.502
14	3.006	15.621	0.540
15	1.979	66.057	0.987

Table 7.7 Same as Table 7.1, but for ESO 208-G21.

I used H-band and F606W (V-band) data from HST proposal 15181 (PI: Rosario). The H-band observation used a 3-point dither pattern which consisted of 3 exposures of 278 seconds

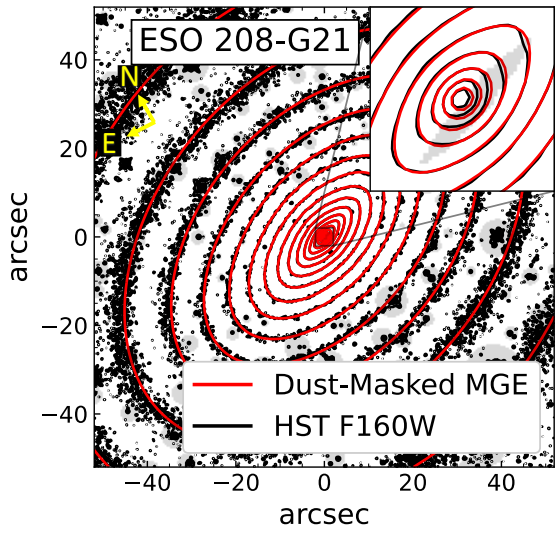

Figure 7.19 Same as Figure 7.2, but for ESO 208-G21. The innermost 2.″0 × 2.″0 region is shown in the inset.

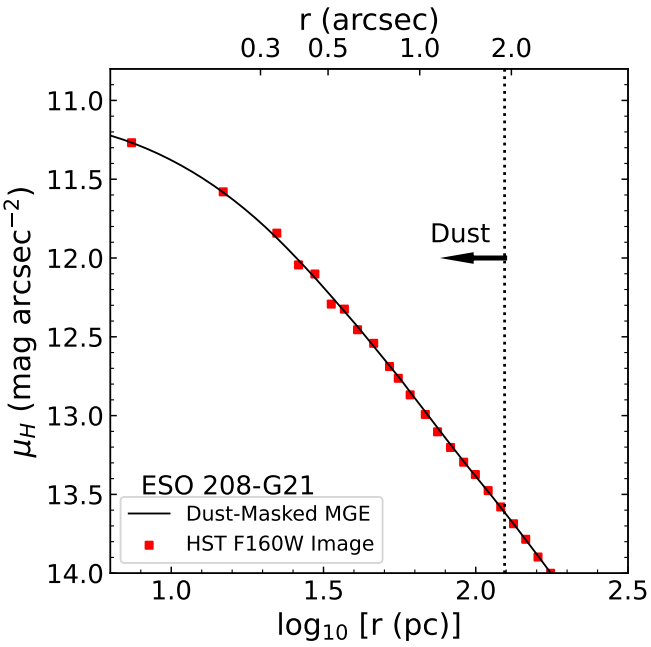

Figure 7.20 Same as Figure 7.3, but for ESO 208-G21.

each, whereas the V-band observation employed a 4-point dither pattern and consisted of 4 exposures, 1 which lasted 358 seconds and 3 that lasted 403 seconds. I used `AstroDrizzle` to align and drizzle the H-band images to a pixel scale of 0.″08 to properly sample the H-band PSF. I then combined the V-band images and aligned the final product with the

drizzled H-band image. To assess the variation of dust attenuation across the circumnuclear disk, I created a $V-H$ map and identified pixels that satisfied $V-H>3.6$ mag. The V, H, and $V-H$ maps are shown in Figure 7.18. Furthermore, I used this map as well as `TinyTim` PSF models to construct a dust-masked MGE of the H-band image in `GALFIT`. The components of this MGE model are presented in Table 7.7. The isophotal contours and major axis surface brightness profiles of the H-band data and the dust-masked MGE model are shown in Figures 7.19 and 7.20.

7.5.3 Preliminary Dynamical Modeling Results

Host Galaxy Model	$r_{\rm fit}$	$M_{\rm BH}$ ($10^8\,M_\odot$)	Υ_H ($M_\odot/L_\odot$)	i (°)	Γ (°)	σ_0 (km s^{-1})	$v_{\rm sys}$ (km s^{-1})	F_0	χ^2_ν
Dust-Masked MGE	1.″2	2.3	1.70	82.7	290.4	15.1	1066.25	1.36	1.345

Table 7.8 Best-fit parameter values obtained by fitting thin disk dynamical models to the ESO 208-G21 data cube. This model has 46,364 degrees of freedom. I found the dynamical center of the fiducial model to be at RA=$7^{\rm h}33^{\rm m}56.2324^{\rm s}$, Dec=$-50°26'34.''606$ for ESO 208-G21.

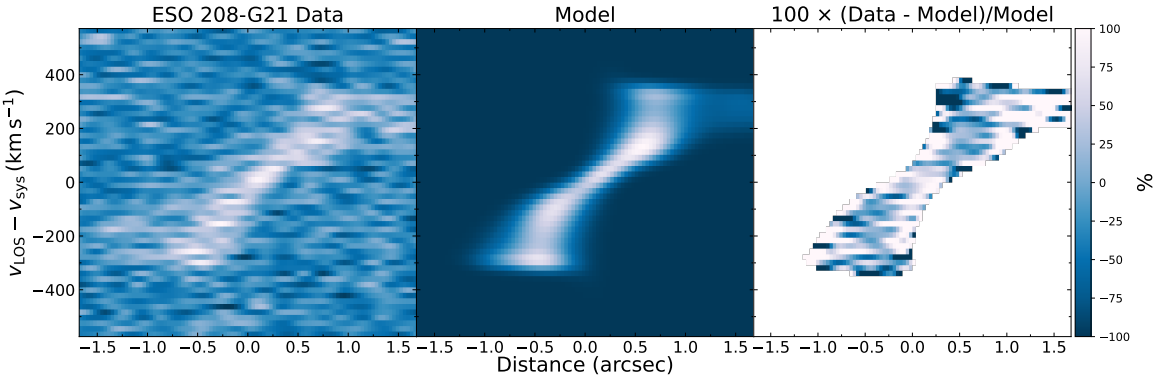

Figure 7.21 PVDs along the major axes of the ESO 208-G21 ALMA data and the best-fit model. Columns show ALMA CO(2−1) data (left), models (center), and fractional residuals (right). The PVDs were extracted with a spatial width equivalent to a resolution element.

I fit dynamical models to the ESO 208-G21 data cube using the dust-masked MGE. The model was fit to the data without any block-averaging to preserve angular resolution of the spatial pixels and allow for maximum sensitivity to the central BH, and was optimized

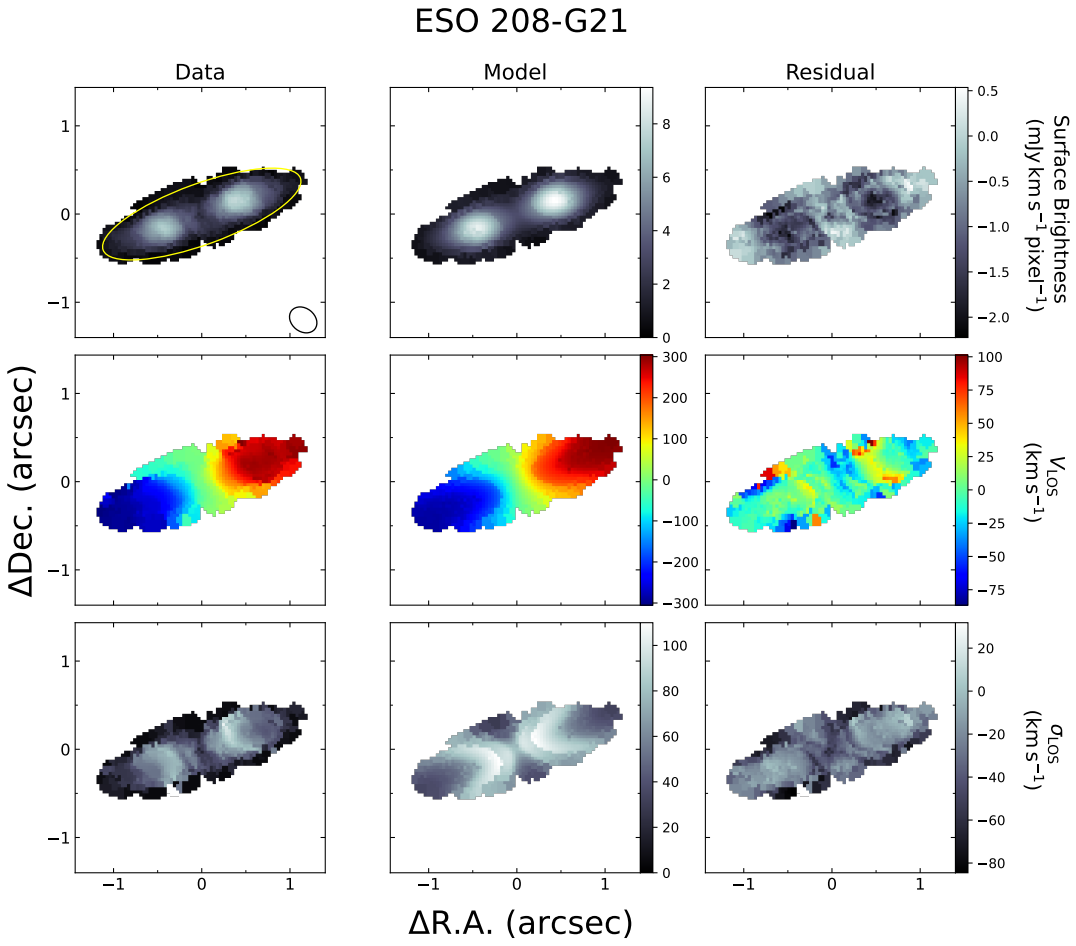

Figure 7.22 Same as Figure 7.5, but for ESO 208-G21.

over an elliptical spatial region with a projected major axis length of 1.″2 and axis ratio of 0.29 that covered the disk. Upon optimizing models, the SMBH mass converged on $M_{\rm BH} = 2.3 \times 10^8\, M_\odot$ with $\chi^2_\nu = 1.345$ over 46,364 degrees of freedom. The results of this optimization are presented in Table 7.8. The model fits the data adequately, but it is not a formally acceptable fit, which should achieve $\chi^2_\nu \leq 1.011$ at the 0.05 significance level. Differences between the data and model are shown in the structure of the PVD shown in Figure 7.21. The model displays a broad spread in velocities in the outer parts of the disk that is not seen in the data. Furthermore, the model's CO surface brightness is higher than what is observed in the data. This could indicate a shortcoming in the weighting of the model line profiles. The flux normalization factor F_0 is 1.36 and is higher than what is typically

observed in ALMA gas-dynamical models. In terms of the gas kinematics, Figure 7.22 shows that the model LOS velocities are well-matched to the data, though the model dispersion map is higher than what is observed in the data. At $i = 82.6°$, the disk in ESO 208-G21 is highly inclined. It has been shown by Barth et al. (2016b) that constraining $M_{\rm BH}$ in these cases can be difficult when using observations that do not highly resolve the projected $r_{\rm SOI}$, as models can conflate rotational and turbulent motions.

Chapter 8

Summary, the Future, and Conclusions

> "And one final point—we never really know where the next great scientific discovery will come from, nor who will make it."
>
> - Stephen Hawking (2018)

8.1 Summary

The completed and preliminary measurements in this dissertation highlight ALMA's unique ability to constrain central SMBH masses through molecular gas-dynamical modeling. These measurements additionally underscore the importance of accounting for a variety of factors when interpreting the results. While ALMA has the ability to make extremely precise $M_{\rm BH}$ measurements in the most favorable scenarios where molecular gas emission extends deep within the expected SMBH $r_{\rm SOI}$ and displays Keplerian-like rotation, these cases are rare. This dissertation features measurements carried out in systems that do not exhibit these features. Limitations such as holes in the central molecular gas distribution, noncircular motions, dust attenuation on the host galaxy starlight, and degeneracies among free pa-

rameters restrict the ability of the dynamical models to tightly constrain $M_{\rm BH}$ when the observations do not highly resolve $r_{\rm SOI}$. Encouragingly, despite the aforementioned limiting factors, ALMA is still able to exquisitely map out the large-scale molecular gas disk kinematics and provide meaningful constraints on $M_{\rm BH}$. Additionally, while this dissertation has been focused on the dynamical mass measurements of central SMBHs, the ALMA data presented in this work could also be used to further studies on the properties of molecular gas clouds, star formation, the effect SMBHs have on the surrounding interstellar medium, the presence of inflows and/or outflows, and gas excitation and chemistry. To conclude this section, I summarize the key findings for each of the eight SMBH mass measurements conducted in this dissertation. Five of the measurements are for SMBHs that have no prior measurement (NGC 1380, NGC 4786, NGC 5193, NGC 5838, and ESO 208-G21) whereas the remaining three measurements have had either prior stellar-dynamical $M_{\rm BH}$ measurements (NGC 6861; Rusli et al., 2013) or ionized gas-dynamical $M_{\rm BH}$ measurements (NGC 3245, NGC 4435, Barth et al., 2001; Coccato et al., 2006).

- *NGC 1380*: I determined $M_{\rm BH} = 1.47 \times 10^8\,M_\odot$ with a systematic uncertainty of about 40%. A slight central rise in CO velocity is noticeable, but given that observations only marginally resolve $r_{\rm SOI}$, the dynamical models exhibited parameter degeneracies, specifically between SMBH and stellar mass. This underscores the importance of building a set of host galaxy models accounting for a plausible range in the host galaxy stellar mass profile, especially in dusty nuclei.

- *NGC 6861*: Due to the presence of a large, $1''$ hole in the CO distribution, there were no kinematic tracers within the expected $r_{\rm SOI}$. This limited the ability of the dynamical models to tightly constrain $M_{\rm BH}$. Instead, dynamical models converged on a plausible range of $M_{\rm BH} = (1-3) \times 10^9\,M_\odot$ that is in agreement with the previous stellar-dynamical $M_{\rm BH}$ measurement by Rusli et al. (2013).

- *NGC 4786*: Using a set of three host galaxy models that account for dust attenuation of the host galaxy's starlight, I determined $(M_{\rm BH}/10^8\,M_\odot) = 5.0 \pm 0.2\,[1\sigma\,\text{statistical}]\,^{+1.4}_{-1.3}\,[\text{systematic}]$. The measurement's error budget is dominated by the systematic uncertainty associated with the host galaxy extinction corrections.

- *NGC 5193*: There is evidence of a central deficit of CO surface brightness at the center of this galaxy from both the ALMA and HST observations. Coupled with the fact that $r_{\rm SOI}$ is most likely unresolved by the observations, the dynamical models found a broad range of $(M_{\rm BH}/10^8\,M_\odot) = 1.4 \pm 0.03\,[1\sigma\,\text{statistical}]\,^{+1.5}_{-0.1}\,[\text{systematic}]$. Given the uncertainty in the inner slope of the stellar mass profile, this measurement in particular emphasizes the need for incorporating multiple host galaxy models when conducting $M_{\rm BH}$ measurements in this regime.

- *NGC 3245*: I optimized two dynamical models to the NGC 3245 data cube. The first model uses a dust-masked MGE to account for the gravitational potential of the host galaxy. Models were fit to an elliptical spatial region with a major axis of about $1''$ and converged on $M_{\rm BH} = 1.4 \times 10^8\,M_\odot$, which is slightly outside the 1σ confidence interval of $(1.6 - 2.6) \times 10^8\,M_\odot$ determined by the previous ionized gas-dynamical measurement by Barth et al. (2001). However, the model fit is statistically poor ($\chi^2_\nu > 3$) and does not capture the molecular gas kinematics over the full extent of the disk. Using the nonparametric $v_{\rm ext}$ model I developed for the host galaxy component over the full disk, the second dynamical model is able to better reproduce the observed kinematic features with a central SMBH of $M_{\rm BH} = 0.9 \times 10^8\,M_\odot$, but is still ultimately a formally inadequate fit to the data ($\chi^2_\nu \approx 4$). More complex modeling approaches will be needed to improve the fit and better constrain $M_{\rm BH}$.

- *NGC 4435*: Dynamical models struggled to provide a quality model fit to the ALMA data. Using both a dust-masked MGE and the nonparametric $v_{\rm ext}$ model for the host galaxy component, the preliminary results find $M_{\rm BH} = (0.5 - 0.8) \times 10^8\,M_\odot$,

but with $\chi^2_\nu \approx 14 - 20$. This range in $M_{\rm BH}$ is about an order of magnitude higher than the suggested upper limit to $M_{\rm BH}$ by Coccato et al. (2006) based on ionized gas-dynamical modeling. While the model fits are currently poor, this target warrants more investigation because a more precise measurement with ALMA could provide crucial insight on the systematic differences between ionized and molecular gas-dynamical $M_{\rm BH}$ measurements.

- *NGC 5838*: The optimization of dynamical models to the innermost $1''$ of the disk in NGC 5838 quickly revealed a parameter degeneracy between $M_{\rm BH}$ and stellar mass. Allowing all free parameters to vary, $M_{\rm BH}$ is effectively driven down to $0\,M_\odot$ in my models. I ran a series of tests where I fixed Υ_H in the optimization process and found that $M_{\rm BH}$ and Υ_H exhibit a negative correlation, as $M_{\rm BH}$ can range between $\sim 10^6\,M_\odot - 10^9\,M_\odot$ depending on the fixed value of Υ_H.

- *ESO 208-G21*: Based on an initial optimization over the full extent of the disk, I derive $M_{\rm BH} = 2.3 \times 10^8\,M_\odot$ in ESO 208-G21. There is evidence of a rise in the projected LOS velocity near the center of the disk, but the disk exhibits only faint CO emission in this region, which could potentially limit the precision on $M_{\rm BH}$. Nevertheless, the preliminary results are promising, as $\chi^2_\nu \approx 1.3$, though more tests are needed to determine the final error budget on $M_{\rm BH}$.

8.2 Future Directions for ALMA Gas-Dynamical Research

ALMA will continue to play an important role in the study of SMBH demographics for years to come. While extremely precise measurements of $M_{\rm BH}$ are not feasible for every circumnuclear disk, those that are dominated by rotation and have sufficient dynamical

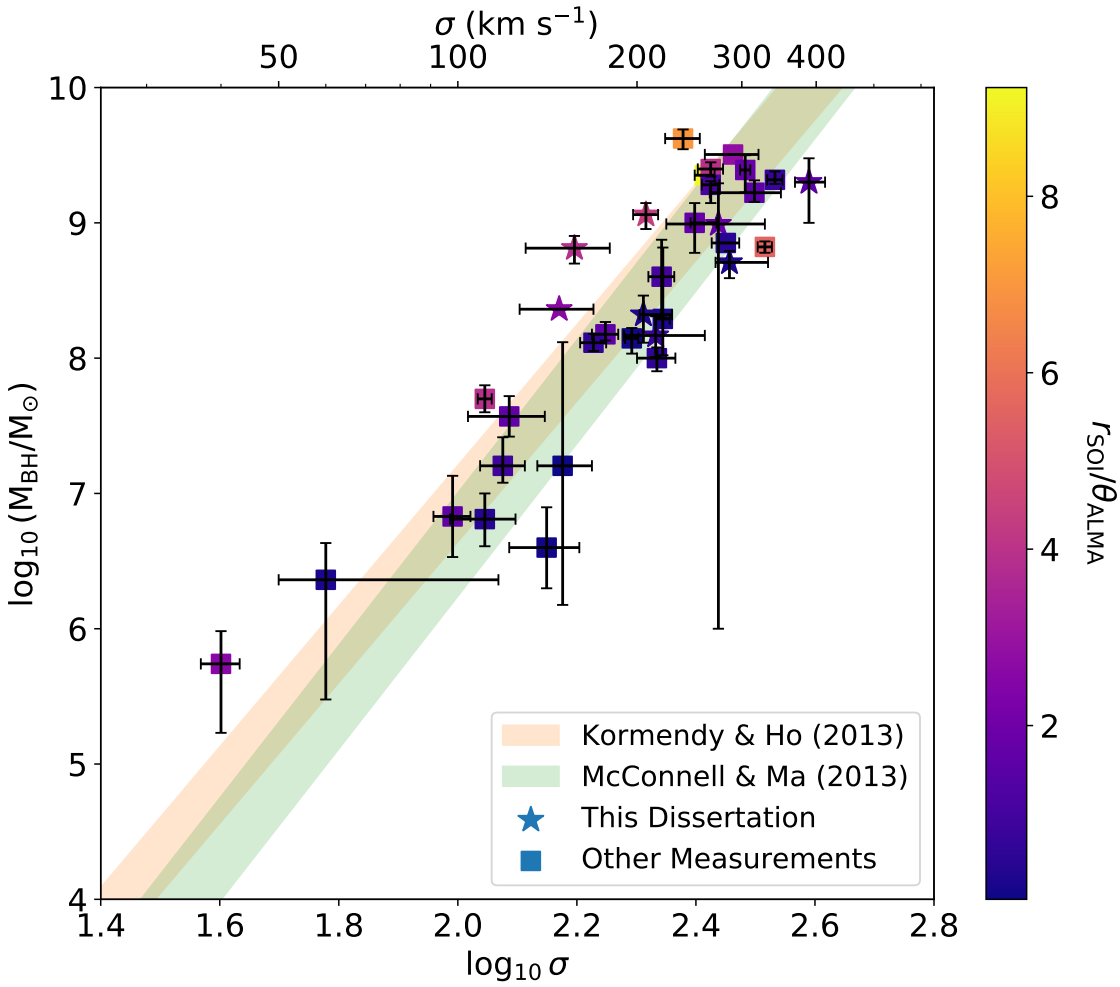

Figure 8.1 $M_{BH} - \sigma_\star$ relations from Kormendy and Ho (2013) and McConnell and Ma (2013), including their intrinsic scatter, shown in the shaded regions. The M_{BH} measurements featured in this dissertation are plotted as stars, whereas all other ALMA M_{BH} measurements from the literature (presented in Table 8.1) are shown as squares. The error ranges on M_{BH} are from the systematic uncertainties presented in the sources. The $\sigma_\star$ values are also taken from the corresponding sources. If a specific measurement of $\sigma_\star$ was used, then the error ranges correspond to the uncertainty on the measurement. If the average $\sigma_\star$ value from Hyperleda (Makarov et al., 2014) was used, then the error range on $\sigma_\star$ uses the lowest and highest reported values in the database.

information near the SMBH SOI will provide important constraints on the SMBH masses in these systems. As we enter a new decade of ALMA science programs, it is an appropriate time to look back on what the first ten years has brought. In Table 8.1, I present a list of all the currently known molecular gas-dynamical M_{BH} measurements made with ALMA. This list includes 25 unique galaxies that have currently published measurements and 10

others that are currently either under review or are featured in this dissertation. These measurements are plotted alongside the Kormendy and Ho (2013) and McConnell and Ma (2013) $M_{\rm BH} - \sigma_\star$ scaling relations in Figure 8.1. Furthermore, following Kormendy and Ho (2013), I have quantified how well-resolved $r_{\rm SOI}$ in each measurement is by empirically calculating $r_{\rm SOI} = GM_{\rm BH}/\sigma_\star^2$ using the quantities in Table 8.1 and taking the ratio of $r_{\rm SOI}$ to the geometric mean of the ALMA synthesized beam in each measurement. Lighter colors represent more well-resolved SOIs. Notably, most of the ALMA $M_{\rm BH}$ measurements are neatly clustered within the predicted $M_{\rm BH}$ ranges, and even the two least massive SMBHs that fall within $10^{5.5}\,M_\odot - 10^{6.5}\,M_\odot$ are not far off from their predicted values. Resoundingly, ALMA has been a game-changing instrument for $M_{\rm BH}$ measurements. With the upcoming arrival of next-generation telescopes on the way, the synergistic collaboration with ALMA will enhance our knowledge of $M_{\rm BH}$ measurement systematics.

There are a few potential avenues for improvement when it comes to making $M_{\rm BH}$ measurements with molecular gas-dynamical modeling. These include:

- *Including more complex, noncircular motions in the gas-dynamics*: The underlying assumption of gas rotating on nearly ideal circular orbits may not always hold even in the relatively dynamically cold disks observed with ALMA. Some physical mechanisms that could be responsible for these deviations include stellar or AGN feedback, inflows or outflows of gas, gravitational instabilities within the disk, and turbulence. While I have developed and incorporated some simple models to account for some of these effects, more complex methods should be incorporated, especially when using very high angular resolution ALMA datasets to further our collective understanding of the small-scale dynamics in these disks. Insights gleaned from investigations into large-scale noncircular gas motions in disk galaxies and irregular dwarf galaxies (Spekkens and Sellwood, 2007; Hunter et al., 2019) can serve as a valuable foundation for the

implementation of these techniques in future gas-dynamical analyses of circumnuclear disks with ALMA.

- *Optimizing fits in the Fourier (uv) plane and comparing with results in the image plane*: The noise in ALMA data cubes exhibits both spatial and spectral correlation. In essence, this correlation arises because interferometric visibility data are Fourier transformed into the image domain. χ^2 minimization typically assumes that the errors in the data are Gaussian and uncorrelated, and optimizing datasets with errors that do not meet these criteria can lead to unreliable estimates of the model parameters. A formally correct, but computationally expensive, approach in the image domain would be to construct a large covariance matrix that contains the covariance among all pairs of variables. This would be technically challenging to do with current ALMA gas-dynamical modeling techniques, which can have tens to hundreds of thousands of data points in a model fit. An alternative approach would be to first construct dynamical models in the image domain, Fourier transform them, and perform model optimizations in the *uv*-plane where the errors in visibility data are Gaussian and uncorrelated. This has not been tried before for $M_{\rm BH}$ measurements, but this type of modeling has been done to dynamically weigh T Tauri stars based on the motions of their circumstellar disks (Czekala et al., 2015; Long et al., 2021).

- *Incorporating more sophisticated techniques involving radiative transfer modeling for handling dust attenuation in these dusty systems*: This thesis has demonstrated that deprojecting a 2D surface brightness profile and converting it into a mass profile of the host galaxy is complicated in dusty nuclei. While masking and simple dust correction methods have been applied, a more sophisticated approach would involve the use of radiative transfer modeling programs such as `FitSKIRT` (De Geyter et al., 2013). While this program has mainly been used to fit UV/optical images of dusty galaxies as a whole, there has been work on modeling smaller scale dust rings in ETGs (Bonfini et al.,

2018). For the purposes of $M_{\rm BH}$ measurements, `FitSKIRT` could be used to model HST near-infrared data and produce models of the intrinsic stellar distribution. In principle, one could fit the intrinsic H-band stellar distribution from a WFC3 F160W image with `FitSKIRT` and generate a dust-free model image based on the results. Then, to derive a mass profile or circular velocity curve to use in a dynamical model, one could then fit an MGE to this dust-free image and deproject the resulting Gaussian components.

8.3 The Next 30 Years (2023 - 2053)

Where do we go from here? The initial three decades were characterized by groundbreaking theoretical work aimed at deciphering the engines driving the luminosity of distant quasi-stellar objects, coupled with the evolution of dynamical modeling techniques that would become indispensable for subsequent observational studies. The successive thirty years witnessed the creation and deployment of several transformative telescopes that facilitated comprehensive studies of SMBH demographics and illuminated the profound connection between SMBHs and their host galaxies. To conclude this dissertation, I speculate on the future of dynamical $M_{\rm BH}$ measurements over the next thirty years.

8.3.1 JWST

We are at the start of a new era in astronomy. With the launch of the JWST and the anticipated construction of several large ground-based observatories in the coming decades, our understanding of SMBHs, as well as the tools to dynamically measure their masses, will dramatically improve. JWST has superior sensitivity and resolution in the near and mid-infrared regimes when compared to its predecessors, particularly HST. As was demonstrated in this thesis, while constructing host galaxy models based on near-infrared images from

HST mitigates the effects of dust extinction, the largest contributor to the error budget of an $M_{\rm BH}$ measurement is still the uncertainty associated with the extinction corrections. JWST will provide the clearest view of the nuclear regions in nearby galaxies to date, and give more robust estimates of the stellar densities and mass distributions on these small scales. Furthermore, more precise spectroscopic observations with the Near Infrared Spectrograph will enable higher precision stellar-dynamical mass measurements and help us to better understand the factors that cause stellar and gas-dynamical $M_{\rm BH}$ measurements to disagree.

8.3.2 Extremely Large Telescopes

There are several extremely large optical/near-infrared telescopes ($D > 20$ m) in development that have the potential to fundamentally transform our current understanding of SMBHs. These include the Extremely Large Telescope (ELT), the Thirty Meter Telescope (TMT), and the Giant Magellan Telescope (GMT). With their unprecedented angular resolutions, these telescopes will be able to dynamically observe SMBHs further than ever before, and allow us to track the SMBH-host galaxy scaling relations over a larger range in redshift. The scaling relations are currently calibrated by $M_{\rm BH}$ measurements in galaxies within $\sim$100 Mpc, and the measurements are not carried out in a representative sample of galaxies. These extremely large telescopes will give us a more detailed picture of SMBH-host galaxy coevolution over a broader range in galaxy type and help us understand if SMBHs and their host galaxies grow in tandem, or if one's growth precedes the other.

8.3.3 ngVLA

The Next Generation Very Large Array (ngVLA) will provide extremely precise $M_{\rm BH}$ measurements in systems that possess cleanly rotating molecular gas at their centers. ngVLA is expected to deliver an order of magnitude increase in maximum angular resolution at the

CO(1−0) transition frequency of 115 GHz, compared to ALMA. While the lessons learned from ALMA have taught us that only a few percent of galaxies will be prime candidates for these kinds of measurements, those that have disks with Keplerian-like rotation are some of the most precisely measured extragalactic SMBH masses to date. Given superior angular resolution to ALMA, ngVLA will also be able to perform these types of measurements in more distant galaxies; current estimates suggest that confident $M_{\rm BH}$ determinations with uncertainties of less than 20% will be possible in galaxies out to 300 Mpc, provided that $M_{\rm BH} \sim 10^9\,M_\odot$, and conversely will be able to detect the signatures of lower mass SMBHs ($M_{\rm BH} \sim 10^7\,M_\odot$) in late-type galaxies out to about 20 Mpc (Boizelle et al., 2018).

8.4 Conclusions

Dynamically measuring the masses of SMBHs will continue to be an important endeavor. Our understanding of the local scaling relations and what they imply about SMBH-host galaxy coevolution hinges on the reliability of these measurements, and will soon be enhanced with the current and future observatories at our disposal. A decade of science operations and about 25 published $M_{\rm BH}$ measurements reveal that circumnuclear disks in ETGs can, in the best cases, provide some of the most precise and reliable $M_{\rm BH}$ measurements, and the results of this dissertation highlight how to conduct $M_{\rm BH}$ measurements with ALMA in non-optimal scenarios. As ALMA enters its next decade of science operations, the findings in this work provide potential future avenues of exploration and may prove to be a valuable reference for future $M_{\rm BH}$ measurements with ALMA. While our collective understanding remains incomplete, and several challenges remain, this dissertation demonstrates the role ALMA has played in enabling more reliable $M_{\rm BH}$ measurements, which will bolster our knowledge of SMBH-host galaxy coevolution. Undoubtedly, it is a role it will continue to play in the decades to come.

Reference	Galaxy	Type	D (Mpc)	$M_{\rm BH}$ ($10^9\,M_\odot$)	$\sigma_\star$ (km s^{-1})	$r_{\rm SOI}$ ($''$)	θ ($''$)	$r_{\rm SOI}/\theta$
(1)	(2)	(3)	(4)	(5)	(6)	(7)	(8)	(9)
This dissertation	ESO 208-G21*	SAB0	13.6	0.23	148	0.683	0.260	2.629
Lelli et al. (2022)	Fairall 49	LIRG	86.7	0.16	···	···	0.188	···
Boizelle et al. (2021)	NGC 315	cD	72.3	2.08	341	0.219	0.285	0.768
North et al. (2019)	NGC 383	SA0	66.6	4.2	239	0.977	0.140	6.981
J. Cohn 2023 (in prep.)	NGC 384*	E/S0	59	0.195	221	0.060	0.230	0.260
Davis et al. (2020)	NGC 404	dE	3.06	0.00055	40	0.099	0.039	2.583
Smith et al. (2019)	NGC 524	SA0	23.3	0.4	220	0.314	0.300	1.047
Ruffa et al. (2023)	NGC 612	S0a	130.4	3.2	290	0.258	0.092	2.808
Combes et al. (2019)	NGC 613	SB(rs)bc	17.2	0.0371	122	0.128	0.078	1.645
Onishi et al. (2015)	NGC 1097	SB(s)b	14.5	0.14	196	0.222	1.900	0.117
Combes et al. (2019)	NGC 1275	cD	73.5	1	250	0.193	0.111	1.744
Combes et al. (2019)	NGC 1326	(R)SB0^+(r)	14.9	0.00646	111	0.031	0.079	0.394
Barth et al. (2016a)	NGC 1332	E/S0	22.3	0.664	328	0.245	0.044	5.568
Combes et al. (2019)	NGC 1365	SB(s)b	17.8	0.00398	141	0.010	0.074	0.135
Kabasares et al. (2022)	NGC 1380	S0	17.1	0.147	215	0.165	0.210	0.784
Combes et al. (2019)	NGC 1566	SAB(s)bc	7.2	0.00676	98	0.087	0.053	1.633
Ruffa et al. (2023)	NGC 1574*	S0	19.9	0.1	216	0.095	0.170	0.561
Combes et al. (2019)	NGC 1672	SB(s)b	11.4	0.05	111	0.315	0.080	3.939
This dissertation	NGC 3245*	SA0^0(r)	20.9	1.15	207	1.137	0.260	4.372
Boizelle et al. (2019)	NGC 3258	E1	31.9	2.249	260	0.923	0.100	9.233
Nguyen et al. (2020)	NGC 3504	(R)SAB(s)ab	32.4	0.016	119	0.031	0.036	0.858
Ruffa et al. (2019)	NGC 3557	E3	44.5	0.71	282	0.178	0.400	0.444
Nguyen et al. (2022)	NGC 3593	SA(s)0/a:	7	0.0023	60	0.081	0.300	0.269
Boizelle et al. (2021) & Ruffa et al. (2023)	NGC 4261	cD/E2-E3	31.6	1.67	315	0.471	0.295	1.598
Davis et al. (2018)	NGC 4429	SA0^+(r)	16.5	0.15	177	0.257	0.160	1.606
This dissertation	NGC 4435*	SB0^0(s)	16.6	0.65	157	1.406	0.365	3.853
Davis et al. (2017)	NGC 4697	E6	11.4	0.13	169	0.353	0.530	0.667
This dissertation	NGC 4786*	cD	64.1	0.51	286	0.086	0.310	0.278
This dissertation	NGC 5193*	E	46.8	0.21	205	0.095	0.310	0.305
This dissertation	NGC 5838*	SA0	22.2	0.9805	274	0.521	0.295	1.765
Kabasares et al. (2022)	NGC 6861	E/S0	27.3	2	389	0.429	0.280	1.531
Smith et al. (2021)	NGC 7052	E6	69.3	2.5	266	0.451	0.115	3.925
Nguyen et al. (2021)	NGC 7469	(R')SAB(rs)a	70.8	0.016	150	0.009	0.300	0.030
J. Cohn 2023, (in prep.)	PGC 11179*	E/S0	94	1.91	266	0.254	0.225	1.130
Cohn et al. (2021)	UGC 2698	E/S0	91	2.46	304	0.259	0.143	1.811

Table 8.1 A compilation of published and unpublished ALMA $M_{\rm BH}$ measurements. (1) is the source of the measurement, (2) is the galaxy name, (3) is the galaxy type as reported in NED, (4) is the assumed distance to the galaxy used in the measurement, (5) is $M_{\rm BH}$ in units of $10^9\,M_\odot$, (6) is the measured central stellar velocity dispersion, (7) is the projected angular $r_{\rm SOI}$, (8) is the resolution of the observation (taken to be the geometric mean of the ALMA FWHM beam sizes), and (9) is the ratio of $r_{\rm SOI}/\theta$, which is used as a measure of how well-resolved $r_{\rm SOI}$ is. $r_{\rm SOI}$ is calculated as $r_{\rm SOI} = GM_{\rm BH}/\sigma_\star^2$ using the empirically measured $M_{\rm BH}$ and $\sigma_\star$ values. Asterisks in (2) indicate $M_{\rm BH}$ measurements that are currently in review or are unpublished. Fairall 49 does not have a well-defined bulge, and thus does not have a measurement of $\sigma_\star$. For NGC 4261, I use the Boizelle et al. (2021) measurement and its larger error range instead of the Ruffa et al. (2023) measurement, which finds a similar $M_{\rm BH}$.

Bibliography

G. O. Abell, J. Corwin, Harold G., and R. P. Olowin. A Catalog of Rich Clusters of Galaxies. *The Astrophysical Journal Supplement*, 70:1, May 1989. doi: 10.1086/191333.

K. Alatalo, T. A. Davis, M. Bureau, L. M. Young, L. Blitz, A. F. Crocker, E. Bayet, M. Bois, F. Bournaud, M. Cappellari, R. L. Davies, P. T. de Zeeuw, P.-A. Duc, E. Emsellem, S. Khochfar, D. Krajnović, H. Kuntschner, P.-Y. Lablanche, R. Morganti, R. M. McDermid, T. Naab, T. Oosterloo, M. Sarzi, N. Scott, P. Serra, and A.-M. Weijmans. The ATLAS^{3D} project - XVIII. CARMA CO imaging survey of early-type galaxies. *Monthly Notices of the Royal Astronomical Society*, 432(3):1796–1844, July 2013. doi: 10.1093/mnras/sts299.

A. J. Barth, M. Sarzi, H.-W. Rix, L. C. Ho, A. V. Filippenko, and W. L. W. Sargent. Evidence for a Supermassive Black Hole in the S0 Galaxy NGC 3245. *The Astrophysical Journal*, 555(2):685–708, July 2001. doi: 10.1086/321523.

A. J. Barth, B. D. Boizelle, J. Darling, A. J. Baker, D. A. Buote, L. C. Ho, and J. L. Walsh. Measurement of the Black Hole Mass in NGC 1332 from ALMA Observations at 0.044 arcsecond Resolution. *The Astrophysical Journal Letters*, 822(2):L28, May 2016a. doi: 10.3847/2041-8205/822/2/L28.

A. J. Barth, J. Darling, A. J. Baker, B. D. Boizelle, D. A. Buote, L. C. Ho, and J. L. Walsh. Toward Precision Black Hole Masses with ALMA: NGC 1332 as a Case Study in Molecular Disk Dynamics. *The Astrophysical Journal*, 823(1):51, May 2016b. doi: 10.3847/0004-637X/823/1/51.

K. G. Begeman. HI rotation curves of spiral galaxies. I. NGC 3198. *Astronomy & Astrophysics*, 223:47–60, Oct. 1989.

J. Binney and G. A. Mamon. M/L and velocity anisotropy from observations of spherical galaxies, of must M 87 have a massive black hole ? *Monthly Notices of the Royal Astronomical Society*, 200:361–375, July 1982. doi: 10.1093/mnras/200.2.361.

J. P. Blakeslee, J. B. Jensen, C.-P. Ma, P. A. Milne, and J. E. Greene. The Hubble Constant from Infrared Surface Brightness Fluctuation Distances. *The Astrophysical Journal*, 911 (1):65, Apr. 2021. doi: 10.3847/1538-4357/abe86a.

B. Boizelle. *Precision Black Hole Mass Measurement in Luminous Early-Type Galaxies*. PhD thesis, University of California, Irvine, 2018.

B. D. Boizelle, A. J. Barth, J. Darling, A. J. Baker, D. A. Buote, L. C. Ho, and J. L. Walsh. ALMA Observations of Circumnuclear Disks in Early-type Galaxies: ^{12}CO(2−1) and Continuum Properties. *The Astrophysical Journal*, 845(2):170, Aug. 2017. doi: 10.3847/1538-4357/aa8266.

B. D. Boizelle, K. Nyland, and T. A. Davis. Precision Gas-dynamical Mass Measurement of Supermassive Black Holes with the ngVLA. In E. Murphy, editor, *Science with a Next Generation Very Large Array*, volume 517 of *Astronomical Society of the Pacific Conference Series*, page 509, Dec. 2018. doi: 10.48550/arXiv.1810.06615.

B. D. Boizelle, A. J. Barth, J. L. Walsh, D. A. Buote, A. J. Baker, J. Darling, and L. C. Ho. A Precision Measurement of the Mass of the Black Hole in NGC 3258 from High-resolution ALMA Observations of Its Circumnuclear Disk. *The Astrophysical Journal*, 881 (1):10, Aug 2019. doi: 10.3847/1538-4357/ab2a0a.

B. D. Boizelle, J. L. Walsh, A. J. Barth, D. A. Buote, A. J. Baker, J. Darling, L. C. Ho, J. Cohn, and K. M. Kabasares. Black Hole Mass Measurements of Radio Galaxies NGC 315 and NGC 4261 Using ALMA CO Observations. *The Astrophysical Journal*, 908(1): 19, Feb. 2021. doi: 10.3847/1538-4357/abd24d.

A. D. Bolatto, T. Wong, D. Utomo, L. Blitz, S. N. Vogel, S. F. Sánchez, J. Barrera-Ballesteros, Y. Cao, D. Colombo, H. Dannerbauer, R. García-Benito, R. Herrera-Camus, B. Husemann, V. Kalinova, A. K. Leroy, G. Leung, R. C. Levy, D. Mast, E. Ostriker, E. Rosolowsky, K. M. Sandstrom, P. Teuben, G. van de Ven, and F. Walter. The EDGE-CALIFA Survey: Interferometric Observations of 126 Galaxies with CARMA. *The Astrophysical Journal*, 846(2):159, Sept. 2017. doi: 10.3847/1538-4357/aa86aa.

P. Bonfini, O. González-Martín, J. Fritz, T. Bitsakis, G. Bruzual, and B. Cervantes Sodi. Modelling dust rings in early-type galaxies through a sequence of radiative transfer simulations and 2D image fitting. *Monthly Notices of the Royal Astronomical Society*, 478(1): 1161–1169, July 2018. doi: 10.1093/mnras/sty1087.

J. Bovy. *Dynamics and Astrophysics of Galaxies. Princeton University Press, Princeton, NJ (in preparation)*. 2023.

E. M. Cackett, M. C. Bentz, and E. Kara. Reverberation mapping of active galactic nuclei: from X-ray corona to dusty torus. *iScience*, 24(6):102557, June 2021. doi: 10.1016/j.isci.2021.102557.

P. Camps and M. Baes. SKIRT: An advanced dust radiative transfer code with a user-friendly architecture. *Astronomy and Computing*, 9:20–33, Mar. 2015. doi: 10.1016/j.ascom.2014.10.004.

M. Cappellari. Efficient multi-Gaussian expansion of galaxies. *Monthly Notices of the Royal Astronomical Society*, 333(2):400–410, June 2002. doi: 10.1046/j.1365-8711.2002.05412.x.

C. L. Carilli and F. Walter. Cool Gas in High-Redshift Galaxies. *Annual Review of Astronomy and Astrophysics*, 51(1):105–161, Aug. 2013. doi: 10.1146/annurev-astro-082812-140953.

G. Chabrier. Galactic Stellar and Substellar Initial Mass Function. *Publications of the Astronomical Society of the Pacific*, 115(809):763–795, July 2003. doi: 10.1086/376392.

L. Coccato, M. Sarzi, A. Pizzella, E. M. Corsini, E. Dalla Bontà, and F. Bertola. NGC 4435: a bulge-dominated galaxy with an unforeseen low-mass central black hole. *Monthly Notices of the Royal Astronomical Society*, 366(3):1050–1066, Mar. 2006. doi: 10.1111/j.1365-2966.2005.09901.x.

J. H. Cohn, J. L. Walsh, B. D. Boizelle, A. J. Barth, K. Gebhardt, K. Gültekin, A. Yıldırım, D. A. Buote, J. Darling, A. J. Baker, L. C. Ho, and K. M. Kabasares. An ALMA Gas-dynamical Mass Measurement of the Supermassive Black Hole in the Local Compact Galaxy UGC 2698. *The Astrophysical Journal*, 919(2):77, Oct. 2021. doi: 10.3847/1538-4357/ac0f78.

F. Combes, L. M. Young, and M. Bureau. Molecular gas and star formation in the SAURON early-type galaxies. *Monthly Notices of the Royal Astronomical Society*, 377(4):1795–1807, June 2007. doi: 10.1111/j.1365-2966.2007.11759.x.

F. Combes, S. García-Burillo, A. Audibert, L. Hunt, A. Eckart, S. Aalto, V. Casasola, F. Boone, M. Krips, S. Viti, K. Sakamoto, S. Muller, K. Dasyra, P. van der Werf, and S. Martin. ALMA observations of molecular tori around massive black holes. *Astronomy & Astrophysics*, 623:A79, Mar. 2019. doi: 10.1051/0004-6361/201834560.

I. Czekala, S. M. Andrews, E. L. N. Jensen, K. G. Stassun, G. Torres, and D. J. Wilner. A Disk-based Dynamical Mass Estimate for the Young Binary AK Sco. *The Astrophysical Journal*, 806(2):154, June 2015. doi: 10.1088/0004-637X/806/2/154.

T. A. Davis. A figure of merit for black hole mass measurements with molecular gas. *Monthly Notices of the Royal Astronomical Society*, 443(1):911–918, Sept. 2014. doi: 10.1093/mnras/stu1163.

T. A. Davis, K. Alatalo, M. Bureau, M. Cappellari, N. Scott, L. M. Young, L. Blitz, A. Crocker, E. Bayet, M. Bois, F. Bournaud, R. L. Davies, P. T. de Zeeuw, P.-A. Duc, E. Emsellem, S. Khochfar, D. Krajnović, H. Kuntschner, P.-Y. Lablanche, R. M. McDermid, R. Morganti, T. Naab, T. Oosterloo, M. Sarzi, P. Serra, and A.-M. Weijmans. The ATLAS^{3D} Project - XIV. The extent and kinematics of the molecular gas in early-type galaxies. *Monthly Notices of the Royal Astronomical Society*, 429(1):534–555, Feb. 2013a. doi: 10.1093/mnras/sts353.

T. A. Davis, M. Bureau, M. Cappellari, M. Sarzi, and L. Blitz. A black-hole mass measurement from molecular gas kinematics in NGC4526. *Nature*, 494(7437):328–330, Feb. 2013b. doi: 10.1038/nature11819.

T. A. Davis, M. Bureau, K. Onishi, M. Cappellari, S. Iguchi, and M. Sarzi. WISDOM Project - II. Molecular gas measurement of the supermassive black hole mass in NGC 4697. *Monthly Notices of the Royal Astronomical Society*, 468(4):4675–4690, July 2017. doi: 10.1093/mnras/stw3217.

T. A. Davis, M. Bureau, K. Onishi, F. van de Voort, M. Cappellari, S. Iguchi, L. Liu, E. V. North, M. Sarzi, and M. D. Smith. WISDOM Project - III. Molecular gas measurement of the supermassive black hole mass in the barred lenticular galaxy NGC4429. *Monthly Notices of the Royal Astronomical Society*, 473(3):3818–3834, Jan. 2018. doi: 10.1093/mnras/stx2600.

T. A. Davis, D. D. Nguyen, A. C. Seth, J. E. Greene, K. Nyland, A. J. Barth, M. Bureau, M. Cappellari, M. den Brok, S. Iguchi, F. Lelli, L. Liu, N. Neumayer, E. V. North, K. Onishi, M. Sarzi, M. D. Smith, and T. G. Williams. Revealing the intermediate-mass black hole at the heart of the dwarf galaxy NGC 404 with sub-parsec resolution ALMA observations. *Monthly Notices of the Royal Astronomical Society*, 496(4):4061–4078, July 2020. doi: 10.1093/mnras/staa1567.

G. De Geyter, M. Baes, J. Fritz, and P. Camps. FitSKIRT: genetic algorithms to automatically fit dusty galaxies with a Monte Carlo radiative transfer code. *Astronomy & Astrophysics*, 550:A74, Feb. 2013. doi: 10.1051/0004-6361/201220126.

G. de Vaucouleurs, A. de Vaucouleurs, J. Corwin, Herold G., R. J. Buta, G. Paturel, and P. Fouque. *Third Reference Catalogue of Bright Galaxies*. 1991.

M. den Brok, A. C. Seth, A. J. Barth, D. J. Carson, N. Neumayer, M. Cappellari, V. P. Debattista, L. C. Ho, C. E. Hood, and R. M. McDermid. Measuring the Mass of the Central Black Hole in the Bulgeless Galaxy NGC 4395 from Gas Dynamical Modeling. *The Astrophysical Journal*, 809(1):101, Aug. 2015. doi: 10.1088/0004-637X/809/1/101.

E. M. Di Teodoro and F. Fraternali. ^{3D} BAROLO: a new 3D algorithm to derive rotation curves of galaxies. *Monthly Notices of the Royal Astronomical Society*, 451(3):3021–3033, Aug. 2015. doi: 10.1093/mnras/stv1213.

T. Do, A. Hees, A. Ghez, G. D. Martinez, D. S. Chu, S. Jia, S. Sakai, J. R. Lu, A. K. Gautam, K. K. O'Neil, E. E. Becklin, M. R. Morris, K. Matthews, S. Nishiyama, R. Campbell, S. Chappell, Z. Chen, A. Ciurlo, A. Dehghanfar, E. Gallego-Cano, W. E. Kerzendorf, J. E. Lyke, S. Naoz, H. Saida, R. Schödel, M. Takahashi, Y. Takamori, G. Witzel, and P. Wizinowich. Relativistic redshift of the star S0-2 orbiting the Galactic Center supermassive black hole. *Science*, 365(6454):664–668, Aug. 2019. doi: 10.1126/science.aav8137.

A. Dressler and D. O. Richstone. Stellar Dynamics in the Nuclei of M31 and M32: Evidence for Massive Black Holes. *The Astrophysical Journal*, 324:701, Jan. 1988. doi: 10.1086/165930.

M. J. Duncan and J. C. Wheeler. Anisotropic velocity distributions in M87 - Is a supermassive black hole necessary. *The Astrophysical Journal Letters*, 237:L27–L31, Apr. 1980. doi: 10.1086/183228.

E. Emsellem, G. Monnet, and R. Bacon. The multi-gaussian expansion method: a tool for building realistic photometric and kinematical models of stellar systems I. The formalism. *Astronomy & Astrophysics*, 285:723–738, May 1994.

P. Erwin. IMFIT: A Fast, Flexible New Program for Astronomical Image Fitting. *The Astrophysical Journal*, 799(2):226, Feb. 2015. doi: 10.1088/0004-637X/799/2/226.

Event Horizon Telescope Collaboration, K. Akiyama, A. Alberdi, W. Alef, K. Asada, R. Azulay, A.-K. Baczko, D. Ball, M. Baloković, J. Barrett, D. Bintley, L. Blackburn, W. Boland, K. L. Bouman, G. C. Bower, M. Bremer, C. D. Brinkerink, R. Brissenden, S. Britzen, A. E. Broderick, D. Broguiere, T. Bronzwaer, D.-Y. Byun, J. E. Carlstrom, A. Chael, C.-k. Chan, S. Chatterjee, K. Chatterjee, M.-T. Chen, Y. Chen, I. Cho, P. Christian, J. E. Conway, J. M. Cordes, G. B. Crew, Y. Cui, J. Davelaar, M. De Laurentis, R. Deane, J. Dempsey, G. Desvignes, J. Dexter, S. S. Doeleman, R. P. Eatough, H. Falcke, V. L. Fish, E. Fomalont, R. Fraga-Encinas, W. T. Freeman, P. Friberg, C. M. Fromm, J. L. Gómez, P. Galison, C. F. Gammie, R. García, O. Gentaz, B. Georgiev, C. Goddi, R. Gold, M. Gu, M. Gurwell, K. Hada, M. H. Hecht, R. Hesper, L. C. Ho, P. Ho, M. Honma, C.-W. L. Huang, L. Huang, D. H. Hughes, S. Ikeda, M. Inoue, S. Issaoun, D. J. James, B. T. Jannuzi, M. Janssen, B. Jeter, W. Jiang, M. D. Johnson, S. Jorstad, T. Jung, M. Karami, R. Karuppusamy, T. Kawashima, G. K. Keating, M. Kettenis, J.-Y. Kim, J. Kim, J. Kim, M. Kino, J. Y. Koay, P. M. Koch, S. Koyama, M. Kramer, C. Kramer, T. P. Krichbaum, C.-Y. Kuo, T. R. Lauer, S.-S. Lee, Y.-R. Li, Z. Li, M. Lindqvist, K. Liu, E. Liuzzo, W.-P. Lo, A. P. Lobanov, L. Loinard, C. Lonsdale, R.-S. Lu, N. R. MacDonald, J. Mao, S. Markoff, D. P. Marrone, A. P. Marscher, I. Martí-Vidal, S. Matsushita, L. D. Matthews, L. Medeiros, K. M. Menten, Y. Mizuno, I. Mizuno, J. M. Moran, K. Moriyama, M. Moscibrodzka, C. Müller, H. Nagai, N. M. Nagar, M. Nakamura, R. Narayan, G. Narayanan, I. Natarajan, R. Neri, C. Ni, A. Noutsos, H. Okino, H. Olivares, G. N. Ortiz-León, T. Oyama, F. Özel, D. C. M. Palumbo, N. Patel, U.-L. Pen, D. W. Pesce, V. Piétu, R. Plambeck, A. PopStefanija, O. Porth, B. Prather, J. A. Preciado-López, D. Psaltis, H.-Y. Pu, V. Ramakrishnan, R. Rao, M. G. Rawlings, A. W. Raymond, L. Rezzolla, B. Ripperda, F. Roelofs, A. Rogers, E. Ros, M. Rose, A. Roshanineshat, H. Rottmann, A. L. Roy, C. Ruszczyk, B. R. Ryan, K. L. J. Rygl, S. Sánchez, D. Sánchez-Arguelles, M. Sasada, T. Savolainen, F. P. Schloerb, K.-F. Schuster, L. Shao, Z. Shen, D. Small, B. W. Sohn, J. SooHoo, F. Tazaki, P. Tiede, R. P. J. Tilanus, M. Titus, K. Toma, P. Torne, T. Trent, S. Trippe, S. Tsuda, I. van Bemmel, H. J. van Langevelde, D. R. van Rossum, J. Wagner, J. Wardle, J. Weintroub, N. Wex, R. Wharton, M. Wielgus, G. N. Wong, Q. Wu, K. Young, A. Young, Z. Younsi, F. Yuan, Y.-F. Yuan, J. A. Zensus, G. Zhao, S.-S. Zhao, Z. Zhu, J.-C. Algaba, A. Allardi, R. Amestica, J. Anczarski, U. Bach, F. K. Baganoff, C. Beaudoin, B. A. Benson, R. Berthold, J. M. Blanchard, R. Blundell, S. Bustamente, R. Cappallo, E. Castillo-Domínguez, C.-C. Chang, S.-H. Chang, S.-C. Chang, C.-C. Chen, R. Chilson, T. C. Chuter, R. Córdova Rosado, I. M. Coulson, T. M. Crawford, J. Crowley, J. David, M. Derome, M. Dexter, S. Dornbusch, K. A. Dudevoir, S. A. Dzib, A. Eckart, C. Eckert, N. R. Erickson, W. B. Everett, A. Faber, J. R. Farah, V. Fath, T. W. Folkers, D. C. Forbes, R. Freund, A. I. Gómez-Ruiz, D. M. Gale, F. Gao, G. Geertsema, D. A. Graham, C. H. Greer, R. Grosslein, F. Gueth, D. Haggard, N. W. Halverson, C.-C. Han, K.-C. Han, J. Hao, Y. Hasegawa, J. W. Henning, A. Hernández-Gómez, R. Herrero-Illana, S. Heyminck, A. Hirota, J. Hoge, Y.-D. Huang, C. M. V. Impellizzeri, H. Jiang, A. Kamble, R. Keisler, K. Kimura, Y. Kono, D. Kubo, J. Kuroda, R. Lacasse, R. A. Laing, E. M. Leitch, C.-T. Li, L. C. C. Lin, C.-T. Liu, K.-Y. Liu, L.-M. Lu, R. G. Marson, P. L. Martin-Cocher, K. D. Massingill,

C. Matulonis, M. P. McColl, S. R. McWhirter, H. Messias, Z. Meyer-Zhao, D. Michalik, A. Montaña, W. Montgomerie, M. Mora-Klein, D. Muders, A. Nadolski, S. Navarro, J. Neilsen, C. H. Nguyen, H. Nishioka, T. Norton, M. A. Nowak, G. Nystrom, H. Ogawa, P. Oshiro, T. Oyama, H. Parsons, S. N. Paine, J. Peñalver, N. M. Phillips, M. Poirier, N. Pradel, R. A. Primiani, P. A. Raffin, A. S. Rahlin, G. Reiland, C. Risacher, I. Ruiz, A. F. Sáez-Madaín, R. Sassella, P. Schellart, P. Shaw, K. M. Silva, H. Shiokawa, D. R. Smith, W. Snow, K. Souccar, D. Sousa, T. K. Sridharan, R. Srinivasan, W. Stahm, A. A. Stark, K. Story, S. T. Timmer, L. Vertatschitsch, C. Walther, T.-S. Wei, N. Whitehorn, A. R. Whitney, D. P. Woody, J. G. A. Wouterloot, M. Wright, P. Yamaguchi, C.-Y. Yu, M. Zeballos, S. Zhang, and L. Ziurys. First M87 Event Horizon Telescope Results. I. The Shadow of the Supermassive Black Hole. *The Astrophysical Journal Letters*, 875(1):L1, Apr. 2019. doi: 10.3847/2041-8213/ab0ec7.

Event Horizon Telescope Collaboration, K. Akiyama, A. Alberdi, W. Alef, J. C. Algaba, R. Anantua, K. Asada, R. Azulay, U. Bach, A.-K. Baczko, D. Ball, M. Baloković, J. Barrett, M. Bauböck, B. A. Benson, D. Bintley, L. Blackburn, R. Blundell, K. L. Bouman, G. C. Bower, H. Boyce, M. Bremer, C. D. Brinkerink, R. Brissenden, S. Britzen, A. E. Broderick, D. Broguiere, T. Bronzwaer, S. Bustamante, D.-Y. Byun, J. E. Carlstrom, C. Ceccobello, A. Chael, C.-k. Chan, K. Chatterjee, S. Chatterjee, M.-T. Chen, Y. Chen, X. Cheng, I. Cho, P. Christian, N. S. Conroy, J. E. Conway, J. M. Cordes, T. M. Crawford, G. B. Crew, A. Cruz-Osorio, Y. Cui, J. Davelaar, M. De Laurentis, R. Deane, J. Dempsey, G. Desvignes, J. Dexter, V. Dhruv, S. S. Doeleman, S. Dougal, S. A. Dzib, R. P. Eatough, R. Emami, H. Falcke, J. Farah, V. L. Fish, E. Fomalont, H. A. Ford, R. Fraga-Encinas, W. T. Freeman, P. Friberg, C. M. Fromm, A. Fuentes, P. Galison, C. F. Gammie, R. García, O. Gentaz, B. Georgiev, C. Goddi, R. Gold, A. I. Gómez-Ruiz, J. L. Gómez, M. Gu, M. Gurwell, K. Hada, D. Haggard, K. Haworth, M. H. Hecht, R. Hesper, D. Heumann, L. C. Ho, P. Ho, M. Honma, C.-W. L. Huang, L. Huang, D. H. Hughes, S. Ikeda, C. M. V. Impellizzeri, M. Inoue, S. Issaoun, D. J. James, B. T. Jannuzi, M. Janssen, B. Jeter, W. Jiang, A. Jiménez-Rosales, M. D. Johnson, S. Jorstad, A. V. Joshi, T. Jung, M. Karami, R. Karuppusamy, T. Kawashima, G. K. Keating, M. Kettenis, D.-J. Kim, J.-Y. Kim, J. Kim, J. Kim, M. Kino, J. Y. Koay, P. Kocherlakota, Y. Kofuji, P. M. Koch, S. Koyama, C. Kramer, M. Kramer, T. P. Krichbaum, C.-Y. Kuo, N. La Bella, T. R. Lauer, D. Lee, S.-S. Lee, P. K. Leung, A. Levis, Z. Li, R. Lico, G. Lindahl, M. Lindqvist, M. Lisakov, J. Liu, K. Liu, E. Liuzzo, W.-P. Lo, A. P. Lobanov, L. Loinard, C. J. Lonsdale, R.-S. Lu, J. Mao, N. Marchili, S. Markoff, D. P. Marrone, A. P. Marscher, I. Martí-Vidal, S. Matsushita, L. D. Matthews, L. Medeiros, K. M. Menten, D. Michalik, I. Mizuno, Y. Mizuno, J. M. Moran, K. Moriyama, M. Moscibrodzka, C. Müller, A. Mus, G. Musoke, I. Myserlis, A. Nadolski, H. Nagai, N. M. Nagar, M. Nakamura, R. Narayan, G. Narayanan, I. Natarajan, A. Nathanail, S. N. Fuentes, J. Neilsen, R. Neri, C. Ni, A. Noutsos, M. A. Nowak, J. Oh, H. Okino, H. Olivares, G. N. Ortiz-León, T. Oyama, F. Özel, D. C. M. Palumbo, G. F. Paraschos, J. Park, H. Parsons, N. Patel, U.-L. Pen, D. W. Pesce, V. Piétu, R. Plambeck, A. PopStefanija, O. Porth, F. M. Pötzl, B. Prather, J. A. Preciado-López, D. Psaltis, H.-Y. Pu, V. Ramakrishnan, R. Rao, M. G. Rawlings, A. W. Raymond, L. Rezzolla, A. Ricarte, B. Ripperda, F. Roelofs, A. Rogers, E. Ros, C. Romero-Cañizales, A. Roshanineshat, H. Rottmann, A. L. Roy, I. Ruiz, C. Ruszczyk,

K. L. J. Rygl, S. Sánchez, D. Sánchez-Argüelles, M. Sánchez-Portal, M. Sasada, K. Satapathy, T. Savolainen, F. P. Schloerb, J. Schonfeld, K.-F. Schuster, L. Shao, Z. Shen, D. Small, B. W. Sohn, J. SooHoo, K. Souccar, H. Sun, F. Tazaki, A. J. Tetarenko, P. Tiede, R. P. J. Tilanus, M. Titus, P. Torne, E. Traianou, T. Trent, S. Trippe, M. Turk, I. van Bemmel, H. J. van Langevelde, D. R. van Rossum, J. Vos, J. Wagner, D. Ward-Thompson, J. Wardle, J. Weintroub, N. Wex, R. Wharton, M. Wielgus, K. Wiik, G. Witzel, M. F. Wondrak, G. N. Wong, Q. Wu, P. Yamaguchi, D. Yoon, A. Young, K. Young, Z. Younsi, F. Yuan, Y.-F. Yuan, J. A. Zensus, S. Zhang, G.-Y. Zhao, S.-S. Zhao, C. Agurto, A. Allardi, R. Amestica, J. P. Araneda, O. Arriagada, J. L. Berghuis, A. Bertarini, R. Berthold, J. Blanchard, K. Brown, M. Cárdenas, M. Cantzler, P. Caro, E. Castillo-Domínguez, T. L. Chan, C.-C. Chang, D. O. Chang, S.-H. Chang, S.-C. Chang, C.-C. Chen, R. Chilson, T. C. Chuter, M. Ciechanowicz, E. Colin-Beltran, I. M. Coulson, J. Crowley, N. Degenaar, S. Dornbusch, C. A. Durán, W. B. Everett, A. Faber, K. Forster, M. M. Fuchs, D. M. Gale, G. Geertsema, E. González, D. Graham, F. Gueth, N. W. Halverson, C.-C. Han, K.-C. Han, Y. Hasegawa, J. L. Hernández-Rebollar, C. Herrera, R. Herrero-Illana, S. Heyminck, A. Hirota, J. Hoge, S. R. Hostler Schimpf, R. E. Howie, Y.-D. Huang, H. Jiang, H. Jinchi, D. John, K. Kimura, T. Klein, D. Kubo, J. Kuroda, C. Kwon, R. Lacasse, R. Laing, E. M. Leitch, C.-T. Li, C.-T. Liu, K.-Y. Liu, L. C. C. Lin, L.-M. Lu, F. Mac-Auliffe, P. Martin-Cocher, C. Matulonis, J. K. Maute, H. Messias, Z. Meyer-Zhao, A. Montaña, F. Montenegro-Montes, W. Montgomerie, M. E. Moreno Nolasco, D. Mudders, H. Nishioka, T. J. Norton, G. Nystrom, H. Ogawa, R. Olivares, P. Oshiro, J. P. Pérez-Beaupuits, R. Parra, N. M. Phillips, M. Poirier, N. Pradel, R. Qiu, P. A. Raffin, A. S. Rahlin, J. Ramírez, S. Ressler, M. Reynolds, I. Rodríguez-Montoya, A. F. Saez-Madain, J. Santana, P. Shaw, L. E. Shirkey, K. M. Silva, W. Snow, D. Sousa, T. K. Sridharan, W. Stahm, A. A. Stark, J. Test, K. Torstensson, P. Venegas, C. Walther, T.-S. Wei, C. White, G. Wieching, R. Wijnands, J. G. A. Wouterloot, C.-Y. Yu, W. Yu , and M. Zeballos. First Sagittarius A* Event Horizon Telescope Results. I. The Shadow of the Supermassive Black Hole in the Center of the Milky Way. *The Astrophysical Journal Letters*, 930(2):L12, May 2022. doi: 10.3847/2041-8213/ac6674.

S. M. Faber, S. Tremaine, E. A. Ajhar, Y.-I. Byun, A. Dressler, K. Gebhardt, C. Grillmair, J. Kormendy, T. R. Lauer, and D. Richstone. The Centers of Early-Type Galaxies with HST. IV. Central Parameter Relations. *The Astronomical Journal*, 114:1771, Nov. 1997. doi: 10.1086/118606.

L. Ferrarese and D. Merritt. A Fundamental Relation between Supermassive Black Holes and Their Host Galaxies. *The Astrophysical Journal Letters*, 539(1):L9–L12, Aug. 2000. doi: 10.1086/312838.

H. Gao, L. C. Ho, A. J. Barth, and Z.-Y. Li. The Carnegie-Irvine Galaxy Survey. VIII. Demographics of Bulges along the Hubble Sequence. *The Astrophysical Journal Supplement*, 244(2):34, Oct. 2019. doi: 10.3847/1538-4365/ab3c6a.

K. Gebhardt and J. Thomas. The Black Hole Mass, Stellar Mass-to-Light Ratio, and Dark Halo in M87. *The Astrophysical Journal*, 700(2):1690–1701, Aug. 2009. doi: 10.1088/0004-637X/700/2/1690.

K. Gebhardt, R. Bender, G. Bower, A. Dressler, S. M. Faber, A. V. Filippenko, R. Green, C. Grillmair, L. C. Ho, J. Kormendy, T. R. Lauer, J. Magorrian, J. Pinkney, D. Richstone, and S. Tremaine. A Relationship between Nuclear Black Hole Mass and Galaxy Velocity Dispersion. *The Astrophysical Journal Letters*, 539(1):L13–L16, Aug. 2000. doi: 10.1086/312840.

R. Genzel, D. Hollenbach, and C. H. Townes. The nucleus of our Galaxy. *Reports on Progress in Physics*, 57(5):417–479, May 1994. doi: 10.1088/0034-4885/57/5/001.

A. M. Ghez, B. L. Klein, M. Morris, and E. E. Becklin. High Proper-Motion Stars in the Vicinity of Sagittarius A*: Evidence for a Supermassive Black Hole at the Center of Our Galaxy. *The Astrophysical Journal*, 509(2):678–686, Dec. 1998. doi: 10.1086/306528.

A. M. Ghez, S. Salim, S. D. Hornstein, A. Tanner, J. R. Lu, M. Morris, E. E. Becklin, and G. Duchêne. Stellar Orbits around the Galactic Center Black Hole. *The Astrophysical Journal*, 620(2):744–757, Feb. 2005. doi: 10.1086/427175.

A. W. Graham, P. Erwin, I. Trujillo, and A. Asensio Ramos. A New Empirical Model for the Structural Analysis of Early-Type Galaxies, and A Critical Review of the Nuker Model. *The Astronomical Journal*, 125(6):2951–2963, June 2003. doi: 10.1086/375320.

GRAVITY Collaboration, R. Abuter, N. Aimar, A. Amorim, J. Ball, M. Bauböck, J. P. Berger, H. Bonnet, G. Bourdarot, W. Brandner, V. Cardoso, Y. Clénet, Y. Dallilar, R. Davies, P. T. de Zeeuw, J. Dexter, A. Drescher, F. Eisenhauer, N. M. Förster Schreiber, A. Foschi, P. Garcia, F. Gao, E. Gendron, R. Genzel, S. Gillessen, M. Habibi, X. Haubois, G. Heißel, T. Henning, S. Hippler, M. Horrobin, L. Jochum, L. Jocou, A. Kaufer, P. Kervella, S. Lacour, V. Lapeyrère, J. B. Le Bouquin, P. Léna, D. Lutz, T. Ott, T. Paumard, K. Perraut, G. Perrin, O. Pfuhl, S. Rabien, J. Shangguan, T. Shimizu, S. Scheithauer, J. Stadler, A. W. Stephens, O. Straub, C. Straubmeier, E. Sturm, L. J. Tacconi, K. R. W. Tristram, F. Vincent, S. von Fellenberg, F. Widmann, E. Wieprecht, E. Wiezorrek, J. Woillez, S. Yazici, and A. Young. Mass distribution in the Galactic Center based on interferometric astrometry of multiple stellar orbits. *Astronomy & Astrophysics*, 657: L12, Jan. 2022. doi: 10.1051/0004-6361/202142465.

R. J. Harms, H. C. Ford, Z. I. Tsvetanov, G. F. Hartig, L. L. Dressel, G. A. Kriss, R. Bohlin, A. F. Davidsen, B. Margon, and A. K. Kochhar. HST FOS Spectroscopy of M87: Evidence for a Disk of Ionized Gas around a Massive Black Hole. *The Astrophysical Journal Letters*, 435:L35, Nov. 1994. doi: 10.1086/187588.

L. C. Ho, M. Sarzi, H.-W. Rix, J. C. Shields, G. Rudnick, A. V. Filippenko, and A. J. Barth. An Efficient Strategy to Select Targets for Gasdynamical Measurements of Black Hole Masses Using the Hubble Space Telescope. *Publications of the Astronomical Society of the Pacific*, 114(792):137–143, Feb. 2002. doi: 10.1086/338546.

D. A. Hunter, L. Laufman, S.-H. Oh, S. E. Levine, and C. E. Simpson. Gas Engaged in Noncircular Motions in LITTLE THINGS Dwarf Irregular Galaxies. *The Astronomical Journal*, 158(1):23, July 2019. doi: 10.3847/1538-3881/ab223d.

T. H. Jarrett, T. Chester, R. Cutri, S. E. Schneider, and J. P. Huchra. The 2MASS Large Galaxy Atlas. *The Astronomical Journal*, 125(2):525–554, Feb. 2003. doi: 10.1086/345794.

J. B. Jensen, J. L. Tonry, B. J. Barris, R. I. Thompson, M. C. Liu, M. J. Rieke, E. A. Ajhar, and J. P. Blakeslee. Measuring Distances and Probing the Unresolved Stellar Populations of Galaxies Using Infrared Surface Brightness Fluctuations. *The Astrophysical Journal*, 583(2):712–726, Feb. 2003. doi: 10.1086/345430.

D. H. Jones, M. A. Read, W. Saunders, M. Colless, T. Jarrett, Q. A. Parker, A. P. Fairall, T. Mauch, E. M. Sadler, F. G. Watson, D. Burton, L. A. Campbell, P. Cass, S. M. Croom, J. Dawe, K. Fiegert, L. Frankcombe, M. Hartley, J. Huchra, D. James, E. Kirby, O. Lahav, J. Lucey, G. A. Mamon, L. Moore, B. A. Peterson, S. Prior, D. Proust, K. Russell, V. Safouris, K.-I. Wakamatsu, E. Westra, and M. Williams. The 6dF Galaxy Survey: final redshift release (DR3) and southern large-scale structures. *Monthly Notices of the Royal Astronomical Society*, 399(2):683–698, Oct. 2009. doi: 10.1111/j.1365-2966.2009.15338.x.

K. M. Kabasares, A. J. Barth, D. A. Buote, B. D. Boizelle, J. L. Walsh, A. J. Baker, J. Darling, L. C. Ho, and J. Cohn. Black Hole Mass Measurements of Early-type Galaxies NGC 1380 and NGC 6861 through ALMA and HST Observations and Gas-dynamical Modeling. *The Astrophysical Journal*, 934(2):162, Aug. 2022. doi: 10.3847/1538-4357/ac7a38.

W. D. Kenworthy, A. G. Riess, D. Scolnic, W. Yuan, J. Luis Bernal, D. Brout, S. Casertano, D. O. Jones, L. Macri, and E. R. Peterson. Measurements of the Hubble Constant with a Two-rung Distance Ladder: Two Out of Three Ain't Bad. *The Astrophysical Journal*, 935 (2):83, Aug. 2022. doi: 10.3847/1538-4357/ac80bd.

J. Kormendy. Evidence for a Supermassive Black Hole in the Nucleus of M31. *The Astrophysical Journal*, 325:128, Feb. 1988. doi: 10.1086/165988.

J. Kormendy and L. C. Ho. Coevolution (Or Not) of Supermassive Black Holes and Host Galaxies. *Annual Review of Astronomy and Astrophysics*, 51(1):511–653, Aug. 2013. doi: 10.1146/annurev-astro-082708-101811.

J. Kormendy and D. Richstone. Inward Bound—The Search For Supermassive Black Holes In Galactic Nuclei. *Annual Review of Astronomy and Astrophysics*, 33:581, Jan. 1995. doi: 10.1146/annurev.aa.33.090195.003053.

J. Krist and R. Hook. The Tiny Tim User's Guide. `http://www.stsci.edu/hst/observatory/focus/TinyTim`, 2004.

P. Kroupa. On the variation of the initial mass function. *Monthly Notices of the Royal Astronomical Society*, 322(2):231–246, Apr. 2001. doi: 10.1046/j.1365-8711.2001.04022.x.

C. Y. Kuo, J. A. Braatz, J. J. Condon, C. M. V. Impellizzeri, K. Y. Lo, I. Zaw, M. Schenker, C. Henkel, M. J. Reid, and J. E. Greene. The Megamaser Cosmology Project. III. Accurate Masses of Seven Supermassive Black Holes in Active Galaxies with Circumnuclear Megamaser Disks. *The Astrophysical Journal*, 727(1):20, Jan. 2011. doi: 10.1088/0004-637X/727/1/20.

T. R. Lauer, J. L. Tonry, M. Postman, E. A. Ajhar, and J. A. Holtzman. The Far-Field Hubble Constant. *The Astrophysical Journal*, 499(2):577–588, May 1998. doi: 10.1086/305671.

T. R. Lauer, K. Gebhardt, S. M. Faber, D. Richstone, S. Tremaine, J. Kormendy, M. C. Aller, R. Bender, A. Dressler, A. V. Filippenko, R. Green, and L. C. Ho. The Centers of Early-Type Galaxies with Hubble Space Telescope. VI. Bimodal Central Surface Brightness Profiles. *The Astrophysical Journal*, 664(1):226–256, July 2007. doi: 10.1086/519229.

T. E. Lavezzi, J. M. Dickey, F. Casoli, and I. Kazès. A Dual-Transition Survey of CO in the Coma Cluster of Galaxies. *The Astronomical Journal*, 117(5):1995–2009, May 1999. doi: 10.1086/300845.

F. Lelli, T. A. Davis, M. Bureau, M. Cappellari, L. Liu, I. Ruffa, M. D. Smith, and T. G. Williams. WISDOM Project - XIII. Feeding molecular gas to the supermassive black hole in the starburst AGN-host galaxy Fairall 49. *Monthly Notices of the Royal Astronomical Society*, 516(3):4066–4083, Nov. 2022. doi: 10.1093/mnras/stac2493.

K. Levenberg. A method for the solution of certain problems in least squares. *Quarterly Journal on Applied Mathematics*, (2):164–168, 1944.

Z.-Y. Li, L. C. Ho, A. J. Barth, and C. Y. Peng. The Carnegie-Irvine Galaxy Survey. II. Isophotal Analysis. *The Astrophysical Journal Supplement*, 197(2):22, Dec. 2011. doi: 10.1088/0067-0049/197/2/22.

E. R. Liepold, C.-P. Ma, and J. L. Walsh. Keck Integral-field Spectroscopy of M87 Reveals an Intrinsically Triaxial Galaxy and a Revised Black Hole Mass. *The Astrophysical Journal Letters*, 945(2):L35, Mar. 2023. doi: 10.3847/2041-8213/acbbcf.

F. Long, S. M. Andrews, J. Vega, D. J. Wilner, C. J. Chandler, E. Ragusa, R. Teague, L. M. Pérez, N. Calvet, J. M. Carpenter, T. Henning, W. Kwon, H. Linz, and L. Ricci. The Architecture of the V892 Tau System: The Binary and Its Circumbinary Disk. *The Astrophysical Journal*, 915(2):131, July 2021. doi: 10.3847/1538-4357/abff53.

D. Lynden-Bell. Galactic Nuclei as Collapsed Old Quasars. *Nature*, 223(5207):690–694, Aug. 1969. doi: 10.1038/223690a0.

D. Lynden-Bell and M. J. Rees. On quasars, dust and the galactic centre. *mnras*, 152:461, Jan. 1971. doi: 10.1093/mnras/152.4.461.

F. Macchetto, A. Marconi, D. J. Axon, A. Capetti, W. Sparks, and P. Crane. The Supermassive Black Hole of M87 and the Kinematics of Its Associated Gaseous Disk. *The Astrophysical Journal*, 489(2):579–600, Nov. 1997. doi: 10.1086/304823.

M. E. Machacek, E. O'Sullivan, S. W. Randall, C. Jones, and W. R. Forman. The Mysterious Merger of NGC 6868 and NGC 6861 in the Telescopium Group. *The Astrophysical Journal*, 711(2):1316–1332, Mar. 2010. doi: 10.1088/0004-637X/711/2/1316.

D. Makarov, P. Prugniel, N. Terekhova, H. Courtois, and I. Vauglin. HyperLEDA. III. The catalogue of extragalactic distances. *Astronomy & Astrophysics*, 570:A13, Oct. 2014. doi: 10.1051/0004-6361/201423496.

E. Maoz. Dynamical Constraints on Alternatives to Supermassive Black Holes in Galactic Nuclei. *The Astrophysical Journal Letters*, 494(2):L181–L184, Feb. 1998. doi: 10.1086/311194.

D. W. Marquardt. An algorithm for least-squares estimation of nonlinear parameters. *Journal of the Society for Industrial and Applied Mathematics*, 11(2):431–441, 1963.

I. Martín-Navarro, M. Lyubenova, G. van de Ven, J. Falcón-Barroso, L. Coccato, E. M. Corsini, D. A. Gadotti, E. Iodice, F. La Barbera, R. M. McDermid, F. Pinna, M. Sarzi, S. Viaene, P. T. de Zeeuw, and L. Zhu. Fornax 3D project: a two-dimensional view of the stellar initial mass function in the massive lenticular galaxy FCC 167. *Astronomy & Astrophysics*, 626:A124, June 2019. doi: 10.1051/0004-6361/201935360.

N. J. McConnell and C.-P. Ma. Revisiting the Scaling Relations of Black Hole Masses and Host Galaxy Properties. *The Astrophysical Journal*, 764(2):184, Feb. 2013. doi: 10.1088/0004-637X/764/2/184.

J. P. McMullin, B. Waters, D. Schiebel, W. Young, and K. Golap. CASA Architecture and Applications. In R. A. Shaw, F. Hill, and D. J. Bell, editors, *Astronomical Data Analysis Software and Systems XVI*, volume 376 of *Astronomical Society of the Pacific Conference Series*, page 127, Oct. 2007.

S. Mei, J. P. Blakeslee, P. Côté, J. L. Tonry, M. J. West, L. Ferrarese, A. Jordán, E. W. Peng, A. Anthony, and D. Merritt. The ACS Virgo Cluster Survey. XIII. SBF Distance Catalog and the Three-dimensional Structure of the Virgo Cluster. *The Astrophysical Journal*, 655(1):144–162, Jan. 2007. doi: 10.1086/509598.

J. Melnick and M. Moles. On the origin of the dipole anisotropy of the cosmic microwave background: beyond the Hydra-Centaurus supercluster. *Revista Mexicana de Astronomía y Astrofísica*, 14:72–76, May 1987.

D. Merritt. *Dynamics and Evolution of Galactic Nuclei*. 2013.

M. Miyoshi, J. Moran, J. Herrnstein, L. Greenhill, N. Nakai, P. Diamond, and M. Inoue. Evidence for a black hole from high rotation velocities in a sub-parsec region of NGC4258. *Nature*, 373(6510):127–129, Jan. 1995. doi: 10.1038/373127a0.

N. Neumayer, M. Cappellari, J. Reunanen, H. W. Rix, P. P. van der Werf, P. T. de Zeeuw, and R. I. Davies. The Central Parsecs of Centaurus A: High-excitation Gas, a Molecular Disk, and the Mass of the Black Hole. *The Astrophysical Journal*, 671(2):1329–1344, Dec. 2007. doi: 10.1086/523039.

M. Newville, T. Stensitzki, D. B. Allen, M. Rawlik, A. Ingargiola, and A. Nelson. Lmfit: Non-Linear Least-Square Minimization and Curve-Fitting for Python, June 2016.

D. D. Nguyen, M. den Brok, A. C. Seth, T. A. Davis, J. E. Greene, M. Cappellari, J. B. Jensen, S. Thater, S. Iguchi, M. Imanishi, T. Izumi, K. Nyland, N. Neumayer, K. Nakanishi, P. M. Nguyen, T. Tsukui, M. Bureau, K. Onishi, N.-L. Quang, and N. M. Le. The MBHBM$_\star$ Project. I. Measurement of the Central Black Hole Mass in Spiral Galaxy NGC 3504 Using Molecular Gas Kinematics. *The Astrophysical Journal*, 892(1):68, Mar. 2020. doi: 10.3847/1538-4357/ab77aa.

D. D. Nguyen, T. Izumi, S. Thater, M. Imanishi, T. Kawamuro, S. Baba, S. Nakano, J. L. Turner, K. Kohno, S. Matsushita, S. Martín, D. S. Meier, P. M. Nguyen, and L. T. Nguyen. Black hole mass measurement using ALMA observations of [CI] and CO emissions in the Seyfert 1 galaxy NGC 7469. *Monthly Notices of the Royal Astronomical Society*, 504(3): 4123–4142, July 2021. doi: 10.1093/mnras/stab1002.

D. D. Nguyen, M. Bureau, S. Thater, K. Nyland, M. den Brok, M. Cappellari, T. A. Davis, J. E. Greene, N. Neumayer, M. Imanishi, T. Izumi, T. Kawamuro, S. Baba, P. M. Nguyen, S. Iguchi, T. Tsukui, T. N. Lam, and T. Ho. The MBHBM* Project - II. Molecular gas kinematics in the lenticular galaxy NGC 3593 reveal a supermassive black hole. *Monthly Notices of the Royal Astronomical Society*, 509(2):2920–2939, Jan. 2022. doi: 10.1093/mnras/stab3016.

E. V. North, T. A. Davis, M. Bureau, M. Cappellari, S. Iguchi, L. Liu, K. Onishi, M. Sarzi, M. D. Smith, and T. G. Williams. WISDOM project - V. Resolving molecular gas in Keplerian rotation around the supermassive black hole in NGC 0383. *Monthly Notices of the Royal Astronomical Society*, 490(1):319–330, Nov. 2019. doi: 10.1093/mnras/stz2598.

W. M. M. Okoń and W. E. Harris. Globular Cluster Systems in Four Brightest Cluster Galaxies: A262, A3560, A3565, and A3742. *The Astrophysical Journal*, 567(1):294–303, Mar. 2002. doi: 10.1086/338386.

K. Onishi, S. Iguchi, K. Sheth, and K. Kohno. A Measurement of the Black Hole Mass in NGC 1097 Using ALMA. *The Astrophysical Journal*, 806(1):39, June 2015. doi: 10.1088/0004-637X/806/1/39.

K. Onishi, S. Iguchi, T. A. Davis, M. Bureau, M. Cappellari, M. Sarzi, and L. Blitz. WISDOM project - I. Black hole mass measurement using molecular gas kinematics in NGC 3665. *Monthly Notices of the Royal Astronomical Society*, 468(4):4663–4674, July 2017. doi: 10.1093/mnras/stx631.

J. Osorno, N. Nagar, T. Richtler, P. Humire, K. Gebhardt, and K. Gultekin. Revisiting the black hole mass of M87* using VLT/MUSE Adaptive Optics Integral Field Unit data I: Ionized gas kinematics. *arXiv e-prints*, art. arXiv:2304.11264, Apr. 2023. doi: 10.48550/arXiv.2304.11264.

G. Paturel, C. Petit, P. Prugniel, G. Theureau, J. Rousseau, M. Brouty, P. Dubois, and L. Cambrésy. HYPERLEDA. I. Identification and designation of galaxies. *Astronomy & Astrophysics*, 412:45–55, Dec. 2003. doi: 10.1051/0004-6361:20031411.

C. Y. Peng, L. C. Ho, C. D. Impey, and H.-W. Rix. Detailed Structural Decomposition of Galaxy Images. *The Astronomical Journal*, 124(1):266–293, July 2002. doi: 10.1086/340952.

V. Petrosian. The Luminosity Function of Quasars and its Evolution: a Comparison of Optically Selected Quasars and Quasars Found in Radio Catalogs. *The Astrophysical Journal*, 183:359–382, July 1973. doi: 10.1086/152233.

V. Pota, A. W. Graham, D. A. Forbes, A. J. Romanowsky, J. P. Brodie, and J. Strader. The SLUGGS survey: probing the supermassive black hole connection with bulges and haloes using red and blue globular cluster systems. *Monthly Notices of the Royal Astronomical Society*, 433(1):235–242, July 2013. doi: 10.1093/mnras/stt718.

S. Ravindranath, L. C. Ho, and A. V. Filippenko. Nuclear Cusps and Cores in Early-Type Galaxies as Relics of Binary Black Hole Mergers. *The Astrophysical Journal*, 566(2):801–808, Feb. 2002. doi: 10.1086/338228.

T. V. Ricci, J. E. Steiner, and R. B. Menezes. Integral field unit spectroscopy of 10 early-type galactic nuclei - I. Principal component analysis Tomography and nuclear activity. *Monthly Notices of the Royal Astronomical Society*, 440(3):2419–2441, May 2014. doi: 10.1093/mnras/stu441.

D. O. Richstone and S. Tremaine. Dynamical models of M 87 without a central black hole. *The Astrophysical Journal*, 296:370–378, Sept. 1985. doi: 10.1086/163455.

G. H. Rieke and M. J. Lebofsky. The interstellar extinction law from 1 to 13 microns. *The Astrophysical Journal*, 288:618–621, Jan. 1985. doi: 10.1086/162827.

A. G. Riess, W. Yuan, L. M. Macri, D. Scolnic, D. Brout, S. Casertano, D. O. Jones, Y. Murakami, G. S. Anand, L. Breuval, T. G. Brink, A. V. Filippenko, S. Hoffmann, S. W. Jha, W. D'arcy Kenworthy, J. Mackenty, B. E. Stahl, and W. Zheng. A Comprehensive Measurement of the Local Value of the Hubble Constant with 1 km s^{-1} Mpc^{-1} Uncertainty from the Hubble Space Telescope and the SH0ES Team. *The Astrophysical Journal Letters*, 934(1):L7, July 2022. doi: 10.3847/2041-8213/ac5c5b.

D. H. Rogstad, I. A. Lockhart, and M. C. H. Wright. Aperture-synthesis observations of H I in the galaxy M83. *The Astrophysical Journal*, 193:309–319, Oct. 1974. doi: 10.1086/153164.

I. Ruffa, T. A. Davis, I. Prandoni, R. A. Laing, R. Paladino, P. Parma, H. de Ruiter, V. Casasola, M. Bureau, and J. Warren. The AGN fuelling/feedback cycle in nearby radio galaxies - II. Kinematics of the molecular gas. *Monthly Notices of the Royal Astronomical Society*, 489(3):3739–3757, Nov. 2019. doi: 10.1093/mnras/stz2368.

I. Ruffa, T. A. Davis, M. Cappellari, M. Bureau, J. S. Elford, S. Iguchi, F. Lelli, F.-H. Liang, L. Liu, A. Lu, M. Sarzi, and T. G. Williams. WISDOM project – XIV. SMBH mass in the early-type galaxies NGC0612, NGC1574, and NGC4261 from CO dynamical modelling. *arXiv e-prints*, art. arXiv:2304.06117, Apr. 2023. doi: 10.48550/arXiv.2304.06117.

S. P. Rusli, J. Thomas, R. P. Saglia, M. Fabricius, P. Erwin, R. Bender, N. Nowak, C. H. Lee, A. Riffeser, and R. Sharp. The Influence of Dark Matter Halos on Dynamical Estimates of Black Hole Mass: 10 New Measurements for High-σ Early-type Galaxies. *The Astronomical Journal*, 146(3):45, Sept. 2013. doi: 10.1088/0004-6256/146/3/45.

E. E. Salpeter. The Luminosity Function and Stellar Evolution. *The Astrophysical Journal*, 121:161, Jan. 1955. doi: 10.1086/145971.

E. E. Salpeter. Accretion of Interstellar Matter by Massive Objects. *The Astrophysical Journal*, 140:796–800, Aug. 1964. doi: 10.1086/147973.

K. M. Sandstrom, A. K. Leroy, F. Walter, A. D. Bolatto, K. V. Croxall, B. T. Draine, C. D. Wilson, M. Wolfire, D. Calzetti, R. C. Kennicutt, G. Aniano, J. Donovan Meyer, A. Usero, F. Bigiel, E. Brinks, W. J. G. de Blok, A. Crocker, D. Dale, C. W. Engelbracht, M. Galametz, B. Groves, L. K. Hunt, J. Koda, K. Kreckel, H. Linz, S. Meidt, E. Pellegrini, H. W. Rix, H. Roussel, E. Schinnerer, A. Schruba, K. F. Schuster, R. Skibba, T. van der Laan, P. Appleton, L. Armus, B. Brandl, K. Gordon, J. Hinz, O. Krause, E. Montiel, M. Sauvage, A. Schmiedeke, J. D. T. Smith, and L. Vigroux. The CO-to-H_2 Conversion Factor and Dust-to-gas Ratio on Kiloparsec Scales in Nearby Galaxies. *The Astrophysical Journal*, 777(1):5, Nov. 2013. doi: 10.1088/0004-637X/777/1/5.

W. L. W. Sargent, P. J. Young, A. Boksenberg, K. Shortridge, C. R. Lynds, and F. D. A. Hartwick. Dynamical evidence for a central mass concentration in the galaxy M87. *The Astrophysical Journal*, 221:731–744, May 1978. doi: 10.1086/156077.

M. Sarzi, E. Iodice, L. Coccato, E. M. Corsini, P. T. de Zeeuw, J. Falcón-Barroso, D. A. Gadotti, M. Lyubenova, R. M. McDermid, G. van de Ven, K. Fahrion, A. Pizzella, and L. Zhu. Fornax3D project: Overall goals, galaxy sample, MUSE data analysis, and initial results. *Astronomy & Astrophysics*, 616:A121, Aug. 2018. doi: 10.1051/0004-6361/201833137.

J. Scharwächter, P. J. McGregor, M. A. Dopita, and T. L. Beck. Kinematics and excitation of the molecular hydrogen accretion disc in NGC 1275. *Monthly Notices of the Royal Astronomical Society*, 429(3):2315–2332, Mar. 2013. doi: 10.1093/mnras/sts502.

E. F. Schlafly and D. P. Finkbeiner. Measuring Reddening with Sloan Digital Sky Survey Stellar Spectra and Recalibrating SFD. *The Astrophysical Journal*, 737(2):103, Aug. 2011. doi: 10.1088/0004-637X/737/2/103.

M. Schmidt. 3C 273 : A Star-Like Object with Large Red-Shift. *Nature*, 197(4872):1040, Mar. 1963. doi: 10.1038/1971040a0.

M. Schmidt. Space Distribution and Luminosity Functions of Quasi-Stellar Radio Sources. *The Astrophysical Journal*, 151:393, Feb. 1968. doi: 10.1086/149446.

M. Schmidt. Space Distribution and Luminosity Functions of Quasars. *The Astrophysical Journal*, 162:371, Nov. 1970. doi: 10.1086/150668.

J. Schulz, U. Fritze-v. Alvensleben, and K. J. Fricke. Wavelength and redshift dependence of bulge/total light ratios in galaxies. *Astronomy & Astrophysics*, 398:89–100, Jan. 2003. doi: 10.1051/0004-6361:20021631.

J. L. Sérsic. Influence of the atmospheric and instrumental dispersion on the brightness distribution in a galaxy. *Boletin de la Asociacion Argentina de Astronomia La Plata Argentina*, 6:41–43, Feb. 1963.

K. L. Shapiro, M. Cappellari, T. de Zeeuw, R. M. McDermid, K. Gebhardt, R. C. E. van den Bosch, and T. S. Statler. The black hole in NGC 3379: a comparison of gas and stellar dynamical mass measurements with HST and integral-field data. *Monthly Notices of the Royal Astronomical Society*, 370(2):559–579, Aug. 2006. doi: 10.1111/j.1365-2966.2006.10537.x.

D. A. Simon, M. Cappellari, and J. Hartke. Supermassive black hole mass in the massive elliptical galaxy M87 from integral-field stellar dynamics using OASIS and MUSE with adaptive optics: assessing systematic uncertainties. *arXiv e-prints*, art. arXiv:2303.18229, Mar. 2023. doi: 10.48550/arXiv.2303.18229.

M. D. Smith, M. Bureau, T. A. Davis, M. Cappellari, L. Liu, E. V. North, K. Onishi, S. Iguchi, and M. Sarzi. WISDOM project - IV. A molecular gas dynamical measurement of the supermassive black hole mass in NGC 524. *Monthly Notices of the Royal Astronomical Society*, 485(3):4359–4374, May 2019. doi: 10.1093/mnras/stz625.

M. D. Smith, M. Bureau, T. A. Davis, M. Cappellari, L. Liu, K. Onishi, S. Iguchi, E. V. North, M. Sarzi, and T. G. Williams. WISDOM project - VII. Molecular gas measurement of the supermassive black hole mass in the elliptical galaxy NGC 7052. *Monthly Notices of the Royal Astronomical Society*, 503(4):5984–5996, June 2021. doi: 10.1093/mnras/stab791.

L. S. Sparke and I. Gallagher, John S. *Galaxies in the Universe*. 2007.

K. Spekkens and J. A. Sellwood. Modeling Noncircular Motions in Disk Galaxies: Application to NGC 2976. *The Astrophysical Journal*, 664(1):204–214, July 2007. doi: 10.1086/518471.

P. J. Teuben. Velocity Fields of Disk Galaxies. In E. Athanassoula, A. Bosma, and R. Mujica, editors, *Disks of Galaxies: Kinematics, Dynamics and Peturbations*, volume 275 of *Astronomical Society of the Pacific Conference Series*, pages 217–228, Dec. 2002. doi: 10.48550/arXiv.astro-ph/0204471.

J. Thomas, R. P. Saglia, R. Bender, P. Erwin, and M. Fabricius. The Dynamical Fingerprint of Core Scouring in Massive Elliptical Galaxies. *The Astrophysical Journal*, 782(1):39, Feb. 2014. doi: 10.1088/0004-637X/782/1/39.

J. L. Tonry. Evidence for a central mass concentration in M 32. *The Astrophysical Journal Letters*, 283:L27–L30, Aug. 1984. doi: 10.1086/184326.

J. L. Tonry. A Central Black Hole in M32. *The Astrophysical Journal*, 322:632, Nov. 1987. doi: 10.1086/165758.

J. L. Tonry, A. Dressler, J. P. Blakeslee, E. A. Ajhar, A. B. Fletcher, G. A. Luppino, M. R. Metzger, and C. B. Moore. The SBF Survey of Galaxy Distances. IV. SBF Magnitudes, Colors, and Distances. *The Astrophysical Journal*, 546(2):681–693, Jan. 2001. doi: 10.1086/318301.

R. B. Tully, H. M. Courtois, A. E. Dolphin, J. R. Fisher, P. Héraudeau, B. A. Jacobs, I. D. Karachentsev, D. Makarov, L. Makarova, S. Mitronova, L. Rizzi, E. J. Shaya, J. G. Sorce, and P.-F. Wu. Cosmicflows-2: The Data. *The Astronomical Journal*, 146(4):86, Oct. 2013. doi: 10.1088/0004-6256/146/4/86.

D. Utomo, L. Blitz, T. Davis, E. Rosolowsky, M. Bureau, M. Cappellari, and M. Sarzi. Giant Molecular Clouds in the Early-type Galaxy NGC 4526. *The Astrophysical Journal*, 803 (1):16, Apr. 2015. doi: 10.1088/0004-637X/803/1/16.

S. Vaddi, C. P. O'Dea, S. A. Baum, S. Whitmore, R. Ahmed, K. Pierce, and S. Leary. Constraints on Feedback in the Local Universe: The Relation between Star Formation and AGN Activity in Early-type Galaxies. *The Astrophysical Journal*, 818(2):182, Feb. 2016. doi: 10.3847/0004-637X/818/2/182.

R. C. E. van den Bosch and P. T. de Zeeuw. Estimating black hole masses in triaxial galaxies. *Monthly Notices of the Royal Astronomical Society*, 401(3):1770–1780, Jan. 2010. doi: 10.1111/j.1365-2966.2009.15832.x.

A. Vazdekis, P. Sánchez-Blázquez, J. Falcón-Barroso, A. J. Cenarro, M. A. Beasley, N. Cardiel, J. Gorgas, and R. F. Peletier. Evolutionary stellar population synthesis with MILES - I. The base models and a new line index system. *Monthly Notices of the Royal Astronomical Society*, 404(4):1639–1671, June 2010. doi: 10.1111/j.1365-2966.2010.16407.x.

G. Vettolani, G. Chincarini, R. Scaramella, and G. Zamorani. Redshifts of Clusters in the Alpha Region. *The Astronomical Journal*, 99:1709, June 1990. doi: 10.1086/115451.

S. Viaene, M. Sarzi, M. Baes, J. Fritz, and I. Puerari. MUSE stares into the shadows: the high-resolution dust attenuation curve of NGC 5626. *Monthly Notices of the Royal Astronomical Society*, 472(2):1286–1299, Dec. 2017. doi: 10.1093/mnras/stx1781.

S. Viaene, M. Sarzi, N. Zabel, L. Coccato, E. M. Corsini, T. A. Davis, P. De Vis, P. T. de Zeeuw, J. Falcón-Barroso, D. A. Gadotti, E. Iodice, M. Lyubenova, R. McDermid, L. Morelli, B. Nedelchev, F. Pinna, T. W. Spriggs, and G. van de Ven. The Fornax 3D project: dust mix and gas properties in the centre of early-type galaxy FCC 167. *Astronomy & Astrophysics*, 622:A89, Feb. 2019. doi: 10.1051/0004-6361/201834465.

J. L. Walsh, A. J. Barth, L. C. Ho, and M. Sarzi. The M87 Black Hole Mass from Gas-dynamical Models of Space Telescope Imaging Spectrograph Observations. *The Astrophysical Journal*, 770(2):86, June 2013. doi: 10.1088/0004-637X/770/2/86.

J. L. Walsh, J. E. Greene, C. Liepold, and C.-P. Ma. Probing the M87 Supermassive Black Hole with Parsec-Scale Stellar Dynamics. JWST Proposal. Cycle 1, ID. #2228, Mar. 2021.

J. A. Willick, S. Courteau, S. M. Faber, D. Burstein, A. Dekel, and M. A. Strauss. Homogeneous Velocity-Distance Data for Peculiar Velocity Analysis. III. The Mark III Catalog of Galaxy Peculiar Velocities. *The Astrophysical Journal Supplement*, 109(2):333–366, Apr. 1997. doi: 10.1086/312983.

C. N. A. Willmer. The Absolute Magnitude of the Sun in Several Filters. *The Astrophysical Journal Supplement*, 236(2):47, June 2018. doi: 10.3847/1538-4365/aabfdf.

C. N. A. Willmer, M. A. G. Maia, S. O. Mendes, M. V. Alonso, L. A. Rios, O. L. Chaves, and D. F. de Mello. Two Galaxy Clusters: A3565 and A3560. *The Astronomical Journal*, 118(3):1131–1145, Sept. 1999. doi: 10.1086/301006.

L. M. Young, M. Bureau, T. A. Davis, F. Combes, R. M. McDermid, K. Alatalo, L. Blitz, M. Bois, F. Bournaud, M. Cappellari, R. L. Davies, P. T. de Zeeuw, E. Emsellem, S. Khochfar, D. Krajnović, H. Kuntschner, P.-Y. Lablanche, R. Morganti, T. Naab, T. Oosterloo, M. Sarzi, N. Scott, P. Serra, and A.-M. Weijmans. The ATLAS^{3D} project - IV. The molecular gas content of early-type galaxies. *Monthly Notices of the Royal Astronomical Society*, 414(2):940–967, June 2011. doi: 10.1111/j.1365-2966.2011.18561.x.

P. J. Young, J. A. Westphal, J. Kristian, C. P. Wilson, and F. P. Landauer. Evidence for a supermassive object in the nucleus of the galaxy M87 from SIT and CCD area photometry. *ApJ*, 221:721–730, May 1978. doi: 10.1086/156076.

N. Zabel, T. A. Davis, M. W. L. Smith, N. Maddox, G. J. Bendo, R. Peletier, E. Iodice, A. Venhola, M. Baes, J. I. Davies, I. de Looze, H. Gomez, M. Grossi, J. D. P. Kenney, P. Serra, F. van de Voort, C. Vlahakis, and L. M. Young. The ALMA Fornax Cluster Survey I: stirring and stripping of the molecular gas in cluster galaxies. *Monthly Notices of the Royal Astronomical Society*, 483(2):2251–2268, Feb. 2019. doi: 10.1093/mnras/sty3234.

N. Zabel, T. A. Davis, M. Sarzi, B. Nedelchev, M. Chevance, J. M. D. Kruijssen, E. Iodice, M. Baes, G. J. Bendo, E. M. Corsini, I. De Looze, P. T. de Zeeuw, D. A. Gadotti, M. Grossi, R. Peletier, F. Pinna, P. Serra, F. van de Voort, A. Venhola, S. Viaene, and C. Vlahakis. AlFoCS + Fornax3D: resolved star formation in the Fornax cluster with ALMA and MUSE. *Monthly Notices of the Royal Astronomical Society*, 496(2):2155–2182, Aug. 2020. doi: 10.1093/mnras/staa1513.

Y. B. Zel'dovich. The Fate of a Star and the Evolution of Gravitational Energy Upon Accretion. *Soviet Physics Doklady*, 9:195, Sept. 1964.

P. Zhu, L. C. Ho, and H. Gao. The Correlation between Black Hole Mass and Stellar Mass for Classical Bulges and the Cores of Ellipticals. *The Astrophysical Journal*, 907(1):6, Jan. 2021. doi: 10.3847/1538-4357/abcaa1.